Wydział Chemii Uniwersytetu Gdańskiego

mgr Adrian Koterwa

Charakterystyka i modyfikacja materiałów elektrodowych w celu uzyskania platform biosensorycznych

Promotor:

dr hab. Paweł Lucjan Niedziałkowski, prof. UG

*Praca doktorska wykonana
w Katedrze Chemii Analitycznej
Uniwersytetu Gdańskiego*

Gdańsk 2024

Bardzo serdecznie dziękuję,

mojemu promotorowi

Panu dr. hab. Pawłowi Niedziałkowskiemu, prof. UG,

za ogrom przekazanej wiedzy, pomocy i wsparcia,

cierpliwość i poświęcony czas,

dr. hab. inż. Jackowi Rylowi, prof. PG,

za trzymanie terminów,

przekazaną wiedzę merytoryczną

i możliwość ciągłego rozwoju,

mojej kochanej żonie Amandzie,

za miłość, wsparcie, cierpliwość

oraz za bycie moją największą inspiracją,

Całej Katedrze Chemii Analitycznej,

za wspaniałą atmosferę w pracy.

SPIS TREŚCI

DOROBEK NAUKOWY

I.   Artykuły wchodzące w cykl rozprawy doktorskiej

1.   P. Niedziałkowski, **A. Koterwa**, A. Olejnik, A. Zieliński, K. Górnicka, M. Brodowski, R. Bogdanowicz, J. Ryl, "Deciphering the molecular mechanism of substrate-induced assembly of gold nanocube arrays toward an accelerated electrocatalytic effect employing heterogeneous diffusion field confinement", Langmuir, 38, 31, 2022, 9597-9610, IF_{2022} 3,9, MNiSW 100 pkt

2.   **A. Koterwa**, M. Pierpaoli, B. Nejman-Faleńczyk, S. Bloch, A. Zieliński, W. Adamus-Białek, Z. Jeleniewska, B. Trzaskowski, R. Bogdanowicz, G. Węgrzyn, P. Niedziałkowski, J. Ryl, "Discriminating macromolecular interactions based on an impedimetric fingerprint supported by multivariate data analysis for rapid and label-free *Escherichia coli* recognition in human urine", Biosensors & Bioelectronics, 238, 2023, 115561, IF_{2023} 10,7, MNiSW 200 pkt

3.   **A. Koterwa**, M. Bojko, J. Ryl, K. Łukaszuk, K. Kozłowska, W. Sieklicki, S. Rodziewicz-Motowidło, P. Niedziałkowski, "An electrochemical biosensor for the determination of hormone Human Chorionic Gonadotropin (hCG) in human serum", Electroanalysis, 2023, 35, 1-9, IF_{2023} 2,7, MNiSW 70 pkt

4.   **A. Koterwa,** I. Kaczmarzyk, Sz. Mania, M. Cieślik, R. Tylingo, T. Ossowski, R. Bogdanowicz, P. Niedziałkowski, J. Ryl, "The role of electrolysis and enzymatic hydrolysis treatment in the enhancement of the electrochemical properties of 3D-printed carbon black/poly(lactic acid) structures", Applied Surface Science, 574, 2022, 151587, IF_{2022} 6,7, MNiSW 140 pkt

II.   Artykuły nie wchodzące w skład rozprawy doktorskiej

1.   K. Kozłowska, M. Cieślik, **A. Koterwa**, K. Formela, J. Ryl, P. Niedziałkowski, "Microwave-induced processing of free-standing 3D printouts: an effortless route to high-redox kinetics in electroanalysis", Materials, 2833, 2024, IF_{2023} 3,1, MNiSW 140 pkt

2.   M. J. Glowacki, M. Cieslik, M. Sawczak, **A. Koterwa**, I. Kaczmarzyk, R. Jendrzejewski, L. Szynkiewicz, T. Ossowski, R. Bogdanowicz, P. Niedzialkowski, J. Ryl, "Helium-assisted, solvent-free electro-activation of 3D printed conductive carbon-polylactide electrodes by pulsed laser ablation", Applied Surface Science, 556, 2021, 149788, 1-11, IF_{2021} 7,392, MNiSW 140 pkt

3. A. Kulpa, J. Ryl, G. Skowierzak, **A. Koterwa**, G. Schroeder, T. Ossowski, P. Niedziałkowski, "Comparison of cadmium Cd^{2+} and lead Pb^{2+} binding by $Fe_3O_4@SiO_2$–EDTA nanoparticles - binding stability and kinetic studies", Electroanalysis, 32, 3, 2020, 588-597, IF_{2022} 3,22, MNiSW 70 pkt

4. A. Kulpa, J. Ryl, G. Schroeder, **A. Koterwa**, J. Sein Anand, T. Ossowski, P. Niedziałkowski, "Simultaneous voltammetric determination of Cd^{2+}, Pb^{2+} and Cu^{2+} ions captured by $Fe_3O_4@SiO_2$ core-shell nanostructures of various outer amino chain length", Journal of Molecular Liquids, 314, 2020, 1-11, IF_{2020} 6,16, MNiSW 100 pkt

III. Rozdziały w monografiach

1. A. Kulpa-Koterwa, G. Schroeder, T. Ossowski, **A. Koterwa**, P. Niedziałkowski, „Nanostruktury magnetyczne typu core-shell $Fe_3O_4@SiO_2$–Nn jako nowe adsorbenty jonów metali ciężkich Cd^{2+}, Pb^{2+} oraz Cu^{2+} – badania elektrochemiczne", Na pograniczu chemii, biologii i fizyki, vol. 3, 2022, Wydawnictwo Naukowe Uniwersytetu Mikołaja Kopernika, ISBN 978-83-231-4836-4, 121-136, MNiSW 20 pkt

2. A. Kulpa, D. Zarzeczańska, P. Niedziałkowski, **A. Koterwa**, T. Ossowski, „Kwasowość oraz trwałość w roztworze dipodstawionych pochodnych kwasu fenyloboronowego", Na pograniczu chemii i biologii, vol. 39, 2019, Wydawnictwo Naukowe Uniwersytetu im. Adama Mickiewicza, ISBN 978-83-232-3593-4, 171-182, MNiSW 20 pkt

STRESZCZENIE

Platformy biosensoryczne oparte na modyfikowanych materiałach elektrodowych mają za zadanie szybko i nieinwazyjnie wykrywać anality i bioanality z roztworów oraz płynów ustrojowych. Dlatego, aby zapewnić stabilną platformę projektuje się biosensory bazujące na nanomateriałach osadzonych na powierzchni elektrod.

Celem rozprawy doktorskiej było opracowanie metody oraz ocena stopnia modyfikacji wybranych elektrod oraz nanomateriałów, które stanowiły podstawę platformy biosensorycznej do elektrochemicznego wykrywania bioanalitów: uropatogennych szczepów bakterii *Escherichia coli* (UPEC-57) i hormonu ludzkiej gonadotropiny kosmówkowej (hCG). Jako przedmiot badań wybrano takie materiały elektrodowe jak GC, ITO, Au oraz CB-PLA, natomiast podstawę elektrochemicznego biosensora stanowiły nanosześciany złota. Wybór AuNCs podyktowany był ich zdolnością do samoorganizacji się na powierzchni elektrody i możliwości modyfikacji. W pierwszym kroku dokładnie scharakteryzowano elektrochemicznie materiały elektrodowe GC, ITO, Au przed i po procesie modyfikacji za pomocą AuNCs. Sprawdzono również, wpływ surfaktantu CTAB na przebieg reakcji elektrodowych. Dowiedziono, że najlepszym materiałem do dalszych badań jest elektroda GC, natomiast surfaktant musi zostać dokładnie usunięty, ponieważ utrudnia dalsze etapy funkcjonalizacji. W kolejnym etapie zoptymalizowano i przeprowadzono proces modyfikacji powierzchni elektrody GC za pomocą AuNCs, wyselekcjonowanymi sekwencjami nici DNA oraz polimerazą RNA, a jego skuteczność sprawdzano metodami elektrochemicznymi: CV, EIS oraz DEIS. Wyniki przeprowadzonych badań udowodniły możliwość detekcji UPEC-57 na bardzo niskim poziomie stężeń i w krótkim czasie. Następnie przeprowadzono modyfikację elektrody złotej za pomocą syntetycznego peptydu specyficznie oddziałowującym z hormonem hCG. Udowodniono, że hormon ten można wykrywać na bardzo niskim poziomie stężeń zarówno w roztworach soli fizjologicznej jak i surowicy ludzkiej. Ponadto zaproponowano użycie CB-PLA jako alternatywy do komercyjnych elektrod. Najpierw należało jednak opracować i porównać sposoby aktywacji nowych elektrod CB-PLA uzyskanych metodą druku 3D poprzez aktywację elektrochemiczną i trawienie enzymatyczne. Wykazano, że zaproponowany sposób aktywacji elektrod w roztworze alkaicznym znacząco poprawił szybkość reakcji elektrodowej oraz zwiększył elektrochemicznie aktywną powierzchnię. Trawienie enzymatyczne, również doprowadziło do aktywacji powierzchni elektrod

w porównywalnym stopniu jak w przypadku aktywacji elektrochemicznej w środowisku zasadowym.

Zaprojektowno platformę sensoryczną na bazie modyfikowanych elektrod CB-PLA za pomocą AuNCs oraz przeciwciał anty-hCG w celu wykrywania hormonu hCG. Skuteczność powyższego biosensora zbadano w roztworze soli fizjologicznej oraz surowicy ludzkiej. Wyniki badań elektrochemicznych pokazały, że powyższy bioczujnik wykrywa hormon na bardzo niskim poziomie, natomiast zastosowanie AuNCs znacznie poprawiło odtwarzalność i powtarzalność wyników pomiarów prowadzonych w ludzkiej surowicy.

DISSERTATION ABSTRACT

Biosensor platforms based on modified electrode materials are designed to quickly and non-invasively detect analytes and bioanalytes from solutions and body fluids. Therefore, to ensure a stable platform, biosensors based on nanomaterials deposited on the surface of electrodes are designed.

The subject of the doctoral dissertation was to develop a method and assess the degree of modification of selected electrodes and nanomaterials, which were the basis of the biosensor platform for electrochemical detection of bioanalytes: propathogenic strains of Escherichia coli bacteria (UPEC-57) and the hormone human chorionic gonadotropin (hCG). The electrode materials selected as the subject of the research were GC, ITO, Au and CB-PLA, while the basis of the electrochemical biosensor were gold nanocubes. The selection of AuNCs was determined their ability to self-organize on the electrode surface and the possibility of further modification. In the first step, the GC, ITO, Au electrode materials were thoroughly electrochemically characterized before and after the modification process using AuNCs. The effect of the CTAB surfactant on the process of electrode reactions was also checked. It was proven that the best material for further research is the GC electrode, but the surfactant must be carefully removed because it inhibit the further modification steps. In the next stage of research, the GC electrode surface modification process was optimized and carried out using AuNCs, selected DNA strand sequences and RNA polymerase. Also, its effectiveness was checked using electrochemical methods: CV, EIS and DEIS. The results of the conducted studies proved the possibility of detecting UPEC-57 at a very low concentration level and in a short time. Subsequently, the gold electrode was modified using a synthetic peptide specifically interacting with the hCG hormone. It was proven that this hormone can be detected at a very low concentration level in both physiological saline solutions and human serum. Moreover, the use of CB-PLA was proposed as an alternative to commercial electrodes. However in the first stage it was necessary to develop and compare the method of activation of new CB-PLA electrodes obtained by 3D printing by electrochemical activation and enzymatic etching. It was shown that the proposed method of electrode activation in an alkaline solution significantly improved the rate of the electrode reaction and increased the electrochemically active surface. Enzymatic etching also led to the activation of the electrode surface to a comparable extent as in the case of electrochemical activation in an alkaline solution.

In the last stage, the results of the research on the modification of CB-PLA electrodes using AuNCs and anty-hCG antibodies to detect the hCG hormone were presented. The effectiveness of the above biosensor platform was tested in physiological saline solution and human serum. The experimental results proved that the proposed biosensor detects the hormone at a very low level, while the use of AuNCs significantly affected the reproducibility and repeatability of the measurement results conducted in human serum.

WYKAZ SYMBOLI I SKRÓTÓW

4-CPDS - sól 4-karboksyfenylodiazoniowa (ang. *4-carboxyphenyl diazonium salt*)

AFM - mikroskopia sił atomowych (AFM) (ang. *Atomic Force Microscopy*)

AgNPs - nanocząstki srebra (ang. *silver nanoparticles*)

AuAg - stop nanoporowaty złota i srebra (ang. *gold and silver nanoporous alloy*)

AQ - antrachinon (ang. *anthraquinone*)

ATP - adenozynotrójfosforan (ang. *adenosine triphosphate*)

AuNCs - nanosześciany złota (ang. *gold nanocubes*)

AuNPs-TiO$_2$ - nanocząstki złota zawierające nanocząstki tytanu (ang. *gold nanoparticles-titanium dioxide nanoparticles*)

AuNPs - nanocząstki złota (ang. *gold nanoparticles*)

AuNWs - nanodruty złota (ang. *gold nanowires*)

BDD - elektroda diamentowa domieszkowana borem (ang. *boron doped diamond electrode*)

BPA - bisfenol A (ang. *bisfenol A*)

CA - chronoamperometria (ang. *Chronoamperometry*)

CB - sadza (ang. *carbon black*)

CB-PLA - sadza/kwas polimlekowy (ang. *carbon black-poly(lactic acid)*)

Chi-PPy-AuNPs MWCNT - nanokompozyt chitozanu z wielościennymi nanorurkami węglowymi oraz polipyrolem i nanocząstkami złota (ang. *chitosan nanocomposite with multi-walled carbon nanotubes, polypyrrole and gold nanoparticles*)

CHT - chitozan (ang. *chitosan*)

CILE - płynna elektroda węglowo-jonowa (ang. *carbon ionic liquid electrode*)

CNTs - nanorurki węglowe (ang. *carbon nanotubes*)

CoPC - ftalocyjanina kobaltu(II) (ang. *cobalt(II) phthalocyanine*)

CPAD - kwas 4-cyjano-4-(fenylokarbonotioilotio)pentanowy (ang. *4-cyano-4-(phenylcarbonothioylthio)pentanoic acid*)

CPE - pastowa elektroda węglowa (ang. *carbon paste electrode*)

CV - woltamperometria cykliczna (ang. *Cyclic Voltammetry*)

CVD - osadzanie chemiczne z fazy gazowej (ang. *Chemical Vapour Deposition*)

CTAB - bromek heksadecylotrimetyloamoniowy (ang. *cetrimonium bromide*)

Cys - cystamina (ang. *cystamine*)

DEIS - dynamiczna elektrochemiczna spektroskopia impedancyjna (ang. *Dynamic Electrochemical* Impedance Spectroscopy)

DFT - teoria funkcjinału gęstości (ang. *density functional theory*)

DMF - dimetyloformamid (ang. *dimethylformamide*)

DNA - kwas deoksyrybonukleinowy (ang. *deoxyribonucleic acid*)

DPA - kwas 3,3-ditiodipropionowy (ang. *3,3-dithiodipropionic acid*)

DPV - różnicowa woltamperometria pulsowa (ang. *Differential Pulse Voltammetry*)

dsDNA - dwuniciowa forma kwasu deoksyrybonukleinowego (ang. *double stranded DNA*)

dsRNA - dwuniciowa forma kwasu rybonukleinowego (ang. *double stranded RNA*)

EASA - powierzchnia aktywna elektrochemicznie (EASA) (ang. *electrochemically active surface*)

EDC - 1-etylo-3-(3-dimetyloaminopropylo)karbodiimid (ang. *1-ethyl-3-(3-dimethylaminopropyl)carbodiimide*)

EIS - elektrochemiczna spektroskopia impedancyjna (ang. *Electrochemical Impedance Spectroscopy*)

Fc - ferrocen (ang. *ferrocene*)

Fe_2O_3 - tlenek żelaza (III) (ang. *iron(III) oxide*)

Fe_3O_4 - tlenek żelaza(II)diżelaza(III) (ang. *iron(II,III) oxide*)

Fe_3O_4-PLA - tlenek żelaza(II)diżelaza(III) z kwasem polimlekowym (ang. *Iron(II,III) oxide - poly(lactic acid)*)

FDM - modelowanie topionego osadzania (ang. *Fused Deposition Modelling*)

FFF - drukowanie włóknem topionego materiału (ang. *Fused Filament Fabrication*)

FSH - hormon folikulotropowy (ang. *follicle stimulating hormone*)

GA - aldehyd glutarowy (ang. *glutaraldehyde*)

GC,GCE - elektroda z węgla szklistego (ang. *glassy carbon electrode*)

GNF - złote nanostruktury w kształcie kwiatów (ang. *gold nanoflowers*)

GO - tlenek grafenu (ang. *graphene oxide*)

G-PLA - grafen z kwasem polimlekowym (ang. *graphene-poly(lactic acid)*)

GQD/GQDs - grafenowe kropki kwantowe (ang. *graphene quantum dots*)

GR - grafen (ang. *graphene*)

GS - arkusze grafenowe (ang. *graphene sheets*)

GS - IL - kompozyt z grafenu i cieczy jonowej (ang. *graphene sheets-ionic liquid*)

hCG - ludzka gonadotropina kosmówkowa (ang. *human chorionic gonadotropin*)

HER2 - receptor ludzkiego naskórkowego czynnika wzrostu - 2, (ang. *human epidermal growth factor receptor-2*)

HRP - peroksydaza chrzanowa (ang. *horseradish peroxidase*)

IL - ciecz jonowa (ang. *ionic liquid*)

In_2O_3 - tlenek indu(III) (ang. *indium(III) oxide*)

ITO - elektroda z tlenku cyny i indu (ang. *indium tin oxide*)

LH - hormon luteinizujący (ang. *luteinizing hormone*)

LSPR - zlokalizowany rezonans plazmonów powierzchniowych (ang. *Localized Surface Plasmon Resonances*)

MACA - kwas merkaptooctowy (ang. *mercaptoacetic acid*)

MB - błękit metylenowy (ang. *methylene blue*)

MCH - 6-merkapto-1-heksanol (ang. *6-mercapto-1-hexanol*)

MIDA - wieloparametryczna analiza dyskryminacyjna impedancji (ang. *multiparametric impedance discriminant analysis*)

MIP - polimer z odciskiem molekularnym (ang. *molecularly imprinted polymer*)

MPA - kwas 3-merkaptopropionowy (ang. *3-mercaptopropionic acid*)

MoS_2 - siarczek molibdenu(IV) (ang. *molybdenum(IV) sulfide*)

Mo_2O_3 - tlenek molibdenu (ang. molybdenum oxide)

rGO - zredukowany tlenek grafenu (ang. *reduced graphene oxide*)

MWCNTs - wielościenne nanorurki węglowe (ang. *multi walled carbon nanotubes*)

NHS - N-hydroksysukcynimid (ang. *N-hydroxysuccinimide*)

NiNPs - nanocząstki niklu (ang. *nickel nanoparticles*)

NPG - nanoporowate złoto (ang. *nanoporous gold*)

UV-Vis - spektroskopia UV-Vis (ang. *UV-Vis śpectroscopy*)

PAMAM - poli(amidoamina) (ang. *poly(amidoamine)*)

PBSE - ester sukcynimidylowy kwasu 1-pirenobutanowego (*1-pyrenebutanoic acid, succinimidyl ester*)

PCR - reakcja łańcuchowa polimerazy (ang. *polymerase chain reaction*)

PDDA - poli(chlorek diallilodimetyloamoniowy) (ang. *poly(diallyl-dimethylammonium chloride*)

PEDOT - poli(3,4-etylenodioksytiofen) (ang. *poly(3,4-ethylenedioxythiophene*))

PEG - polietylenoglikol (ang. *polyethylene glycol*)

PEI - poli(etylenoimina) (ang. *poly(ethylenimine*))

PGE - ołówkowa elektroda grafitowa (ang. *pencil graphite electrode*)

PG - grafit pirolityczny (ang. *pyrolytic graphite*)

PICA - kwas poli(indolo-6-karboksylowy) (ang. *poly(indole-6-carboxylic acid*))

PLA - kwas polimlekowy (ang. *poly(lactic acid*))

pLys - poli-L-lizyna, (ang. *poly-L-lysine*)

PNA - peptydowe kwasy nukleinowe (ang. *peptide nucleic acid*)

Ppy - polipirol (ang. *polypyrrole*)

PVD - fizyczne osadzanie z fazy gazowej (ang. *Physical Vapour Deposition*)

RNA - kwas rybonukleinowy (ang. *ribonucleic acid*)

SAM - samoorganizująca się monowarstwa (ang. *self-assambled monolayer*)

SEM - skaningowa mikroskopia elektronowa (ang. *Scanning Electron Microscop*y)

SG - sulfonowany grafen (ang. *sulfonated graphene*)

SPAN - sulfonowana polianilina (ang. *sulfonated polyaniline*)

SPCE - sitodrukowana elektroda węglowa (ang. *screen-printed carbon electrode*)

SPE - elektrody sitodrukowane (ang. *screen-printed electrodes*)

SP-IDME - modyfikowana mikroelektroda sitodrukowana (ang. *modified screen-printed interdigitated microelectrode*)

SnO_2 - tlenek cyny (IV) (ang. *tin (IV) oxide*)

ssDNA - jednoniciowa forma kwasu deoksyrybonukleinowego (ang. *single stranded DNA*)

ssRNA - jednoniciowa forma kwasu rybonukleinowego (ang. *single stranded RNA*)

SWCNT/SWNTs - jednościenne nanorurki węglowe (ang. *single-walled nanotube*)

SWV - woltamperometria fali prostokątnej (ang. *Square Wave Voltammetry*)

Tb - trombina (ang. *thrombin*)

TGA - analiza termograwimetryczna (ang. *Thermogravimetric Analysis*)

TET - tetracyklina (ang. *tetracycline*)

TiO_2 - tlenek tytanu(IV) (ang. *titanium(IV) oxide*)

TSH - hormon tyreotropowy (ang. *thyroid stimulating hormone*)

ZUT - zakażenie dróg moczowych (ang. *urinary tract infection*)

UPEC - uropatogenne szczepy bakterii *Escherichia coli* (ang. *uropathogenic Escherichia coli strains*)

XRD - dyfrakcja rentgenowska *(ang. X-ray Diffraction)*

XPS - spektroskopia fotoelektronów w zakresie promieniowania X (ang. *X-Ray Photoelectron Spectroscopy*)

I.   WPROWADZENIE

W ciągu ostatniej dekady biosensory elektrochemiczne stały się najbardziej dynamicznie rozwijającym się narzędziem do prostej i szybkiej elektroanalizy, wykorzystywanym w medycynie, badaniach środowiskowych i przemysłowych. Urządzenia te stanowią tańszą, szybszą i bardziej skuteczną alternatywę dla klasycznych technik stosowanych w wykrywaniu analitów i bioanalitów, co odgrywa kluczową rolę w badaniach laboratoryjnych.

Istnieje wiele biosensorów elektrochemicznych opartych na materiałach elektrodowych modyfikowanych za pomocą nanomateriałów i bioreceptorów, które selektywnie i specyficznie rozpoznają i wykrywają istotne cząsteczki w roztworach. Najczęściej wykorzystywanymi materiałami są nanostruktury złota, ze względu na prostotę syntezy oraz możliwości ich zastosowania w wielu obszarach badawczych. Nanostruktury złota można swobodnie modyfikować i projektować platformy biosensoryczne. Bioreceptory na bazie nanomateriałów zdolne są do selektywnego wychwytywania bioanalitów docelowych takich jak: enzymy, peptydy, przeciwciała, kwasy nukleinowe i wiele innych. Mimo, iż znanych jest wiele biosensorów elektrochemicznych bazujących na modyfikowanych materiałach elektrodowych za pomocą nanostruktur złota jest to wciąż aktualny temat badań.

Badania przedstawione w rozprawie doktorskiej obejmują opracowanie i ocenę stopnia modyfikacji materiałów elektrodowych nakierunkowanych na wykrywanie uropatogennych szczepów bakterii *Escherichia coli* (UPEC-57) oraz hormonu ludzkiej gonadotropiny kosmówkowej (hCG). Wykonano szereg eksperymentów elektrochemicznych z wykorzystaniem technik CV, DEIS oraz SECM. Na podstawie wykonanych badań DEIS przeprowadzono również wieloparametryczną analizę dyskryminacyjną impedancji (MIDA). Dodatkowo w prezentowanych artykułach wykonano charakterystykę platformy biosensorycznych technikami fizykochemicznymi: SEM, AFM, XPS, XRD, UV-Vis, TG. Ponadto, wyniki eksperymentalne zostały uzupełnione o techniki obliczeniowe, które wykonano za pomocą metod kwantowo-mechanicznych z wykorzystaniem teorii funkcjonału gęstości (DFT).

II. CZĘŚĆ LITERATUROWA

1. Biosensory elektrochemiczne

Biosensor elektrochemiczny jest urządzeniem analitycznym, które rejestruje sygnał oraz zmiany zarówno fizyczne, chemiczne jak i biologiczne w wymierną i przetwarzalną odpowiedź elektryczną (np. prąd, napięcie, impedancja itp.) [1]. Definicja biosensora elektrochemicznego na bazie elektrody jonoselektywnej po raz pierwszy została sformułowana przez Karla Cammanna w 1977 roku [2]. Koncepcja ta opierała się na definicji zintegrowanego urządzenia składającego się z receptora, przetwornika i wzmacniacza [3]. Aktualna definicja biosensora elektrochemicznego określa go jako samodzielne zintegrowane narzędzie, które ma możliwość dostarczania ilościowych lub półilościowych danych analitycznych [4]. Urządzenie to służy do analizy reakcji obejmujących transfery elektronów, które związane są ze zmianami chemicznymi i fizycznymi zachodzącymi w obszarze roboczym biosensora. Klasyczny biosensor elektrochemiczny składa się z następujących elementów (Rysunek 1.):

a) **bioreceptora** - cząsteczki lub biologicznej molekuły, która specyficznie rozpoznaje docelowy analit. Rolę bioreceptora mogą pełnić enzymy, komórki, białka, peptydy, kwas deoksyrybonukleinowy (DNA), kwas rybonukleinowy (RNA), tkanki czy przeciwciała. Interakcja, w wyniku której generowany jest sygnał elektryczny nazywana jest biorozpoznaniem molekularnym.

b) **przetwornika -** czyli elementu detektora, który przetwarza sygnał powstający w wyniku oddziaływania analitu z analizowaną substancją biologiczną. Przetworniki generują sygnały optyczne, piezoelektryczne, elektryczne, elektrochemiczne proporcjonalne do ilości interakcji zachodzących na granicy analit-bioreceptor na elektrodach.

c) **układu elektronicznego -** czyli układu rejestrującego sygnał elektryczny, powstający na zasadzie rozpoznania biomolekuły, który jest następnie przetwarzany i wyświetlany w postaci cyfrowej.

d) **wyświetlacza** - układu generującego uzyskane wyniki w postaci cyfrowej. W zależności od wymagań, dane wyjściowe mogą mieć postać wartości numerycznej graficznej, tabelarycznej [5].
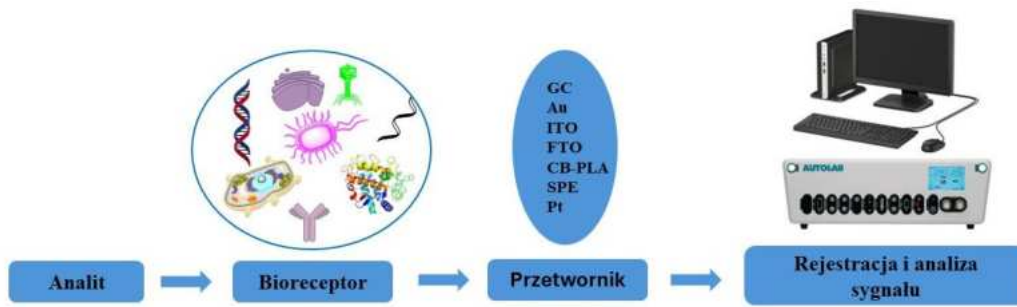
Rysunek 1. Schemat budowy biosensora elektrochemicznego.

1.1. Zastosowanie biosensorów elektrochemicznych

Projektowanie nowych biosensorów do detekcji biomolekuł ma stanowić ekonomiczniejszą alternatywę dla kosztownych, klasycznych analiz laboratoryjnych. onadto może wpływać na poprawę jakości życia poprzez coraz to większą prostotę ich użycia. Graficzne zestawienie przykładów zastosowania biosensorów przedstawiono na rysunku 2. Biosensory elektrochemiczne stosowane są w wielu obszarach takich jak przemysł, medycyna, weterynaria, analiza żywności, farmacja, kontrola jakości, hodowla zwierząt, badania zanieczyszczeń środowiskowych, przemysł wojskowy, analiza gazów toksycznych, kontrola odpadów oraz wielu innych [6].

Rysunek 2. Przykłady zastosowań biosensorów elektrochemicznych.

Biosensory często wykorzystuje się w medycynie. Zapoczątkował to amerykański biochemik Leland Charles Clark, który jako pierwszy opracował biosensor

do wykrywania procentowej zawartości tlenu we krwi. Wykorzystaną przez niego elektrodę nazwano elektrodą Clarka lub elektrodą tlenową [7]. W 1962 roku Leland Charles Clark opracował, również amperometryczną elektrodę enzymatyczną na bazie oksydazy glukozowej do detekcji glukozy we krwi, której idea do dzisiaj jest wykorzystywana przez osoby chore na cukrzycę, nawet w warunkach domowych [8].

Za pomocą biosensorów oznacza się i monitoruje produkty biologiczne takie jak enzymy, białka, markery zawału serca, markery nowotworowe, glukozę, mocznik i inne metabolity. Najczęściej jednak nowoczesne biosensory wykorzystuje się w medycynie i diagnostyce medycznej, ze względu na możliwość ich miniaturyzacji, czułość i krótki czas analizy.

1.2. Klasyfikacja biosensorów

Biosensory można podzielić ze względu na rodzaj elementu rozpoznającego (bioreceptor) lub ze względu na sposób przekazywania sygnału (przetwornik) [9].

Biosensory ze względu na rodzaj receptora dzielą się na biosensory enzymatyczne, które są najpopularniejsze oraz immunosensory, posiadające wysoką specyficzność i czułość. Ponadto do tej grupy należą sensory oparte na bazie aptamerów lub kwasów nukleinowych, które w zależności od sekwencji DNA posiadają wysoką specyficzność wobec różnych szczepów drobnoustrojów, a także rozpoznają analit zawierający komplementarny materiał genetyczny oraz biosensory mikrobiologiczne i tkankowe, które służą do wykrywania bakterii oraz specyficznych analitów.

Na podstawie rodzajów przetwornika można wyróżnić: biosensory elektroniczne, termiczne, optyczne, masowe, termograwimetryczne i elektrochemiczne, które z kolei dzielą się na potencjometryczne, amperometryczne, impedancyjne i konduktometryczne. Schemat podziału biosensorów przedstawiono na rysunku 3.
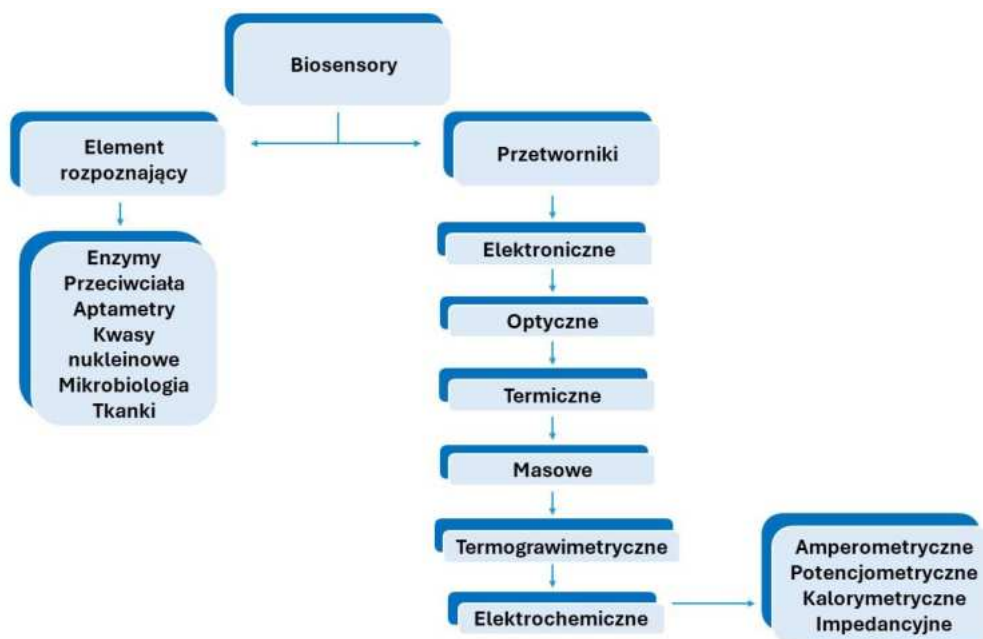
Rysunek 3. Podział biosensorów.

1.3. Charakterystyka wybranych biosensorów elektrochemicznych

1.3.1. Biosensory na bazie DNA

Biosensory elektrochemiczne na bazie DNA mogą zawierać zarówno syntetyczne jak i naturalne cząsteczki DNA i RNA, komplementarne do nici otrzymanych na bazie ściśle zdefiniowanych wirusów lub genomów plazmidowych i chromosomalnych. Grupą biosensorów opartych na DNA są również te wykorzystujące aptametry, czyli krótkie fragmenty jednoniciowego DNA (ssDNA) lub RNA (ssRNA) wyselekcjonowane *in vitro*. Mogą one wiązać się w szerokim zakresie z cząsteczkami docelowymi takimi jak: aminokwasy, leki, białka lub indywidua biologiczne [10].

Mechanizm immobilizacji DNA do powierzchni elektrody polega na przyłączeniu jednoniciowego kwasu nukleinowego, który pełni rolę sondy w bioreceptorze. Sonda może zidentyfikować i związać się ze swoją komplementarną nicią w docelowym roztworze analitu, a proces ten nazywa się hybrydyzacją, czyli rozpoznaniem par zasad nukleinowych Watsona-Cricka [6]. Rozpoznanie par zasad w biosensorze przyczynia się do zmiany prądu faradajowskiego, który jest rejestrowany. Proces hybrydyzacji zazwyczaj wykrywa się dwoma różnymi metodami przez określenie wskaźnika elektroaktywnego (znakowanie) oraz sygnału wytwarzanego przez najbardziej

elektroaktywną zasadę DNA [11]. Na rysunku 4 przedstawiono schemat ideowy budowy biosensora elektrochemicznego na bazie DNA:
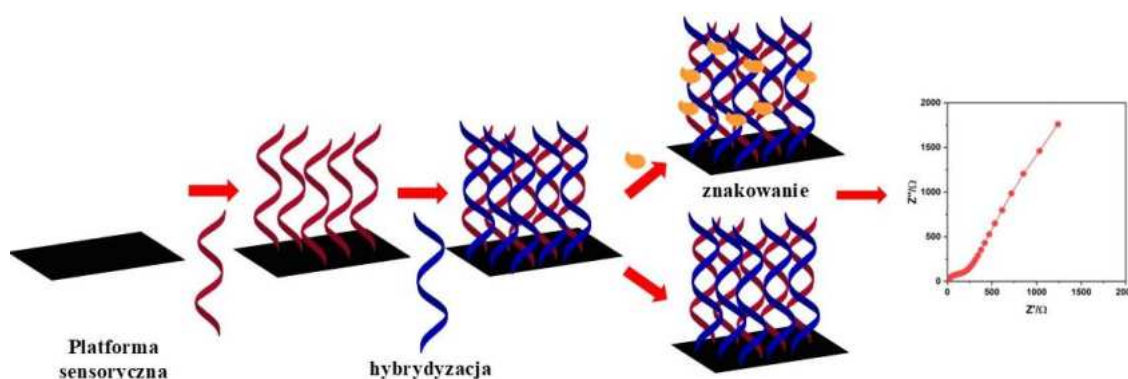
Rysunek 4. Schemat budowy biosensora elektrochemicznego na bazie DNA.

Znanych jest kilka technik immobilizacji pojedynczej nici DNA na powierzchni platformy sensorycznej, m.in. adsorpcja, wiązanie chemiczne czy interakcja z zastosowaniem kompleksu typu awidyna-biotyna. Unieruchomienie fragmentu DNA zazwyczaj jest przeprowadzane w taki sposób, aby zachować reaktywność kwasu nukleinowego, jego stabilność i dostęp do docelowego analitu przy zachowaniu optymalnej orientacji. Jedną z metod modyfikacji powierzchni elektrod jest proces adsorpcji sondy DNA na jej powierzchni, który może zachodzić na drodze elektrostatycznej, pomiędzy ujemnie naładowaną grupą fosforanową łańcucha DNA, a dodatnio naładowaną modyfikowaną powierzchnią [12]. Immobilizacja DNA może również zachodzić poprzez wiązania kowalencyjne. W metodzie tej zazwyczaj wykorzystuje się modyfikację na końcach 3′ lub 5′ łańcucha DNA grupą tiolową (-SH) lub aminową (-NH$_2$). Dzięki powyższym grupom może zachodzić reakcja chemiczna w celu kowalencyjnego związania DNA z powierzchnią lub specyficzną grupą funkcyjną osadzoną na powierzchni elektrody [13]. Dodatkowo istnieje metoda niekowalencyjnej immobilizacji DNA na powierzchni elektrody poprzez utworzenie kompleksu awidyny (lub streptawidyny) i biotyny, które jest jednym z najsilniejszych oddziaływań niekowalencyjnych w przyrodzie. Bardzo duże białko awidyny/streptawidyny o masie około 70 kDa ma budowę tetrameryczną i zapewnia cztery miejsca wiążące cząsteczki biotyny. Ogólna zasada modyfikacji elektrody nicią DNA polega na zmodyfikowaniu 3′ lub 5′ końca sekwencji DNA cząsteczką biotyny, a następnie wprowadzeniu jej na powierzchnię uprzednio zmodyfikowanej elektrody awidyną lub streptawidyną [15].

W tabeli 1 przedstawiono zestawienie biosensorów elektrochemicznych otrzymanych na bazie DNA uwzględniając różne sposoby modyfikacji elektrod i immobilizacji DNA na powierzchni elektrody.

Tabela 1. Zestawienie przykładowych biosensorów elektrochemicznych na bazie DNA.

Modyfikacja	Technika	Analit	LOD	Źródło
Au/MCH-PNA-DNA/AuNPs	EIS, SWV	MikroRNA 145	0,37 fM	[16]
CHT/SPCE/PNA/AQ/DNA	SWV	DNA wirusa brodawczaka ludzkiego	4 nM	[17]
Au/ssDNA/dsDNA/AuNPs	EIS	Gen BRCA1 raka piersi	1 pM	[18]
GCE/Gr/DNA-c/DNA-t/DNA-r/AuNP	CA	Gen BRCA1 raka piersi	1 fM	[19]
CPE/SWMTs/pLys/ssDNA-dsDNA	EIS	Fragment genu acetylotransferazy fosfinotrycyny	31 pM	[20]
CILE/SPAN/Fe_2O_3/ssDNA-dsDNA	EIS	DNA karboksylazy fosfoenolopirogroni anowej	0,2 fM	[21]
GCE/AuNPs@MoS_2/DNA1/MCH/DNA2	DPV, EIS	Mikro-RNA 21	0,78 fM, 0,45 fM	[22]
Au/PEDOT/DPA/ssDNA	CV, SWV	17β-Estradiol	0,1 nM	[23]
GCE/GQDs/CoPc(ππ)/Aptametr	EIS, DPV	Swoisty antygen sterczowy (PSA)	0,018 ng	[24]
SPE/SAM/TET/ssDNA	CV, SWV	Tetracykliny	10 nM	[25]
Au/PEG/aptametr	CV	Białko HER2 (biomarker raka piersi)	1 pM	[26]

Au - elektroda złota, AuNPs - nanocząstki złota, BPA - bisfenol A, DPV - różnicowa woltamperomteria pulsowa, GCE - elektroda z węgla szklistego, GNF - złote nanostruktury w kształcie kwiatów, HER2 - biomarker raka piersi, NiNPs - nanocząstki niklu, PEDOT - poli(3,4-etylenodioksylotiofen), PEG - polietylenoglikol, CILE - płynna elektroda węglowo - jonowa, CHT - chitozan, SPCE - sitodrukowane elektrody węglowe, ssDNA - pojedyncza nić DNA, dsDNA - podwójna nić DNA, SWNTs - jednościenne nanorurki węglowe, pLys - poli-L-lizyna, CPE - pastowa elektorda węglowa, MCH - 6-merkapto-1-heksanol, PNA - nukleinowe kwasy peptydowe, AQ - antrochinon, GR - grafen, SPAN - sulfonowana polianilina, Fe_2O_3 - tlenek żelaza(III), MoS_2 - siarczek molibdenu(IV), DPA - kwas 3,3-ditiodipropionowy, GQDs - kwantowe kropki grafenu, CoPC - ftalocyjanina kobaltu TET - tetracyklina

1.3.2. Biosensory na bazie przeciwciał

Amber Donahue i Maher Albitar jako pierwsi wykorzystali przeciwciała, w celu zaprojektowania nowego czujnika stosowanego w immunodiagnostyce [27]. Od tego czasu wielu naukowców poszukuje nowych immunosensorów, ze względu na wysoce specyficzną interakcję pomiędzy przeciwciałem i antygenem, która służy jako narzędzie

do: diagnostyki klinicznej, monitorowania środowiska, czy wykrywania różnych patogenów [28].

Biosensory bazujące na konstrukcji przeciwciało-antygen nazywane są immunosensorami. Przeciwciała to białka odpornościowe, które oddziałują z określoną cząsteczką obcego antygenu. Każde przeciwciało to struktura w kształcie litery „Y" składająca się z czterech łańcuchów polipeptydowych, mających dwa miejsca wiązania antygenu, które specyficznie oddziałują z unikalnym epitopem obecnym w antygenie lub cząsteczce docelowej.

Przeciwciała wykazują zmienną interakcję w zależności od tego, czy są monoklonalne czy poliklonalne. Przeciwciała monoklonalne mogą specyficznie rozpoznawać pojedynczy epitop cząsteczki docelowej i są mniej podatne na reaktywność krzyżową. Przeciwciała poliklonalne mogą rozpoznawać różne epitopy tej samej cząsteczki docelowej. Antygeny natomiast to substancje, które mogą wywołać odpowiedź immunologiczną poprzez rozpoznanie epitopu przez przeciwciało. Epitopy są powiązane przez paratypy przeciwciał, które znajdują się w zmiennych odcinkach zmiennych ich łańcuchów. W wiązaniu przeciwciało-antygen pośredniczą słabe oddziaływania niekowalencyjne, takie jak wiązania wodorowe, oddziaływania van der Waalsa, oddziaływania elektrostatyczne i hydrofobowe [16].

Wyróżnia się wiele metod immobilizacji przeciwciał do podłoża materiału elektrodowego poprzez: wytworzenie wiązania kowalencyjnego, wiązania niekowalencyjnego, osobliwe ułożenie przeciwciała na podłożu lub wiązanie przeciwciała z peptydami czy też DNA oraz rekombinowanymi przeciwciałami [29]. Klasyczny układ przyłączania przeciwciała do podłoża elektrody przedstawiono na rysunku 5.

Jedną z najczęściej wykorzystywanych metod immobilizacji przeciwciała do powierzchni elektrody jest metoda polegająca na reakcji z wytworzeniem wiązania kowalencyjnego. Metoda ta opiera się na utworzeniu grup aminowych, karboksylowych lub epoksydowych na podłożu materiału elektrodowego. Następnie do tak przygotowanej powierzchni powierzchni następuje przyłączenie przeciwciała, polegające na reakcji chemicznej pomiędzy reaktywną grupą funkcyjną przeciwciała z grupą obecną na zmodyfikowanej powierzchni elektrody. Jedną z najpopularniejszych metod modyfikacji elektrody jest przyłączanie do grupy karboksylowej obecnej na elektrodzie grupy aminowej poprzez mieszaninę EDC/NHS w środowisku wodnym [30].
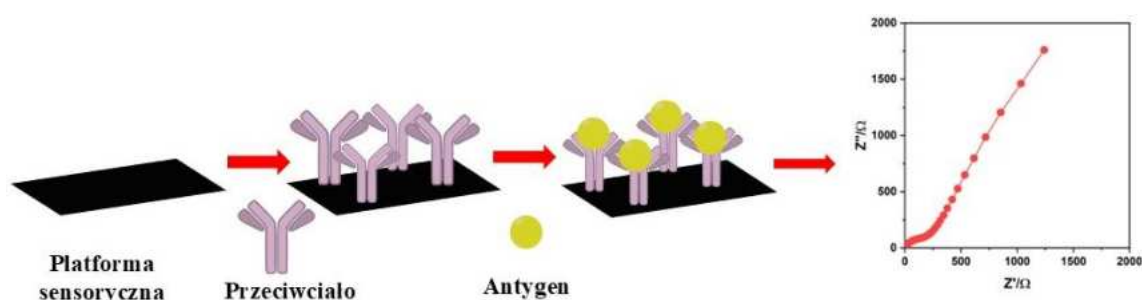
Rysunek 5. Schemat budowy biosensora na bazie przeciwciał.

Immunosensory zapewniają łatwą, szybką i wydajną identyfikację analitów wykazując większą dokładnością i czułością w porównaniu z tradycyjnie stosowanymi metodami. w diagnostyce medycznej. Dodatkowym atutem immunosensorów jest możliwość wykonywania szybkiej analizy ilościowej badanego analitu. Warto wspomnieć, że czujniki tego typu zapewniają możliwość analizy oraz ciągłego monitorowanie stężenia biomolekuł w czasie rzeczywistym. Przykłady wybranych imunosensorów projektowane do odziaływania z wybranymi analitami analit przedstawionow tabeli 2.

Tabela 2. Zestawienie biosensonsorów elektrochemicznych na bazie przeciwciał.

Modyfikacja	Technika	Analit	LOD	Źródło
Au/PEDOT/AuNP/Ab	CV, SWV	17β-Estradiol	0,1 nM	[31]
Au/4-CPDS/Ab	CV, EIS	Ochratoskyna A	0,5 ng	[32]
Au/PPy/Ab	EIS	Cyprofloksacyna	10 pg	[33]
ITO/Fc-PEI/SWNT/Ab	DPV	Białko HER2 (biomarker raka piersi)	0,220 ng	[34]
Au/GR/AgNP/AuNP/Ab	CV, DPV	Wirus ptasiej grypy szczep H7	1,6 pg	[35]
GCE/GQD-SH/AgNPs/Ab	CV, EIS, DPV	Antygen wirusa zapalenia wątroby (HCV) typu C	3 fg	[36]
GC/rGO-Au/Ab	SWV, EIS	Swoisty antygen sterczowy (PSA)	2 pg	[37]
GCE/GO/MB/AuNPs	EIC, CV	Alfa-fetoproteina	1,5 pg	[38]
Cu/GR/PBSE/Ab	CV, EIS	Antygen karcinoembrionalny - rakowo-płodowy (CEA)	0,23 ng	[39]

GC/GR/TiO$_2$/AuNP/Ab	CV, DPV	Antygen karcinoembrionalny - rakowo-płodowy (CEA)	3,33 pg	[40]
GCE/erGO/PICA/IL/AuNP/Ab	CV, EIS	Antygen karcinoembrionalny - rakowo-płodowy (CEA)	0,02 ng	[41]

Au - złota elektroda, PEDOT - poli(3,4-etylenodioksylotiofen), ITO - elektroda z tlenku indu i cyny, Fc - ferrocen, PEI - poli(etylenoimina), 4-CPDS - sól 4-karboksyfenylodiazoniowa, Ab - przeciwciało, AgNP - nanocząstki srebra, GQD - grafenowe kropki kwantowe, SWNT - jednościenne nanorurki węglowe, GC - elektroda z węgla szklistego, rGO-Au - nanocząstki słota ze zredukowanym tlenkiem grafenu, AuNPs - nanocząstki złota, TiO$_2$ - dwutlenek tytanu, PICA - kwas poli(indolo-6-karboksylowy), IL - ciecz jonowa, MB - błękit metylenowy, PPy - poli(pirol), Cu - folia miedziowa, PBSE - ester sukcynimidylowy kwasu 1-pirenobutanowego, GO - tlenek grafenu

1.3.3. Biosensory na bazie peptydów i białek

Peptydy w biosensorach elektrochemicznych, najczęściej wykorzystane są jako bezpośredni element biorozpoznawania molekularnego. Mogą również pełnić rolę pośrednią poprzez przyłączenie innych układów biologicznych do powierzchni elektrody uwzględniając: enzymy, aptametry, DNA, RNA, a także przeciwciała [42]. Większość biosensorów na bazie peptydów działa w oparciu o selektywną strategię wiązania analitu. Utworzony biosensor wykrywa docelowe białko za pomocą specyficznych sekwencji peptydowych, które wykazują silne powinowactwo i selektywność wobec docelowego białka [43]. Pomiar wytworzonego biosensora opiera się na konwersji sygnału pochodzącego od wiązania analitu przez przetwornik na przetwarzalny sygnał elektroniczny po biokoniugacji docelowego białka ze specyficzną sekwencją peptydową, co zostało schematycznie przedstawione na rysunku 6. Ze względu na elektrochemiczną nieaktywność peptydów konieczne jest przeprowadzenie modyfikacji powierzchni za pomocą pochodnych tioli [44], amin [45] i pochodnych zawierających grupy karboksylowe [46] lub biotynę [47]. Modyfikacje z zastosowaniem wyżej wymienionych molekuł pełnią rolę katalizatora reakcji elektrochemicznej i wzmacniają transfer elektronów między powierzchnią elektrody a analitem [48].
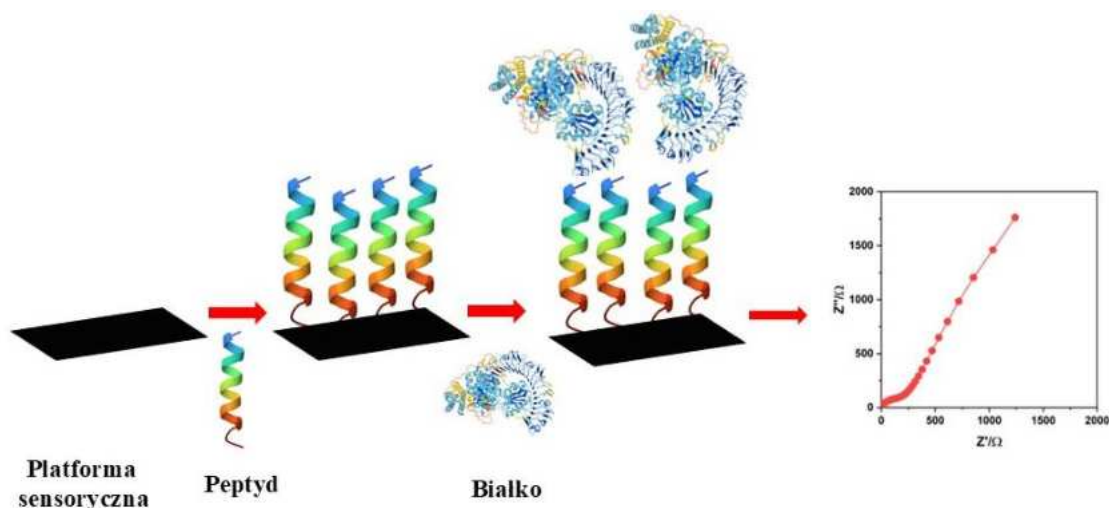
Rysunek 6. Schemat budowy biosensora wytworzonego na bazie peptydów i białek.

Główną zaletą stosowania biosensorów peptydowych, oprócz zwiększenia ich stabilności, wzrostu czułości i selektywności, jest ograniczanie kosztów ich produkcji w porównaniu z biosensorami opartymi na białkach czy przeciwciałach. Dodatkowo sekwencje peptydowe mogą być projektowane docelowo pod kątem diagnostycznym. W przypadku, gdy peptydy są stosowane jako element bioreceptora mogą z łatwością samodzielnie przyłączać się do powierzchni elektrody poprzez różne odziaływania uwzględniając: wewnątrzcząsteczkowe wiązania niekowalencyjne, wiązania wodorowe, siły van der Waalsa lub oddziaływania typu π-π [43,44]. Istnieje wiele rodzajów biosensorów elektrochemicznych na bazie peptydów do zastosowań w medycynie, które przykłady przedstawiono w tabeli 3.

Tabela 3. Porównanie biosensonsorów elektrochemicznych na bazie peptydów i białek.

Modyfikacja	Technika	Analit	LOD	Źródło
Au/MCH/P$_{COOH}$/Zr(IV)/CPAD	EIC, CV	Metaloproteinaza 2 (MMP-2)	0,27 pg	[49]
GC/rGO@MoS$_2$/AuNPs/Cys	DPV	Swoisty antygen sterczowy (PSA)	0,3 fg	[50]
Pt/SAM/peptyd/MCH	CV, SWV	Trypsyna	2,9 nM	[51]
Au/Tb/peptyd/MCH/Zr(IV)/CPAD/	CV, SWV, EIS	Trombina	2,7 μU	[52]
Au/MCH/peptyd	SWV	Ludzka neutrofilowa elastaza (HNE)	4 nM	[53]
GCE/MWCNTs/PAMAM	CV, LSV	Swoisty antygen sterczowy (PSA)	0,7 pg	[54]
Au/SAM	CV, SWV	Metaloproteinaza (MMP-7)	3,4 pM	[55]
GC/peptyd/GO	CV	Kaspaza-3	0,2 pg	[46]

Au/rGO/PA/	EIS, DPV	Toksyna botulinowa typu A	8,6 pg	[56]
PGE/PDDA/AuNPs	EIS	Przeciwciało alergenu orzeszków ziemnych Ara h2	5 pg	[57]

Au - elektroda złota, MCH - 6-merkapto-1-heksanol, CPAD - kwas 4-cyjano-4-(fenylokarbonotioilotio)pentanowy, GC - elektroda z węgla szklistego, MoSe$_2$@rGO - kompozyt diselenku molibdenu ze zredukowanym grafenem, AuNPs- nanocząstki złota, Cys - cystamina, CV - woltamperometria cykliczna, SWV - woltamperometria fali prostokątnej, EIS - elektrochemiczna spektroskopia impedancyjna, PDDA - poli(chlorek diallilodimetyloamoniowy), SPCE - sitodrukowana elektroda węglowa, Phe - 4-aminotiofenol, SAM - samoorganizująca się monowarstwa, Tb - trombina, MWCNTs - wielościenne nanorurki węglowe, PAMAM - poli(amidoamina), GO - tlenek grafenu, rGO - zredukowany tlenek grafenu, PGE - grafit pirolityczny, PA - kwas pirenobutyrowy

2. Materiały elektrodowe

W ostatnim czasie wzrasta zainteresowanie otrzymywaniem nowych materiałów wykorzystywanych w elektrochemii i inżynierii materiałowej. Na szczególną uwagę zasługuje fakt, ze elektrody znajdują bardzo szerokie zastosowanie w badaniach biosensorycznych.

Platforma biosensoryczna działa prawidłowo w przypadku kiedy elektroda spełnia kilka określonych wymagań m.in. jest biokompatybilna z wykrywanym materiałem biologicznym i podczas detekcji elektrochemicznej nie tworzą się bariery dyfuzyjne. Dodatkowo elektroda musi charakteryzować się dobrą przewodnością, tak aby zapewnić szybki transfer elektronów, być stabilna przy zmianach temperatury, pH, siły jonowej czy mikrośrodowiska. Elektroda musi cechować się wysoką czułością i selektywnością względem badanego analitu a koszt jej wytworzenia powinien być niski, co umożliwiłoby wykorzystanie go w masowej produkcji. Ponadto materiały elektrodowe do projektowania platform biosensorycznych powinny posiadać grupy funkcyjne zdolne do modyfikacji i przyłączania biomolekuł [58]. Wśród powszechnie stosowanych materiałów elektrodowych wyróżnia się materiały węglowe takie jak: węgiel szklisty (GC), diament domieszowany borem (BDD), sadza (CB), grafen, grafit, nanorurki, tlenek grafenu, zredukowany tlenek grafenu czy wielościenne nanorurki węglowe (MWCNT). Wyróżnić można również materiały metaliczne do których zaliczane są elektrody złote (Au), platynowe (Pt), srebrne (Ag), rtęciowe (Hg), czy mieszaniny tlenków żelaza (Fe$_3$O$_4$). Przykładem elektrod są również materiały oparte na tlenkach takich jak: mieszanina tlenków indu i cynku (ITO), tlenek cyny z domieszką fluoru (FTO), tlenek tytanu (II) (TiO$_2$) i tlenek molibdenu (III) (Mo$_2$O$_3$). Stosunkowo nowymi materiałami elektrodowymi są elektrody drukowane w technologii 3D, które zawierają głównie kwas

polimlekowy (PLA) z różnymi napełniaczami węglowymi takimi jak sadza (CB-PLA), grafen(G-PLA) i nanorurki węglowe (Ampre-PLA). Dodatkowo elektrody te mogą wykazywać właściwości magnetyczne, ze względu na zawartość w strukturze nanocząstek tlenku żelaza (Fe_3O_4-PLA).

W prezentowanej rozprawie doktorskiej do badań wykorzystano następujące elektrody: GC, Au, ITO oraz CB-PLA, dlatego też zostały one szczegółowo opisane w kolejnych podrozdziałach.

2.1. Elektrody wykonane z węgla szklistego (GC)

Węgiel szklisty uzyskuje się w wyniku pirolizy bogatych w węgiel żywic polimerowych w atmosferze gazu obojętnego zwykle argonu lub azotu, czy też sporadycznie w próżni. W procesie powstawania GC bierze udział wiele prekursorów organicznych takich jak: fenol, formaldehyd, poli(alkohol furfurylowy), poli(naftalen), poliimid, poli(chlorek winylu) i bezwodnik maleinowy. Proces formowania odmian GC odbywa się w podwyższonej temperaturze. Powstały rodzaj węgla po pirolizie posiada wygląd przypominający szkło, dlatego określany jest mianem węgla szklistego (GC). Materiał ten jest ciężki i kruchy w przeciwieństwie do miękkich grafitowych form węgla [59]. W strukturze GC występują atomy węgla, które wykazują zdolność do tworzenia różnych odmian alotropowych o różnej hybrydyzacji wiązania pomiędzy atomami węgla (sp, sp^2, sp^3), co sprawia, że węgiel szklisty charakteryzuje się niezwykłą wszechstronnością strukturalną.

Budowa GC po raz pierwszy została zaproponowana przez G. M. Jenkinsa, który określił, że włóknista część polimerycznego prekursora zostaje częściowo zachowana po pirolizie, tworząc sieć splątanych grafitowych wstęg [60]. Zgodnie z tym modelem materiał składa się z losowo zorientowanych, izotropowych splecionych mikrowłukien. Rozpatrując strukturalną budowę GC można stwierdzić, że zawiera dużo pustych przestrzeni oraz posiada niższą gęstość niż grafit (około 1,5 vs 2,3 g/cm^3). Krystalograficzny model poszczególnych wstęg grafitowych przedstawiony na rysunku 7 opisano za pomocą parametrów wewnątrz płaszczyznowej długości mikrokrystalicznej (La) i międzypłaszczyznowej długości mikrokrystalicznej, zwanej również grubością ułożenia (Lc). Pierwsza płaszczyzna jest prostopadła, natomiast druga równoległa do osi c grafitu, w kierunku której płaszczyzny grafenu w poszczególnych wstęgach są ułożone [61].
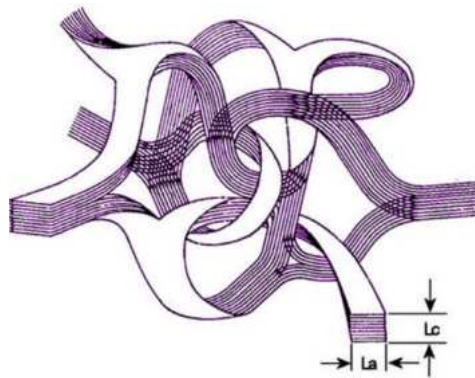
Rysunek 7. Budowa strukturalna węgla szklistego (GC) *[62]*.

Węgiel szklisty posiada bardzo dobre właściwości elektryczne i mechaniczne, charakteryzuje się szerokim zakresem pracy potencjałów, obojętnością chemiczną, odpornością na degradację i ścieranie, wysoką odpornością na działanie kwasów i zasad, a także nieprzepuszczalnością dla gazów [63]. Węgiel szklisty jest materiałem przetwarzalnym, oznacza to, że można z niego wytworzyć wiele innych tworzyw takich jak tygle. Dodatkowo GC można również wykorzystać w postaci drobnych cząstek, cienkich filmów, arkuszy czy włókien.

GC, na przestrzeni dziesięcioleci, wykorzystywany jest jako standardowy materiał elektrodowy, ponieważ wykazuje bardzo szybką odpowiedź elektrochemiczną podczas reakcji redoks. GC pozwala również na badanie różnych związków chemicznych, bez zanieczyszczania elektrody, co jest jego główną zaletą. Węgiel szklisty używany jako elektroda wykazuje szerokie okno potencjałów, łatwość czyszczenia powierzchni pomiędzy pomiarami i zerową toksyczność, co umożliwia wykorzystanie tego materiału w wielu pomiarach elektrochemicznych.

Pierwsze doniesienia literaturowe związane z wykorzystaniem czystych lub modyfikowanych elektrod GC pojawiły się w roku 1964. Grupy badawcze z Oak Ridge National Laboratory w Tennessee w USA i Gifu University w Japonii wykorzystały elektrody GC do anodowego oznaczania złota z użyciem metody kulometrycznej [64]. W podobnym czasie pojawiła się również praca, w której elektrodę GC wykorzystano do woltamperometrycznego oznaczania jonów [65].

Ze względu na to, że elektroda GC jest odmianą węgla, istnieje możliwość modyfikacji jej powierzchni z utworzeniem wiązań kowalencyjnych. Dodatkowo powierzchnię GC można zmodyfikować wieloma molekułami organicznymi poprzez zjawisko fizysorpcji. Dlatego też, elektroda GC wykorzystywana jest w badaniach katalitycznych i w elektroanalizie. Pierwszą w historii chemiczną modyfikację elektrody

GC wykonano poprzez zakotwiczenie na jej powierzchni organosilanów, co umożliwiło przyłączenie do niej grup aminowych, etylenodiaminy, pirydyny i chlorku alkilu [66]. Do dziś elektroda GC stanowi podstawową elektrodę w wielu laboratoriach oraz jest wykorzystywana do dalszych modyfikacji i funkcjonalizacji biomolekułami, co stanowi wciąż aktualny temat badań.

2.2. Elektrody na bazie złota (Au)

Złoto jest pierwiastkiem chemicznym, a jego symbol pochodzi od łacińskiego słowa *Aurum*. Jest to kowalny i ciągliwy metal o dużej gęstości i niskiej twardości. Pod względem chemicznym złoto zaliczane jest do metali szlachetnych. W standardowych warunkach złoto charakteryzuje się dużą odpornością chemiczną na działanie większości czynników korozyjnych, dzięki czemu wykorzystywane jest do pokryć ochronnych bardziej reaktywnych metali. Złoto, ze względu na swoje właściwości wykorzystywane jest w jubilerstwie, przemyśle, elektronice, chemii przemysłowej i medycynie [67].

Złoto ma bardzo wysokie przewodnictwo elektryczne dzięki czemu znajduje zastosowanie w otrzymywaniu elektrod, które mogą być modyfikowane w celu konstruowania skomplikowanych biosensorów elektrochemicznych.

Materiały elektrodowe ze złota mogą mieć inną morfologię, budowę krystalograficzną, topologię powierzchni i chropowatość [68]. Produkcja elektrod opiera się na osadzaniu złota na podłożu przewodzącym. Elektrody złote można także uzyskać w procesie litografii, poprzez zastosowanie odpowiednich wzorów. Najczęściej stosowanymi technikami do otrzymywania elektrod złotych to osadzanie chemiczne z fazy gazowej (CVD, ang. *Chemical Vapour Deposition*) oraz fizyczne osadzanie z fazy gazowej (PVD, ang. *Physical Vapour Deposition*) w postaci cienkiej warstwy czystego metalu na podłożu [69,70].

Na elektrodach złotych bardzo często tworzone są platformy biosensoryczne ze względu na ich unikatowe właściwości: przewodnictwo elektryczne i cieplne i możliwość swobodnej modyfikacji powierzchni a także duża powtarzalność wynikowa [71]. Jedną z najważniejszych własności złota w porównaniu z innymi materiałami elektrodowymi jest jego obojętność biologiczna, co umożliwia prowadzanie pomiarów w próbkach fizjologicznych. Najczęstszym sposobem modyfikacji powierzchni Au jest zdolność do tworzenia samoorganizujących się monowarstw (SAM) z zastosowaniem związków

organicznych, głównie tioli [72]. Wytworzenie warstw SAM na elektrodach złotych pozwala na dalszą modyfikację za pomocą odpowiednich linkerów i detekcję wielu biomolekuł [48].

Komercyjnie dostępne materiały elektrodowe coraz częściej zastępowane są przez złote nanostruktury o różnych kształtach, właściwościach fizycznych i chemicznych. Najczęściej stosowanymi pochodnymi są formy złota w postaci nanocząstek, nanosfer, nanoklastrów, nanodrutów, nanogwiazd, nanosześcianów i wielu innych (Rysunek 8). Wybrane przykłady nanostruktur przedstawiono na rysunku 8 [73]. Synteza i modyfikacja złotych nanomateriałów o różnych rozmiarach i kształtach umożliwia uzyskanie nowych surowców, które mogą wykazywać niezwykłą czułość w wykrywaniu analitów

i bioanalitów. Nanostruktury złota posiadają duże powinowactwo do alkanotioli, grup aminowych, a także do pochodnych disulfidowych [74].
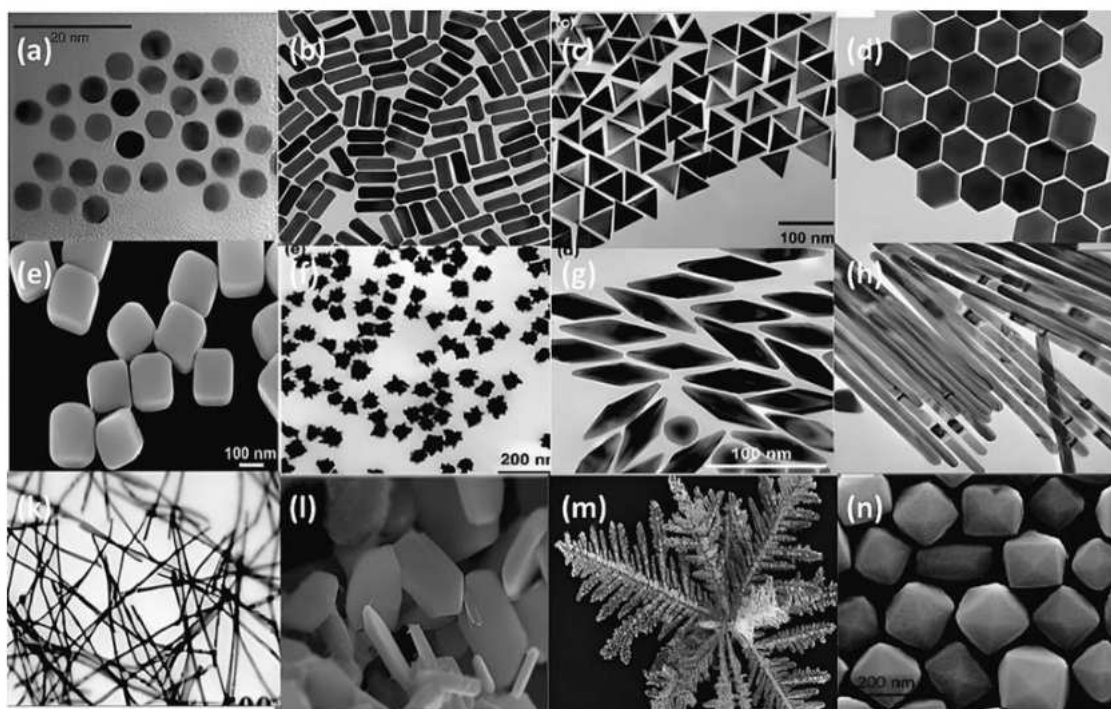
Rysunek 8. Mikrografie najczęściej występujących nanostruktur złota wykorzystywanych w elektrochemii [73].

Na podstawie doniesień literaturowych można stwierdzić, że najczęściej badanymi nanostrukturami są nanocząstki złota (AuNPs). AuNPs ze względu na ich właściwości chemiczne, optyczne, elektryczne i katalityczne najczęściej wykorzystywane są

w diagnostyce chemicznej, terapii nowotworowej, dostarczaniu leków i konstruowaniu biosensorów [75]. Struktury te charakteryzują się również wyjątkową stabilnością, niską rezystancją i dużym stosunkiem powierzchni do objętości. W latach 2019-2024 powstało 71 tysięcy artykułów naukowych w których użyto różne struktury złota w skali nano. AuNPs wykorzystuje się do detekcji wielu skomplikowanych analitów takich jak: adenozynotrójfosforan (ATP), kwas deoksyrybonukleinowy (DNA), kwas rybonukleinowy (RNA), białka, bakterie, wirusy i wiele innych [76].

W badaniach stosuje się, nie tylko nanocząstki ale również nanodruty (AuNWs), modyfikowane enzymami w celu detekcji glukozy [77]. Nanodruty złota wykorzystano również do wykrywania hemoglobiny [78] i wychwytywania cholesterolu z próbki ludzkiej krwi [79]. Z kolei nanogwiazdy użyto do selektywnego wykrywania bakterii *Escherichia coli* [80].

W ostatnich latach dużym zainteresowaniem w pracach elektrochemicznych cieszą się nanosześciany złota (AuNCs). Nanostruktury te posiadają trójwymiarową strukturę o podobnym kształcie i rozmiarze. Dodatkowym atutem jest ich zdolność do samoorganizacji na powierzchni modyfikowanego materiału elektrodowego. Podobnie jak w przypadku innych nanostruktur AuNCs cechuje stabilność chemiczna i możliwość dalszej modyfikacji. Ponadto pojedyncze AuNCs lub ich aglomeraty mogą powodować wzmocnienie pól elektromagnetycznych oddziałując z sąsiednimi cząsteczkami, zwiększając ich aktywność, co pozwala na wykorzystanie tych cząsteczek w tworzeniu czujników optycznych [81]. Jednym z pierwszych zastosowań AuNCs w elektrochemii jest osadzenie ich na elektrodzie dyskowej i badanie redukcji tlenu na powierzchni elektrody [82]. Istnieje wiele możliwości zastosowań AuNCs, przykładowo do wykrywania biomarkerów nowotworowych za pomocą technik zlokalizowanego rezonansu plazmonów powierzchniowych (LSPR) [83,84]. Na bazie AuNCs opracowano również elektrochemiczne aptasensory i immunosensory do czułego i selektywnego wykrywania chloramfenikolu [85] oraz kardiologicznego biomarkera (troponiny) [86]. Dodatkowo wykorzystuje się je do szybkiego wykrywania uropatogennej bakterii *Escherichia coli* w ludzkim moczu za pomocą dynamicznej spektroskopii impedancyjnej [87].

2.3. Elektroda z tlenku indu i cyny (ITO)

Elektroda ITO to mieszanina tlenku cyny(IV) (SnO_2) i tlenku indu(III) (In_2O_3). Materiał ten to przezroczysty tlenek, będący półprzewodnikiem typu n. Skład chemiczny ITO to 5,6% cyny (wagowo) w matrycy indu co zapewnia najniższą rezystancję elektrody przy transmisji optycznej większej niż 80%. Elektrody te stosowane są w badaniach elektrochemicznych ze względu na ich szerokie okno potencjału, wysoką przewodność elektryczną i dobrą transparentność [88].
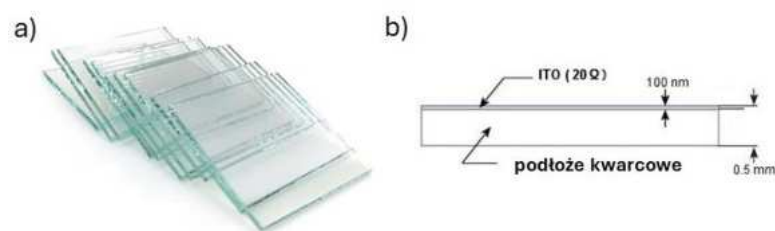
Rysunek 9. Elektroda ITO a) szkło pokryte ITO, b) wymiary elektrod [89].

Elektrody ITO mają wiele zalet, do których zalicza się wysoką wydajność fizyczną, stabilność elektrochemiczną, biokompatybilność, niskie prądy tła, niski opór elektryczny i łatwość do modyfikacji chemicznej [90]. W porównaniu do innych komercyjnych materiałów elektrodowych ITO jest najtańszym [91].

Pomimo niezwykłych właściwości, elektrody oparte na ITO mają ograniczenia związane z bardzo powolną kinetyką przeniesienia ładunku do oznaczania większości form elektroaktywnych w porównaniu z elektrodami GC i elektrodami metalicznymi. Wspomniane ograniczenie jest problemem w oznaczeniach elektroanalitycznych, dlatego niezbędna jest ich modyfikacja, która wpływa na polepszenie kinetyki przeniesienia ładunku. Najczęściej modyfikację ITO przeprowadza się metodą chemiczną na mokro przy użyciu dużej gamy odczynników w tym organicznych i metaloorganicznych alkoksysilanów, amin, kwasów karboksylowych i nanostruktur [92].

2.4. Elektrody drukowane w technologii 3D (CB-PLA)

Poszukiwanie nowych materiałów elektrodowych jest aktualnym tematem badań wielu jednostek badawczych. Powstałe modele i prototypy uzyskane metodą druku 3D wykorzystuje się w badaniach naukowych oraz przemyśle. Szeroka gama komercyjnie dostępnych filamentów powoduje, że elektrody uzyskane metodą druku 3D posiadają

właściwości takie jak: biodegradowalność, biokompatybilność, a przede wszystkim niski koszt otrzymywania.

Jednym z najczęściej wykorzystywanych materiałów do druku jest kwas polimlekowy, czyli polilaktyd (PLA), który pozyskiwany jest z naturalnych źródeł takich jak skrobia kukurydziana, ziemniaczana czy trzcina cukrowa [93].

Najbardziej popularną techniką do wytworzenia struktur 3D jest technika FDM lub alternatywnie FFF, w której materiał w formie żyłki, wprowadzany jest przez ekstruder do nagrzanej głowicy drukującej, gdzie zmienia się w stan półpłynny. Filament następnie jest tłoczony i rozprowadzany przez głowicę warstwa po warstwie w trzech osiach aż do momentu wytworzenia gotowego elementu.

Rozwój technologii druku 3D i dostępność filamentów przewodzących umożliwił wytwarzanie nowych materiałów elektrodowych. Elektrody uzyskiwane w druku 3D zazwyczaj złożone są z kwasu polimlekowego (PLA), przewodzącego napełniacza węglowego w postaci grafenu, sadzy czy nanorurek węglowych. Jednym z najpopularniejszych filamentów używanych w elektrochemii jest przewodzący kompozyt złożony z sadzy i PLA (CB-PLA), w którym cząstki węgla przewodzącego są związane z resztą kompozytu tworząc aglomeraty w wyniku słabych oddziaływań van der Waalsa. Jako napełniacz najczęściej wykorzystuje się sadze opisywaną w literaturze jako CB (ang. *carbon black*). Cząstki CB wykazują kulistą morfologię o wielkości od około 10 do 100 nm. W trakcie produkcji filametów, CB agregują tworząc skupiska o różnych rozmiarach i kształtach. Dodanie ich w tej postaci do odpowiedniego polimeru pozwala na formowanie filamentu zdolnego do druku [94]. Właściwości fizykochemiczne materiałów węglowych i ich przewodnictwo w elektrodach, zależą od metody ich wytwarzania, struktury molekularnej materiału przewodzącego, obecności grup chemicznych na powierzchni elektrody, a także wcześniejszych procesów chemicznych i elektrochemicznych przeprowadzonych na elektrodzie.

Drukowanie elektrod z filamentu CB-PLA jest bardzo ekonomicznym sposobem uzyskiwania nowych elektrod, który w przyszłości może z powodzeniem zastąpić te komercyjnie dostępne. Dodatkowo elektrody CB-PLA wykazują większą powierzchnię aktywną oraz wysoką przewodność cieplną i elektryczną. Każda elektroda po wydruku częściowo przewodzi prąd, a jej oporność właściwa warstwy wynosi 30 $\Omega\cdot$cm [95].

Właściwości elektrochemiczne elektrod CB-PLA zależą od formy agregacji mikrokrystalitów w całej objętości elektrody. Materiał CB-PLA w celu polepszenia

szybkości przeniesienia elektronu na granicy faz elektroda/elektrolit, musi zostać w odpowiedni sposób zaktywowany poprzez usunięcie warstwy matrycy polimerowej i odsłonięcie przewodzącego napełniacza węglowego. Pierwsze doniesienia literaturowe dotyczące aktywacji powierzchni elektrody CB-PLA dotyczą usuwania polimeru poprzez zanurzanie w rozpuszczalnikach organicznych takich jak dimetyloformamid (DMF) [96]. Ze względu na toksyczność odchodzi się od stosowania rozpuszczalników organicznych i poszukuje się nowych sposobów aktywacji powierzchni CB-PLA. Jednym z alternatywnych sposobów jest fizyczne usuwanie matrycy polimerowej z zastosowaniem papieru ściernego lub ablację laserową przeprowadzaną w atmosferze helu [97]. Do elektrochemicznych metod aktywacji powierzchni zalicza się aktywację przeprowadzoną w roztworze kwasów lub zasad, w wyniku której zwiększa się powierzchnia aktywna przez hydrolizę polimeru [95].

3.   Wykrywane bioanality

3.1.   Uropatogenne szczepy bakterii *Escherichia coli* (UPEC)

Uropatogenne szczepy bakterii *Escherichia coli* (UPEC) to szczepy bakterii gram-ujemnych występujących w kształcie pałeczek [98]. Bakterie UPEC występują głównie w układzie pokarmowym, oddechowym i moczowo-płciowym. Największe zagrożenie ze strony UPEC to infekcja dróg moczowych, którą przedstawiono schematycznie na rysunku 10. Choroby wywołane przez patogeny dotykają rocznie 150 milionów ludzi i powodują silne zakażenie dróg moczowych (ZUT) u kobiet i mężczyzn, szczególnie chorych na cukrzycę. Dlatego niezwykle ważne jest poszukiwanie nowych, tanich i szybkich testów diagnostycznych na bakterie różnych szczepów *Escherichia coli* z wykorzystaniem technik elektrochemicznych.

W przypadku infekcji, bakterie kałowe kolonizują w cewce moczowej i rozprzestrzeniają się z dróg moczowych do pęcherza moczowego, a także do nerek. Za powstające choroby odpowiedzialne są czynniki zjadliwości - czyli cechy charakterystyczne bakterii, które pozwalają na namnażanie i uszkodzenie tkanek zainfekowanego organizmu co oznaczane jest jako dawka śmiertelna 50 (LD_{50}). Czynniki zjadliwości powierzchni komórek bakteryjnych najczęściej obejmują fimbrie, głównie fimbrie typu 1 i fimbrie P. Fimbrie te pomagają w adhezji do powierzchni komórki gospodarza, inwazji tkanek (co jest ważne w patogenezie UPEC powodujących zakażenia dróg moczowych), tworzeniu biofilmu i indukcji cytokin. Czynniki zjadliwości

powierzchni komórki bakteryjnej obejmują także wici, lipopolisacharydy otoczkowe i białka błony zewnętrznej. Do wydzielanych przez organizm czynników zjadliwości zalicza się hemolizę i siderofory. Czynniki te odgrywają ważną rolę w umożliwieniu bakteriom kolonizacji w drogach moczowych i przetrwania pomimo skutecznie funkcjonującego mechanizmu obronnego gospodarza [99].
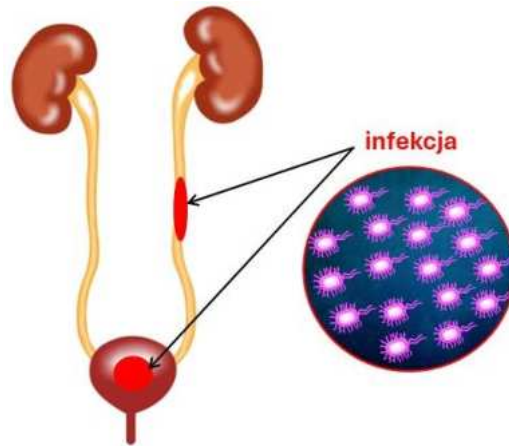
Rysunek 10. Schemat przedstawiający miejsca infekcji dróg moczowych.

Pojawienie się lekoopornych drobnoustrojów wśród szczepów UPEC zwiększa zagrożenie dla zdrowia człowieka. W związku z czym, wczesne i niedrogie wykrywanie bakterii chorobotwórczych jest bardzo ważne, ponieważ *Escherichia coli* bardzo szybko potrafią przekształcać się w patogeny wielolekooporne. Bakterie te rozprzestrzeniają się w organizmach ludzkich i zwierzęcych stałocieplnych, a w końcowym etapie przedostają się do środowiska. Główne powikłania po infekcjach wywołanymi bakteriami *Escherichia coli* to zapalenie pęcherzyka żółciowego, zapalenie dróg żółciowych oraz moczowych.

3.1.1. Metody wykrywania uropatogennych bakterii *Escherichia coli*

Konwencjonalne metody wykrywania upropatogennych *Escherichia coli* polegają na selektywnej hodowli i izolacji komórek, a następnie biochemicznym i serologicznym wykrywaniu oraz identyfikacji. Metody te są niezawodne i bardzo dokładne jednak niestety są czasochłonne i wieloetapowe, trwające około 2-3 dni. Główną ich wadą jest bardzo wysoki koszt aparatury i czas niezbędny do analizy próbek. Do najczęściej używanych technik detekcji UPEC zalicza się reakcję łańcuchową polimerazy (PCR), cytometrię przepływową oraz spektrometrię masową, które zapewniają wczesną i czułą detekcję [100]. Alternatywą dla powszechnie stosowanych technik jest projektowanie

nowych biosensorów, które umożliwią wykrycie UPEC w stosunkowo niedługim czasie na wysokim poziomie detekcji. W tabeli 4 przedstawiono sposoby detekcji bakterii *Escherichia coli* metodami elektrochemicznymi .

Tabela 4. Zestawienie biosensorów elektrochemicznych do wykrywania bakterii *Escherichia coli*.

| Elektroda/Modyfikacja	Technika	LOD (CFU/ml)	Źródło
PGE/Chi-PPy-AuNPs MWCNT	CV	30	[101]
ITO	EIS	1	[102]
SPCE/MNP-Ab/cell-Ab/AuNP	DPV	1	[103]
GCE/SG/PEDOT/AuNPs	EIS	34	[104]
Au/bio-aptametr	DPV	80	[105]
AuSPE	EIS	3	[106]
Au/rGO-CysCu	EIS	3,8	[107]
SP-IDME	EIS	1000	[108]
Au/MACA	EIS	50	[109]
SPE/SWCNT	CV, DPV	17	[110]
GC/AuNCs-aptamter	Impedymetryczny odcisk palca	10	[87]

PGE - ołówkowa elektroda grafitowa, Chi-PPy-AuNPs MWCNT - nanokompozyt chitozanu z wielościennymi nanorurkami węglowymi oraz polipyrolem i nanocząstkami złota, ITO - elektroda z tlenku cyny i indu, SPCE - sitodrukowana elektroda węglowa, MNP - magnetyczne nanocząstki, Ab - przeciwciała, AuNP - nanoczastki złota, GCE - elektroda z węgla szklistego, SG - sulfonowany grafen, PEDOT - poli-(3,4-etylenodioksytiofen), Au - elektroda złota, AuSPE - złota elektroda z nadrukiem sitodrukowym, rGO-CysCu - kompozt zredukowanego tlenku grafenu z cysteina i miedzią, SP-IDME - sitodrukowana mikroelektroda, AuNCs - nanosześciany złota, SPE - elektrody sitodrukowane, SWCNT - jednościenna nanorurka węglowa, MACA - kwas merkaptooctowy

3.2. Hormon ludzkiej gonadotropiny kosmówkowej (hCG)

Ludzka gonadotropina kosmówkowa (hCG) jest hormonem składającym się z 2 podjednostek- alfa i beta, które zbudowane są z łańcuchów białkowych, natomiast pozostałe składniki budulcowe to łańcuchy glikanowe. W skład hormonu hCG wchodzi 237 aminokwasów o masie cząsteczkowej 36,7 kDa, około 14,5 kDa α-hCG i 22,2 kDa β-hCG [111]. Podjednostka α (alfa) ma długość 92 aminokwasów, podjednostka β gonadotropiny hCG (beta-hCG) zawiera 145 aminokwasów, które połączone są ze sobą przez wiązania kowalencyjne, a dodatkową stabilizację cząsteczki zapewniają wiązania wodorowe [112].

hCG należy do klasy hormonów glikoproteinowych produkowanych przez komórki przedniego płata przysadki (gonadotropiny), do których zalicza się również hormon luteinizujący (LH), tyreotropowy (TSH) oraz folikulotropowy (FSH). Hormon hCG wytwarzany jest przez fuzyjne i zróżnicowane komórki syncytiotrofoblastu łożyska

[113]. Podjednostka β-hCG, choć strukturalnie podobna do podjednostki β-LH, różnicuje hiperglikozylowaną hCG i przysadkową hCG od innych związków. Zarówno hCG, jak i LH wiążą się i działają poprzez wspólny receptor hCG/LH, a różnica pomiędzy nimi to okres półtrwania w układzie krążenia wynoszący odpowiednio dla LH 25-30 minut i hCG 37 godzin, czyli 80-krotnie dłużej [114].
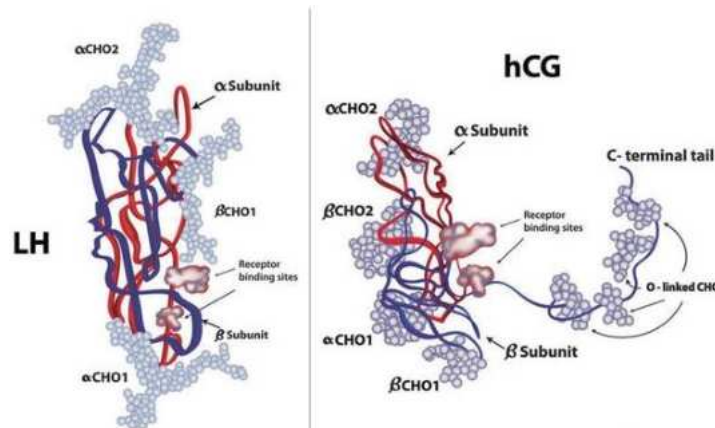
Rysunek 11. Budowa strukturalna hormonu LH i hCG *[115]*.

hCG jest pierwszym znanym sygnałem hormonalnym poczęcia, a jego oznaczenie można wykonywać we krwi ciężarnej już 10 dni po zapłodnieniu. Szczyt produkcji hCG przez łożysko pojawia się pomiędzy 10 a 11 tygodniem ciąży, następnie produkcja spada aż do 12 tygodnia i od tego momentu może utrzymywać się na stałym poziomie. hCG pośredniczy w ratowaniu ciałka żółtego i zapewnia ciągłą produkcję progesteronu [115]. Prawidłowy przyrost stężenia hormonu we krwi przedstawiono w tabeli 5. Obecność hormonu w moczu bada się w pierwszym momencie za pomocą testów ciążowych opartych na wykorzystaniu przeciwciał, które wychwytują hormon jednak nie określają jego stężenia. Wieloetapowa diagnostyka próbek krwi opiera się na wykorzystaniu zaawansowanej i kosztowanej aparatury pomiarowej. Dlatego kluczowe jest poszukiwanie nowych, alternatywnych sposobów wykrywania i oznaczania hormonu hCG o dokładnie określonym stężeniu, co pozwoli na kontrolowanie prawidłowego przebiegu hormonalnego w czasie ciąży. Wszystkie nieprawidłowości związane z przyrostem stężenia hormonu hCG muszą zostać szybko zdiagnozowane, aby uniknąć rozwinięcia się chorób nowotworowych czy też zmian hormonalnych u kobiet i mężczyzn.

Tabela 5. Zestawienie prawidłowego stężenia hormonu β-hCG w zależności od tygodnia ciąży [116].

Tydzień	Stężenie [mIU/ml]
3	5-50
4	5-426
5	18-7340
6	1080-56500
7-8	7650-229000
9-12	25700-280000
13-16	13300-254000
17-24	4060-165400
25-40	3640-117000

3.2.1. Metody wykrywania hormonu hCG

Testy ciążowe, ze względu na swoją prostotę użycia są bardzo popularnym narzędziem do podstawowej detekcji hormon samodzielnie w domu. Dostępne komercyjnie testy służą do potwierdzenia obecności hormonu ludzkiej gonadotropiny kosmówkowej (hCG) w moczu. Obecna generacja testów opiera się na przeciwciałach monoklonalnych zakotwiczonych na powierzchni specjalistycznie dobranego materiału, które specyficznie oddziałowujące z podjednostką β-hCG, co schematycznie przedstawiono na rysunku 12. Przeciwciała wykazują dużą selektywność względem hormonu hCG przez co całkowicie eliminuje się wystąpienie reakcji krzyżowej z hormonem luteinizującym przysadki mózgowej (LH).
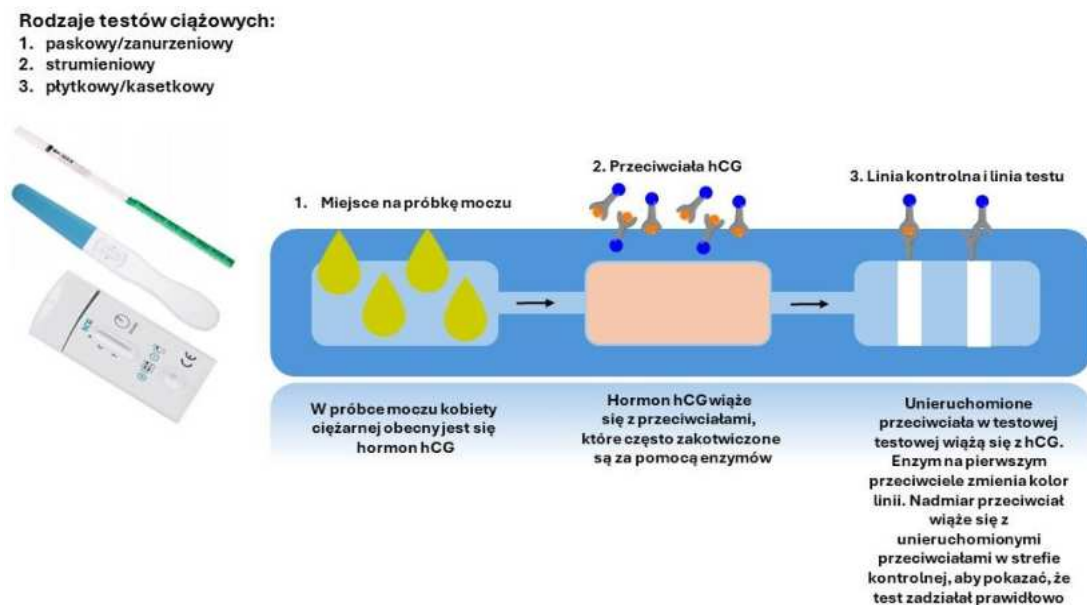
Rysunek 12. Rodzaje testów ciążowych oraz przykładowy mechanizm ich działania.

W ostatnim czasie pojawiła się informacja na temat nowego testu ciążowego zaprojektowanego przez izraelski start-up Salignostics: SaliStick, który ma wykrywać hormon β-hCG obecny w ślinie. Zgodnie z danymi literaturowymi hormon ten obecny jest w ślinie pomiędzy 3 a 4 tygodniem ciąży [117].

Badania eksperymentalne dotyczące detekcji hormonu hCG na różnego rodzaju podłożach elektrodowych są wciąż aktualnym tematem badań. Testy ciążowe obecnie wykazują poziom czułości i swoistości na bardzo niskim poziomie. Alternatywą dla komercyjnie dostępnych testów może być wykorzystanie technik elektroanalitycznych nie tylko w moczu, ale również w surowicy ludzkiej, czy też płynach hodowlanych stosowanych w badaniach *in vitro*. Przykładowe platformy biosensoryczne oparte na bazie przeciwciał i peptydów do wykrywania hormonu hCG przedstawiono w tabeli 6.

Tabela 6. Zestawienie metod elektroanalitycznych do oznaczania hormonu hCG:

Modyfikacja	Technika	LOD	Źródło
Au/Cys/GO/aptametr	SPR	0,065 nM	[118]
4-nitrofenol/AuNPs/aptametr	Kolorymetria	15 mIU/ml	[119]
Au/AgNPs/aptametr	LSV	0,4 mIU/ml	[120]
SPE/AuNPs/peptyd	EIS	5 mIU/ml	[121]
GC/MIP/MWCNTs	DPV	0,35 fg/ml	[122]
GC/Chi/AuNRs/anty-hCG	Amperometria	0,17 pM/ml	[123]
GC/GS/NPG/anti-hCG	Amperometria	0,92 pM/ml	[124]
SPCE/CNTs/anty-hCG	DPV	5,0 pg/ml	[125]
GC/SAM/anty-hCG	CV	2,2 IU/ml	[126]
GC/PEG/AuNPs/CNOs/anty-hCG	DPV	0,1 pg/ml	[127]
GCE/GS/IL/HNP-AuAg/anty-hCG	CV, EIS	0,01 ng/ml	[128]
SPCE/GR/anty-hCG/AuMAb-hCG	DPV	5 pg/ml	[129]
GC/MWNTs-CS/GA/AuNPs-TiO$_2$/anty-hCG	CA	0,08 mIU/ml	[130]

Au - elektroda złota, Cys - cystamina, AuNPs - nanocząstki złota, AgNPs - nanocząstki srebra, Chi - chitozan, CNTs - nanorurki węglowe, MIP – polimery z odciskiem molekularnym, MWCNTs - wielościenne nanorurki węglowe, GC - węgiel szklisty, GO - tlenek grafenu, GS - arkusze grafenowe, GS-IL - kompozyt z grafenu i cieczy jonowej, GA - aldehyd glutarowy, GCE - elektroda z węgla szklistego, GR - grafen, HNP-AuAg - stop nanoporowaty złota i srebra, NPG - nanoporowate złoto, HRP - peroksydaza chrzanowa, SPE - elektrody sitodrukowane, SPCE - sitodrukowana elektroda węglowa, MWNTs-CS kompozyt wielościennych nanorurek węglowych i chitosanu, AuNP - TiO$_2$ nanocząstki złota z nanocząstkami tytanowymi, SAM - monowarstwa samoorganizująca

III. CEL PRACY

Biosensory elektrochemiczne to zintegrowane urządzania elektroanalityczne, które mają za zadanie przekształcić zmiany fizyczne, chemiczne i biologiczne w odpowiedzi sygnału elektrycznego. Urządzenia te służą do projektowania platform biosensorycznych na bazie modyfikowanych materiałów elektrodowych, które zawierają zakotwiczone bioreceptory odpowiedzialne za wychwytywanie analitu z roztworu. W celu poszukiwania bardziej ekonomicznych materiałów elektrodowych tworzy się biosensory elektrochemiczne bazując na technologii druku 3D, dzięki której można szybko i stosunkowo niskim kosztem wytwarzać biosensory oraz projektować układy do pomiarów elektrochemicznych.

Celem pracy doktorskiej było opracowanie metody oraz ocena stopnia modyfikacji wybranych materiałów elektrodowych, które stanowiły podstawę do elektrochemicznego wykrywania bioanalitów: uropatogennych szczepów bakterii *Escherichia coli* (UPEC) oraz hormonu ludzkiej gonadotropiny kosmówkowej (hCG). Zaprojektowane biosensory elektrochemiczne oparto na nanosześcianach złota (AuNCs) ze względu na ich unikalne właściwości, co stanowi element wiążący wszystkie prace ujęte w cyklu publikacji wybranych do dysertacji.

Mając na uwadze postawiony cel należało zweryfikować wpływ badanych nanostruktur złota na właściwości elektrochemiczne komercyjnie dostępnych materiałów elektrodowych takich jak: GC, ITO oraz Au. Dodatkowo jako bardziej ekonomiczną alternatywę zaproponowano wytworzenie biosensorów na elektrodach uzyskanych metodą druku 3D.

W ramach realizacji niniejszej pracy doktorskiej postawiono następujące zadania badawcze:

1. Zoptymalizowanie warunków modyfikacji elektrody GC, Au i ITO oraz dobór optymalnego materiału elektrodowego do modyfikacji powierzchni nonosześcianami złota (AuNCs) na potrzeby dalszej funkcjonalizacji uwzględniając zmianę ich właściwości elektrochemicznych.

2. Zbadanie wpływu bromku heksadecylotrimetyloamoniowego (CTAB) użytego w syntezie AuNCs na przebieg reakcji elektrodowych zachodzących na badanych elektrodach.

3. Sprawdzenie siły adsorpcji AuNCs do powierzchni badanych materiałów elektrodowych.

4. Opracowanie i optymalizacja warunków modyfikacji powierzchni elektrody GC wyselekcjonowaną nicią DNA oraz polimerazą RNA.

5. Charakterystyka modyfikowanej elektrody GC na poszczególnych etapach funkcjonalizacji z wykorzystaniem metod elektrochemicznych.

6. Opracowanie metody pomiarów modyfikowanych elektrod GC z wykorzystaniem techniki dynamicznej spektroskopii impedancyjnej (DEIS).

7. Optymalizacja warunków i dobór parametrów modyfikacji elektrody złotej w celu detekcji hormonu ludzkiej gonadotropiny kosmówkowej (hCG) z wykorzystaniem syntetycznego peptydu.

8. Badania i charakterystyka elektrody złotej na każdym etapie modyfikacji w użyciem metod elektrochemicznych do detekcji hormonu (hCG) opartych na syntetycznym peptydzie.

9. Optymalizacja zdolności detekcji hormonu (hCG) w roztworze soli fizjologicznej (PBS) oraz ludzkiej surowicy z wykorzystaniem syntetycznego peptydu na modyfikowanej elektrodzie złotej.

10. Opracowanie i porównanie sposobu aktywacji elektrod uzyskanych metodą druku 3D z uwzględnieniem różnych metod aktywacji (aktywacja elektrochemiczna oraz aktywacja enzymatyczna).

11. Wykorzystanie nanosześcianów złota do modyfikacji elektrod CB-PLA uzyskanych w technologii 3D do selektywnego wykrywania hormonu ludzkiej gonadotropiny kosmówkowej (hCG) z wykorzystaniem przeciwciał.

12. Badania i charakterystyka elektrod CB-PLA na każdym etapie modyfikacji w użyciem metod elektrochemicznych do detekcji hormonu (hCG) uzyskanych na bazie odpowiednich przeciwciał.

13. Porównanie zdolności detekcji hormonu (hCG) z wykorzystaniem elektrod CB-PLA w roztworze soli fizjologicznej (PBS) oraz ludzkiej surowicy w odniesieniu do elektrod opartych na bazie przeciwciał.

IV. METODOLOGIA

W trakcie realizacji prezentowanej rozprawy doktorskiej przeprowadzono badania eksperymentalne wykorzystując szereg technik badawczych, które przedstawiono w tabeli 7.

Tabela 7. Techniki badawczych użyte w dysertacji.

Techniki badawcze	Nazwa metody wraz z jej nazwą angielską
Elektrochemiczne	Woltamperometria cykliczna (CV) (ang. *Cyclic Voltammetry*) Elektrochemiczna spektroskopia impedancyjna (EIS) (ang. *Electrochemical Impedance Spectroscopy*) Skaningowa mikroskopia elektrochemicznea (SECM) (ang. *Scanning Electrochemical Microscopy*) Dynamiczna elektrochemiczna spektroskopia impedancyjna (DEIS) (ang. *Dynamic Electrochemical Impedance Spectroscopy*)
Inne metody fizykochemiczne	Skaningowa mikroskopia elektronowa (SEM) (ang. *Scanning Electron Microscopy*) Mikroskopia sił atomowych (AFM) (ang. *Atomic Force Microscopy*) Dyfrakcja rentgenowska (XRD) (ang. *X-ray Diffraction*) Analiza termograwimetryczna (TGA) (ang. *Thermogravimetric Analysis*)
Spektroskopowe	Spektroskopia fotoelektronów w zakresie promieniowania X (XPS) (ang. *X-Ray Photoelectron Spectroscopy*) Spektroskopia UV-Vis (ang. *UV-Vis Spectroscopy*)
Obliczeniowe	Teoria funkcjinału gęstości (DFT) (ang. *density functional theory*)

Techniki elektrochemiczne posłużyły do charakterystyki czystych oraz modyfikowanych materiałów elektrodowych. Wyniki pomiarów woltamperometrii cyklicznej (CV), elektrochemicznej spektroskopii impedancyjnej (EIS) (Artykuły 1-4) i skaningowej mikroskopii elektrochemicznej (SECM) (Artykuł 1) określały aktywność elektrochemiczną wybranych materiałów elektrodowych przed i po procedurze modyfikacji. W ramach prowadzonych eksperymentów badano kinetykę przeniesienia ładunku, obliczano aktywną powierzchnię elektrochemiczną (EASA), sprawdzano wpływ modyfikacji na rozkład pola dyfuzyjnego, wyznaczano parametr heterogenicznej stałej szybkości przenoszenia elektronów (k^0) oraz opór przenoszenia ładunku (R_{ct}).

Nowością przedstawioną w powyższej rozprawie doktorskiej, było wykorzystanie metody dynamicznej elektrochemicznej spektroskopii impedancyjnej (DEIS) w detekcji bioanalitów. Powyższą metodę zastosowano do badań zmian impedancyjnych związanych z detekcją uropatogennych szczepów bakterii *Escherichia coli* (UPEC-57) w analizowanych próbkach roztworów wzorcowych oraz próbkach zawierających ludzki mocz (Artykuł 2).

Ze względu na innowacyjność techniki DEIS zastosowanej do detekcji biomolekuł, która nie często jest opisywana w literaturze, zdecydowano się na krótki opis tej techniki. DEIS wykorzystuje wieloczęstotliwościowy sygnał perturbacyjny ze wszystkimi elementarnymi częstotliwościami nałożonymi i zastosowanymi jednocześnie w badanym systemie. Sygnał wzbudzenia jest generowany w sposób ciągły podczas eksperymentu, a zarejestrowane zmiany potencjału i prądu są selekcjonowane w odpowiednie części i przekształcane za pomocą transformacji Fouriera. Pomiar DEIS daje możliwość natychmiastowego uzyskania widm impedancyjnych, umożliwiając zbadanie procesów niestacjonarnych. Pomiary DEIS zapewniają możliwość szybkiego monitorowania czasu, potencjału polaryzacji lub stężenia analitu. Podejście to jest szczególnie korzystne w badaniu złożonych oddziaływań analitu na naładowanych powierzchniach elektrod [131].

Techniki EIS i DEIS wykorzystano do charakterystyki materiałów elektrodowych i zaprojektowania biosensorów czułych na uropatogenne szczepy bakterii *Escherichia coli* (UPEC-57) oraz hormonu ludzkiej gonadotropiny kosmówkowej (hCG) (Artykuł 2-3).

Rysunek 13. Aparatura pomiarowa wykorzystana do pomiarów elektrochemicznych.

Wszystkie pomiary elektrochemiczne CV i EIS, DEIS wykonywano z użyciem potencjostatu Autolab 128N (Metrohm, Holandia) (Rysunek 13) przy użyciu układu trójelektrodowego: elektrod pracujących (GC, Au, ITO, CB-PLA), elektrody odniesienia Ag|AgCl (3 M KCl), a jako przeciwelektrody używano drutu platynowego. Pomiary CV przeprowadzono w roztworze mieszaniny 1 mM $K_3[Fe(CN)_6]$ i $K_4[Fe(CN)_6]$ rozpuszczonych w 0,01 M PBS (pH 7,4). Wszystkie woltamperogramy cykliczne rejestrowano w różnych zakresach potencjału z szybkością skanowania 100 mV/s.

Eksperymenty elektrochemicznej spektroskopii impedancyjnej EIS wykonano w warunkach potencjału obwodu otwartego (OCP) z amplitudą sygnału 10 mV i zakresem częstotliwości od 100 kHz do 0,1 Hz, (40 punktów na dekadę).

Monitorowanie impedancji pomiarów DEIS przeprowadzono przy użyciu sygnału AC składającego się z pakietu 21 elementarnych sinusoid, w zakresie od 3 do 4500 Hz, nałożonego na skan woltamperometrii cyklicznej, od - 0,35 V do 0,60 V przy szybkości skanowania 2 mV/s. W tym celu użyto potencjostatu Autolab 128N (Metrohm, Holandia) połączonego z zestawem komputerowym wyposażonym w kartę 24-bitową, PCI-4461 (National Instruments, USA).

Określenie morfologii powierzchni wszystkich materiałów elektrodowych wykonano za pomocą technik mikroskopowych używając mikroskopu sił atomowych poprzez pomiar chropowatości powierzchni, wysokości i położenia cząstek (Artykuł 1 i 2). Powierzchnie modyfikowanych i funkcjonalizowanych materiałów elektrodowych, wielkości nanostruktur, morfologię i topografię zbadano wykorzystując skaningową mikroskopią elektronową SEM (Artykuł 1, 2 i 4). Dyfraktometrii

rentgenowskiej XRD używano do badań czystości fazowej badanego materiału oraz potwierdzenia rozmiaru i obecności nanostruktur na powierzchni badanych materiałów elektrodowych (Artykuł 1). Analiza termograwimetryczna posłużyła do określenia ilościowej zawartości przewodzącego napełniacza węglowego w komercyjnie dostępnych filamentach do druku 3D (Artykuł 4).

Na podstawie widm ze spektroskopii fotoelektronów w zakresie promieniowania X uzyskano informacje o zmianach strukturalnych, identyfikując powstające wiązania na czystych oraz modyfikowanych materiałach elektrodowych (Artykuł 2 i 4). Spektroskopię UV-Vis wykorzystano do oceny skuteczności siły adsorpcji nanostruktur złota do powierzchni badanych materiałów elektrodowych (Artykuł 1).

Ponadto badania eksperymentalne zostały uzupełnione o badania teoretyczne, w których wykorzystano teorię funkcjonału gęstości (DFT). Otrzymane wyniki pozwoliły na wyznaczenie energii adsorpcji nanostruktur złota do powierzchni elektrod i zbadania zmian spowodowanych obecnością CTAB podczas procesu syntezy (Artykuł 1).

V. CYKL PRAC WCHODZĄCYCH W SKŁAD ROZPRAWY DOKTORSKIEJ

1. Artykuł 1.

"Deciphering the molecular mechanism of substrate-induced assembly of gold nanocube arrays toward an accelerated electrocatalytic effect employing heterogeneous diffusion field confinement"

Langmuir, 38, 31, 2022, 9597-9610, IF_{2022} 3,9, MNiSW 100 pkt

Autorzy: Paweł Niedziałkowski, **Adrian Koterwa**, Adrian Olejnik, Artur Zieliński, Karolina Górnicka, Mateusz Brodowski, Robert Bogdanowicz, Jacek Ryl

1.1 Opis wykonanej pracy badawczej

W artykule 1 (Langmuir, 38, 31, 2022, s. 9597-9610) zbadano wpływ syntezowanych wcześniej nanosześcianów złota (AuNCs) z trzema najczęściej używanymi podłożami elektrodowymi, wykorzystywanymi do tworzenia biosensorów: węglem szklistym (GC), elektrody z tlenku cyny i indu (ITO) i elektrody złotej(Au). Opracowano i zoptymalizowano procedurę modyfikacji wyżej wymienionych podłoży z wykorzystaniem AuNCs metodą „drop casting". Następnie scharakteryzowano elektrody stosując metody fizykochemiczne (XRD, UV-VIS, SEM) udowadniając skuteczność procesu modyfikacji. Na podstawie wyników badań CV i EIS porównano właściwości elektrochemiczne badanych materiałów elektrodowych przed oraz po modyfikacji ich powierzchni. Badania te miały na celu dobór podłoża elektrodowego, które zmodyfikowane za pomocą AuNCs stworzy platformę o najlepszym efekcie elektrokatalitycznym. Tak przygotowane podłoże można wykorzystywać do dalszej modyfikacji biomolekułami. Dodatkowo w pracy zbadano wpływ środka powierzchniowo czynnego (CTAB), na oddziaływanie analizowanego wskaźnika redoks z badanymi powierzchniami elektrodowymi.

2.   Artykuł 2.

"Discriminating macromolecular interactions based on an impedimetric fingerprint supported by multivariate data analysis for rapid and label-free *Escherichia coli* recognition in human urine",
Biosensors & Bioelectronics, 238, 2023, 115561, IF$_{2023}$ 10,7, MNiSW 200 pkt

Autorzy: **Adrian Koterwa**, Mattia Pierpaoli, Bożena Nejman-Faleńczyk, Sylwia Bloch, Artur Zieliński, Wioletta Adamus-Białek, Zofia Jeleniewska, Bartosz Trzaskowski, Robert Bogdanowicz, Grzegorz Węgrzyn, Paweł Niedziałkowski, Jacek Ryl

1.2   Opis wykonanej pracy badawczej

W artykule 2 (Biosensors & Bioelectronics, 238, 2023, 115561) opracowano i zoptymalizowano metodykę modyfikacji powierzchni elektrod oraz wykorzystano nową technikę pomiarową do wykrywania dużych biocząsteczek przy użyciu modulowanych oddziaływań elektrostatycznych indukowanych przez polaryzację elektrody (DEIS).

Elektrodę GC w pierwszym etapie zmodyfikowano samoorganizującymi się warstwami AuNCs, a następnie użyto modyfikowanej łańcuchem alkilotiolowym struktury ssDNA o znanej sekwencji do utworzenia podwójnej nici dsDNA na elektrodzie, która powstała w procesie hybrydyzacji.

Otrzymaną platformę biosensoryczną wykorzystano do wykrywania uropatogennych szczepów bakterii *Escherichia coli* (UPEC-57) w roztworach soli fizjologicznej (PBS) i rzeczywistych próbkach ludzkiego moczu za pomocą polimerazy RNA. W ramach wykonywanych badań eksperymentalnych przeprowadzono pomiary z wykorzystaniem następujących technik pomiarowych: CV, EID, DEIS, które stosowano przed i po każdym procesie modyfikacji oraz detekcji stężeniowej w różnych warunkach pomiarowych.

3. Artykuł 3.

"An electrochemical biosensor for the determination of hormone Human Chorionic Gonadotropin (hCG) in human serum,
Electroanalysis, 2023, 35, 1-9, IF_{2023} 2,7, MNiSW 70 pkt

Autorzy: **Adrian Koterwa**, Magdalena Bojko, Jacek Ryl, Krzysztof Łukaszuk, Kornelia Kozłowska, Wiktor Sieklicki, Sylwia Rodziewicz-Motowidło, Paweł Niedziałkowski

3.1. Opis wykonanej pracy badawczej

W artykule 3 (Electroanalysis, 2023, 35, 1-9) zaprezentowano elektrochemiczną platformę biosensoryczną, którą uzyskano na bazie modyfikowanej elektrody złotej za pomocą syntetycznego oligopeptydu (PPLRINRHILTR) do wykrywania hormonu ludzkiej gonadotropiny kosmówkowej (hCG).

Opracowano metodę modyfikacji elektrody złotej peptydem (PPLRINRHILTR) oraz scharakteryzowano elektrody na każdym etapie modyfikacji. Następnie zbadano jej zdolność do wykrywania hCGw roztworze buforu fosforanowego (PBS, pH 7,4) stosowanym jako roztwór odniesienia w zakresie stężeń od 1×10^{-12} do 1×10^{-7} M (0,5 mIU/ml - 50 000 mIU/ml) oraz w roztworze ludzkiej surowicy. Wykrywanie hCG przeprowadzono w surowicy ludzkiej o stężeniu 1×10^{-12} M (0,5 mIU/ml) oraz w surowicy ludzkiej, do której dodano hCG.

4. Artykuł 4.

"The role of electrolysis and enzymatic hydrolysis treatment in the enhancement of the electrochemical properties of 3D-printed carbon black/poly(lactic acid) structures", Applied Surface Science, 574, 2022, 151587, IF_{2022} 6,7, MNiSW 140 pkt

Autorzy: **Adrian Koterwa**, Iwona Kaczmarzyk, Szymon Mania, Mateusz Cieślik, Robert Tylingo, Tadeusz Ossowski, Robert Bogdanowicz, Paweł Niedziałkowski, Jacek Ryl

4.1 Opis wykonanej pracy badawczej

W artykule 4 (Applied Surface Science, 574, 2022, 151587) przedstawiono optymalizację i porównanie metod aktywacji powierzchni elektrod drukowanych w technologii 3D (CB-PLA). W trakcie prac eksperymentalnych porównano aktywację elektrod w środowisku kwaśnym (1M HCl) i zasadowym (1M NaOH), porównano właściwości elektrochemiczne i fizykochemiczne uzyskanych elektrod CB-PLA i zaproponowano mechanizm ich aktywacji. Przeprowadzono również aktywację elektrod CB-PLA z wykorzystaniem proteinazy K. Dodatkowo, sprawdzono efektywność jednoczesnego przeprowadzenia hydrolizy enzymatycznej i aktywacji elektrochemicznej w środowisku alkalicznym.

5. Materiały dodatkowe, nieopublikowane

**5.1.1 Opis wykonanej pracy badawczej**

W wyniku przeprowadzonych prac eksperymentalnych, których rezultaty zostaną opublikowane w najbliższym czasie (5.5. Materiały dodatkowe, nieopublikowane), przeprowadzano dodatkowe badania łączące ze sobą Artykuły 1, 3 i 4.

Głównym założeniem prezentowanych badań eksperymentalnych było przeprowadzenie modyfikacja elektrody CB-PLA nanoszcześcianami złota (AuNCs) w celu detekcji hormonu ludzkiej gonadotropiny kosmówkowej (hCG). Najważniejszym rozwiązaniem w wykonanych pracach było zastosowanie taniej, wydrukowanej w technologii 3D elektrody CB-PLA. Użycie elektrody CB-PLA do stworzenia platformy biosensorycznej umożliwiły rezultaty badań wcześniej zaprezentowane w Artykule 4. Zaproponowaną metodą aktywacji elektrody CB-PLA była aktywacja elektrochemiczna w 1M roztworze NaOH. Na podstawie Artykułu 1 i 2, w których opisano unikatowe właściwości nanoszcześcianów złota AuNCs zdecydowano się na ich użycie w celu zwiększenia czułości zaprojektowanego biosensora. Zdobyte doświadczenia w modyfikacji elektrod GC przedstawione w Artykule 2 pozwoliły na zastosowanie innego bioreceptora w postaci przeciwciała anty-hCG. Uzyskane wyniki badań omówione w materiałach dodatkowych, posłużyły do porównania wyników detekcji hormonu hCG z zastosowaniem złotej elektrody modyfikowanej syntetycznym peptydem (Artykuł 3).

5.1.2 Metoda modyfikacji elektrody CB-PLA

Wydrukowaną elektrodę CB-PLA zaktywowano elektrochemicznie w 1M roztworze NaOH zgodnie z procedurą opisaną w Artykule 4. Następnie przeprowadzono dalszą modyfikację elektrody CB-PLA za pomocą zawiesiny AuNCs, których syntezę opisano w Artykule 1. Szczegółowy opis optymalizacji osadzania AuNCs na powierzchni materiałów elektrodowych zaprezentowano w artykule 1. W kolejnym etapie użyto kwasu 3-merkaptopropionowego (MPA) w celu modyfikacji AuNCs obecnych na elektrodzie CB-PLA. Do uzyskanych grup karboksylowch na powierzchni nonoszcześcianów złota przyłączono przeciwciała anty-hCG stosując mieszaninę EDC/NHS. Schemat procedury modyfikacji elektrody CB-PLA zaprezentowano na rysunku 14. Zaprojektowaną platformę biosensoryczną wykorzystano do detekcji

hormonu ludzkiej gonadotropiny kosmówkowej (hCG) w roztworze soli fizjologicznej (PBS, pH 7,4) oraz ludzkiej surowicy.
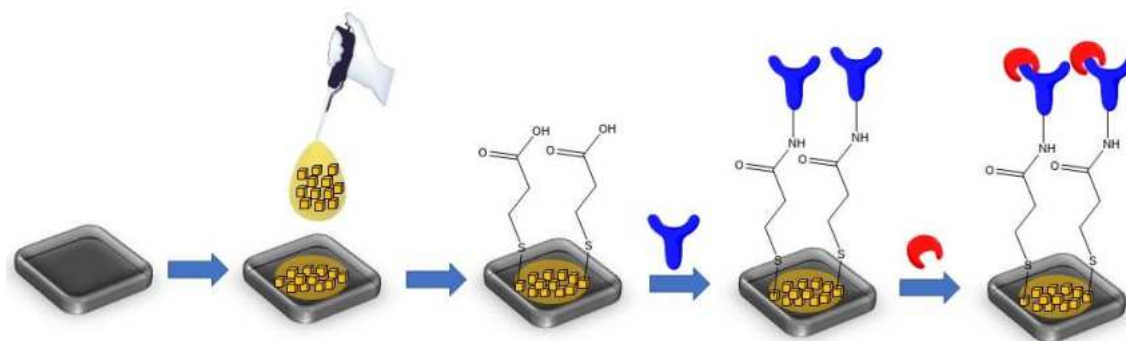
Rysunek 14. Schemat procedury modyfikacji elektrody CB-PLA za pomocą AuNCs oraz przeciwciał anty-hCG.

5.1.3 Wyniki badań elektrochemicznych

Zgodnie z procedurą na każdym etapie modyfikacji elektrody CB-PLA przeprowadzano pomiary charakterystyki elektrod z wykorzystaniem techniki CV i EIS. Po otrzymaniu założonej platformy biosensorycznej dokonano detekcji hormonu ludzkiej gonadotropiny kosmówkowej (hCG) w takich samych zakresach stężeń, jakie stosowano w Artykule 3 (od 1×10^{-12} do 1×10^{-7} M (0.5 mIU/ ml-50 000 mIU/ml)). Zamierzeniem takiego postępowania było porównanie dwóch platform różniących się sposobem modyfikacji oraz dodatkowe zastosowanie nanosześcianów złota (AuNCs). Uzyskana wartość granicy oznaczalności (LOD) dla badanej biosensora detekcji hCG metodą EIS w roztworze PBS wynosił $3,03 \times 10^{-15}$. Wartość ta jest niższa od tej, którą otrzymano dla złotych elektrod modyfikowanych syntetycznym peptydem ($1,91 \times 10^{-14}$ M), mierzoną w tych samych warunkach pomiarowych (Artykuł 3). Niewątpliwą zaletą zastosowania elektrod CB-PLA i nanosześcianów złota (AuNCs) jest możliwość stężeniowej detekcji hormonu hCG w surowicy ludzkiej. W Artykule 3 przedstawiono możliwość detekcji hormonu hCG w stężeniu 1×10^{-12} M, natomiast w badaniach dodatkowych wykorzystano nową platformę sensoryczną do detekcji hormonu hCG w całym zakresie stężeń(od 1×10^{-12} do 1×10^{-7} M (0.5 mIU/ ml-50 000 mIU/ml)).

Można stwierdzić, że w badaniach umieszczonych w materiałach dodatkowych przedstawiono nową metodę modyfikacji elektrody CB-PLA uzyskując platformę biosensoryczną do detekcji hormonu ludzkiej gonadotropiny kosmówkowej (hCG) charakteryzującą się większą czułością w stosunku do elektrod opisanych

w Artykule 3. Właściwości powyższych elektrod determinowane są obecnością modyfikowanych przeciwciałem anty-hCG nanosześcianów złota (AuNCs).

VI. PODSUMOWANIE I WNIOSKI

Prezentowane badania eksperymentalne umieszczone w artykułach 1,2,3,4 oraz materiały dodatkowe wchodzą w skład rozprawy doktorskiej, której głównym celem było opracowanie i ocena stopnia modyfikacji materiałów elektrodowych na potrzebę elektrochemicznego wykrywania bioanalitów. W realizowanych badaniach skupiono się na upropatogennych szczepach bakterii *Escherichia coli* (UPEC-57) i hormonie ludzkiej gonadotropiny kosmówkowej (hCG).

W pierwszym etapie badań określono własności katalityczne metodami elektrochemicznymi samoorganizujących się nanocześcianów złota (AuNCs) na powierzchni materiałów elektrodowych GC, Au oraz ITO. Przeprowadzona charakterystyka elektrochemiczna metodami CV pozwoliła na wyznaczenie powierzchni aktywnej elektrochemicznie (EASA) dla czystych i modyfikowanych powierzchni. Wykazano wzrost o 65% w przypadku elektrody GC i wzrost o 27% w przypadku elektrody Au, podczas gdy dla elektrody ITO wartość EASA pozostała niezmieniona. Modyfikacja elektrody GC za pomocą AuNCs spowodowała wzrost kinetyki transferu elektronów, z najwyższą heterogeniczną stałą szybkości pośród wszystkich badanych układów, osiągającą odpowiednio $1,81\times10^{-2}$ i $4,00\times10^{-2}$ cm·s^{-1} w badaniach CV i SECM. Udowodniono, że, przyspieszony efekt elektrokatalityczny w przypadku elektrody GC związany jest z wykorzystaniem heterogenicznego ograniczenia pola dyfuzyjnego, a także najniższe ograniczenie transferu elektronów przez CTAB względem pozostałych elektrod. Podobnego efektu nie zaobserwowano dla modyfikowanych elektrod ITO lub Au, gdzie szybkość transferu elektronów była ograniczona ze względu na samodyfuzję Au-Au i obecność CTAB. Dodatkowo sprawdzono siły adsorpcji AuNCs do powierzchni materiałów elektrodowych GC, ITO i Au metodami elektrochemicznymi CV i spektroskopowymi UV-Vis. Wyniki pomiarów CV udowodniły, że AuNCs są obecne na powierzchni badanych elektrod, ponieważ przy potencjale 0.75V pojawia się nieodwracany pik redukcji złota. Metodami spektroskopowymi potwierdzono, że AuNCs na zmodyfikowanej elektrodzie nie przechodzą do roztworu są stabilne na powierzchni elektrody.

W drugim etapie badań otrzymano biosensor elektrochemiczny oparty na aptametrze DNA dołączonym do samoorganizujących się nanosześcianów złota (AuNCs). Poprzednie badania udowodniły, że najlepszymi własnościami katalitycznym charakteryzuje się elektroda GC dlatego na niej utworzono platformę biosensoryczną do

szybkiego wykrywania uropatogennych szczepów bakterii *Escherichia coli* za pomocą polimerazy RNA. Skuteczność biosensora badano za pomocą technik CV i EIS. Prezentowany biosensor wykrywa UPEC-57 z LOD osiągającym wartości 11,3 CFU/ml po zaledwie 2 minutach. Ponadto w badaniach wykorzystano technikę DEIS, a jej wyniki poddano wieloparametrycznej analizie dyskryminacyjnej impedancji (MIDA). Udowodniono, że wykrywanie analitu obecnego w roztworze zachodzi nie tylko przez silne siły międzycząsteczkowe, ale także przez słabe oddziaływania kulombowskie, mierzonew różnych warunkach polaryzacji.

Kolejno zaprezentowano nowy biosensor na hormon ludzkiej gonadotropiny kosmówkowej (hCG) z wykorzystaniem modyfikowanej elektrody złotej. W tym celu zoptymalizowano warunki i dobory parametrów modyfikacji z wykorzystaniem syntetycznego peptydu, który był czuły na hormonu hCG. Biosensor badano za pomocą CV oraz EIS wykorzystując tą technikę po raz pierwszy do wykrywania hCG. Wykazano, że hormon na modyfikowanej elektrodzie złotej wykrywany jest na poziomie LOD $1{,}91 \times 10^{-14}$ M (0,0095 mIU/ml). Skuteczność biosesnsora zbadano również w surowicy ludzkiej pochodzącej od pacjentów, co może być w przyszłości niezwykle ważne ze względu na badania kliniczne.

W dysertacji zaprezentowano, również nowe sposobu aktywacji elektrod CB-PLA uzyskanych metodą druku 3D. Przedstawiono dwa sposoby aktywacji poprzez aktywację elektrochemiczną oraz trawienie enzymatyczne za pomocą Proteinazy K. Udowodniono, że aktywacja elektrochemiczna elektrody CB-PLA przeprowadzana w środowisku zasadowym jest najskuteczniejsza, generując wyższą EASA i wzrost szybkość transferu elektronów. Warunki zasadowe wykazują lepszą zdolność do aktywacji elektrod CB-PLA, ponieważ łańcuch polimerowy PLA degraduje poprzez wewnątrzcząsteczkową transestryfikację.

Ostatni etap badań opierał się na uzyskaniu platformy biosensorycznej na elektrodzie CB-PLA modyfikowanej za pomocą AuNCs oraz przeciwciał monoklonalnych oddziałowujących z hormonem hCG. W wyniku przeprowadzonych badań uzyskano biosensor zdolny do detekcji hormonu (hCG). Na każdym etapie modyfikacji elektrod przeprowadzono charakterystykę elektrochemiczną oraz zbadano zdolność detekcji hormonu (hCG) z wykorzystaniem zmodyfikowanych elektrod w roztworze soli fizjologicznej (PBS) oraz ludzkiej surowicy. Otrzymane wyniki wskazują na to, że detekcja hormonu (hCG) w roztworze PBS może być prowadzona na

niskim poziomie stężeń. Wyznaczona wartość granicy oznaczalności (LOD) wynosiła $3{,}03 \times 10^{-15}$ w zakresie stężeń (od 1×10^{-12} do 1×10^{-7} M (0.5 mIU/ ml-50 000 mIU/ml)). Główną zaletą powyższego biosensora jest zdolność detekcji hormonu hCG w ludzkiej surowicy krwi.

Reasumując, wyniki pomiarowe przedstawione w prezentowanej rozprawie doktorskiej opublikowane w renomowanych czasopismach z zakresu chemii i elektrochemii stanowią istotne poszerzenie wiedzy z zakresu projektowania platform biosensorycznych. Jednoznacznie wskazano, że biosernsory oparte na nanosześcianach złota (AuNCs) mają duży potencjał badawczy. Udowodniono, że modyfikacja chemiczna AuNCs z wykorzystaniem takich biomolukuł jak DNA, syntetyczne peptydy i przeciwciała pozwalają na uzyskanie selektywnych bioczujników elektrochemicznych.

Przyszłościowo, przedstawione metody modyfikacji materiałów elektrodowych mogą zostać wykorzystane jako alternatywne biosensory, których produkcja może być bardziej ekonomiczna w zestawieniu z powszechnie stosowanymi procedurami diagnostycznymi.

VII. BIBLIOGRAFIA

1. Cho I-H, Kim DH, Park S. *Biomaterials Research*, 2020, 24: 6
2. Cammann K. *Z Anal Chem*, 1977, 287: 1–9
3. Clark LC, Lyons C. *Annals of the New York Academy of Sciences*, 1962, 102: 29–45
4. Irkham I, Ibrahim AU, Pwavodi PC, Al-Turjman F, Hartati YW. *Sensors*, 2023, 23: 2240
5. Ronkainen NJ, Halsall HB, Heineman WR. *Chem Soc Rev*, 2010, 39: 1747
6. Mehrotra P. *Journal of Oral Biology and Craniofacial Research*, 2016, 6: 153–159
7. Heineman WR, Jensen WB. *Biosensors and Bioelectronics*, 2006, 21: 1403–1404
8. Malik S, Singh J, Goyat R, Saharan Y, Chaudhry V, Umar A, Ibrahim AA, Akbar S, Ameen S, Baskoutas S. *Heliyon*, 2023, 9
9. Naresh V, Lee N. *Sensors*, 2021, 21: 1109
10. Hai X, Li Y, Zhu C, Song W, Cao J, Bi S. *TrAC Trends in Analytical Chemistry*, 2020, 133: 116098
11. Shanbhag MM, Manasa G, Mascarenhas RJ, Mondal K, Shetti NP. *Chemical Engineering Journal Advances*, 2023, 16: 100516
12. Pividori MI, Merkoçi A, Alegret S. *Biosensors and Bioelectronics*, 2000, 15: 291–303
13. Wang L, Chen X, Wang X, Han X, Liu S, Zhao C. *Biosens Bioelectron*, 2011, 30: 151–157
14. R S, R V, G S, Ak S, S S, Rk G, Bd M. *Bioelectrochemistry (Amsterdam, Netherlands)*, 2012, 86
15. Lee H-E, Kang Y, Choi S. *International Journal of Electrochemical Science*, 2014, 9: 6793–6808
16. Jolly P, Batistuti MR, Miodek A, Zhurauski P, Mulato M, Lindsay MA, Estrela P. *Sci Rep*, 2016, 6: 36719
17. Jampasa S, Wonsawat W, Rodthongkum N, Siangproh W, Yanatatsaneejit P, Vilaivan T, Chailapakul O. *Biosens Bioelectron*, 2014, 54: 428–434
18. Yang Y, Li C, Yin L, Liu M, Wang Z, Shu Y, Li G. *ACS Appl Mater Interfaces*, 2014, 6: 7579–7584
19. Rasheed PA, Sandhyarani N. *Sensors and Actuators B: Chemical*, 2014, 204: 777–782
20. Jiang C, Yang T, Jiao K, Gao H. *Electrochimica Acta*, 2008, 53: 2917–2924
21. W Z, T Y, X L, D W, K J. *Biosensors & bioelectronics*, 2009, 25
22. Su S, Cao W, Liu W, Lu Z, Zhu D, Chao J, Weng L, Wang L, Fan C, Wang L. *Biosens Bioelectron*, 2017, 94: 552–559
23. Olowu RA, Arotiba O, Mailu SN, Waryo TT, Baker P, Iwuoha E. *Sensors*, 2010, 10: 9872–9890
24. Nxele SR, Nyokong T. *Journal of Inorganic Biochemistry*, 2021, 221: 111462
25. Kim Y-J, Kim YS, Niazi JH, Gu MB. *Bioprocess Biosyst Eng*, 2010, 33: 31–37
26. Salimian R, Kékedy-Nagy L, Ferapontova EE. *ChemElectroChem*, 2017, 4: 872–879
27. Donahue AC, Albitar M. Antibodies in Biosensing. In: Zourob M, Ed. Recognition Receptors in Biosensors. New York, NY: Springer, 2010. 221–248
28. Conroy PJ, Hearty S, Leonard P, O'Kennedy RJ. *Semin Cell Dev Biol*, 2009, 20: 10–26
29. Zeng X, Shen Z, Mernaugh R. *Anal Bioanal Chem*, 2012, 402: 3027–3038
30. Dixit CK, Vashist SK, MacCraith BD, O'Kennedy R. *Nat Protoc*, 2011, 6: 439–445

31. Olowu RA, Arotiba O, Mailu SN, Waryo TT, Baker P, Iwuoha E. *Sensors*, 2010, 10: 9872–9890

32. Radi A-E, Muñoz-Berbel X, Lates V, Marty J-L. *Biosensors and Bioelectronics*, 2009, 24: 1888–1892

33. Ionescu RE, Jaffrezic-Renault N, Bouffier L, Gondran C, Cosnier S, Pinacho DG, Marco M-P, Sánchez-Baeza FJ, Healy T, Martelet C. *Biosensors and Bioelectronics*, 2007, 23: 549–555

34. Zhong H, Zhao C, Chen J, Chen M, Luo T, Tang W, Liu J. *RSC Adv*, 2020, 10: 22291–22296

35. Huang J, Xie Z, Xie Z, Luo S, Xie L, Huang L, Fan Q, Zhang Y, Wang S, Zeng T. *Analytica Chimica Acta*, 2016, 913: 121–127

36. Valipour A, Roushani M. *Biosensors and Bioelectronics*, 2017, 89: 946–951

37. Assari P, Rafati AA, Feizollahi A, Asadpour Joghani R. *Microchim Acta*, 2019, 186: 484

38. Shen C, Wang L, Zhang H, Liu S, Jiang J. *Front Chem*, 2020, 8: 589560

39. Singh VK, Kumar S, Pandey SK, Srivastava S, Mishra M, Gupta G, Malhotra BD, Tiwari RS, Srivastava A. *Biosensors and Bioelectronics*, 2018, 105: 173–181

40. Chen Y, Li Y, Deng D, He H, Yan X, Wang Z, Fan C, Luo L. *Biosensors and Bioelectronics*, 2018, 102: 301–306

41. Zhao D, Wang Y, Nie G. *Microchim Acta*, 2016, 183: 2925–2932

42. Morales MA, Halpern JM. *Bioconjugate Chem*, 2018, 29: 3231–3239

43. Vanova V, Mitrevska K, Milosavljevic V, Hynek D, Richtera L, Adam V. *Biosensors and Bioelectronics*, 2021, 180: 113087

44. Negahdary M, Heli H. *Microchim Acta*, 2019, 186: 766

45. Zhao J, Wang S, Zhang S, Zhao P, Wang J, Yan M, Ge S, Yu J. *Biosensors and Bioelectronics*, 2020, 150: 111958

46. Deng D, Hao Y, Yang S, Han Q, Liu L, Xiang Y, Tu F, Xia N. *Sensors and Actuators B: Chemical*, 2019, 286: 415–420

47. Eissa S, Zourob M. *Microchim Acta*, 2020, 187: 486

48. Gatto E, Venanzi M, Palleschi A, Stella L, Pispisa B, Lorenzelli L, Toniolo C, Formaggio F, Marletta G. *Materials Science and Engineering: C*, 2007, 27: 1309–1312

49. Hu Q, Su L, Mao Y, Gan S, Bao Y, Qin D, Wang W, Zhang Y, Niu L. *Biosensors and Bioelectronics*, 2021, 178: 113010

50. Ye Z, Li G, Xu L, Yu Q, Yue X, Wu Y, Ye B. *Talanta*, 2020, 209: 120611

51. Ucar A, González-Fernández E, Staderini M, Avlonitis N, Murray AF, Bradley M, Mount AR. *Analyst*, 2020, 145: 975–982

52. Hu Q, Bao Y, Gan S, Zhang Y, Han D, Niu L. *Anal Chem*, 2020, 92: 3470–3476

53. González-Fernández E, Staderini M, Yussof A, Scholefield E, Murray AF, Mount AR, Bradley M. *Biosensors and Bioelectronics*, 2018, 119: 209–214

54. He Y, Xie S, Yang X, Yuan R, Chai Y. *ACS Appl Mater Interfaces*, 2015, 7: 13360–13366

55. Liu G, Wang J, Wunschel DS, Lin Y. *J Am Chem Soc*, 2006, 128: 12382–12383

56. Chan C-Y, Guo J, Sun C, Tsang M-K, Tian F, Hao J, Chen S, Yang M. *Sensors and Actuators B: Chemical*, 2015, 220: 131–137

57. Liu H, Malhotra R, Peczuh MW, Rusling JF. *Anal Chem*, 2010, 82: 5865–5871

58. Andreescu D, Andreescu S, Sadik OA. New Materials for Biosensors, Biochips and Molecular Bioelectronics. Comprehensive Analytical Chemistry. Vol 44. Elsevier, 2005. 285–327

59. Basharin AYu, Dozhdikov VS, Dubinchuk VT, Kirillin AV, Lysenko IYu, Turchaninov MA. *Tech Phys Lett*, 2009, 35: 428–431

60. Jenkins GM. *Proc R Soc Lond A*, 1972, 327: 501–517

61. Jenkins GM, Kawamura K, Ban LL, Ubbelohde ARJP. *Proceedings of the Royal Society of London A Mathematical and Physical Sciences*, 1997, 327: 501–517

62. Uskoković V. *Carbon Trends*, 2021, 5: 100116

63. Dasgupta K, Sathiyamoorthy D. *Materials Science and Technology*, August 2003

64. Fischer E. *Analytica Chimica Acta*, 1999, 8

65. Zittel HE, Miller FJ. *Anal Chem*, 1965, 37: 200–203

66. Elliott CMichael, Murray RW. *Anal Chem*, 1976, 48: 1247–1254

67. Corti CW, Holliday RJ. *Gold Bull*, 2004, 37: 20–26

68. Lipkowski J. *Phys Chem Chem Phys*, 2010, 12: 13874

69. Chambers DL, Wan CT. Physical Vapor Deposition of Gold and Its Alloys. Precious Metals 1981. Elsevier, 1982. 219–238

70. Larson CE, Baum TH, Jackson RL. *MRS Proc*, 1986, 75: 721

71. Vafaiee M, Vossoughi M, Mohammadpour R, Sasanpour P. *Sci Rep*, 2019, 9: 2985

72. Vulcu A, Grosan C, Muresan LM, Pruneanu S, Olenic L. *Electrochimica Acta*, 2013, 88: 839–846

73. Ghobashy MM, Alkhursani ShA, Alqahtani HA, El-damhougy TK, Madani M. *Materials Science and Engineering: B*, 2024, 301: 117191

74. Jc L, La E, Jk K, Rg N, Gm W. *Chemical reviews*, 2005, 105

75. Chen G, Tong H, Gao T, Chen Y, Li G. *Anal Chim Acta*, 2014, 849: 1–6

76. G S, A A, Ms C, A T, A F, F F, G G, E P. *Talanta*, 2024, 268

77. Cui J, Adeloju SB, Wu Y. *Anal Chim Acta*, 2014, 809: 134–140

78. Yang M, Qu F, Li Y, He Y, Shen G, Yu R. *Biosens Bioelectron*, 2007, 23: 414–420

79. Aravamudhan S, Ramgir NS, Bhansali S. *Sensors and Actuators B: Chemical*, 2007, 127: 29–35

80. Razmi N, Hasanzadeh M, Willander M, Nur O. *Anal Methods*, 2022, 14: 1562–1570

81. Park J-E, Lee Y, Nam J-M. *Nano Lett*, 2018, 18: 6475–6482

82. Hernández J, Solla-Gullón J, Herrero E, Aldaz A, Feliu JM. *J Phys Chem C*, 2007, 111: 14078–14083

83. Zhang L, Wang J, Zhang J, Liu Y, Wu L, Shen J, Zhang Y, Hu Y, Fan Q, Huang W, Wang L. *ACS Sens*, 2017, 2: 1435–1440

84. Baek SH, Song HW, Lee S, Kim J-E, Kim YH, Wi J-S, Ok JG, Park JS, Hong S, Kwak MK, Lee HJ, Nam S-W. *Front Chem*, 2020, 8: 285

85. Bagheri Hashkavayi A, Bakhsh Raoof J, Ojani R, Hamidi Asl E. *Electroanalysis*, 2015, 27: 1449–1456

86. Lv H, Zhang X, Li Y, Ren Y, Zhang C, Wang P, Xu Z, Li X, Chen Z, Dong Y. *Microchim Acta*, 2019, 186: 416

87. Koterwa A, Pierpaoli M, Nejman-Faleńczyk B, Bloch S, Zieliński A, Adamus-Białek W, Jeleniewska Z, Trzaskowski B, Bogdanowicz R, Węgrzyn G, Niedziałkowski P, Ryl J. *Biosensors and Bioelectronics*, 2023, 238: 115561

88. Tavakkoli N, Soltani N, Tabar ZK, Jalali MR. *Chem Pap*, 2019, 73: 1377–1388

89. Bouden S, Dahi A, Hauquier F, Randriamahazaka H, Ghilane J. *Sci Rep*, 2016, 6: 36708

90. Fu Y, Liang F, Tian H, Hu J. *Electrochimica Acta*, 2014, 120: 314–318

91. Aydın EB, Aydın M, Sezgintürk MK. *Sensors and Actuators B: Chemical*, 2020, 306: 127613

92. Silah H, Erkmen C, Demir E, Uslu B. *TrAC Trends in Analytical Chemistry*, 2021, 141: 116289

93. Bayer I. *Materials*, 2017, 10: 748

94. Marsh H, Reinoso FR. Activated Carbon. Amsterdam Boston, 2006

95. Koterwa A, Kaczmarzyk I, Mania S, Cieslik M, Tylingo R, Ossowski T, Bogdanowicz R, Niedziałkowski P, Ryl J. *Applied Surface Science*, 2022, 574: 151587

96. Manzanares Palenzuela CL, Novotný F, Krupička P, Sofer Z, Pumera M. *Anal Chem*, 2018, 90: 5753–5757

97. Glowacki MJ, Cieslik M, Sawczak M, Koterwa A, Kaczmarzyk I, Jendrzejewski R, Szynkiewicz L, Ossowski T, Bogdanowicz R, Niedzialkowski P, Ryl J. *Applied Surface Science*, 2021, 556: 149788

98. Calafat AM, Ye X, Wong L-Y, Bishop AM, Needham LL. *Environmental Health Perspectives*, 2010, 118: 679–685

99. Johnson JR. *Clin Microbiol Rev*, 1991, 4: 80–128

100. Dicle Y, Karamese M. *Future Microbiol*, 2024, 19: 281–291

101. Güner A, Çevik E, Şenel M, Alpsoy L. *Food Chemistry*, 2017, 229: 358–365

102. Barreiros dos Santos M, Azevedo S, Agusil JP, Prieto-Simón B, Sporer C, Torrents E, Juárez A, Teixeira V, Samitier J. *Bioelectrochemistry*, 2015, 101: 146–152

103. Wang Y, Alocilja EC. *Journal of Biological Engineering*, 2015, 9: 16

104. Guo Y, Wang Y, Liu S, Yu J, Wang H, Cui M, Huang J. *Analyst*, 2014, 140: 551–559

105. Wang H, Zhao Y, Bie S, Suo T, Jia G, Liu B, Ye R, Li Z. *Applied Sciences*, 2019, 9: 295

106. Cimafonte M, Fulgione A, Gaglione R, Papaianni M, Capparelli R, Arciello A, Bolletti Censi S, Borriello G, Velotta R, Della Ventura B. *Sensors*, 2020, 20: 274

107. Pandey CM, Tiwari I, Singh VN, Sood KN, Sumana G, Malhotra BD. *Sensors and Actuators B: Chemical*, 2017, 238: 1060–1069

108. Xu M, Wang R, Li Y. *Talanta*, 2016, 148: 200–208

109. Geng P, Zhang X, Meng W, Wang Q, Zhang W, Jin L, Feng Z, Wu Z. *Electrochimica Acta*, 2008, 53: 4663–4668

110. Housaindokht mohammad R, Verdian A, Sheikhzadeh E, Pordeli P, rouhbakhsh zaeri Z, Janati fard F, Nosrati M, Mashreghi M, Haghparast A, Nakhaeipour A, Esmaeili AA, Soleymani S. *Advanced Materials Letters*, 2018, 9: 369–374

111. Canfield RE, O'Connor JF, Birken S, Krichevsky A, Wilcox AJ. *Environ Health Perspect*, 1987, 74: 57–66

112. de Medeiros SF, Norman RJ. *Human Reproduction Update*, 2009, 15: 69–95

113. Handschuh K, Guibourdenche J, Tsatsaris V, Guesnon M, Laurendeau I, Evain-Brion D, Fournier T. *Endocrinology*, 2007, 148: 5011–5019

114. Faiman C, Ryan RJ, Zwirek SJ, Rubin ME. *J Clin Endocrinol Metab*, 1968, 28: 1323–1329

115. Ghumman S, Ed. Principles and Practice of Controlled Ovarian Stimulation in ART. 1st ed. 2016 edition. New York, NY: Springer, 2015

116. Korevaar TIM, Steegers EAP, Rijke YB de, Schalekamp-Timmermans S, Visser WE, Hofman A, Jaddoe VWV, Tiemeier H, Visser TJ, Medici M, Peeters RP. *European Journal of Epidemiology*, 2015, 30: 1057

117. Mahajan M, Belgaumi UI, Baad R, Vibhute N, Kadashetti V, Bommanavar S, Kamate W. *Gynecol Minim Invasive Ther*, 2019, 8: 59–61

118. Chiu N-F, Kuo C-T, Lin T-L, Chang C-C, Chen C-Y. *Biosens Bioelectron*, 2017, 94: 351–357

119. Chang C-C, Chen C-P, Lee C-H, Chen C-Y, Lin C-W. *Chem Commun*, 2014, 50: 14443–14446

120. Xia N, Chen Z, Liu Y, Ren H, Liu L. *Sensors and Actuators B: Chemical*, 2017, 243: 784–791
121. Li H, Cai T, Ren Y, Huang J, Jiang H, Hou Y, Tang C, Yang J, Zhao J, Yu P. *Anal Methods*, 2021, 13: 4442–4451
122. Shen X, Ma Y, Zeng Q, Huang J, Tao J, Wang L. *ChemistrySelect*, 2017, 2: 6549–6555
123. Yang G, Yang X, Yang C, Yang Y. *Colloids and Surfaces A: Physicochemical and Engineering Aspects*, 2011, 389: 195–200
124. Li R, Wu D, Li H, Xu C, Wang H, Zhao Y, Cai Y, Wei Q, Du B. *Anal Biochem*, 2011, 414: 196–201
125. Viet NX, Hoan NX, Takamura Y. *Materials Chemistry and Physics*, 2019, 227: 123–129
126. Akram M, Stuart MC, Wong DKY. *Electroanalysis*, 2006, 18: 237–246
127. Rizwan M, Hazmi M, Lim SA, Ahmed MU. *Journal of Electroanalytical Chemistry*, 2019, 833: 462–470
128. Zhao D, Yu Y, Xu C. *RSC Adv*, 2015, 6: 87–93
129. Lim SA, Yoshikawa H, Tamiya E, Yasin HM, Ahmed MU. *RSC Adv*, 2014, 4: 58460–58466
130. Yang H, Yuan R, Chai Y, Zhuo Y. *Colloids Surf B Biointerfaces*, 2011, 82: 463–469
131. Niedzialkowski P, Slepski P, Wysocka J, Chamier-Cieminska J, Burczyk L, Sobaszek M, Wcislo A, Ossowski T, Bogdanowicz R, Ryl J. *Sensors and Actuators B: Chemical*, 2020, 323: 128664

VIII. SPIS WYSTĄPIEŃ KONFERENCYJNYCH

I. Referaty

1. **A. Koterwa**, J. Ryl, K. Łukaszuk, P. Niedziałkowski, Platformy sensoryczne wykrywające hormon ludzkiej gonadotropiny kosmówkowej (hCG) w ludzkiej surowicy, XIX Ogólnopolskie Seminarium Doktorantów i Studentów, Na pograniczu chemii i biologii, 2023

2. K. Kozłowska, M. Cieślik, **A. Koterwa**, K. Formela, J. Ryl, P. Niedziałkowski, Wykorzystanie domowego sprzętu do aktywacji powierzchni elektrod otrzymanych metodą druku 3D, V Konferencja Naukowa Chemia-Biznes-Środowisko, 2023

3. K. Kozłowska, M. Cieślik, **A. Koterwa**, K. Formela, J. Ryl, P. Niedziałkowski, Wykorzystanie promieniowania mikrofalowego do aktywacji elektrochemicznej elektrod, XIX Ogólnopolskie Seminarium Doktorantów i Studentów, Na pograniczu chemii i biologii, 2023

4. P. Niedziałkowski, **A. Koterwa**, A. Olejnik, A. Zieliński, K. Górnicka , M. Brodowski, R. Bogdanowicz, J. Ryl, Gold nanocubes (AuNCs) - synthesis, characterization and selection of a relevant surface modification - for biosensing application, 11th International Workshop on Surface Modification for Chemical and Biochemical Sensing, 2023

5. A. Kulpa-Koterwa, **A. Koterwa**, P. Niedziałkowski, Nowe nanoadsorbenty jonów metali ciężkich na bazie magnetycznego tlenku żelaza i cyklenu $Fe_3O_4@SiO_2$-A4C12, IV Konferencja Naukowa, Chemia - Biznes - Środowisko, 2022

6. M. Karman, **A. Koterwa**, G. Romanowski, Kompleksy molibdenu(VI) z zasadami Schiffa, pochodnymi aminoalkoholi - synteza, struktura oraz aktywność katalityczna, III Konferencja Naukowa,Chemia - Biznes - Środowisko, 2021

7. **A. Koterwa**, J. Ryl, M. Karman, A. Kulpa-Koterwa, T. Ossowski, P. Niedziałkowski, Badania i optymalizacja warunków wykorzystania Proteinazy K w trawieniu kwasu polimlekowego w matrycach C-PLA w celu uzyskania proekologicznych elektrod otrzymywanych w technologii druku 3D, II Pomorskie Studenckie Sympozjum Chemiczne, 2021

8. **A. Koterwa**, J. Ryl, T. Ossowski, A. Kulpa-Koterwa, P. Niedziałkowski, Elektroaktywacja drukowanych w 3D przewodzących elektrod węglowo-

polilaktydowych za pomocą pulsacyjnej ablacji laserowej, III Konferencja Naukowa "Chemia - Biznes - Środowisko", 2021

9. **A. Koterwa**, J. Ryl, M. Cieślik, A. Kulpa-Koterwa, T. Ossowski, P. Niedziałkowski, Elektrody drukowane w technologii 3D - sposoby aktywacji powierzchni, VI Interdyscyplinarna Akademicka Konferencja Ochrony Środowiska, 2021

10. **A. Koterwa**, J. Ryl, A. Kulpa-Koterwa, T. Ossowski, P. Niedziałkowski, Metody otrzymywania nowych materiałów elektrodowych z wykorzystaniem technologii druku 3D, Ogólnopolska Studencka Konferencja Naukowa, Bliżej Chemii, 2021

11. **A. Koterwa**, T. Ossowski, A. Kulpa-Koterwa, P. Niedziałkowski, Detekcja hormonu ludzkiej gonadotropiny kosmówkowej (hCG) z wykorzystaniem metod elektroanalitycznych, XIV Kopernikańskie Seminarium Doktoranckie, 2021

12. A. Kulpa-Koterwa, **A. Koterwa**, T. Ossowski, P. Niedziałkowski, Elektroda GC modyfikowana nanocząstkami magnetycznymi typu rdzeń - otoczka opartymi na Fe_3O_4 - charakterystyka, VI Interdyscyplinarna Akademicka Konferencja Ochrony Środowiska, 2021

13. A. Kulpa-Koterwa, E. Adamska, **A. Koterwa**, T. Ossowski, P. Niedziałkowski, Optymalizacja warunków modyfikacji elektrody GC sfunkcjonalizowanymi nanocząstkami Fe_3O_4 w celu efektywnej detekcji wybranych analitów, II Pomorskie Studenckie Sympozjum Chemiczne, 2021

14. A. Kulpa-Koterwa, **A. Koterwa**, T. Ossowski, P. Niedziałkowski, Wykorzystanie nanostruktur opartych na nanocząstkach Fe_3O_4 w celu stworzenia sensora elektrochemicznego - optymalizacja warunków modyfikacji elektrody, XIV Kopernikańskie Seminarium Doktoranckie, 2021

15. **A. Koterwa**, A. Kulpa, J. Ryl, P. Niedziałkowski, Metodologia aktywacji powierzchni elektrod drukowanych w technologii 3D, I Pomorskie Studenckie Sympozjum Chemiczne, 2020

16. A. Kulpa, **A. Koterwa**, E. Szczepańska, T. Ossowski, P. Niedziałkowski, Elektrochemiczne badania zdolności wiążących nanomateriałów magnetycznych, I Ogólnopolskie Sympozjum Studentów Chemii, UWiedzeni Chemią 2020

17. A. Kulpa, **A. Koterwa**, E. Szczepańska, T. Ossowski, P. Niedziałkowski, Nanoadsorbenty typu core-shell oparte na magnetycznym rdzeniu tlenku żelaza, I Pomorskie Studenckie Sympozjum Chemiczne, 2020

18. **A. Koterwa**, P. Niedziałkowski , A. Kulpa, T. Ossowski, Modyfikacja elektrody GC kwasem 4-aminofenyloboronowym - charakterystyka elektrody i badania jej czułości na wybrane cukry, VI Ogólnopolskie Seminarium, Postępy w chemii boru 2019

19. A. Kulpa, **A. Koterwa**, D. Zarzeczańska, T. Ossowski, P. Niedziałkowski, Nanocząstki magnetyczne $Fe_3O_4@SiO_2$-EDTA jako adsorbenty jonów Cd^{2+}- badania elektrochemiczne, II Konferencja Naukowa Chemia - Biznes - Środowisko 2019

II.   Postery

1. M. Cieślik, **A. Koterwa**, P. Niedziałkowski, K. Formela, M. Sawczak, R. Bogdanowicz, J. Ryl, The charge transfer kinetics enhancement of 3D printed electrodes: the role of polymer matrix, 11th International Workshop on Surface Modification for Chemical and Biochemical Sensing, 2023

2. **A. Koterwa**, K. Łukaszuk, J. Ryl, P. Niedziałkowski, Comparison of different methods of electrode modification towards human chorionic gonadotropin (hCG) detection in human serum, 11th International Workshop on Surface Modification for Chemical and Biochemical Sensing, 2023

3. **A. Koterwa**, I. Kaczmarzyk, M. Cieślik, A. Kulpa-Koterwa, R. Bogdanowicz, J. Ryl, P. Niedziałkowski, Enzymatic hydrolysis as a new method activation of 3D-printed polylactide carbon black electrodes (CB-PLA), 18th International Conference on Electroanalysis, 2022

4. **A. Koterwa**, I. Kaczmarzyk, M. Cieślik, A. Kulpa-Koterwa, R. Bogdanowcz, J. Ryl, P. Niedziałkowski, Hydroliza enzymatyczna jako nowa metoda aktywacji elektrod (CB-PLA) drukowanych w technologii 3D, IV Konferencja Naukowa, Chemia - Biznes - Środowisko, 2022

5. P. Niedziałkowski, J. Ryl, **A.Koterwa**, M. Bojko, A. Wcisło, M. Spodzieja, K. Magiera-Mularz, K. Guzik, T. Ossowski, S. Rodziewicz-Motowidło, Electrochemical detection of the cancer biomarkers on modified electrodes, 18th International Conference on Electroanalysis, 2022

6. I. Kaczmarzyk, **A. Koterwa**, M. Cieślik, T. Ossowski, R. Bogdanowicz, J. Ryl, P. Niedziałkowski, Electroactivation of 3D-printed polylactide carbon-based electrodes for electroanalytical sensing applications, 3rd International Workshop on Functional Nanostructured Materials, 2021

7. **A. Koterwa**, K. Łukaszuk, T. Ossowski, A. Kulpa-Koterwa, P. Niedziałkowski, Detekcja hormonu ludzkiej gonadotropiny kosmówkowej (hCG) na modyfikowanej elektrodzie złotej, VI Interdyscyplinarna Akademicka Konferencja Ochrony Środowiska, 2021

8. A. Kulpa-Koterwa, **A. Koterwa**, T. Ossowski, P. Niedziałkowski, Modyfikacja elektrody GC z wykorzystaniem magnetycznych nanostruktur Fe_3O_4, III Konferencja Naukowa,Chemia - Biznes - Środowisko, 2021

9. A. Kulpa-Koterwa, **A. Koterwa**, T.Ossowski, P. Niedziałkowski, Wykorzystanie nanostruktur $Fe_3O_4@SiO_2$-NX o różnej ilości grup aminowych w łańcuchu zewnętrznym do oznaczania jonów Cd^{2+}, Pb^{2+} i Cu^{2+}, VI Interdyscyplinarna Akademicka Konferencja Ochrony Środowiska, 2021

10. **A. Koterwa**, A. Kulpa, T. Ossowski, P. Niedziałkowski, Ocena metody modyfikacji elektrody GC (Glassy Carbon) za pomocą mocznika w celu oznaczania kwasu moczowego, I Ogólnopolskie Sympozjum Studentów Chemii, UWiedzeni Chemią, 2020

11. **A. Koterwa**, J. Ryl, A. Kulpa-Koterwa, T. Ossowski, P. Niedziałkowski, Technologia druku 3D – zalety i wady nowego materiału elektrodowego, e-Zjazd Zimowy Sekcji Studenckiej Polskiego Towarzystwa Chemicznego, 2020

12. A. Kulpa, **A. Koterwa**, T. Ossowski, P. Niedziałkowski , Nanomateriały magnetyczne Fe_3O_4 jako adsorbenty jonów metali ciężkich, XVI Wrocławskie Studenckie Sympozjum Chemiczne, 2020

13. A. Kulpa-Koterwa, P. Niedziałkowski, **A. Koterwa**, T. Ossowski, Modyfikacja powierzchni elektrody GC magnetycznymi nanostrukturami typu core-shell- badania elektrochemiczne, e-Zjazd Zimowy Sekcji Studenckiej Polskiego Towarzystwa Chemicznego, 2020

14. **A. Koterwa**, T. Ossowski, P. Niedziałkowski, Elektrochemiczna modyfikacja elektrody GC (glassy carbon) mocznikiem w celu detekcji kofeiny, kwasu moczowego i teobrominy, 2019, XXII Zjazd Zimowy Sekcji Studenckiej Polskiego Towarzystwa Chemicznego 2019,

15. **A. Koterwa**, P. Niedziałkowski, A. Kulpa, T. Ossowski, Opracowanie metody modyfikacji elektrody GC (Glassy Carbon) kwasem 4-aminofenyloboronowym w celu elektrochemicznej analizy wybranych cukrów prostych, II Konferencja Naukowa,Chemia - Biznes - Środowisko, 2019

16. **A. Koterwa**, I. Wróblewska, A. Kulpa, T. Ossowski, Niedziałkowski Paweł, Elektrochemiczne oznaczanie kofeiny metodą CV i DPV w różnych napojach, 2018, II Konferencja Doktorantów Pomorza, BioMed Session, 2018

17. A. Kulpa, D. Zarzeczańska, **A. Koterwa**, T. Ossowski, Stabilność w roztworze tetrafluoropochodnych kwasu fenyloboronowego, II Konferencja Doktorantów Pomorza,BioMed Session 2018

18. I. Wróblewska, **A. Koterwa**, P. Niedziałkowski, T. Ossowski, Detekcja wybranych parabenów stosowanych w kosmetykach z wykorzystaniem metod elektrochemicznych, II Konferencja Doktorantów Pomorza, BioMed Session, 2018

III.   Uczestnictwo w projektach i grantach

1.   OPUS 19 „Elektrochemiczny Au-Minecraft: nowe podejście do budowy systemów biosensoryki impedancyjnej" finansowany ze środków NCN, UMO-2020/37/B/ST7/03262, 2021-2024 – stypendysta/doktorant

2.   Program małych grantów – UGrants – start 2 realizowany w ramach Inicjatywy Doskonałości Uczelnia Badawcza (IDUB) w Uniwersytecie Gdańskim,
533-0C20-GS25-22, 2022 – kierownik projektu

3.   Program małych grantów – UGrants – start 4 realizowany w ramach Inicjatywy Doskonałości Uczelnia Badawcza (IDUB) w Uniwersytecie Gdańskim,
533-T000-GS62-24 2024 – kierownik projektu

IV.   Działalność pozanaukowa

1. Organizacja Drzwi Otwartych na Wydziale Chemii UG, 2019

2. Prowadzenie warsztatów: „Zastosowanie druku 3D w elektrochemii", podczas drzwi otwartych Wydziału Chemii UG, 2024

Artykuły

Article

Deciphering the Molecular Mechanism of Substrate-Induced Assembly of Gold Nanocube Arrays toward an Accelerated Electrocatalytic Effect Employing Heterogeneous Diffusion Field Confinement

Pawel Niedzialkowski, Adrian Koterwa, Adrian Olejnik, Artur Zielinski, Karolina Gornicka, Mateusz Brodowski, Robert Bogdanowicz, and Jacek Ryl*

ACCESS | Metrics & More | Article Recommendations | SI Supporting Information

ABSTRACT: The complex electrocatalytic performance of gold nanocubes (AuNCs) is the focus of this work. The faceted shapes of AuNCs and the individual assembly processes at the electrode surfaces define the heterogeneous conditions for the purpose of electrocatalytic processes. Topographic and electron imaging demonstrated slightly rounded AuNC (average of 38 nm) assemblies with sizes of ≤ 1 μm, where the dominating patterns are (111) and (200) crystallographic planes. The AuNCs significantly impact the electrochemical performance of the investigated electrode [indium−tin oxide (ITO), glassy carbon (GC), and bulk gold] systems driven by surface electrons promoting the catalytic effect. Cyclic voltammetry in combination with scanning electrochemical microscopy allowed us to decipher the molecular mechanism of substrate-induced electrostatic assembly of gold nanocube arrays, revealing that the accelerated electrocatalytic effect should be attributed to the confinement of the heterogeneous diffusion fields with tremendous electrochemically active surface area variations. AuNC drop-casting at ITO, GC, and Au led to various mechanisms of heterogeneous charge transfer; only in the case of GC did the decoration significantly increase the electrochemically active surface area (EASA) and ferrocyanide redox kinetics. For ITO and Au substrates, AuNC drop-casting decreases system dimensionality rather than increasing the EASA, where Au−Au self-diffusion was also observed. Interactions of the gold, ITO, and GC surfaces with themselves and with surfactant CTAB and ferrocyanide molecules were investigated using density functional theory.
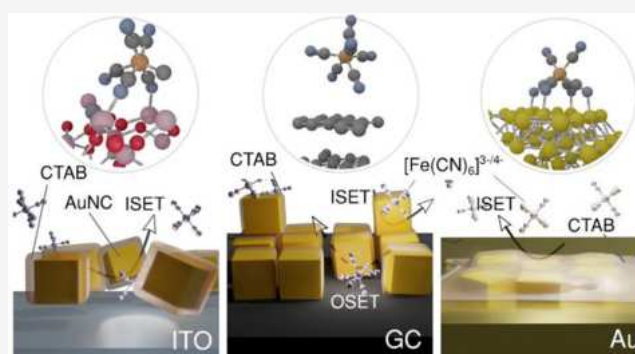
1. INTRODUCTION

Gold nanoparticles (AuNPs) possess many excellent properties as a consequence of their shapes, sizes, and molecular structures. These parameters mainly affect their biocompatibility,[1] chemical stability, and optical and electrical properties,[2] which mainly determine their practical application as catalysts,[3,4] as sensors, and for nanotechnology and biomedical purposes.[5] Additionally, the properties of AuNPs are determined by further modifications with either organic species or hybrid or inorganic nanomaterials. The possibility of their modification with amines,[6] phosphine,[7] and thiol derivatives[8,9] has a remarkable influence on the practical application of AuNPs for biosensing[10] and many biomedical applications such as cancer treatment,[11,12] drug delivery,[13] optoelectronic devices and bioimaging,[14] and therapeutics.[15] There is broad interest in the recognition of electrochemical and physicochemical surface properties after deposition and functionalization with various gold nanostructures. The application of AuNPs is mainly focused on biosensors and electrocatalysis. Among many notable examples, functionalized AuNP/Au systems were used for sensitive microRNA detection and enzymatic amplification[16] and bacterial lipopolysaccharide recognition.[17] The assessment of tau proteins in Alzheimer's patients was also possible with AuNP structured at screen-printed carbon electrodes.[18] Molecular tethering of AuNPs at boron-doped diamond[19] or GC[20] offers versatility through its electrocatalytic behavior and reproducible responses. Oxide electrodes are commonly modified by AuNPs with the aim of providing an easy alternative for their surface modification. Such an approach was reported for the detection of oral cancer salivary biomarker interleukin-8
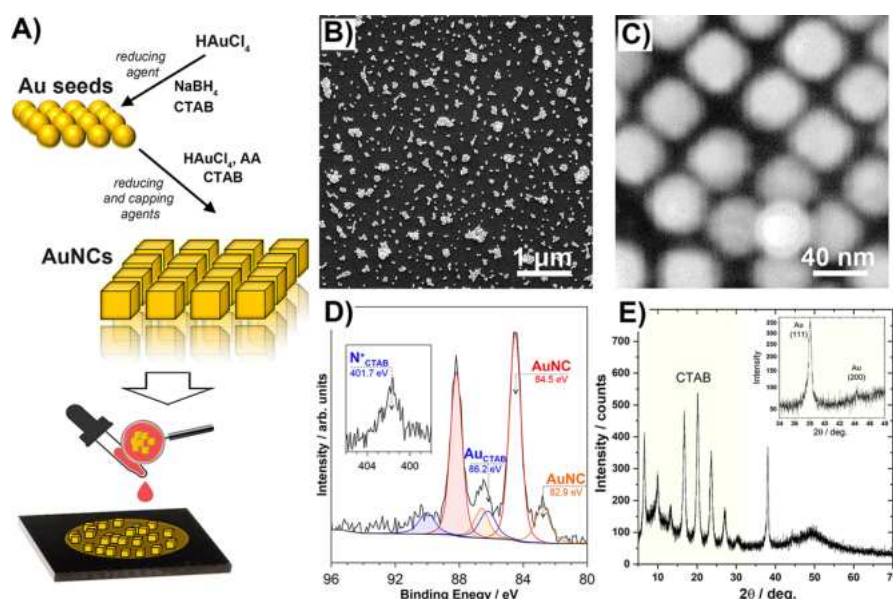
Figure 1. (A) Schematic presentation of AuNC synthesis and application. (B and C) SEM images of the AuNCs decorated at the GC surface. (D) AuNC/GC system XPS analysis in the Au 4f core-level energy range, with the N 1s spectrum shown in the inset. (E) X-ray diffraction pattern for AuNC. The inset shows the (111) and (200) reflections of a gold phase.

(IL8) using AuNPs-rGO/ITO[21] and non-enzymatic sensors for methyl parathion.[22] An antigalvanic replacement by surface-confined AuNPs revealed the size-dependent catalytic properties.[23]

The electrochemical activity of nanoparticles depends on the abilities of the surface electrons to promote a catalytic process. Therefore, the electrical and electrocatalytic properties of AuNPs are directly connected with their structure, size, or crystallographic orientation.[24] Many different synthetic approaches have been invented to obtain nanoparticles consisting of regular or irregular shapes, influencing the surface atom densities, physical properties, electronic structure, and chemical activity. Currently, there are several methods known for the synthesis of nanoparticles resulting in regular shapes of various morphologies such as cubes, rods, spikes, hexagonal or triangular plates, cages, and pyramids.[11,25,26] On the basis of their electrocatalytic activities toward glucose oxidation, it has been shown that gold nanocrystals possess different activities. For gold nanobelts and nanoplates, it has been found that the (110) surface of gold is more active than the (111) surface for glucose oxidation, while for methanol oxidation in an alkaline solution, the activity of the (110) surface is lower than that of the (111) surface.[24,27] Additionally, it has been proved that Au nanocrystals bound with (100) surfaces are significantly more active than (110)-bound rhombic dodecahedral and (111)-bound octahedral Au nanocrystals toward glucose oxidation.[28] In the case of gold nanorods, glucose oxidation is enhanced in the presence of (100) facets.[29] The presence of ions or surfactants during the synthesis influences the structure of the obtained nanoparticles, which directly influences the electrochemical properties. For instance, the presence of iodine during the synthesis results in a higher ratio of (100) and (111) facets in the presence of sulfides.[30] Hexadecyltrimethylammonium bromide (CTAB) is commonly used in the synthesis of nanoparticles in the seed-mediated methods. The choice of CTAB for synthesis makes it possible to obtain large single-crystal nanoparticles.[25] Furthermore, a specific shape and a specific crystallographic

orientation of AuNPs are possible upon adsorption of CTAB, because it interacts differently with gold facets in the (100) ≈ (110) > (111) order.[24] The presence of a surfactant will further influence the electrocatalytic activity of the AuNPs.[31]

In recent years, gold nanocubes (AuNCs) have been of great interest due to their three-dimensional structure. In addition to the fact that all AuNCs possess the same dimensions, each can form more regular or random forms, self-organizing more predictably, which strengthens the attraction to this material. The major advantage of AuNCs in comparison to AuNPs is their chemical stability, the possibility of further functionalization, and their unique tunable plasmonic properties. In addition, single AuNCs or their agglomerates can cause amplification of electromagnetic fields interacting with neighboring particles, enhancing their activity, which allows these particles to be used in the creation of optical sensors.[32] Gold cubic nanoparticles were also investigated with respect to the oxygen reduction reaction deposited on a disc electrode.[33] The unusual properties resulting from the regular shape of the AuNCs allow the application of localized surface plasmon resonance (LSPR) techniques for detecting biomolecules.[34,35] Today, AuNCs may be used for the preparation of label-free electrochemical aptasensors and immunosensors. AuNCs were deposited on a gold substrate in a multistage modification with cysteamine and, after aptamer immobilization, used for sensitive and selective chloramphenicol detection.[36] Lv et al. used AuNCs deposited on graphene oxide to create a sandwich immunoassay for the detection of a cardiac biomarker (troponin). The aim of using AuNCs was to immobilize the antibody and accelerate the electron transfer through the interface.[37]

There is no description of the mechanism of interaction of AuNPs with various common electrode substrates in the literature. AuNPs affect the electrochemical activity of the studied systems to different degrees due to the ability of surface electrons to promote the catalytic processes.[12,38] The regular shapes with defined facets of AuNCs and the ease of their specific self-organization at the electrode surface offer

desirable conditions for the determination of electrocatalytic processes. To the best of our knowledge, no research has focused on evaluation of the self-organization of AuNCs at common electrode surfaces. Therefore, it is very important to improve our understanding of those interactions, which often remains unclear. Herein, we present fresh insight into the interaction of AuNCs with the three most commonly used transmitters for electrochemical sensors, namely, glassy carbon (GC), indium−tin oxide (ITO), and gold. We discuss the enhancement of the electrochemical activity and the complexity of the electrode/electrolyte interface, which are affected by AuNCs' three-dimensional self-assembly at the electrode substrates through different molecular interactions, the appearance of the coffee-ring effect during the drop-casting procedure,[39,40] and the non-negligible impact of the surfactant (CTAB) and different electron transfer pathways (tunneling and bridging) on the electroactive compounds.

2. EXPERIMENTAL SECTION

2.1. AuNC Synthesis and Deposition. All chemicals were of analytical grade and used as received without further purification. Cetyltrimethylammonium bromide (CTAB), sodium borohydride (NaBH$_4$), potassium hexacyanoferrate(III) [K$_3$Fe(CN)$_6$], and potassium hexacyanoferrate(II) [K$_4$Fe(CN)$_6$] were purchased from Sigma-Aldrich. Phosphate-buffered saline (PBS) buffer from Thermo-Fisher Scientific was obtained by dissolving tablets in deionized water. Ascorbic acid (AA) and hydrogen tetrachloroaurate(III) (HAuCl$_4$·4H$_2$O) were obtained from POCH.

A two-step seeding growth procedure was used to synthesize Au nanocubes according to the modified procedure described previously.[36,41] The first step involved the synthesis of Au seeds. First, 0.3 mL of 0.01 M NaBH$_4$ was added in dropwise fashion over 5 min to a flask containing a mixture of 3.75 mL of 0.1 M CTAB and 0.125 mL of 0.01 M HAuCl$_4$·4H$_2$O, under stirring. Then, the obtained solution was stirred at room temperature for 12 h.

In the next step, the AuNCs' growth solution was obtained by mixing 6.4 mL of 0.1 M CTAB, 0.8 mL of 0.01 M HAuCl$_4$·4H$_2$O, and 3.8 mL of 0.1 M AA. Then 30 μL of Au seeds was added, diluted 10-fold, to the growth solution. After the mixture had been vortex mixed for 30 s, the obtained solution was left overnight. After 24 h, the AuNCs were centrifuged (5000 rpm, 20 min) and washed twice with a 0.001 M CTAB solution. The scheme of this procedure is simplified in Figure 1A. The AuNCs were stored in a 0.001 M CTAB solution and used for further investigations.

Electrode surface modification was performed by dropping different amounts of AuNCs of suspended 0.001 M CTAB from 10 to 50 μL on the surface of GC, ITO, and Au electrodes. The GC and Au electrodes were first polished with 50 nm aluminum oxide on a polishing cloth, cleaned with water, and dried under a stream of nitrogen. Then, 10 μL of the AuNC solution was drop-cast on the electrode surface and left to dry in the air for 30 min at room temperature. The electrodes with deposited AuNCs were washed twice with water before use. The same modification procedure was applied for the ITO electrode previously cleaned by ultrasonication in methanol for 5 min and dried in air.

2.2. Electrochemical Studies. All electrochemical measurements were performed on an Autolab M204 potentiostat (Metrohm) using a three-electrode system. The working electrode was GC or a thin ITO film on glass, while a thin Au film on glass or Ag/AgCl (3 M KCl) was used as the reference electrode; a platinum wire was used as the counter electrode. All potentials are presented versus the reference electrode. The electrochemical cell volume was 5 mL, and the electrolyte-exposed electrode surface area was 0.20 cm^2.

Cyclic voltammetry (CV) measurements were conducted in a solution consisting of equimolar amounts of 1 mM K$_3$[Fe(CN)$_6$] and K$_4$[Fe(CN)$_6$] dissolved in 0.01 M PBS (pH 7.4). All cyclic voltammograms were recorded in the potential range of −0.35 to 0.60 V with a scan rate from 0.5 to 500 mV s^{-1}. The electrochemically

active surface area (EASA) for the investigated electrodes was calculated by the Randles−Sevcik equation (R−S). The CV measurements were also performed in 0.1 M H$_2$SO$_4$ as the electrolyte solution in the potential range of −0.10 to 1.50 V with a scan rate of 20 mV s^{-1}. The electrochemical impedance spectroscopy (EIS) experiment was carried out under open circuit potential (OCP) conditions with a voltage perturbation amplitude of 10 mV and a frequency range from 100 kHz to 0.1 Hz, with 40 points per frequency decade.

Scanning electrochemical microscopy (SECM) measurements were performed using a commercially available positioning setup (Sensolytics GmbH). It consists of three stepper motor-controlled precision linear stages that allow a maximum travel range of 25 mm × 25 mm × 25 mm with a step width of 20 nm. Additionally, the positioning system contains a piezoelectric system (P-611.3 Nano-Cube XYZ Piezo System, Physik Instrumente GmbH & Co. KG) that provides a travel range of 100 μm × 100 μm × 100 μm with a resolution of 1 nm. The positioning system was combined with an Autolab PGSTAT302N potentiostat (Metrohm) with an additional ECD module for low-current measurements. SECM measurements were performed in the three-electrode configuration consisting of a gold microelectrode (active electrode area with a 10 μm diameter, RG ratio of 20) as the working electrode, a platinum wire as the counter electrode, and a Ag/AgCl gel electrode as the reference electrode. All of the electrodes were purchased from Sensolytics GmbH. Before the measurements, the microelectrode was polished using alumina oxide and characterized via CV. The electrolyte utilized during the measurements was 5 mM K$_3$[Fe(CN)$_6$] dissolved in PBS (pH 7.4) and deoxygenated prior to experiments. The reduction of [Fe-(CN)$_6$]$^{3-}$ was carried out at −0.2 V versus Ag/AgCl (gel). The working distance was established by touching the sample's surface. All experiments were performed in feedback mode (unbiased investigated sample). The approach curves were registered from ∼10 radii of a utilized microelectrode using a piezo positioning system with a step of 100 nm and a speed of 1 μm s^{-1} until the touching point was observed. The illustrative areas of SECM and AFM analyses are presented in section S1 of the Supporting Information.

2.3. Physicochemical Studies. Scanning electron microscopy (SEM) studies were used to analyze the AuNC distribution. The measurements were carried out using an FEI Quanta 250 FEG instrument (ThermoFisher Scientific) equipped with a Schottky field emission gun, operating at an accelerating voltage of 30 kV.

The X-ray diffraction (XRD) measurement was carried out at room temperature on a Bruker D2 Phaser diffractometer with Cu Kα radiation (λ = 1.54056 Å) and an XE-T detector. The data were collected for the 2Θ range of 5−70°. For the AuNCs, the measurement was performed on the silicon plate.

AFM topographic measurements were taken using a NTegra II device produced by NT-MDT Corp. Imaging was performed under atmospheric conditions but with the use of mechanical and electrical insulation with a protective cover. Images were taken sequentially for areas ranging from 10 to 2 μm to identify and magnify the surface structures observed. Imaging was performed in semicontact mode, with a set point equal to half the amplitude of free oscillation. NSG30 probes by NT-MDT were used for the measurements dedicated to semicontact measurements. Cantilever geometrical parameters were 125 μm (L) × 40 μm (W) × 4 μm (T). The measurement frequency was 296 kHz.

X-ray photoelectron spectroscopy (XPS) studies were carried out using an Escalab 250Xi instrument (ThermoFisher Scientific), operating with an AlKα source. The X-ray spot diameter was 650 μm, and the pass energy was 20 eV. The low-energy electron and Ar$^+$ ion flow served charge compensation purposes, with final calibration of the spectra on adventitious carbon C 1s (284.8 eV).

2.4. Density Functional Theory (DFT) Calculations. The surface and molecular structures were designed using a builder tool provided by Atomistic ToolKit Quantumwise (ATK, Synopsys) as reported in ref 42. Interactions of the gold, ITO, and GC surfaces with themselves and with the CTAB and ferrocyanide molecules were investigated by performing geometry optimizations and calculating
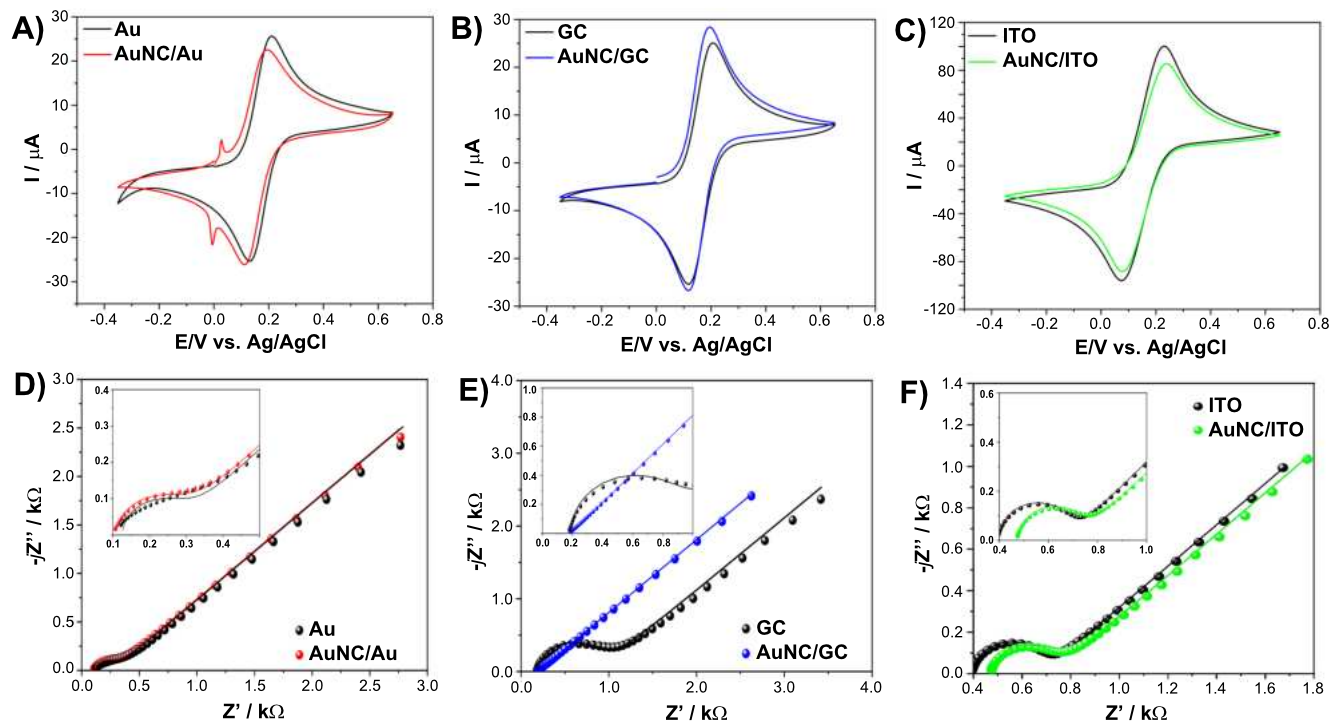
Figure 2. (A−C) CVs and (D−F) EIS data for (A and D) gold, (B and E) GC, and (C and F) ITO electrodes prior to (black) and after deposition of 10 μL of AuNC (colored). Studies in 0.01 M PBS containing 1.0 mM $K_3Fe(CN)_6$.

electron density maps on the optimized structures. Surface calculations were performed using slabs (flat surfaces) of cubic Au (100), hexagonal graphitic carbon (001), and cubic ITO model cleaved across the (100) plane. DFT at the generalized gradient approximation (GGA) level of the theory with the Perdew−Burke−Ernzerhof (PBE) functional was applied as implemented in the package for most calculations. Application of DFT-D3 correction for van der Waals interactions is indicated in the text.[43] The linear combination of atomic orbitals (LCAO) method[44] with PseudoDojo norm-conserving pseudopotentials and the medium ATK basis set were applied.[45]

The ferrocyanide and CTAB adsorption phenomena were investigated only on flat surfaces with slab models with the size appropriate for the DFT level of theory. Gibbs free energies of CTAB adsorption were calculated according to eq 1:

$$G_{adsorption} = G_{CTAB-surface} - G_{CTAB} - G_{surface} \quad (1)$$

An analogous equation was used for adsorption of ferrocyanide ions on the unoccupied surface. The energies of adsorption on the CTAB-occupied surfaces, however, were calculated according to eq 2:

$$G'_{adsorption} = G_{ferrocyanide-surface} + G_{CTAB} - G_{CTAB-surface}$$
$$- G_{ferrocyanide} \quad (2)$$

The disturbance energy is defined as the difference between $G_{adsorption}$ and $G'_{adsorption}$.

3. RESULTS AND DISCUSSION

3.1. AuNC Characterization.
The topography of the obtained AuNCs is presented in panels B and C of Figure 1. Moreover, Figure 1B demonstrates the homogeneous spatial distribution of AuNCs at the GC surface using the proposed drop-cast method. Some of the AuNCs form larger clusters reaching up to ~500 nm in size. On the basis of the micrographs taken in the center of the drop-cast area, the thickness of these clusters typically does not exceed two AuNC

layers. A great majority of the AuNCs are slightly rounded cube-like polyhedra with a uniform size of 38 ± 2 nm.

High-resolution XPS analysis of the AuNCs drop-cast at the GC substrate was performed in the Au 4f core-level binding energy (BE) range. The studies revealed a complex spectral structure that was deconvoluted using three components (Figure 1D). The major Au $4f_{7/2}$ component (70% [Au]) was found at 84.5 eV, the energy typically reported for gold nanoparticles[46,47] and thus ascribed to AuNCs. With a [Au] share of 13%, the next peak is shifted by +1.7 eV and originates from oxidized Au(III) complexed by CTAB.[48,49] The presence of a stabilizing agent was further confirmed by the N 1s signal of the pure ligand (Figure 1D, inset).[50] Determination of the origin of the third Au 4f component is the most problematic. Its share within [Au] is roughly 17%. Passiu et al.[47] recognized the appearance of a −0.4 eV-shifted surface component, yet in our case, the peak is shifted by −1.6 eV versus the main component. The chemistry of AuNCs decorated at Au and ITO substrates revealed similar chemistry, but altered shares of individual components, as deconvoluted in section S2 of the Supporting Information. These analyses suggest a significantly higher level of Au(III) species complexed by CTAB compared to the GC substrate and hint at different mechanisms of the AuNC−electrode interaction.

The XRD pattern of the AuNCs is presented in Figure 1E. The first and highest reflection at (111) for Au is observed near a 2Θ of 38°, in agreement with the ASTM powder diffraction data. The diffraction peaks observed for the 2Θ range of 5−35° are attributed to the CTAB.[51] The ideal nanocubes should be predominantly enclosed by (200) facets.[52] On the contrary, different AuNC synthesis approaches, including ours, lead to the formation of cube-like polyhedra with (111) and (200) crystallographic planes dominant in the XRD patterns.[53,54] For a randomly oriented

polycrystalline gold powder, the theoretical value of the $I_{(200)}/I_{(111)}$ ratio is 0.5,[55] while in our case, the $I_{(200)}/I_{(111)}$ ratio is 0.1. This suggests that crystallites in AuNCs are oriented along the (111) direction, in accordance with the CTAB interaction propensity with major Au crystallographic planes.[24] The average crystallite size was estimated from the Scherrer formula on the basis of the line broadening at half of the maximum intensity of reflection (111). The estimated crystallite size for the AuNCs is 25 nm, which is smaller than the particle size that might consist of a number of crystallites arranged in the same orientation.

3.2. Electrochemically Active Surface Area Development by AuNCs.

Deposition of AuNCs on the GC, Au, and ITO electrode substrates was carried out by drop-casting 10 μL of AuNCs suspended in 0.001 M CTAB, leaving the decorated electrodes to dry at room temperature. The deposition resulted in the adsorption of the AuNCs, expectedly resulting in the development of charge transfer kinetics and/or an EASA, to be verified by CV and EIS analyses. The CV results are shown in Figure 2.

Drop-casting AuNCs on the GC surface notably increased the peak redox currents compared with that of the pristine GC electrode (Figure 2B). A similar observation was previously made in the case of decoration with gold nanoparticles and was connected to the increase in electrical conductivity.[56] Furthermore, the effective increase in the electron transfer kinetics was confirmed by tracking the decrease in anodic−cathodic peak separation (ΔE_p) from 84 to 71 mV after AuNC deposition. A similar feature was observed for Au, but not for ITO, where ΔE_p remained around 155 mV, suggesting a significantly higher irreversibility of the electron transfer. Furthermore, unlike in the case of the GC substrate, AuNC drop-casting at either ITO or Au decreased the ferrocyanide oxidation/reduction currents, as seen in panels A and C of Figure 2. A repeatable occurrence of small side CV peaks in Figure 2A is probably a result of electrocatalytic hydrogen redox chemistry on gold nanoparticles.[57] The detailed information is provided in section S3 of the Supporting Information. The electron transfer rate increased at the AuNC/GC electrode due to better electrochemical catalytic behavior. This is a consequence of the high activity of AuNCs.[58]

The ferrocyanide oxidation kinetics made it possible to draw conclusions about the EASA development by AuNC drop-casting. To do this, CV scans were performed at various scan rates (see section S3 of the Supporting Information) to exercise the R−S relationship for the reversible reaction (eq 3).

$$i_p = 2.69 \times 10^5 n^{3/2} A D^{1/2} C \upsilon^{1/2} \tag{3}$$

where i_p is the peak current in amperes, υ is the scan rate in volts per second, C (1×10^{-6} mol cm^{-3}) is the [Fe(CN)$_6$]$^{3-}$ concentration, D (6.67×10^{-6} cm^2 s^{-1}) is its diffusion coefficient,[59] n (=1) is the number of electrons transferred, and A is the EASA in square centimeters. On the contrary, heterogeneous rate constant k^0 was estimated from ΔE_p at a υ of 100 mV s^{-1} using the Nicholson approach[60,61] (see eq 4).

$$k^0 = \Psi\left(\pi D \frac{nF\upsilon}{RT}\right)^{1/2} \tag{4}$$

with Ψ being the dimensionless, empirically determined kinetic parameter. The results are summarized in Table 1.

Table 1. Electric Parameters Obtained from EIS Analyses after Fitting with $R_S[\text{CPE}(R_{CT}W)]$ EEC

	sample	Au	GC	ITO
k^0 (cm s^{-1})	bare	1.32×10^{-2}	9.11×10^{-3}	1.82×10^{-3}
	AuNC	1.82×10^{-3}	1.81×10^{-2}	1.64×10^{-3}
EASA (cm^2)	bare	0.72	0.63	0.88
	AuNC	0.92	1.04	0.88
R_{CT} (Ω)	bare	219	812	304
	AuNC	322	41	282
C_{DL}* (μF)	bare	1.25	1.31	1.40
	AuNC	2.31	0.11	1.74
α	bare	0.84	0.89	0.92
	AuNC	0.70	0.82	0.88
W ($\mu\Omega$ s$^{-1/2}$)	bare	0.36	0.37	0.91
	AuNC	0.34	0.36	0.86

Importantly, it was noted that the calculated EASA for the GC electrode after AuNC decoration undergoes a tremendous 65% increase, reaching 1.04 cm^2. A smaller yet notable 27% increase was observed for the Au electrode after decoration, while the AuNC-decorated ITO EASA remained completely unchanged. The obtained results demand answers to questions about the origin of the relevant alteration of the EASA, the mechanism of interaction of AuNCs with different electrode surfaces, and the electron transfer mitigation by CTAB, the surfactant used for AuNC stabilization.

An EIS analysis was also performed for the same batch of samples. The detailed data analysis was performed after fitting the experimental results (Figure 2D−F, points) with an electric equivalent circuit (EEC) (Figure 2D−F, line). The EEC selected, $R_S[\text{CPE}(R_{CT}W)]$, was a derivative of the Randles circuit, represented by series resistance R_S (electrolyte resistance) and charge transfer resistance R_{CT}, the latter connected in series to the Warburg diffusion impedance (W) and in parallel to the constant phase element (CPE), representing the electric double-layer quasi-capacitance (C_{DL}). The CPE was introduced to consider the frequency dispersion of capacitance upon the occurrence of the electrode electric heterogeneities, introduced upon AuNC decoration in particular, but also present due to other effects, such as the surface roughness and porosity, polycrystallinity, adsorption phenomena, etc.[61] The CPE's impedance is defined by eq 5

$$Z_{CPE} = [Q(j\omega)^\alpha]^{-1} \tag{5}$$

where Q is the quasi-capacitance and CPE exponent α describes the level of surface heterogeneity. The homogeneous surface is represented by the ideal capacitor when $\alpha = 1$, and the lower the α value, the greater the dispersion of capacitance due to disturbances in the diffusion layer. The surface time constant distribution model was chosen to estimate the effective C_{DL}* value.[62] The results of the impedance analysis are summarized in Table 1.

Charge transfer resistance R_{CT} of the bare electrode expectedly largely depends on the substrate and, under the studied conditions, is lowest for the ITO and Au electrodes. This parameter manifests changes in the charge transfer pathways. No notable changes were observed upon AuNC decoration on ITO, while for Au, the increase in R_{CT} most likely originates from CTAB adsorption at the electrode surface, as discussed below. Furthermore, there are no notable changes observed in this parameter upon AuNC decoration, suggesting that the charge transfer pathways were not

significantly affected. A different situation is observed in the case of the GC substrate, where the initially highest R_{CT} value decreased by >1 order of magnitude to merely 40 Ω upon AuNC decoration, testifying to the substantial alteration of the electrode transfer kinetics.

An important observation can be made about the capacitance of the electric double layer. The parameter represented by the CPE parameter shows a clear dependence on AuNC decoration. Initially, quasi-capacitance Q is similar for all of the studied electrodes with small differences occurring most likely due to different Volta potentials and their influence on the charge accumulation by the electric double layer as well as the surface electric heterogeneities of the studied substrates. The $C_{DL}*$ parameter notably decreases for the AuNC-decorated GC electrode, yet a similar feature was not observed for the ITO or Au substrate. This is an interesting observation, in particular when combined with the simultaneous decrease in R_{CT}, suggesting a significantly faster rate at which the charged interface of the electrode is established (time constant $\tau = R_{CT}C_{DL}*$), which decreased by >2 orders of magnitude to 4.5 μs. In all cases for the other electrodes, with or without decoration, $\tau \sim 0.3-0.7$ ms. This effect could possibly be explained by the presence of attraction forces with the electrode substrates and AuNC, easing the electron mediation mechanism.

It should also be noted that the proposed surface functionalization affects the electric heterogeneity of the Au and GC substrates while leaving the ITO nearly unaffected. This observation allows us to hypothesize (i) a very homogeneous distribution of the AuNCs or (ii) a limited interaction of the AuNCs with the ITO surface. At the same time, the results prove a negligible role of the AuNC in the transport of the reagent through the diffusion layer.

The results of AFM topographic imaging allow us to discuss the effectiveness of deposition of AuNCs on each of the studied substrates, as shown in Figure 3. These micrographs allow the clear recognition of the modification of the electrode topography upon AuNC solution drop-casting. A follow-up topography profile study determined the average roughness of both substrate electrodes and differentiated the dispersion of nanocubic systems following their agglomeration for each substrate, affecting the homogeneity of the obtained surfaces.

Panels A, C, and E of Figure 3 reveal a complex topography of the AuNC-decorated electrodes, with the reference unmodified samples presented in section S4 of the Supporting Information. At first glance, every surface seems to be enriched with features that can be interpreted as AuNC agglomerates. However, the topography profiles suggest that only in the case of gold and GC electrodes can these features exceed the typical AuNC dimensions of 40 nm. Following this observation, much smaller and more evenly distributed species at the ITO surface (Figure 3E) may have different origins, e.g., CTAB. Section S5 of the Supporting Information describes the AuNC/ITO system after the drop-casting procedure. The amount of deposited AuNCs is negligible when compared to the amount of the GC substrate, while the surface is uniformly covered by the surfactant.

Additionally, a statistical analysis led to roughness parameter S_q defined by eq 6:

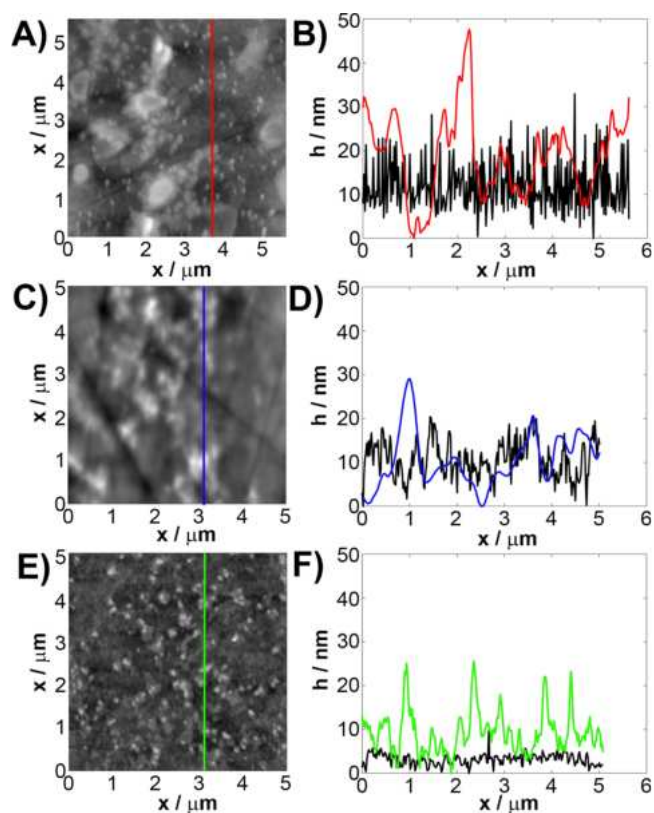$$S_q = \sqrt{\frac{1}{N} \sum_{x,y} h_{(x,y)}^2} \tag{6}$$

Figure 3. (A, C, and E) AFM semicontact mode topographic images and (B, D, and F) topographic profiles of AuNC-decorated studied samples: (A and B) gold, (C and D) GC, and (E and F) ITO. Black lines represent profiles of bare substrates for comparison.

corresponding to the standard deviation of the height on the AFM images (Figure 3A,C,E and Figure S2) with the number of pixels equal to N. A summary of the parameter defined above for images with sizes of 256 pixels × 256 pixels is presented in Table 2. These studies confirm previously

Table 2. AFM-Measured Roughness of the Studied Samples and Analysis of the Statistical Data from SECM Mapping, before and after AuNC Decoration

	sample	Au	GC	ITO
S_q (nm)	bare	5.08	5.08	1.21
	AuNC	15.60	30.40	4.36
i_{avg} (nA)	bare	−9.38	−8.69	−7.65
	AuNC	−5.39	−9.22	−7.79
i_{Sq} (pA)	bare	31.2	31.4	45.2
	AuNC	220.1	145.3	36.2
k^0 (cm s^{-1})	bare	3.88×10^{-2}	2.29×10^{-2}	1.67×10^{-2}
	AuNC	6.40×10^{-4}	4.00×10^{-2}	1.53×10^{-2}

obtained information, as the S_q parameter changes by only 3.15 nm in the case of the ITO sample upon AuNC decoration. On the contrary, the average change in S_q for the GC electrode reaches 25.32 nm, a result to be expected for the evenly distributed cubic monolayer. An interesting feature observed for the Au substrate shows something of a middle ground, as S_q was changed by 10.42 nm upon decoration with the nanocubes. Such a response may be explained by weaker interaction between the AuNCs and the substrate in this case, or other phenomena, such as gold self-diffusion.

3.3. Stability and Interactions of Adsorbed AuNC. To simulate the interactions of the AuNCs with the Au, ITO, and GC surfaces, a series of pairwise interacting Au−ITO, Au−GC, and Au−Au slabs were constructed. Geometry optimization was performed with one of the slabs allowed to move freely (Au) and the other (GC/Au/ITO) fixed in space. Interactions between the surfaces are illustrated in Figure 4A−C, where pictures of optimized geometries along with surface density maps are presented.
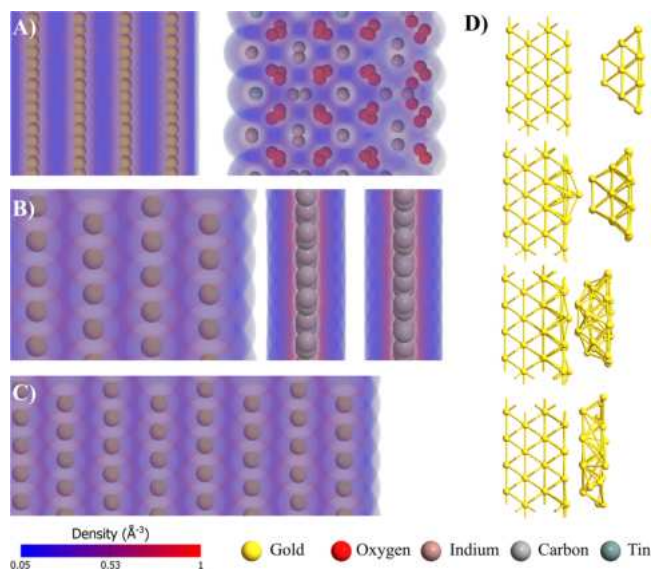

Figure 4. Optimized geometry of interactions between surfaces with electron density maps: (A) Au−ITO, (B) Au−GC, and (C) Au−Au interfaces. (D) Simulation of adsorption of 1 nm gold nanoparticles on flat gold surfaces [the first frame is the as-prepared non-optimized geometry, the second frame after 25 steps, the third frame after 75 steps, and the fourth frame the fully optimized geometry (262 steps)].

In the case of the Au−ITO interface, the optimized distance between the surfaces is equal to 5.4 Å and the electron densities of two surfaces do not overlap. Considering the relatively long distance between these surfaces, electron tunnelling is significantly hampered.[63,64] Moreover, due to the non-overlapping electron densities, no bonds between surfaces are found, and therefore, the hopping mechanism of charge transfer would not be observed either.[65] These observations suggest that electrical contact between flat Au−ITO surfaces is not likely to form spontaneously. This corollary can explain the experimentally observed phenomenon that application of AuNCs on the surface of ITO does not result in any change in the EASA with negligible changes in the charge transfer resistance (Table 1) as well as minor disturbances in the AFM-deciphered surface topography (Table 2). However, in the case of the Au−GC interface, the optimized distance is significantly shorter (3.5 Å) and there is a small overlap between the electron density of the Au layer and the carbon layer. The distance is even shorter than the spacing between graphite sheets (4.1 Å) and suggests that charge transfer between Au and GC flat surfaces is likely to occur. This is reflected experimentally in the largest increase in the EASA after application of AuNCs among all three surfaces and the significant decrease in charge transfer resistance.

Surprising phenomena are observed when Au−Au interactions are considered. The optimized distance between

surfaces is equal to 2.4 Å, which is almost on par with the distance between Au layers in the slabs (2.1 Å). In other words, an optimized structure of two parallel Au slabs consisting of four Au layers is almost identical to that with one large Au slab with eight layers. This observation suggests that the presence of Au−Au self-diffusion[66,67] led to the gluing of the two gold surfaces. To further examine this phenomenon, a geometry optimization was performed with a 1 nm nanoparticle on the flat slab. Several frames from this simulation are depicted in Figure 4D. After 25 optimization steps, the nanoparticle translates toward the flat surface, which extends several gold atoms in the direction of the incoming nanoparticle. Then, frontier layers of the nanoparticle are distorted so that they approach the flat gold surface. Finally, in the last frame of the optimization, the gold nanoparticle is shape-shifted so strongly that two parallel flat surfaces remain. Presumably, this phenomenon is responsible for the AuNC decoration effect on the electrode topography and EASA, when compared to GC as well as the unique surface morphology of Au modified by AuNCs registered by SEM (see Figure 5F).

To confirm the conclusion regarding the significantly altered interaction of the nanocubes with various electrode substrates, four independent physicochemical techniques were proposed, and their results are visualized in Figure 5.

XRD and UV−vis analyses were performed for the AuNC drop-cast (10 μL) electrodes after exposure to the electrolyte to evaluate the strength of adsorption of AuNC at the electrode surface throughout the 30 min exposure to the electrolyte. XRD analyses of AuNCs on the GC and ITO electrode substrates are presented in panels A and B of Figure 5, respectively. The intensity is on the square root scale. For both samples, only one XRD reflection of AuNCs was found on the XRD patterns (see the insets of panels A and B). Comparing the (111) reflections observed at a 2Θ of 38.1°, we found that the Au−GC sample has a doubly intense reflection compared to that of the Au−ITO sample, a feature testifying to differences in AuNC self-assembly on these electrodes and having an impact on the electrochemical properties. The average crystallite size for AuNCs, calculated from the Scherrer formula, is equal to 35 and 30 nm for the Au−GC and Au−ITO samples, respectively. Bragg reflections were observed for the 2Θ range of 5−35° and belong to the CTAB. The relative intensity of CTAB reflections slightly increases for the Au−ITO sample, suggesting stronger adsorption of the CTAB to the ITO than to the GC substrate.

On the contrary, the UV−vis absorption spectra shown in Figure 5D do not indicate the presence of the absorption peak characteristic of AuNCs. The 536 nm absorption peak, characteristic of gold nanocubes[50] and other colloids,[6] was recognized only for reference AuNCs in a 0.001 M CTAB solution. The lack of this peak in the case of the decorated electrodes corroborates the presence of the AuNCs on the surface of the electrodes; thus, the employed modification method can be successfully applied for electrochemical measurements.

Moreover, the surfaces of 100 μL of AuNC-decorated electrodes were electrochemically characterized in a 0.1 M H_2SO_4 solution. As shown in Figure 5E, for all of the CVs characteristic of $Au^0|Au^{3+}$, oxidation and reduction peaks are observed. The shape of the voltammograms is characteristic of the presence of AuNPs, which is different from the bare Au electrode in an acidic solution.[68,69] The oxidation peak is recorded at 1.04 V for AuNCs/GC and AuNCs/ITO, whereas
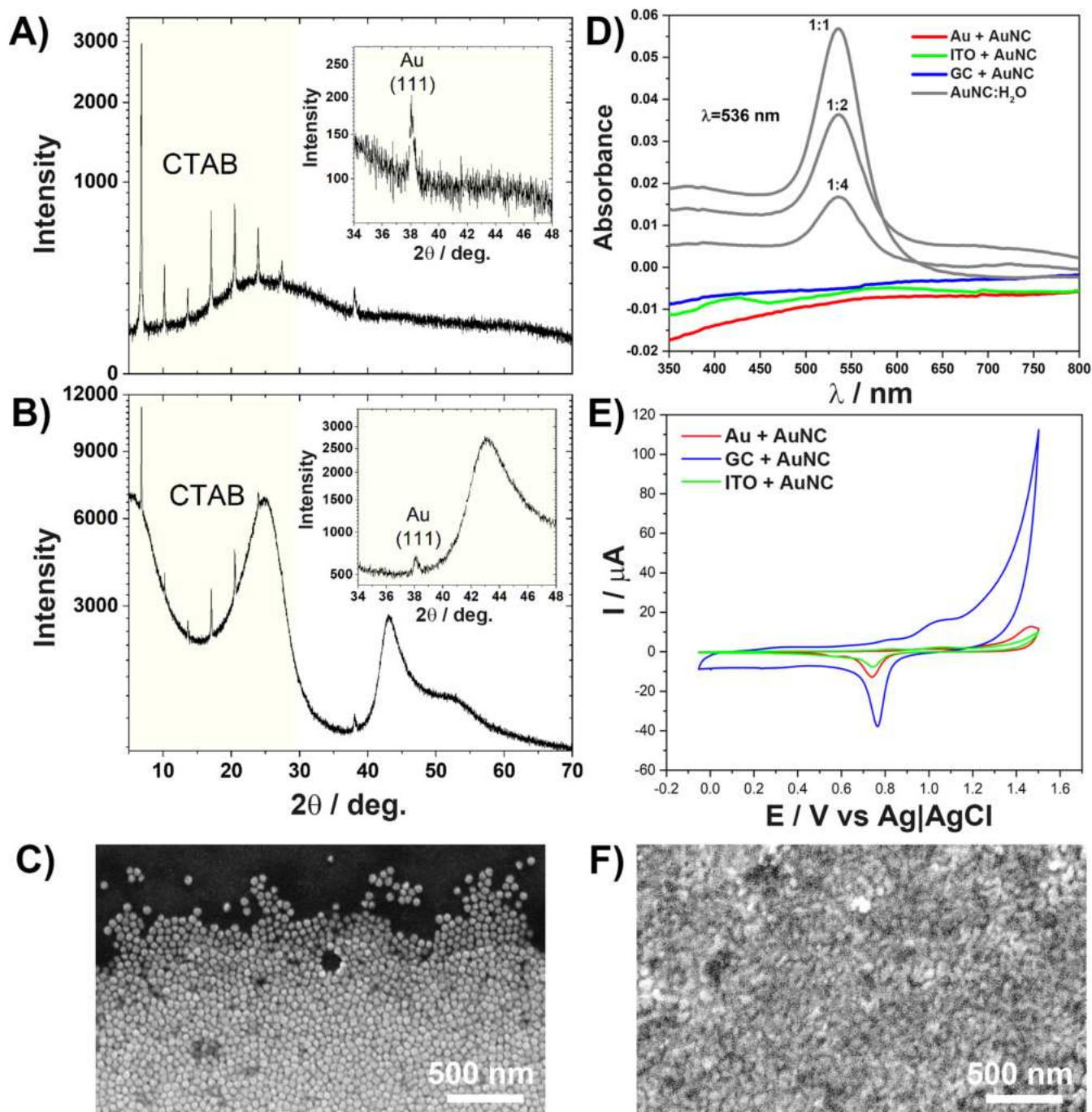
Figure 5. XRD diffraction patterns for (A) AuNC/ITO and (B) AuNC/GC. The inset of panel A shows the XRD pattern of the (111) crystallographic plane. SEM images of (C) AuNC/GC and (F) AuNC/Au surfaces in the area of appearance of the coffee-ring effect. (D) UV–vis absorption spectra recorded after deposition of AuNC on electrodes and in diluted solutions (1:1, 1:2, and 1:4). (E) CVs for electrodes with drop-cast AuNCs in 0.1 M H_2SO_4 at a scan rate of 20 mV s^{-1}.

for AuNCs/Au, it is shifted to 1.46 V. The irreversible Au_2O_3 reduction occurs at 0.76 V (AuNCs/GC) or 0.74 V (AuNCs/ITO and AuNCs/Au).[70−72] Tracking the area under the cathodic peak makes it possible to analyze the total charge that has flowed during Au_2O_3 electroreduction at the AuNC surface. This phenomenon is attributed to electrocatalytic active sites.[73] The smallest amount of electrocatalytic active sites is present on AuNC/ITO electrode (2 times less than AuNC/Au), and the largest amount on AuNC/GC (4.5 times more than AuNC/Au), which also contributes to the presence of AuNCs on the electrode surface.

We were unable to find any AuNCs drop-cast at the Au surface by SEM observations, even when the analysis was performed within 5 min of the decoration. Thus, we greatly increased the volume of cast AuNCs and focused on the outer ring of the droplet, where the concentration is supposed to be the highest on the basis of the appearance of the coffee-ring effect. Comparative analyses of the coffee-ring effect formed by the AuNC at GC and Au are given in panels C and F of Figure 5, respectively. Rapid Au−Au self-diffusion has rapidly led to decay in the nanocubic structure, only slightly disturbing the observed surface topography.
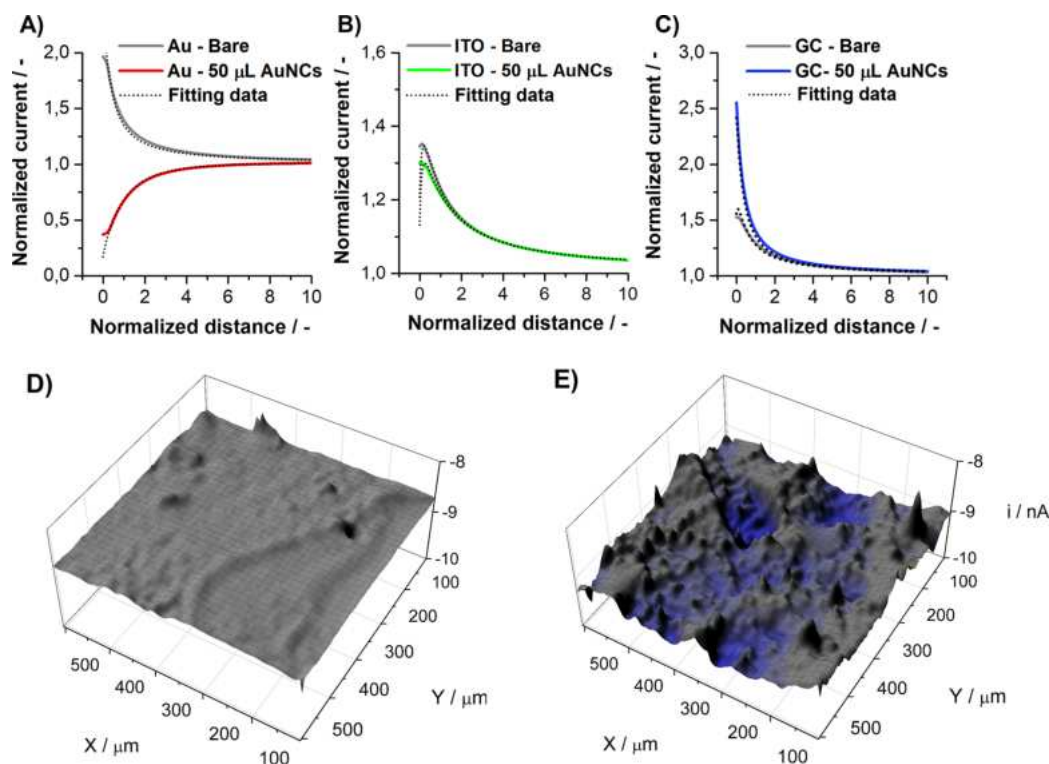
Figure 6. Approach curves for samples before and after drop-casting of AuNCs on different substrates: (A) Au, (B) ITO, and (C) GC. SECM maps of the GC surface (D) before and (E) after AuNC drop-casting, imaged at a working distance of 5 μm. The redox probe was $Fe(CN)_6^{3-}$.

3.4. Influence of AuNC on the Distribution of the Diffusion Field.

The approach curves were registered at the beginning of each SECM measurement to determine the position of each sample. These characteristics provide valuable information about the kinetics of the electrochemical reaction occurring at the surface of the electrode under investigation.[74] Standardized data obtained during the approach are shown in Figure 6A−C. The normalized current was plotted versus the normalized distance, and more detailed information is presented in section S6 of the Supporting Information. After a successful approach, surface imaging was performed at a working distance of 5 μm. Panels D and E of Figure 6 present the SECM mapping of the GC surface before and after AuNC drop-casting, respectively. The SECM maps of the remaining electrodes are shown in Figure S5.

For all electrode materials prior to AuNC decoration, the approach curves represent positive feedback, meaning spontaneous regeneration of the mediator occurring at each studied surface.[75] By fitting the approach curve for each material, we obtained the $Fe(CN)_6^{3-}$ reduction rate constant k^0 [at −0.2 V vs Ag/AgCl(gel)]. The k^0 values are listed in Table 2, and the procedure is explained in detail in section S6.2 of the Supporting Information. The k^0 for the bare substrates increases sequentially: ITO < GC < Au (likewise calculated from the CVs in Table 1). Also, similar to Table 1, the k^0 for Au decreases after AuNC deposition. Here, the negative feedback of the approach curve reveals that regeneration of the mediator has been blocked. There is only a slight change in the rate constant in the case of AuNCs/ITO, while an increase in k^0 was observed after GC decoration. All observations are in good correlation with the data obtained using the Nicholson approach.

Importantly, for the AuNCs/GC, the current registered at the tip of the microelectrode decreased upon reaching the touching point and a second, identical approach curve could not be obtained without additional polishing of the microelectrode. This behavior was explained by desorption of CTAB from the AuNC/GC surface and its attachment to the active part of the microelectrode, suggesting greater energy for adsorption of CTAB to Au than to GC, as explained below. The SEM images of the microelectrode taken after the SECM experiment are shown in Figure S4. Moreover, the approach curve toward the AuNCs/GC surface is the only one without a clear touching point, as current overflow occurred. This can be explained by exchanging electrons directly between the substrate surface and the microelectrode tip by the tunneling effect.[76]

Current distortion i_{Sq}, describing profile height deviations, was determined by analyzing the SECM maps. It is defined in the same way as AFM roughness S_q, although computed from whole area of the sample. In SECM studies, i_{Sq} is connected to the surface topography and local electrode kinetics; thus, higher values are expected after AuNC deposition. All of the data from the analysis were obtained for all surfaces and are listed in Table 2.

The highest average current value i_{avg} is observed for the bare Au electrode and decreases significantly after AuNC drop-casting. Such behavior corresponds well with the data from the approach curves and DFT simulations and can be assigned to the stronger interactions between the Au and CTAB molecules, hindering the electron transfer through the interphase. In contrast, i_{avg} increases for the GC after AuNC deposition, which may be explained by the strong interactions of the AuNCs with the GC surface and weak interaction between the GC and CTAB. Among all of the studied systems,

the ITO appears to be affected the least by the presence of AuNC.

As one can see in Table 2, the heterogeneity of the charge transfer within the diffusion field increases upon drop-casting for GC and Au. This observation corroborates perfectly what we already know about the AuNC self-assembly mechanism on these substrates. For the Au substrate, as i_{avg} decreases upon AuNC decoration, the increase in i_{Sq} is most likely connected to locally altered aggregation of CTAB molecules that are hindering electron transfer. This is supported by the topography changes seen in Figure 3. On the contrary, such a situation does not occur for the GC, for which i_{Sq} is directly connected to the increase in EASA and improvement of the charge transfer kinetics. The fact that the roughness parameter does not change for the ITO surface could be caused by a weak attraction of ITO to both AuNCs and (unlike the Au substrate) CTAB, providing a negligible change in the electrochemical response.

To support the electrochemical results further, adsorption of the CTAB surfactant and $(FeCN_6)^{4-}$ on Au, GC, and ITO surfaces was simulated (Figure 7). To the best of our
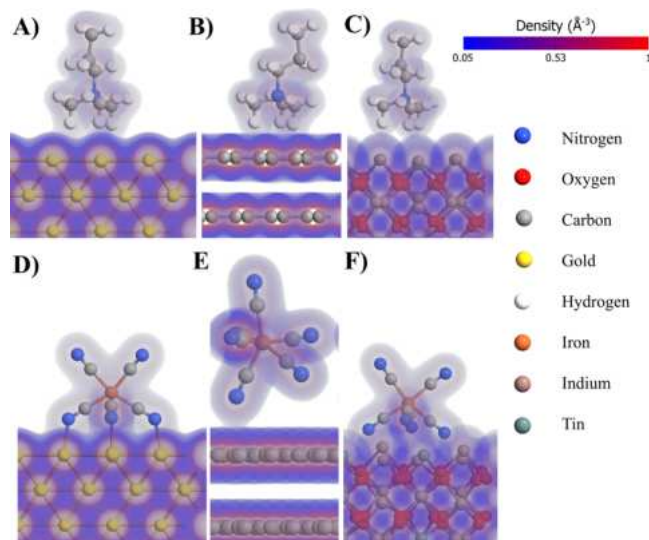

Figure 7. Electron density maps of adsorption of (A−C) CTAB and (D−F) ferrocyanide on different surfaces: (A and D) Au, (B and E) GC, and (C and F) ITO.

knowledge, DFT analysis of the adsorption of ferrocyanides on those surfaces is reported for the first time. For computational reasons, the alkyl chain of the CTAB was shortened so that the studied molecule is *N*-trimethyl isopropylamine. The effects of counterions were neglected. CTAB adsorbs on all three surfaces in a similar geometry with three electrostatic bonds and a small degree of overlapping electron density. In the case of Au, the C−H−Au bond lengths vary in the range of 2.53−2.64 Å, GC C−H−C bond lengths in the range of 2.41−2.54 Å, and ITO bond lengths in the range of 2.87−3.06 Å. Negative values of the Gibbs energy for CTAB adsorption strongly suggest that those processes are thermodynamically favorable for all three surfaces. However, the lowest energetic drive is observed for GC and is equal to −0.49 eV (Table 3). This fact might explain why the intensities of the CTAB signals observed on XRD are higher for the Au substrate than for the GC substrate.

Table 3. Adsorption Energies (in electronvolts) of CTAB and Ferrocyanides on Different Surfaces

	Au	GC	ITO
CTAB	−2.28	−0.49	−2.15
$Fe(CN)_6^{4-}$	−7.74	−4.36	−7.77
$Fe(CN)_6^{4-}$ in the presence of adsorbed CTAB	−5.46	−3.87	−5.63
$Fe(CN)_6^{4-}$ disturbance energy due to the presence of CTAB	2.28	0.49	2.15

Adsorption of $(FeCN_6)^{4-}$ on Au occurs via formation of four surface bonds between Au atoms and nitrogen atoms from cyanide groups with lengths from 2.13 to 2.16 Å. Considering their relatively short length and high degree of electron density overlap, the nature of those N−Au bonds is highly covalent, in contrast to the case for CTAB. On the contrary, the adsorption of $(FeCN_6)^{4-}$ on GC is very weak and monodentate. A 2.97 Å N−C bond is formed with minimal overlap of electron density, suggesting an electrostatic character of this interaction. This observation explains the fact that before the modification with AuNCs, glassy carbon exhibits the highest charge transfer resistance (see Table 1). The strongest adsorption of $(FeCN_6)^{4-}$ occurs on the surface of ITO. The geometry of the formed covalent/coordination bonds is similar to that in the case of gold; however, the overlap of electron densities is significantly larger. Surface bonds are created between cyanide nitrogen atoms and both indium and tin on the ITO side; in particular, the In−N bond lengths vary in the range of 2.11−2.28 Å, and the Sn−N bond lengths are equal to 2.55 Å. Similarly, as in the case of CTAB, the free energies of $(FeCN_6)^{4-}$ adsorption are negative for all three surfaces and the thermodynamic drive is the weakest for GC, while for ITO and Au, its strength is comparable (approximately −7.7 eV). Considering that the adsorption of ferrocyanide ions is the first step in the mechanism of electrode reactions,[75] the adsorption Gibbs free energy can be used as an indirect measure relating the experimentally calculated electrochemical properties to the ab initio simulations.

The disturbance energy is defined as the difference between the ferrocyanide adsorption energy on the pristine surface and the adsorption energy on the CTAB-occupied surface by eqs 1 and 2 and is equal to the CTAB adsorption energy with a negative sign. If the surface is already occupied with CTAB, the adsorption free energies are still negative for all surfaces but are shifted to higher values (Table 3). However, the magnitude of this shift (disturbance energy) for Au and ITO is equal to ~2.2 eV, while that of glassy carbon is shifted by only 0.5 eV. In other words, the surface at which CTAB disturbs ferrocyanide adsorption the least is GC. This result stands in perfect agreement with the voltammograms and EIS spectra in Figure 2. After application of AuNCs on GC, the electrochemical activity increases toward the ferrocyanide redox pair and is the highest among all three of the surfaces because the potentially blocking effect of CTAB is minimal.

Moreover, reasoning based on the adsorption geometries suggests that the charge transfer between the ferrocyanide and electrode observed in the experiments occurs via the ISET (inner sphere electron transfer) mechanism on the Au and ITO but via OSET (outer sphere electron transfer) on the GC.[77] Therefore, the activation energy of the electron transfer on the GC is expected to be the highest,[78] which is reflected in the electrochemical results by the highest overpotentials and slowest charge transfer kinetics. On the contrary, the height of

the electron transfer energy barrier on the GC surface should be less prone to change with distortion of the coordination environment, which is typical for OSET reactions.[75] In other words, longer distances of electron tunnelling from the d orbitals of ferrocyanide through the solvent layers to the quasi-continuous energy levels of the GC electrode are more likely than to the ITO and Au electrodes. As a result, in the SECM experiment, a reduction signal from both the AuNC and the substrate is observed only for the GC template. Notably, the enhancement of the electrochemical performance by AuNC/GC was previously discussed to be solely contributed by the good electrical conductivity of the electrode surface.[56] Our findings also explain the increasing $Fe(CN)_6^{3-}$ reduction rate constant k^0, which is noted only in the case of AuNC/GC. Upon decoration with AuNCs, the ISET reaction of gold is competitive with the OSET reaction of GC.[77] This situation is schematically visualized in Figure 8.
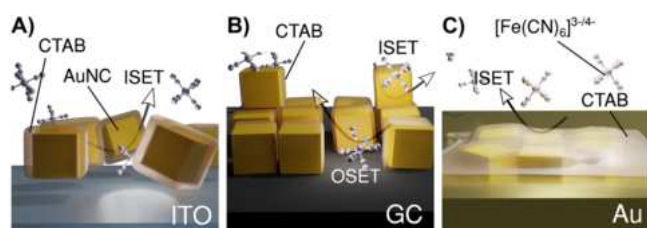
Figure 8. Schematic illustration of the self-assembly of AuNCs at (A) ITO, (B) GC, and (C) Au surfaces and modulation of the charge transfer mechanism by $[Fe(CN)_6]^{3-}$ and $[Fe(CN)_6]^{4-}$.

The scheme in Figure 8 illustrates different mechanisms of interaction of AuNC and electrode substrates with CTAB. As revealed with the electrochemical studies and DFT simulations, only the GC among the studied surfaces creates optimal conditions for AuNC self-assembly by developing agglomerates and enhancing both the electrocatalytic activity and the electrochemically active surface area of the electrode (Figure 8B). Moreover, a relatively low energy of adsorption of CTAB to the GC substrate, as seen in the XPS analysis, is not a critical aspect with respect to the charge transfer by the redox probe.

In the case of the AuNC/ITO interface (Figure 8A), the electron densities of the two surfaces do not overlap; thus, the electrical contact is not likely to form spontaneously by by the hopping or tunnelling mechanism.[63] This is further reflected by the negligible presence of physisorbed AuNC at the ITO surface, as revealed by the XRD, UV−vis, AFM, and CV studies. Additionally, the CTAB energy of adsorption is slightly stronger toward Au than toward ITO, indicating a stronger propensity for adsorption.[50] Overall, the AuNC/Au surface remains intact after decoration and neither EASA nor the charge transfer kinetics is affected. Finally, due to self-diffusion of AuNC into the Au substrate, both surfaces are spontaneously gluing (Figure 8C), which has a minor effect on the topography and EASA development in comparison to the other substrates. The AuNC/Au surface is the most electrochemically heterogeneous among all of the studied systems, which is presumably due to the appearance of non-uniform CTAB adsorbed layers in the AuNC agglomerate after-effects.[50] Therefore, due to CTAB adsorption, the $Fe(CN)_6^{3-}$ reduction rate constant k^0, estimated from CV and SECM studies, decreases by >1 order of magnitude.

Notably, one should also consider that the geometric factor arising from various interactions of AuNCs, but also $(FeCN_6)^{4-}$ and CTAB, with the studied surfaces may have an influence on the R−S equation (eq 3), even for the reversible processes. On the basis of the theoretical analysis of the Laplace space, it has been noticed that there may be a relationship in which $i_p \propto \nu^p$, where $p = (D_H - 1)/2$ and D_H is the Hausdorff dimension of the analyzed surface.[79] The statistical quality of the fit of the relationship given in section S3 of the Supporting Information is much better in the case of AuNC cast at the ITO and Au substrates when the scan rate ν exponent is different from 0.5. In the case of AuNC/GC, we could not find a better fit than 0.5, i.e., two dimensions. These data are summarized in section S7 of the Supporting Information. This interesting finding suggests that the improvement of the R−S relationship is obtained by decreasing the dimensionality for the AuNC/ITO and AuNC/Au systems rather than by increasing the EASA. Moreover, the observed trend contradicts the changes in the AFM roughness (Table 2). It turns out that improving the fit by changing the Hausdorff dimension should be explained by modification of the electrode kinetics through increasing the irreversibility of the redox process.

The effects of the electrochemical heterogeneity and the geometry of the diffusion fields are intertwined and in principle cannot be deconvoluted, because both are spatially dependent and the surface morphology determines both effects.[80,81] CTAB decreases the local kinetic constant because the alignment of energy levels for electron transfer is altered so that adsorption of the ferrocyanide is energetically more demanding, as shown in the DFT results. Locally, kinetic and diffusive effects can act synergistically or antagonistically depending on the spatial distribution of the CTAB deposits.

4. CONCLUSIONS

In summary, we have demonstrated that the molecular mechanism of assembly of gold nanocubes (AuNCs) at commonly utilized electrode surfaces is different and strongly affects the resultant electrocatalytic effect, and thus eventually the electrode selection. The most valuable findings drawn from this study are summarized here.

- The synthesized AuNCs (38 ± 2 nm), the dominating patterns being the (111) and (200) crystallographic planes, self-assembled at the GC electrode as confirmed by SEM and AFM analyses (S_q = 30.04 nm).

- The development of the electrochemically active surface area after AuNC decoration showed a tremendous 65% increase for the GC electrode and a less notable 27% increase for the Au electrode, while that of ITO remained unchanged.

- DFT simulations manifested that the enhanced electro-catalytic effect is driven by specific adsorption of ferrocyanide and CTAB at the electrodes, revealing the ISET mechanism on Au and ITO and the OSET on GC.

- The AuNC decoration at GC revealed improved electron transfer kinetics, with the highest heterogeneous rate constant among all studied systems, reaching 1.81×10^{-2} and 4.00×10^{-2} cm s^{-1} in CV and SECM studies, respectively.

- The accelerated electrocatalytic effect at GC employed heterogeneous diffusion field confinement as well as the

lowest electron transfer mitigation by CTAB, the surfactant used for AuNC stabilization.

- A similar electrocatalytic effect was not observed for the ITO or Au substrates. For the latter, the electron transfer rate was confined due to Au−Au self-diffusion and the presence of CTAB.
- The XRD, UV−vis, AFM, and CV studies revealed diminished AuNC physisorption at the ITO substrate due to strong repulsive forces, explaining the immutability of both EASA and charge transfer.
- The CTAB may play an important role in increasing the electrode's electric heterogeneity, in particular for the AuNC−Au system. The effect results from the energy of adsorption of CTAB to the studied substrate and the influence of AuNC on the surface topography.

There are papers in the literature on the use of gold nanoparticles at electrodes in biosensing, electrocatalysis, and other electrochemical research. Nevertheless, no explicit evaluation of the impact of gold nanoparticles on the electrode performance or the electrocatalytic mechanism that aids in understanding and improving the surface kinetics has been published so far. We have collectively elaborated and revealed the particular gold particle framework effect, paving the way to assessing the efficacy of electron transfer behavior at the nanoscale considering the molecular interactions in the tailored electroanalytical and electrocatalytical application.

■ ASSOCIATED CONTENT

Ⓢ Supporting Information

The Supporting Information is available free of charge at https://pubs.acs.org/doi/10.1021/acs.langmuir.2c01001.

Additional experimental details, including CV, SECM, and XPS analysis for AuNC drop-casted at each of the investigated surfaces (GC, ITO, and Au), and AFM substrate topography maps (PDF)

■ AUTHOR INFORMATION

Corresponding Author

Jacek Ryl − *Institute of Nanotechnology and Materials Engineering and Advanced Materials Center, Gdańsk University of Technology, 80-233 Gdańsk, Poland;* ⓞ orcid.org/0000-0002-0247-3851; Email: jacek.ryl@pg.edu.pl

Authors

Pawel Niedzialkowski − *Department of Analytic Chemistry, University of Gdańsk, 80-952 Gdańsk, Poland*

Adrian Koterwa − *Department of Analytic Chemistry, University of Gdańsk, 80-952 Gdańsk, Poland*

Adrian Olejnik − *Department of Metrology and Optoelectronics, Faculty of Electronics, Telecommunications and Informatics, Gdańsk University of Technology, 80-233 Gdańsk, Poland; Centre for Plasma and Laser Engineering, The Szewalski Institute of Fluid-Flow Machinery, Polish Academy of Sciences, 80-231 Gdańsk, Poland*

Artur Zielinski − *Department of Electrochemistry, Corrosion and Materials Engineering, Gdańsk University of Technology, 80-233 Gdańsk, Poland*

Karolina Gornicka − *Institute of Nanotechnology and Materials Engineering and Advanced Materials Center, Gdańsk University of Technology, 80-233 Gdańsk, Poland*

Mateusz Brodowski − *Institute of Nanotechnology and Materials Engineering and Advanced Materials Center, Gdańsk University of Technology, 80-233 Gdańsk, Poland*

Robert Bogdanowicz − *Department of Metrology and Optoelectronics, Faculty of Electronics, Telecommunications and Informatics, Gdańsk University of Technology, 80-233 Gdańsk, Poland;* ⓞ orcid.org/0000-0002-7543-2620

Complete contact information is available at:
https://pubs.acs.org/10.1021/acs.langmuir.2c01001

Author Contributions

Conceptualization: J.R. Methodology: P.N. and J.R. Validation: P.N. and J.R. Formal analysis: A.O. Investigation: P.N., A.K., A.O., A.Z., K.G., M.B., and J.R. Resources: P.N. and A.K. Data curation: P.N. and J.R. Writing of the original draft: P.N., A.O., K.G., M.B., R.B., and J.R. Review and editing: R.B. and J.R. Visualization: A.O., M.B., and J.R. Supervision: J.R. Funding acquisition: J.R.

Notes

The authors declare no competing financial interest.

■ ACKNOWLEDGMENTS

■ REFERENCES

(1) Shukla, R.; Bansal, V.; Chaudhary, M.; Basu, A.; Bhonde, R. R.; Sastry, M. Biocompatibility of Gold Nanoparticles and Their Endocytotic Fate Inside the Cellular Compartment: A Microscopic Overview. *Langmuir* **2005**, *21* (23), 10644−10654.

(2) Ong, S. W.; Ong, B. L.; Tok, E. S. Optical and Chemical Stability of Sputtered-Au Nanoparticles and Film in Ambient Environment. *Appl. Surf. Sci.* **2019**, *488*, 753−762.

(3) Donoeva, B. G.; Ovoshchnikov, D. S.; Golovko, V. B. Establishing a Au Nanoparticle Size Effect in the Oxidation of Cyclohexene Using Gradually Changing Au Catalysts. *ACS Catal.* **2013**, *3* (12), 2986−2991.

(4) Mezni, A.; Ibrahim, M. M.; El-Kemary, M.; Shaltout, A. A.; Mostafa, N. Y.; Ryl, J.; Kumeria, T.; Altalhi, T.; Amin, M. A. Cathodically Activated Au/TiO2 Nanocomposite Synthesized by a New Facile Solvothermal Method: An Efficient Electrocatalyst with Pt-like Activity for Hydrogen Generation. *Electrochim. Acta* **2018**, *290*, 404−418.

(5) Daniel, M.-C.; Astruc, D. Gold Nanoparticles: Assembly, Supramolecular Chemistry, Quantum-Size-Related Properties, and Applications toward Biology, Catalysis, and Nanotechnology. *Chem. Rev.* **2004**, *104* (1), 293−346.

(6) Leff, D. V.; Brandt, L.; Heath, J. R. Synthesis and Characterization of Hydrophobic, Organically-Soluble Gold Nanocrystals Functionalized with Primary Amines. *Langmuir* **1996**, *12* (20), 4723−4730.

(7) Weare, W. W.; Reed, S. M.; Warner, M. G.; Hutchison, J. E. Improved Synthesis of Small ($d_{CORE} \approx 1.5$ Nm) Phosphine-Stabilized Gold Nanoparticles. *J. Am. Chem. Soc.* **2000**, *122* (51), 12890−12891.

(8) Zhang, X.; Servos, M. R.; Liu, J. Instantaneous and Quantitative Functionalization of Gold Nanoparticles with Thiolated DNA Using a PH-Assisted and Surfactant-Free Route. *J. Am. Chem. Soc.* **2012**, *134* (17), 7266−7269.

(9) Xu, Q.; Lou, X.; Wang, L.; Ding, X.; Yu, H.; Xiao, Y. Rapid, Surfactant-Free, and Quantitative Functionalization of Gold Nanoparticles with Thiolated DNA under Physiological PH and Its

Application in Molecular Beacon-Based Biosensor. *ACS Appl. Mater. Interfaces* **2016**, *8* (40), 27298−27304.

(10) Aldewachi, H.; Chalati, T.; Woodroofe, M. N.; Bricklebank, N.; Sharrack, B.; Gardiner, P. Gold Nanoparticle-Based Colorimetric Biosensors. *Nanoscale* **2018**, *10* (1), 18−33.

(11) Bi, C.; Chen, J.; Chen, Y.; Song, Y.; Li, A.; Li, S.; Mao, Z.; Gao, C.; Wang, D.; Möhwald, H.; Xia, H. Realizing a Record Photothermal Conversion Efficiency of Spiky Gold Nanoparticles in the Second Near-Infrared Window by Structure-Based Rational Design. *Chem. Mater.* **2018**, *30* (8), 2709−2718.

(12) Wang, J.; Zhang, L.; Peng, F.; Shi, X.; Leong, D. T. Targeting Endothelial Cell Junctions with Negatively Charged Gold Nanoparticles. *Chem. Mater.* **2018**, *30* (11), 3759−3767.

(13) Li, W.; Cao, Z.; Liu, R.; Liu, L.; Li, H.; Li, X.; Chen, Y.; Lu, C.; Liu, Y. AuNPs as an Important Inorganic Nanoparticle Applied in Drug Carrier Systems. *Artificial Cells, Nanomedicine, and Biotechnology* **2019**, *47* (1), 4222−4233.

(14) Lu, X.; Huang, Y.; Liu, B.; Zhang, L.; Song, L.; Zhang, J.; Zhang, A.; Chen, T. Light-Controlled Shrinkage of Large-Area Gold Nanoparticle Monolayer Film for Tunable SERS Activity. *Chem. Mater.* **2018**, *30* (6), 1989−1997.

(15) Mahato, K.; Nagpal, S.; Shah, M. A.; Srivastava, A.; Maurya, P. K.; Roy, S.; Jaiswal, A.; Singh, R.; Chandra, P. Gold Nanoparticle Surface Engineering Strategies and Their Applications in Biomedicine and Diagnostics. *3 Biotech* **2019**, *9* (2), 57.

(16) Peng, Y.; Jiang, J.; Yu, R. A Sensitive Electrochemical Biosensor for MicroRNA Detection Based on Streptavidin−Gold Nanoparticles and Enzymatic Amplification. *Anal. Methods* **2014**, *6* (9), 2889−2893.

(17) Oliveira, M. D. L.; Andrade, C. A. S.; Correia, M. T. S.; Coelho, L. C. B. B.; Singh, P. R.; Zeng, X. Impedimetric Biosensor Based on Self-Assembled Hybrid Cystein-Gold Nanoparticles and CramoLL Lectin for Bacterial Lipopolysaccharide Recognition. *J. Colloid Interface Sci.* **2011**, *362* (1), 194−201.

(18) Razzino, C. A.; Serafín, V.; Gamella, M.; Pedrero, M.; Montero-Calle, A.; Barderas, R.; Calero, M.; Lobo, A. O.; Yáñez-Sedeño, P.; Campuzano, S.; Pingarrón, J. M. An Electrochemical Immunosensor Using Gold Nanoparticles-PAMAM-Nanostructured Screen-Printed Carbon Electrodes for Tau Protein Determination in Plasma and Brain Tissues from Alzheimer Patients. *Biosens. Bioelectron.* **2020**, *163*, 112238.

(19) Young, S. L.; Kellon, J. E.; Hutchison, J. E. Small Gold Nanoparticles Interfaced to Electrodes through Molecular Linkers: A Platform to Enhance Electron Transfer and Increase Electrochemically Active Surface Area. *J. Am. Chem. Soc.* **2016**, *138* (42), 13975−13984.

(20) Alba-Molina, D.; Puente Santiago, A. R.; Giner-Casares, J. J.; Martín-Romero, M. T.; Camacho, L.; Luque, R.; Cano, M. Citrate-Stabilized Gold Nanoparticles as High-Performance Electrocatalysts: The Role of Size in the Electroreduction of Oxygen. *J. Phys. Chem. C* **2019**, *123* (15), 9807−9812.

(21) Verma, S.; Singh, A.; Shukla, A.; Kaswan, J.; Arora, K.; Ramirez-Vick, J.; Singh, P.; Singh, S. P. Anti-IL8/AuNPs-RGO/ITO as an Immunosensing Platform for Noninvasive Electrochemical Detection of Oral Cancer. *ACS Appl. Mater. Interfaces* **2017**, *9* (33), 27462−27474.

(22) Rodrigues, G. H. S.; Miyazaki, C. M.; Rubira, R. J. G.; Constantino, C. J. L.; Ferreira, M. Layer-by-Layer Films of Graphene Nanoplatelets and Gold Nanoparticles for Methyl Parathion Sensing. *ACS Appl. Nano Mater.* **2019**, *2* (2), 1082−1091.

(23) Pattadar, D. K.; Masitas, R. A.; Stachurski, C. D.; Cliffel, D. E.; Zamborini, F. P. Reversing the Thermodynamics of Galvanic Replacement Reactions by Decreasing the Size of Gold Nanoparticles. *J. Am. Chem. Soc.* **2020**, *142* (45), 19268−19277.

(24) Hebié, S.; Kokoh, K. B.; Servat, K.; Napporn, T. W. Shape-Dependent Electrocatalytic Activity of Free Gold Nanoparticles toward Glucose Oxidation. *Gold Bull.* **2013**, *46* (4), 311−318.

(25) Personick, M. L.; Mirkin, C. A. Making Sense of the Mayhem behind Shape Control in the Synthesis of Gold Nanoparticles. *J. Am. Chem. Soc.* **2013**, *135* (49), 18238−18247.

(26) Rashid, Md. H.; Bhattacharjee, R. R.; Kotal, A.; Mandal, T. K. Synthesis of Spongy Gold Nanocrystals with Pronounced Catalytic Activities. *Langmuir* **2006**, *22* (17), 7141−7143.

(27) Chen, Y.; Schuhmann, W.; Hassel, A. W. Electrocatalysis on Gold Nanostructures: Is the {110} Facet More Active than the {111} Facet? *Electrochem. Commun.* **2009**, *11* (10), 2036−2039.

(28) Wang, J.; Gong, J.; Xiong, Y.; Yang, J.; Gao, Y.; Liu, Y.; Lu, X.; Tang, Z. Shape-Dependent Electrocatalytic Activity of Monodispersed Gold Nanocrystals toward Glucose Oxidation. *Chem. Commun.* **2011**, *47* (24), 6894.

(29) Hebié, S.; Cornu, L.; Napporn, T. W.; Rousseau, J.; Kokoh, B. K. Insight on the Surface Structure Effect of Free Gold Nanorods on Glucose Electrooxidation. *J. Phys. Chem. C* **2013**, *117* (19), 9872−9880.

(30) Hernández, J.; Solla-Gullón, J.; Herrero, E. Gold Nanoparticles Synthesized in a Water-in-Oil Microemulsion: Electrochemical Characterization and Effect of the Surface Structure on the Oxygen Reduction Reaction. *J. Electroanal. Chem.* **2004**, *574* (1), 185−196.

(31) Ferreira, V. C.; Solla-Gullón, J.; Aldaz, A.; Silva, F.; Abrantes, L. M. Progress in the Understanding of Surface Structure and Surfactant Influence on the Electrocatalytic Activity of Gold Nanoparticles. *Electrochim. Acta* **2011**, *56* (26), 9568−9574.

(32) Park, J.-E.; Lee, Y.; Nam, J.-M. Precisely Shaped, Uniformly Formed Gold Nanocubes with Ultrahigh Reproducibility in Single-Particle Scattering and Surface-Enhanced Raman Scattering. *Nano Lett.* **2018**, *18* (10), 6475−6482.

(33) Hernández, J.; Solla-Gullón, J.; Herrero, E.; Aldaz, A.; Feliu, J. M. Electrochemistry of Shape-Controlled Catalysts: Oxygen Reduction Reaction on Cubic Gold Nanoparticles. *J. Phys. Chem. C* **2007**, *111* (38), 14078−14083.

(34) Zhang, L.; Wang, J.; Zhang, J.; Liu, Y.; Wu, L.; Shen, J.; Zhang, Y.; Hu, Y.; Fan, Q.; Huang, W.; Wang, L. Individual Au-Nanocube Based Plasmonic Nanoprobe for Cancer Relevant MicroRNA Biomarker Detection. *ACS Sens.* **2017**, *2* (10), 1435−1440.

(35) Baek, S. H.; Song, H. W.; Lee, S.; Kim, J.-E.; Kim, Y. H.; Wi, J.-S.; Ok, J. G.; Park, J. S.; Hong, S.; Kwak, M. K.; Lee, H. J.; Nam, S.-W. Gold Nanoparticle-Enhanced and Roll-to-Roll Nanoimprinted LSPR Platform for Detecting Interleukin-10. *Front. Chem.* **2020**, *8*, 285.

(36) Bagheri Hashkavayi, A.; Bakhsh Raoof, J.; Ojani, R.; Hamidi Asl, E. Label-Free Electrochemical Aptasensor for Determination of Chloramphenicol Based on Gold Nanocubes-Modified Screen-Printed Gold Electrode. *Electroanalysis* **2015**, *27* (6), 1449−1456.

(37) Lv, H.; Zhang, X.; Li, Y.; Ren, Y.; Zhang, C.; Wang, P.; Xu, Z.; Li, X.; Chen, Z.; Dong, Y. An Electrochemical Sandwich Immunosensor for Cardiac Troponin I by Using Nitrogen/Sulfur Co-Doped Graphene Oxide Modified with Au@Ag Nanocubes as Amplifiers. *Microchim Acta* **2019**, *186* (7), 416.

(38) Lipińska, W.; Ryl, J.; Slepski, P.; Siuzdak, K.; Grochowska, K. Exploring Multi-Step Glucose Oxidation Kinetics at GOx-Functionalized Nanotextured Gold Surfaces with Differential Impedimetric Technique. *Measurement* **2021**, *174*, 109015.

(39) Huang, Q.; Wang, W.; Vikesland, P. J. Implications of the Coffee-Ring Effect on Virus Infectivity. *Langmuir* **2021**, *37* (38), 11260−11268.

(40) Devineau, S.; Anyfantakis, M.; Marichal, L.; Kiger, L.; Morel, M.; Rudiuk, S.; Baigl, D. Protein Adsorption and Reorganization on Nanoparticles Probed by the Coffee-Ring Effect: Application to Single Point Mutation Detection. *J. Am. Chem. Soc.* **2016**, *138* (36), 11623−11632.

(41) Kou, X.; Sun, Z.; Yang, Z.; Chen, H.; Wang, J. Curvature-Directed Assembly of Gold Nanocubes, Nanobranches, and Nanospheres. *Langmuir* **2009**, *25* (3), 1692−1698.

(42) *Atomistix Toolkit*, ver. 2019.03; Synopsys QuantumWise A/S.

(43) Moellmann, J.; Grimme, S. DFT-D3 Study of Some Molecular Crystals. *J. Phys. Chem. C* **2014**, *118* (14), 7615−7621.

(44) Soler, J. M.; Artacho, E.; Gale, J. D.; García, A.; Junquera, J.; Ordejón, P.; Sánchez-Portal, D. The SIESTA Method for *Ab Initio* Order- *N* Materials Simulation. *J. Phys.: Condens. Matter* **2002**, *14* (11), 2745−2779.

(45) van Setten, M. J.; Giantomassi, M.; Bousquet, E.; Verstraete, M. J.; Hamann, D. R.; Gonze, X.; Rignanese, G.-M. The PseudoDojo: Training and Grading a 85 Element Optimized Norm-Conserving Pseudopotential Table. *Comput. Phys. Commun.* **2018**, *226*, 39−54.

(46) Miranda, A.; Malheiro, E.; Eaton, P.; Carvalho, P. A.; de Castro, B.; Pereira, E. Synthesis of Gold Nanocubes in Aqueous Solution with Remarkable Shape-Selectivity. *J. Porphyrins Phthalocyanines* **2011**, *15* (05n06), 441−448.

(47) Passiu, C.; Rossi, A.; Weinert, M.; Tysoe, W.; Spencer, N. D. Probing the Outermost Layer of Thin Gold Films by XPS and Density Functional Theory. *Appl. Surf. Sci.* **2020**, *507*, 145084.

(48) Fu, L.; Huo, C.; He, X.; Yang, H. Au Encapsulated into Al-MCM-41 Mesoporous Material: In Situ Synthesis and Electronic Structure. *RSC Adv.* **2015**, *5* (26), 20414−20423.

(49) Rodríguez-Fernández, J.; Pérez-Juste, J.; Mulvaney, P.; Liz-Marzán, L. M. Spatially-Directed Oxidation of Gold Nanoparticles by Au(III)−CTAB Complexes. *J. Phys. Chem. B* **2005**, *109* (30), 14257−14261.

(50) Maack, I.; Osmić, M.; Mohrhusen, L.; Buhani, P.; Al-Shamery, K. Fitting A Square Peg into A Round Hole: Shape Control in Phase Transfer of Cubic Gold Nanoparticles. *ChemNanoMat* **2021**, *7* (6), 658−671.

(51) Norbert, A.; Brun, B.; Chan-Dara. Constantes cristallographiques du bromure de tétradécyltriméthylammonium et du bromure d'hexadécyltriméthylammonium. *bulmi* **1975**, *98* (1), 111−112.

(52) Yang, S.; Gao, L. Controlled Synthesis and Self-Assembly of CeO$_2$ Nanocubes. *J. Am. Chem. Soc.* **2006**, *128* (29), 9330−9331.

(53) Huang, C.-J.; Wang, Y.-H.; Chiu, P.-H.; Shih, M.-C.; Meen, T.-H. Electrochemical Synthesis of Gold Nanocubes. *Mater. Lett.* **2006**, *60* (15), 1896−1900.

(54) Kundu, S.; Panigrahi, S.; Praharaj, S.; Basu, S.; Ghosh, S. K.; Pal, A.; Pal, T. Anisotropic Growth of Gold Clusters to Gold Nanocubes under UV Irradiation. *Nanotechnology* **2007**, *18* (7), 075712.

(55) Davey, W. P. Precision Measurements of the Lattice Constants of Twelve Common Metals. *Phys. Rev.* **1925**, *25* (6), 753−761.

(56) Zakaria, N. D.; Omar, M. H.; Ahmad Kamal, N. N.; Abdul Razak, K.; Sönmez, T.; Balakrishnan, V.; Hamzah, H. H. Effect of Supporting Background Electrolytes on the Nanostructure Morphologies and Electrochemical Behaviors of Electrodeposited Gold Nanoparticles on Glassy Carbon Electrode Surfaces. *ACS Omega* **2021**, *6* (38), 24419−24431.

(57) Brust, M.; Gordillo, G. J. Electrocatalytic Hydrogen Redox Chemistry on Gold Nanoparticles. *J. Am. Chem. Soc.* **2012**, *134* (7), 3318−3321.

(58) Xu, X.; Duan, G.; Li, Y.; Liu, G.; Wang, J.; Zhang, H.; Dai, Z.; Cai, W. Fabrication of Gold Nanoparticles by Laser Ablation in Liquid and Their Application for Simultaneous Electrochemical Detection of Cd^{2+}, Pb^{2+}, Cu^{2+}, Hg^{2+}. *ACS Appl. Mater. Interfaces* **2014**, *6* (1), 65−71.

(59) Niedziałkowski, P.; Białobrzeska, W.; Burnat, D.; Sezemsky, P.; Stranak, V.; Wulff, H.; Ossowski, T.; Bogdanowicz, R.; Koba, M.; Śmietana, M. Electrochemical Performance of Indium-Tin-Oxide-Coated Lossy-Mode Resonance Optical Fiber Sensor. *Sens. Actuators, B* **2019**, *301*, 127043.

(60) Nicholson, R. S. Theory and Application of Cyclic Voltammetry for Measurement of Electrode Reaction Kinetics. *Anal. Chem.* **1965**, *37* (11), 1351−1355.

(61) Ryl, J.; Burczyk, L.; Zielinski, A.; Ficek, M.; Franczak, A.; Bogdanowicz, R.; Darowicki, K. Heterogeneous Oxidation of Highly Boron-Doped Diamond Electrodes and Its Influence on the Surface Distribution of Electrochemical Activity. *Electrochim. Acta* **2019**, *297*, 1018−1027.

(62) Hirschorn, B.; Orazem, M. E.; Tribollet, B.; Vivier, V.; Frateur, I.; Musiani, M. Determination of Effective Capacitance and Film Thickness from Constant-Phase-Element Parameters. *Electrochim. Acta* **2010**, *55* (21), 6218−6227.

(63) Velický, M.; Hu, S.; Woods, C. R.; Tóth, P. S.; Zólyomi, V.; Geim, A. K.; Abruña, H. D.; Novoselov, K. S.; Dryfe, R. A. W.

Electron Tunneling through Boron Nitride Confirms Marcus−Hush Theory Predictions for Ultramicroelectrodes. *ACS Nano* **2020**, *14* (1), 993−1002.

(64) Pan, J.; Jing, T. W.; Lindsay, S. M. Tunneling Barriers in Electrochemical Scanning Tunneling Microscopy. *J. Phys. Chem.* **1994**, *98* (16), 4205−4208.

(65) Song, X.; Han, B.; Yu, X.; Hu, W. The Analysis of Charge Transport Mechanism in Molecular Junctions Based on Current-Voltage Characteristics. *Chem. Phys.* **2020**, *528*, 110514.

(66) Dávila López, A. C.; Pehlke, E. DFT Study of Au Self-Diffusion on Au(001) in the Presence of a Cl Adlayer. *J. Chem. Phys.* **2019**, *151* (6), 064709.

(67) Keith, J. A.; Fantauzzi, D.; Jacob, T.; van Duin, A. C. T. Reactive Forcefield for Simulating Gold Surfaces and Nanoparticles. *Phys. Rev. B* **2010**, *81* (23), 235404.

(68) Hamelin, A. Cyclic Voltammetry at Gold Single-Crystal Surfaces. Part 1. Behaviour at Low-Index Faces. *J. Electroanal. Chem.* **1996**, *407* (1−2), 1−11.

(69) Hamelin, A.; Martins, A. M. Cyclic Voltammetry at Gold Single-Crystal Surfaces. Part 2. Behaviour of High-Index Faces. *J. Electroanal. Chem.* **1996**, *407* (1−2), 13−21.

(70) Cinti, S.; Politi, S.; Moscone, D.; Palleschi, G.; Arduini, F. Stripping Analysis of As(III) by Means of Screen-Printed Electrodes Modified with Gold Nanoparticles and Carbon Black Nanocomposite. *Electroanalysis* **2014**, *26* (5), 931−939.

(71) Lv, H.; Xu, D.; Henzie, J.; Feng, J.; Lopes, A.; Yamauchi, Y.; Liu, B. Mesoporous Gold Nanospheres *via* Thiolate−Au(i) Intermediates. *Chem. Sci.* **2019**, *10* (26), 6423−6430.

(72) McCormick, W.; McDonagh, P.; Doran, J.; McCrudden, D. Covalent Immobilisation of a Nanoporous Platinum Film onto a Gold Screen-Printed Electrode for Highly Stable and Selective Non-Enzymatic Glucose Sensing. *Catalysts* **2021**, *11* (10), 1161.

(73) Lv, H.; Xu, D.; Sun, L.; Liu, B. Surfactant Design Strategy for One-Pot Seedless Synthesis of Hollow Mesoporous AuAg Alloy Nanospheres. *J. Phys. Chem. Lett.* **2020**, *11* (14), 5777−5784.

(74) Bard, A. J.; Mirkin, M. V.; Unwin, P. R.; Wipf, D. O. Scanning Electrochemical Microscopy. 12. Theory and Experiment of the Feedback Mode with Finite Heterogeneous Electron-Transfer Kinetics and Arbitrary Substrate Size. *J. Phys. Chem.* **1992**, *96* (4), 1861−1868.

(75) Bard, A. J.; Faulkner, L. R. *Electrochemical Methods: Fundamentals and Applications*, 2nd ed.; Wiley: New York, 2001.

(76) Sun, T.; Wang, D.; Mirkin, M. V. Electrochemistry at a Single Nanoparticle: From Bipolar Regime to Tunnelling. *Faraday Discuss.* **2018**, *210*, 173−188.

(77) Bard, A. J. Inner-Sphere Heterogeneous Electrode Reactions. Electrocatalysis and Photocatalysis: The Challenge. *J. Am. Chem. Soc.* **2010**, *132* (22), 7559−7567.

(78) Matyjaszewski, K. Atom Transfer Radical Polymerization: From Mechanisms to Applications. *Isr. J. Chem.* **2012**, *52* (3−4), 206−220.

(79) Isidorsson, J.; Strømme, M.; Gåhlin, R.; Niklasson, G. A.; Granqvist, C. G. Ion Transport in Porous Sn Oxide Films: Cyclic Voltammograms Interpreted in Terms of a Fractal Dimension. *Solid State Commun.* **1996**, *99* (2), 109−111.

(80) Compton, R. G.; Banks, C. E. *Understanding Voltammetry*; World Scientific: Singapore, 2007.

(81) Banks, C. E.; Davies, T. J.; Wildgoose, G. G.; Compton, R. G. Electrocatalysis at Graphite and Carbon Nanotube Modified Electrodes: Edge-Plane Sites and Tube Ends Are the Reactive Sites. *Chem. Commun.* **2005**, *7*, 829.

Supplementary Information file

For

Deciphering the molecular mechanism of substrate-induced assembling of gold nanocube arrays toward accelerated electrocatalytic effect employing heterogeneous diffusion fields confinement

Pawel Niedzialkowski[1], Adrian Koterwa[1], Adrian Olejnik[2,3], Artur Zielinski[4], Karolina Gornicka[5], Mateusz Brodowski[5], Robert Bogdanowicz[2] and Jacek Ryl[5,*]

[1]Department of Analytic Chemistry, University of Gdańsk, Wita Stwosza 63, 80-952 Gdańsk, Poland
[2]Department of Metrology and Optoelectronics, Gdańsk University of Technology, Narutowicza 11/12, 80-233 Gdańsk, Poland
[3]Centre for Plasma and Laser Engineering, The Szewalski Institute of Fluid-Flow Machinery, Polish Academy of Sciences, Fiszera 14, Gdańsk 80-231, Poland
[4]Department of Electrochemistry, Corrosion and Materials Engineering, Gdańsk University of Technology, Narutowicza 11/12, 80-233 Gdańsk, Poland
[5]Institute of Nanotechnology and Materials Engineering and Advanced Materials Center, Gdańsk University of Technology, Narutowicza 11/12, 80-233 Gdańsk, Poland

* corresponding author (J.R): jacek.ryl@pg.edu.pl

S1. The schematic representation of the location for SECM and AFM measurements
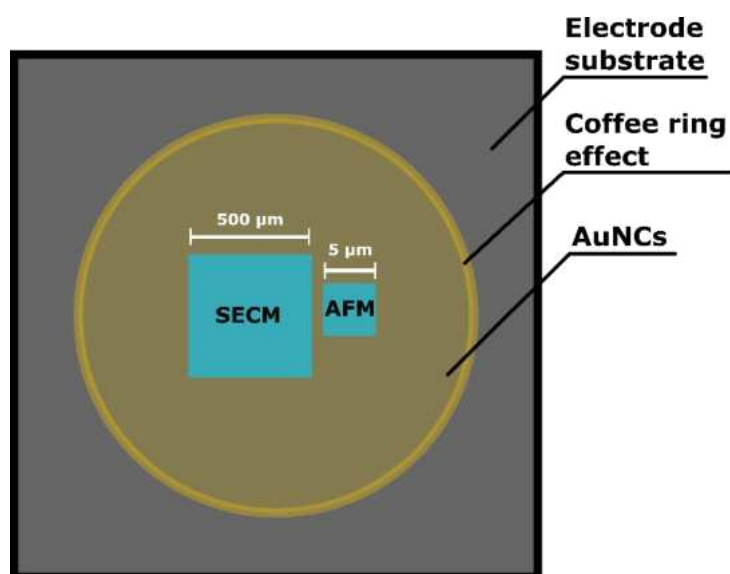
S2. High-resolution *Au 4f_{7/2}* XPS results for AuNC drop-casted at ITO and Au substrates
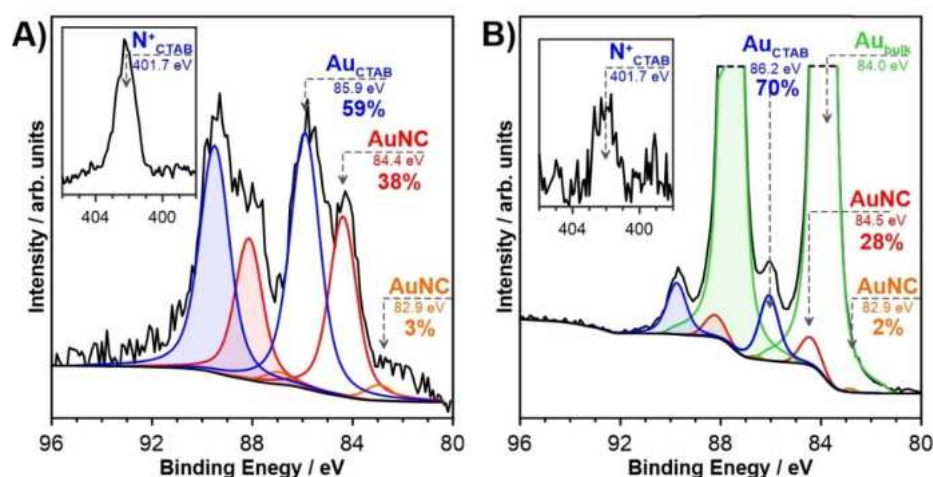

Fig S1 – XPS analysis in *Au 4f* core-level energy range for AuNCs decorated on A) ITO and B) Au substrates. The *N 1s* spectrum in the inset.

The deconvoluted data reveal the presence of the same spectral components as in the case of decorated GC electrodes. On the other hand, the share of each oxidation state within the AuNCs was different, suggesting a much higher amount of Au(III) CTAB-complexed species for both ITO and Au (59% and 70% total [Au], respectively), compared with GC substrate (13%). The presence of CTAB at the electrode surface was confirmed by *N 1s* spectra, where a single peak at approx. 401.7 eV originates from N^+_{CTAB} species.

The Au substrate peaks Au^0 bulk Au $4f_{7/2}$ signal at 84.0 eV. Its contribution was not accounted for when calculating the shares of species contribution to AuNC chemistry. However, it should be

considered that its presence may underestimate the AuNC peak at 84.5 eV and hinder the actual Au_{CTAB} ratio. A smaller share of Au(III) species complexed by CTAB is hinted at by the low intensity of the *N 1s* signal for Au substrate.

S3. The cyclic voltammetry studies of the AuNC decorated Au, ITO, and GC electrode kinetics.

Results of cyclic voltammograms of bare substrates and electrodes after drop-casting of 10 µL of AuNCs in 0.01 M PBS pH 7.4 containing 1 mM $K_3[Fe(CN)_6]$ and $K_4[Fe(CN)_6]$ at various scan rates: 0.5, 1, 2, 5, 10, 20, 50, 100, 200, 500 mV s^{-1} and the R-S relationship for $[Fe(CN)_6]^{3-/4-}$ oxidation/reduction peaks vs $\sqrt{\nu}$, obtained for different electrode configurations.

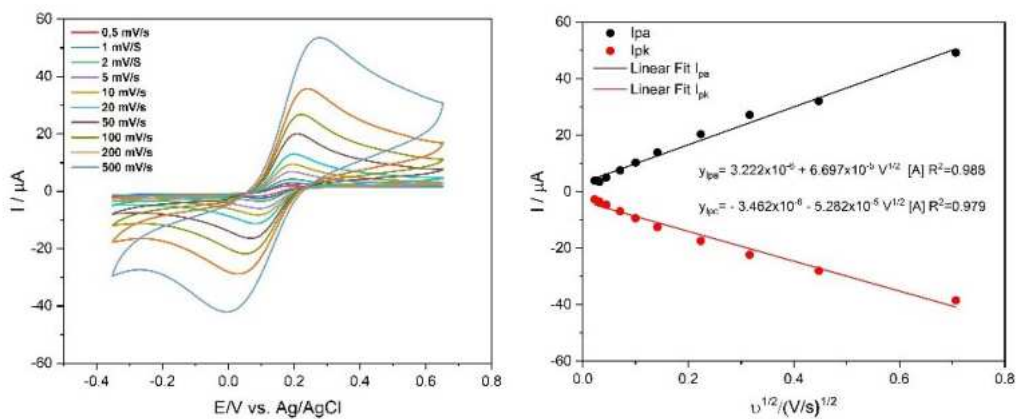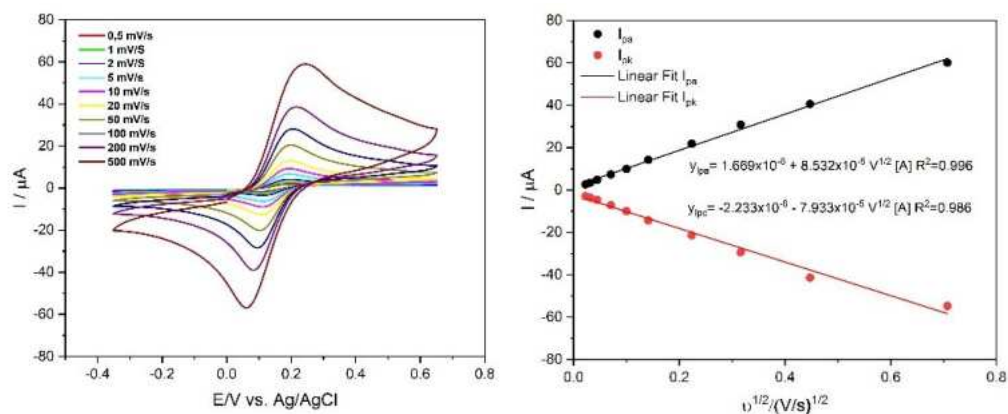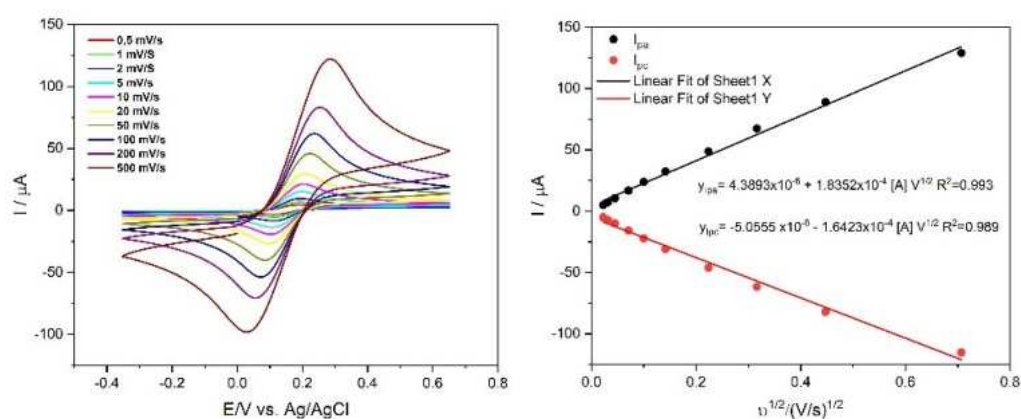## S3.1. GC electrode
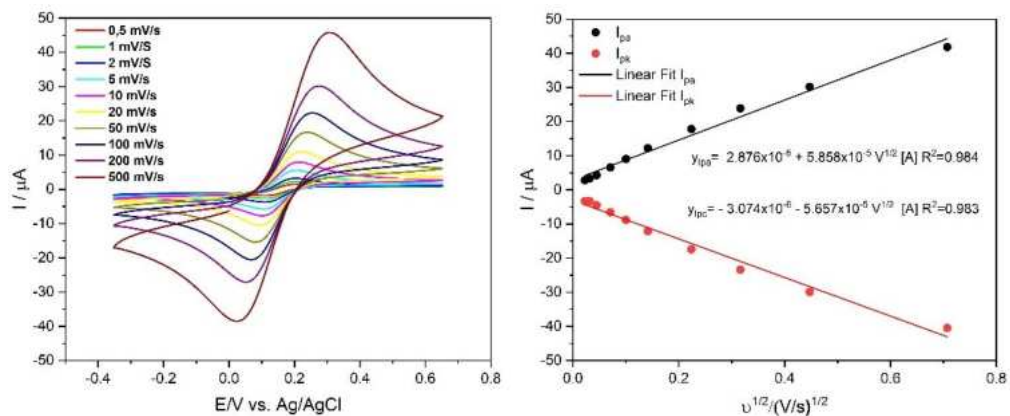
S3.2. AuNCs/GC system
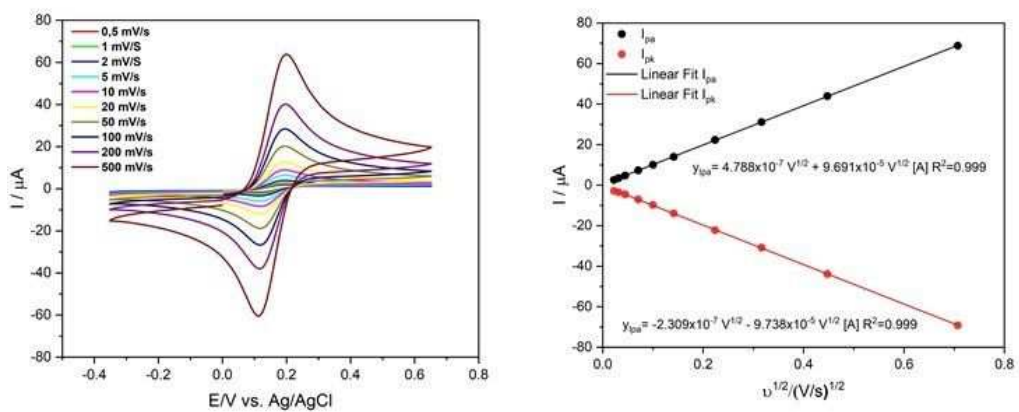
S3.3. Au electrode

S3.4. AuNCs/Au system

S3.5. ITO electrode

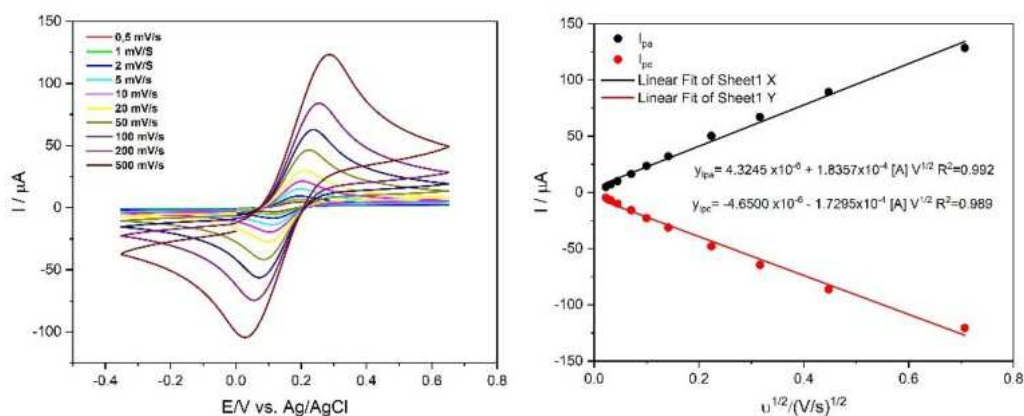
S3.6. AuNCs/ITO system

Table S1 - Characteristic CV parameters obtained for each studied electrode configuration at the 100 mV s^{-1} scan rate.

	ΔE_p / V		$i_{A\ 100\ mV/s}$ / μA		$i_{C\ 100\ mV/s}$ / μA	
	bare	AuNC	bare	AuNC	bare	AuNC
Au	81	71	25.8	21.1	-25.0	-26.2
GC	84	71	25.7	28.4	-26.0	-28.4
ITO	151	155	60.5	50.7	-57.6	-53.1

S4. The topography AFM mapping of reference electrode surfaces
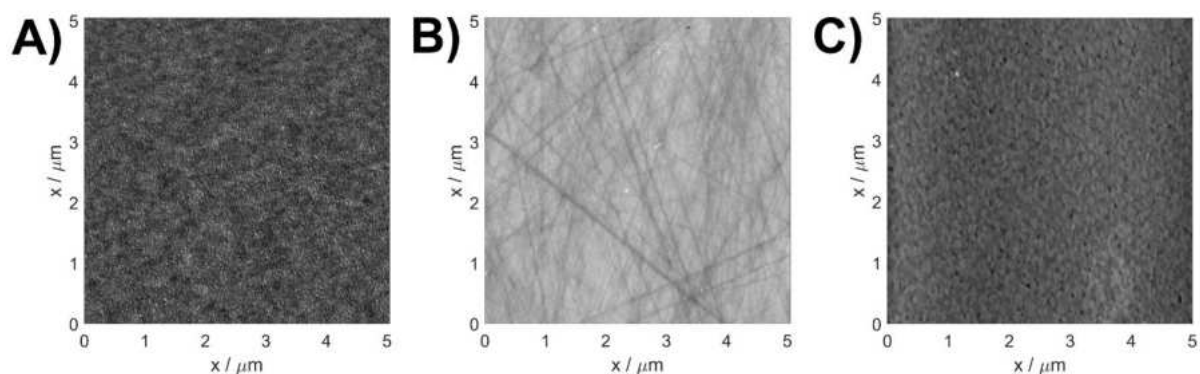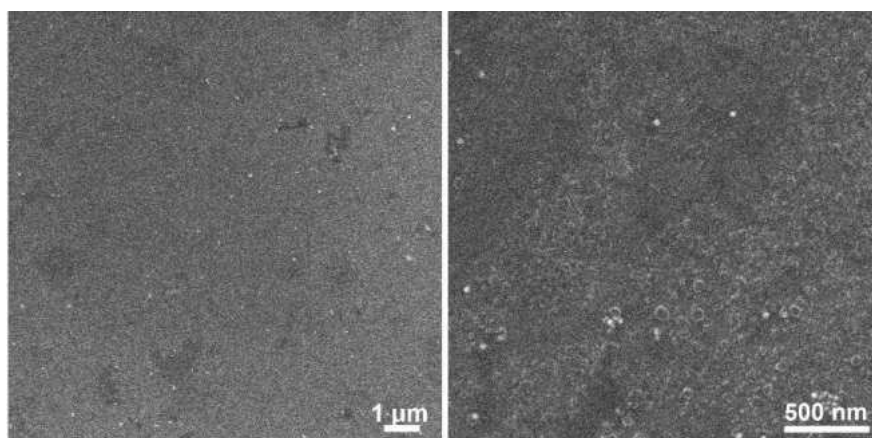

Fig S2 – AFM topographic images of reference samples: A) Au; B) GC; C) ITO

S5. The SEM micrograph of the ITO surface after AuNC drop-casting

S6. Scanning electrochemical microscopy (SECM) measurements

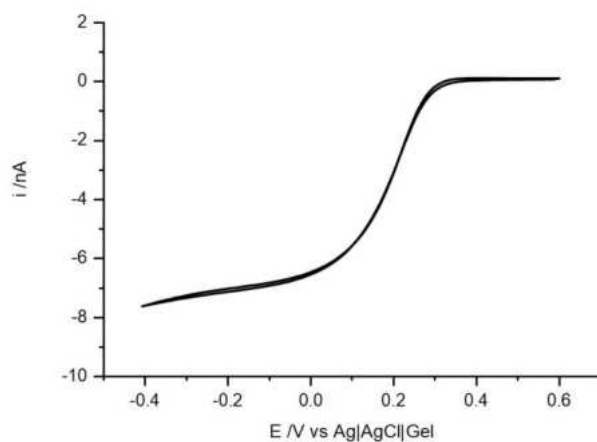### S6.1. Cyclic voltammetry at the gold microelectrode before SECM measurements

Fig. S3 – The CV registered for gold microelectrode in deoxygenated 5 mM $K_3[Fe(CN)_6]$ in PBS, scan rate 25 mV s^{-1}.

S6.2. Fitting of steady-state SECM approach curves

The most basic parameters that need to be determined for calculations presented in this section are the radius of the microelectrode active part (r_T) and the radius of the insulating part (glass) (r_{glass}). The r_T and r_{glass} have been obtained by SEM imagining of the microelectrode. The SEM images of the microelectrode taken after SECM scan are presented in **Fig. S4.** Next, the RG parameter has been computed as: $RG = r_{glass} / r_T$.
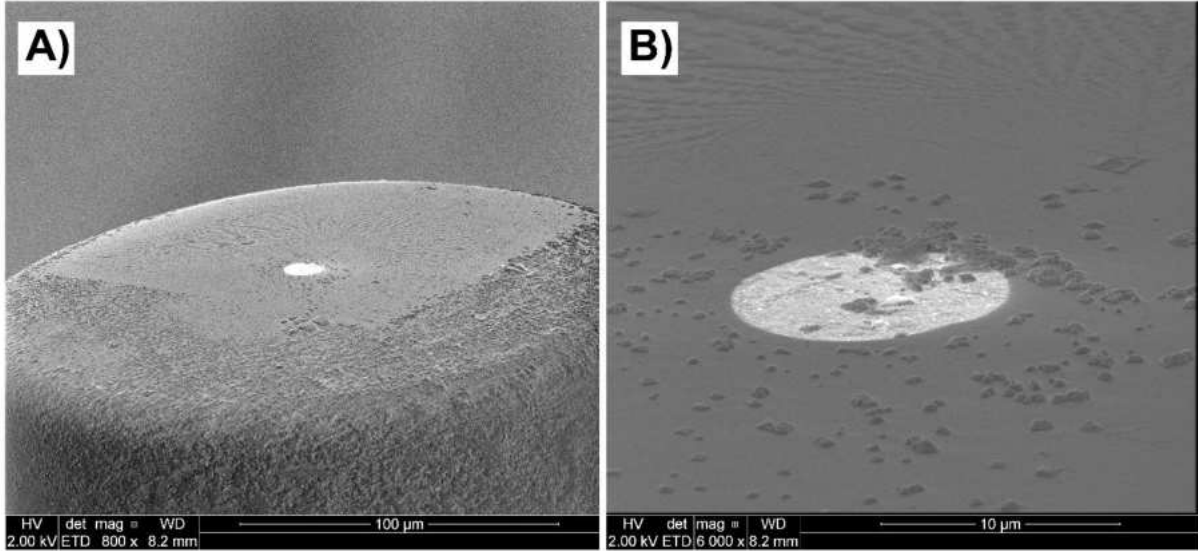

Fig. S4 - SEM images for A) microelectrode embedded in glass, B) microelectrode active part

The approach curves have been normalized according to the following formula (eqs S1, S2):

$$I_T = \frac{i_T}{i_{T,\infty}} \tag{S1}$$

$$L = \frac{l}{r_T} \tag{S2}$$

The normalized current (I_T) is the proportion between tip current (i_T) and tip current at an infinite distance from the substrate ($i_{T,\infty}$). The normalized distance is expressed as the ratio of the electrode's relative position to the active microelectrode part.

To calculate the theoretical, I_t value for each experiment the approximation of Cornut and Lefrou[S1] was used. The main equations utilized are briefly presented below (eqs (S3-S8)), and a full description can be found in the original work [S1].

$$I_T(L, \kappa, RG) = I_T^{cond}\left(L + \frac{1}{\kappa}, RG\right) + \frac{I_T^{ins}(L,RG) - 1}{(1 + 2.47RG^{0.31}L\,\kappa)(1 + L^{0.006RG + 0.113}\,\kappa^{-0.0236RG + 0.91})} \tag{S3}$$

$$I_T^{cond}\left(L + \frac{1}{\kappa}, RG\right) = \propto (RG) + \frac{1}{2\beta(RG)\xi\left(L + \frac{1}{\kappa}\right)} + \left(1 - \propto (RG) - \frac{1}{2\beta(RG)}\right)\xi\left(L + \frac{1}{\kappa}\right) \quad \text{(S4)}$$

$$I_T^{ins}(L,RG) = \frac{\frac{2.08}{RG^{0.358}}\left(L - \frac{0.145}{RG}\right) + 1.585}{\frac{2.08}{RG^{0.358}}(L + 0.0023RG) + 1.57 + \frac{\ln RG}{L} + \frac{2}{\pi RG}\ln\left(1 + \frac{\pi RG}{2L}\right)} \quad \text{(S5)}$$

$$\alpha(RG) = \ln 2 + \ln 2\left(1 - \frac{2}{\pi}arccos\left(\frac{1}{RG}\right)\right) - \ln 2\left(1 - \left(\frac{2}{\pi}arccos\left(\frac{1}{RG}\right)\right)^2\right) \quad \text{(S6)}$$

$$\beta(RG) = 1 + 0.639\left(1 - \frac{2}{\pi}arccos\left(\frac{1}{RG}\right)\right) - 0.186\left(1 - \left(\frac{2}{\pi}arccos\left(\frac{1}{RG}\right)\right)^2\right) \quad \text{(S7)}$$

$$\xi\left(L + \frac{1}{\kappa}\right) = \frac{2}{\pi}arctan\left(L + \frac{1}{\kappa}\right) \quad \text{(S8)}$$

Fitting data obtained from experiments allowed us to estimate the normalized constant rate (κ) from the SECM approach curves. which later allowed us to calculate the heterogeneous rate constant (k^0) of first-order reaction according to eq. (3):

$$\kappa = \frac{k^0 r_T}{D} \quad \text{(S9)}$$

As can be seen in eq. (S3) the parameters r_T and D are constant for all measurements presented in this specific work. The κ values for each studied setup were summarized in **Table S2.**

Table S2 – κ values estimated from SECM the approach curves.

Parameter	Sample	Au	GC	ITO
κ / -	bare	2.91	1.72	1.25
	AuNC	0.048	3.00	1.48

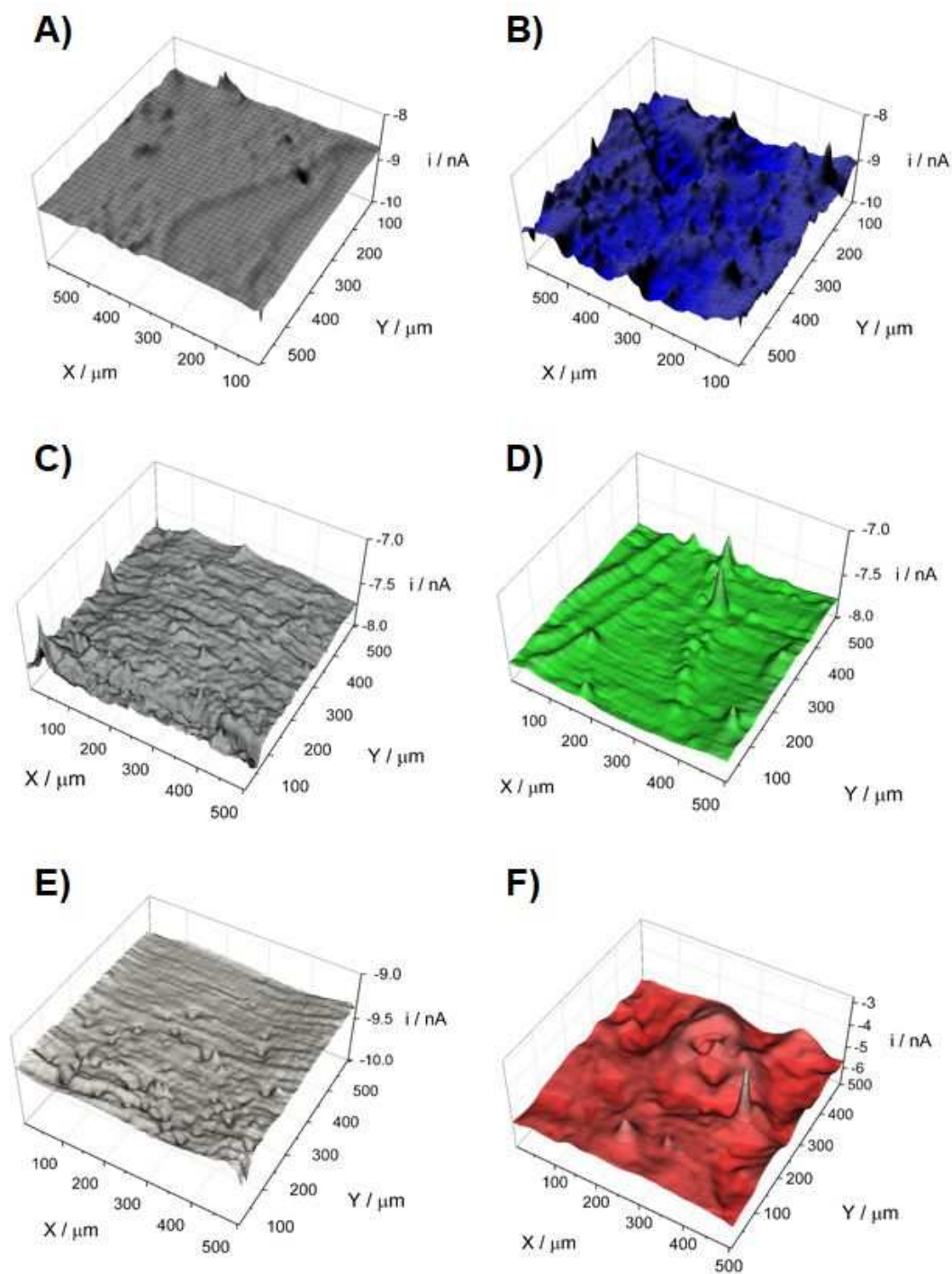**S6.3. The SECM maps obtained for each studied system**

Fig S5 – SECM maps for different systems: A,B) GC; C,D) ITO; E,F) Au, characterizing the electrochemical homogeneity A,C,E) of bare electrodes and B,D,F) after AuNCs drop-casting. For all measurements, the working distance of the microelectrode was 5 μm, step 5 μm, and speed 10 μm s^{-1}.

S7. Calculation of the optimal R-S fit for different Hausdorf dimensions

Table S3 - The values of the least-square function R^2 for R-S formula ($D_H = 2$) and at D_H dimension offering the highest R^2

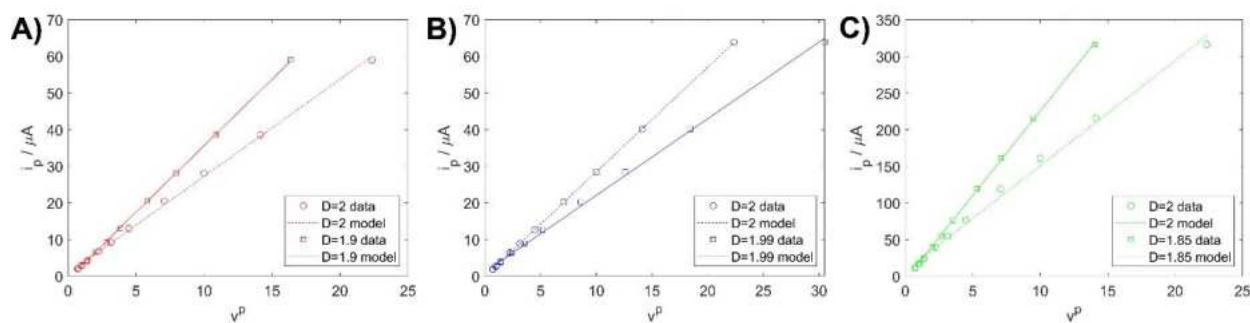|	GC	Au	ITO
$D_H = 2$	0.9967	0.9735	0.9477
$D_H = 1.99$	0.9949		
$D_H = 1.90$		0.9896	
$D_H = 1.85$			0.9828

Fig S6 – Graphical representation of the Hausdorf dimension fitting after AuNCs drop-casting at each electrode surface: A) AuNC/Au; B) AuNC/GC; C) AuNC/ITO.

References:

(S1) Cornut, R.; Lefrou, C. New Analytical Approximation of Feedback Approach Curves with a Microdisk SECM Tip and Irreversible Kinetic Reaction at the Substrate. *Journal of Electroanalytical Chemistry* **2008**, *621* (2), 178–184. https://doi.org/10.1016/j.jelechem.2007.09.021.

Discriminating macromolecular interactions based on an impedimetric fingerprint supported by multivariate data analysis for rapid and label-free *Escherichia coli* recognition in human urine

Adrian Koterwa [a,1], Mattia Pierpaoli [b,1], Bożena Nejman-Faleńczyk [c], Sylwia Bloch [c], Artur Zieliński [d], Wioletta Adamus-Białek [e], Zofia Jeleniewska [f], Bartosz Trzaskowski [g], Robert Bogdanowicz [b], Grzegorz Węgrzyn [c], Paweł Niedziałkowski [a,**], Jacek Ryl [f,*]

[a] *Department of Analytical Chemistry, Faculty of Chemistry, University of Gdańsk, Wita Stwosza 63, 80-308, Gdańsk, Poland*
[b] *Department of Metrology and Optoelectronics, Gdańsk University of Technology, Narutowicza 11/12, 80-233, Gdańsk, Poland*
[c] *Department of Molecular Biology, Faculty of Biology, University of Gdansk, Wita Stwosza 59, 80-308, Poland*
[d] *Faculty of Chemistry, Gdańsk University of Technology, Narutowicza 11/12, 80-233, Gdańsk, Poland*
[e] *Institute of Medical Sciences, Jan Kochanowski University of Kielce, IX Wieków Kielc 19A, 25-317, Kielce, Poland*
[f] *Division of Electrochemistry and Surface Physical Chemistry, Faculty of Applied Physics and Mathematics, Gdańsk University of Technology, Narutowicza 11/12, Gdańsk, 80-233, Poland*
[g] *Centre of New Technologies, University of Warsaw, Banach 2c, 02-097, Warsaw, Poland*

ARTICLE INFO

ABSTRACT

This manuscript presents a novel approach to address the challenges of electrode fouling and highly complex electrode nanoarchitecture, which are primary concerns for biosensors operating in real environments. The proposed approach utilizes multiparametric impedance discriminant analysis (MIDA) to obtain a fingerprint of the macromolecular interactions on flat glassy carbon surfaces, achieved through self-organized, drop-cast, receptor-functionalized Au nanocube (AuNC) patterns. Real-time monitoring is combined with singular value decomposition and partial least squares discriminant analysis, which enables selective identification of the analyte from raw impedance data, without the use of electric equivalent circuits. As a proof-of-concept, the authors demonstrate the ability to detect *Escherichia coli* in real human urine using an aptamer-based biosensor that targets RNA polymerase. This is significant, as uropathogenic *E. coli* is a difficult-to-treat pathogen that is responsible for the majority of hospital-acquired urinary tract infection cases. The proposed approach offers a limit of detection of 11.3 CFU/mL for the uropathogenic *E. coli* strain No. 57, an analytical range in all studied concentrations (up to 10^5 CFU/mL), without the use of antifouling strategies, yet not being specific vs other *E.coli* strain studied (BL21(DE3)). The MIDA approach allowed to identify negative overpotentials (-0.35 to -0.10 V vs Ag/AgCl) as most suitable for the analysis, offering over 80% sensitivity and accuracy, and the measurement was carried out in just 2 min. Moreover, this approach is scalable and can be applied to other biosensor platforms.

1. Introduction

Developing an electrochemical biosensing platform that is both industrially scalable and repeatable is a challenging task that requires meeting various requirements. To achieve low limits of detection (LOD) and selectivity, many available technologies rely on complex synthetic

---

methods and nanoarchitecture designs, difficult to control when expanding production, thus leading to sub-ideal structural features or loss in their special, surface-related functions (Chen et al., 2022; Sharifi et al., 2019). Additionally, the ability to develop platforms with high sensitivity and selectivity in complex biological samples is of paramount importance (Russo et al., 2021). Popular strategies to reduce fouling are through nanoengineered surfaces (Chapman et al., 2015; Zhou et al., 2009) or the application of nanoporous membranes (Sun et al., 2016), which further increase the complexity and reduce the reproducibility and scale-up potential of the proposed approaches. Another strategy includes developing antifouling coatings to prevent the non-specific molecules adsorption. Here, single-molecule fouling agents after receptor grafting (Niedzialkowski et al., 2020), molecular brushes (Emilsson et al., 2015), zwitterionic coatings (Gui et al., 2013), but also supramolecular hydrogels (Wu et al., 2017) should be considered.

Owing to the high surface area-to-volume ratio and unique electronic and catalytic properties, gold nanoparticles are excellent candidates for enhancing the sensitivity and selectivity of electrochemical biosensors (Xiao et al., 2020). Gold nanocubes (AuNCs) have recently gained particular attention due to their uniform dimensions, higher self-organization predictability, and the ability to finely tune their plasmonic properties, as well as chemical stability (Park et al., 2018). The molecular mechanism of AuNC assembly essentially depends on the electrode substrate, strongly affecting the resultant electrocatalytic effect. Among commonly utilized electrode substrates, AuNCs decorated at GC provide over 65% increase in electrochemically active surface area and 75% increase in heterogeneous rate constant (Niedzialkowski et al., 2022). Voltammetry aptasensors based on AuNCs were used for the determination of chloramphenicol (LOD = 2.8 pM) (Lu et al., 2021), progesterone in diluted blood (LOD = 1 ng/mL) (Velayudham et al., 2021) and even a prostate cancer gene sequence (10 nM), also exhibiting low disturbance in the presence of fouling agents (Abedi et al., 2021). DNA biosensors for pathogenic *Vibrio cholerae*, responsive even at quantities of 10 CFU/mL, and selective detection in bacterial cultures belonging to the same and distant genera (Ali et al., 2021). Moreover, surface modification of AuNC makes it possible to produce a signal-enhanced interface, such as in the case of the paper-based chikungunya virus platform built based on magnetic $Fe_3O_4@AuNC$ (Singhal et al., 2018), or the hollow Ag@AuNC core-shell for surface-enhanced Raman scattering and non-enzymatic uric acid and ascorbic acid detection (Bhattacharjee et al., 2020).

Human urine is a product of the filtration system – the kidneys – and was conventionally considered as sterile (Kass, 1962). Even though the results of next generation sequencing analyses provide evidence of the existence of the urine microbiome, there are still many controversial aspects to this topic (Frimodt-Møller, 2019; Grine et al., 2019; Shah Utsav et al., 2021) and the common belief is that urine in the bladder of a healthy person is not contaminated with bacteria. However, bacteria can enter the urinary system, causing problems such as infection and inflammation. Urinary tract infection (UTI) is considered the second most common bacterial disease after pneumonia and affects about 150 million people every year worldwide (Flores-Mireles et al., 2015). Annually, UTIs are diagnosed in more than 10% of women and 3% of men, and more than 60% of women will be diagnosed with a UTI in their lifetime (Klein and Hultgren, 2020). The clinical picture of the UTI ranges from a mild self-limiting illness, chronic or acute infection, to urosepsis. Additionally, urosepsis comprises 25% of all adult sepsis cases and is associated with an overall mortality rate of 20–40%. Primary hospitalized patients due to UTIs result in a total cost of $2.8 billion USD in the United States, annually; epidemiological reports also indicate 1 million visits to the emergency department and 7 million office visits (Klein and Hultgren, 2020). Uropathogenic *Escherichia coli* (UPEC) is the most common pathogen, responsible for 85% and 50% of community and hospital-acquired UTI cases, respectively, and can form biofilms on urological catheters, making them very difficult to treat and remove due to the high tolerance of biofilm structures to antibiotics.

The standard urine culture protocol represents the primary tool for detecting bacteria in clinical microbiology laboratories with LOD > 10^5 CFU/mL (Kass, 1962; Price et al., 2016). Dipsticks and culturing methods take long time (hours, even days), limiting rapid intervention. In turn, the use of some molecular methods as polymerase chain reaction (PCR) could improve the speed and accuracy of UPEC detection; however, their applicability is complicated by the high genomic variability within uropathogenic *E. coli* strains (Brons et al., 2020). Other diagnostic technologies for UTIs are also known, i.e. urinalysis and microscopy, fluorescent *in situ* hybridization (FISH), MALDI-TOF MS, microfluidics, immunology-based and forward light scattering assays; however, their limiting factors, described recently in detail (Davenport et al., 2017), prevent their use in clinics. A powerful approach to the detection of *E. coli* via electrochemical biosensors is by immunosensors (Felix and Angnes, 2018). Many electrode modifications were performed to obtain as low limits of detection (LOD) as possible, such as photochemical immobilization of anti-*E. coli* antibodies on gold (Cimafonte et al., 2020), gold modified by graphene-wrapped copper (II)-assisted cysteine hierarchical structure, and antibodies (Pandey et al., 2017). Wang et al. show a 10 CFU/mL LOD with composite biosensors based on magnetic nanoparticles (NPs) and functionalized gold nanoparticles (AuNPs) conjugated with lead sulfide NPs via oligonucleotide linkage (R. R. Wang et al., 2015; Y. Y. Wang et al., 2015). Another route to use immuno-functionalized magnetic beads is by glucose oxidase (GOx)–antibody conjugates at interdigitated microelectrodes (10^3 CFU/mL) (Xu et al., 2016). A bionanocomposite based on pencil graphite modified with chitosan, multiwalled carbon nanotubes, polypyrrole and AuNPs offers a LOD of 30 CFU/mL (Güner et al., 2017). The utilization of nucleic acid hybridization or connection to DNA is also used in *E. coli* biosensors. The gold electrode modified by thiolated capture probes and biotinylated aptamer probes had an 80 CFU/mL E. *coli* LOD (Wang et al., 2019). Limits of detection under 10 CFU/mL were obtained with biosensors based on metal–organic frameworks functionalized by polyaniline at glassy carbon electrode (GCE) (Shahrokhian and Ranjbar, 2018) and indium-tin oxide (ITO) modified by 3-Aminopropyltrimethoxysilane and DNA genetic markers (Deshmukh et al., 2020).

Detecting analytes in real human urine poses significant challenges due to the potential for unknown interactions to occur between the biosensor surface, the analyte, and other molecules present in the sample (Aitekenov et al., 2021). As a result, only a limited number of studies have proposed electrochemical methods for detecting analytes in urine. Typically, detection in urine is based on the use of antibody-modified electrodes, and the measurements focus on the clinical utility of the biosensors that have been designed. Such examples include a GCE functionalized by a nanocomposite of polyaniline with AuNPs and MoS_2 modified by antibodies or Au modified with thin reduced graphene oxide and polyethylenimine (Jijie et al., 2018), both with LODs of 10 to 10^5 CFU/mL (Raj et al., 2021). The screen-printed carbon electrode with an AuNP-decorated polyaniline film and anti-digoxigenin-labeled horseradish peroxidase was manifested to detect 4 to 4×10^6 CFU/mL *E. coli* in urine (Shoaie et al., 2018). However, despite the efforts, achieving uniform PANI distribution and volume for scale-up remains a critical challenge (Yang et al., 2023), while quantitative analysis is required in specific sensing scenarios.

In this work, we have developed a novel approach to the detection of large biomolecules using modulated electrostatic interactions induced by electrode polarization, mitigating common biofouling and indirect readout. Simultaneous biosystem perturbations by a package of multiple pre-selected frequency signals was analyzed by the Singular Value Decomposition (SVD) followed by Partial Least Squares Discriminant Analysis (PLS-DA) to effectively discriminate the signal response in the presence or absence of the target molecule. Such a strategy delivers an explicit impedimetric fingerprint of the macromolecular interactions, which is dependent not only on binding moieties but also coulombic interactions at different charge states at the electrode surface. We have demonstrated the functionality of the proposed proof-of-concept at an

aptamer-based biosensor composed of self-organized Au nanocube patterns at a flat glassy carbon electrode, applied for the rapid detection of *E. coli* in real human urine samples through polymerase RNA. Importantly, the measured impedance values were directly used for the analyses, avoiding errors that may accumulate during the standard fitting procedures with electric equivalent circuits.

2. Experimental

2.1. Chemicals and bacteria strains used

All chemicals were of analytical grade and were used as purchased without further purifications. Plates of glassy carbon electrode (GCE), 12x12x3 mm, SIGRADUR G, were purchased from (HTW Hochtemperatur-Werkstoffe GmbH, Germany). All electrochemical measurements were carried out in vessels containing a circular seal with a radius of 7 mm. AuNCs were obtained according to the procedure previously described in the paper (Niedzialkowski et al., 2022), see detailed instruction in the **SI file**, **section 1**. The AuNCs were stored in a 1 mM cetyltrimethylammonium bromide (CTAB) solution.

The *E. coli* RNA polymerase holoenzyme (RNAP) used in this study, composed of the core enzyme and sigma factor 70, was obtained from the New England Biolabs company (cat No. M0551S). Both strands of the strong $p_{rrnG-P1}$ promoter – nontemplate (coding) strand with -10 and -35 motifs indicated in bold: 5′-CGA TAA AGT TTT TAT ATT TTT CGC **TTG TCA** GGC CGG AAT AAC TCC C**TA TAA T**GC GCC ACC A-3′, and template (noncoding) strand: 5′-TGG TGG CGC ATT ATA GGG AGT TAT TCC

GGC CTG ACA AGC GAA AAA TAT AAA AAC TTT ATC G-3′ – were synthesized by Genomed SA. The nontemplate strand was also modified at its 5′ end using thiol linker: 5′-SH-(CH$_2$)$_6$-CGA TAA AGT TTT TAT ATT TTT CGC TTG TCA GGC CGG AAT AAC TCC CTA TAA TGC GCC ACC A-3′. The RNAP holoenzyme is solely capable of unwinding the dsDNA helix (Bae et al., 2015; Glyde et al., 2017).

The nonpathogenic *E. coli* B strain BL21(DE3) (Clock et al., 2008) (EC-B) was obtained from the collection of the Department of Molecular Biology of the University of Gdańsk (Poland). The uropathogenic *E. coli* strain No. 57 (UPEC-57) was identified in the urine of a 14-year-old male patient from the Nephrology Clinic and donated with an antibiogram for research from the Department of Microbiology of the Regional Hospital in Kielce, Poland, in 2017. All liquid bacterial cultures were grown in Luria-Bertani medium (LB; EPRO, Poland) with aeration at 37 °C in a shaking incubator (200 RPM). Details on bacterial strain growth and suspension preparation are given in the **SI file, section S2**. The Petri dishes with LB solid medium with 1.5% bacteriological agar (LA; BTL Company, Poland) were incubated at 37 °C for approximately 18 h.

2.2. Biosensor electrode modification

All GCEs were cleaned with a polishing cloth and 0.03 μm aluminum oxide powder (Buehler, USA) before use. AuNCs dissolved in a 0.001 M CTAB solution were deposited onto the GCE surface using a 10 μL drop casting method (see SEM micrograph in Fig. 1b). The solution was allowed to dry on the electrode surface for 30 min at room temperature, then the electrodes were washed with warm water to remove the CTAB
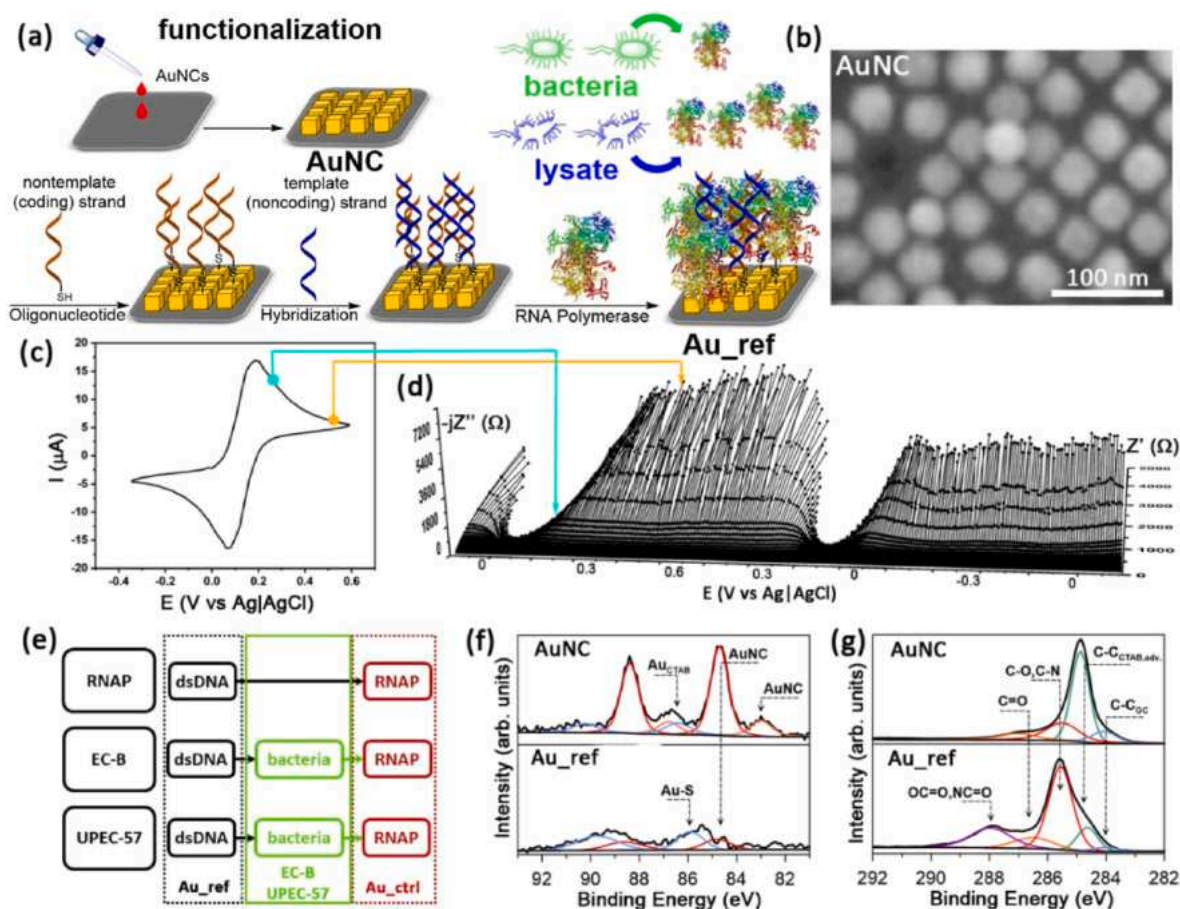
Fig. 1. (a) scheme of GCE decoration with AuNC and functionalization toward RNAP recognition; (b) SEM micrograph of drop-cast AuNC at GCE; (d) exemplary CV and (e) DEIS impedance plot obtained during the CV scan, with arrows identifying individual spectra collected at a given polarization; (e) identification of electroanalytical experiment labels; (f,g) high-resolution XPS spectra with proposed deconvolution for AuNCs at GC before and after functionalization with dsDNA: (f) *Au 4f* and (g) *C 1s*.

residue. A homogeneous GCE surface modified with AuNCs was obtained according to the previously described procedure (Niedzialkowski et al., 2022).

For the functionalization, as schematically presented in Fig. 1a, we used the sequence of one of the P1 promoters, $p_{rrnG-P1}$, allowing for the transcription of rRNA genes of the *rrnG* operon. The selected promoter sequence enabled the binding of *E. coli* RNAP and thus was effectively used as a biosensor receptor. AuNCs were modified by applying 200 μL of 0.2 μmol/L nontemplate (coding) oligonucleotide strand dissolved in TRIS-HCl buffer, pH 7.56. After a 12-h modification at room temperature, the electrode surface was thoroughly rinsed with Tris HCl buffer, pH 7.56. Then, a hybridization process was performed using an oligonucleotide with a complementary sequence. The 200 μL of 0.1 μmol/L template (noncoding) oligonucleotide stand dissolved in TRIS-HCl buffer, pH 7.56, was placed on the electrode surface and left for 2 h at room temperature. Such functionalized electrodes served for RNAP detection.

2.3. Biorecognition methodology

The Multiparametric Impedance Discriminant Analysis (MIDA) combines multisine impedimetric monitoring with singular value decomposition of raw impedance data, followed by partial least squares discriminant analysis. No electric equivalent circuit was used during impedance data analysis. All electrochemical measurements were performed in the three-electrode setup, with AuNC drop-cast and functionalized at GCE as the working electrode (0.38 cm^2 electrolyte-exposed area), silver chloride-coated silver wire (150 x 1.5 mm) as the reference electrode, and coiled platinum wire (100 x 0.5 mm) as the auxiliary electrode. The impedance monitoring was performed using an AC signal consisting of a package of 21 elementary sinusoids, ranging from 3 to 4500 Hz, superimposed on a DC voltammetry scan, from −0.35 V to 0.60 V, scan rate 2 mV/s. The exact procedure was previously described by the authors (Brodowski et al., 2022; Niedzialkowski et al., 2020). Exemplary impedance spectra recorded during a voltammetry scan are given in Fig. 1c and d. An Autolab (PGSTAT30) potentiostat/galvanostat by Metrohm, The Netherlands, was linked to a computer equipped with a 24 Bit, 204.8 kS/s, PCI-4461 card by National Instruments, USA, and used to generate the AC perturbation signal package.

In the analysis, each impedance dataset at a specific bias (among the 1890 applied biases), is given by the measured complex impedance, expressed as follows (eq. (1)):

$$\mathbf{Z}_{bias} = \mathbf{Z'}_{bias} + j\mathbf{Z''}_{bias} \tag{1}$$

where $\mathbf{Z}_{bias}$ is a total impedance, $\mathbf{Z'}_{bias}$ and $\mathbf{Z''}_{bias}$ are the real and imaginary parts of $\mathbf{Z}_{bias}$, respectively, and $j^2 = -1$. Thus, $\mathbf{Z}_{bias}$ is a complex number matrix with dimensions of 18 (number of independent tests) × 21 (number of elementary frequencies in a single measurement). The 18 tests include six replicates for each condition (EC-B and UPEC-57 strains) assisted by a reference Au_ref study and control Au_ctrl study in excess of RNAP. In this manner, 1850 matrices were prepared for each experiment (the first 30 and last 10 measurements were discarded). No data centering or scaling was applied to the datasets.

To treat a large amount of collected data, singular value decomposition (SVD) is applied to complex impedance datasets. Let $\mathbf{Z}_{bias}$ be the above-reported 18×21 matrix, which can be decomposed with SVD into 3 matrices (eq. (2)):

$$\mathbf{Z}_{bias} = \mathbf{U\Sigma V}^T \tag{2}$$

where $\mathbf{\Sigma}$ is a matrix with real, nonnegative entries, σ_i, on the diagonal and zeros off the diagonal, organized so that $\sigma_1 > \sigma_2 > \ldots > \sigma_r$; and $\mathbf{U}$ and $\mathbf{V}$ are unitary orthonormal matrices. Different experimental conditions (e.g. the presence/absence of the analyte) were arranged in a matrix with each column containing all the measurements at a given frequency.

Thus, if the columns of $\mathbf{Z}_{bias}$ are analyte measurements at a frequency, then $\mathbf{U}$ distinguishes the analyte patterns, and $\mathbf{V}$ encodes the frequency patterns. Hence, the right singular vectors could be interpreted as an EIS spectrum, or a linear combination of any, so it would be possible to reconstruct the original EIS by linear combinations of the singular EIS. Then, two different paths are followed.

Path 1: PLS Discriminant Analysis (PLS-DA) is a discrimination method based on PLS regression. A dummy response variable, y, was added to the dataset, which is equal to +1 for positive samples, and −1 for the control group. Now, considering the linear system of equations $\mathbf{y} = \mathbf{Z}_{bias}\ \mathbf{x}$, the goal is to determine the weighting $\mathbf{x}$ that relates to the presence of the bacteria, restricted to the first two components. For this aim, a truncated SVD (to the first three singular values) was employed. This path can provide useful information about the frequencies most involved in the sensing mechanism (Pierpaoli et al., 2022).

Path 2: Linear regression is performed on both real and imaginary (treated as real) parts of $\mathbf{u}_1$ and $\mathbf{u}_2$, using the same response variable, $\mathbf{y}$.

Finally, in order to evaluate the ideal polarization potential intervals (PPI) to better discriminate between control and positive samples, the conventional metrics, such as accuracy, sensitivity and specificity, were calculated as follows (eqs (3)–(5)) (Van Stralen et al., 2009):

$$\text{accuracy} = (TP + TN)/(TP + TN + FP + FN) \tag{3}$$

$$\text{sensitivity} = TP/(TP + FN) \tag{4}$$

$$\text{specificity} = TN/(TN + FP) \tag{5}$$

where TP = true positive, TN = true negative, FP = false positive, and FN = false negative.

Two strains of bacteria labeled, EC-B and UPEC-57, were presented in the form of suspended intact bacterial cells or bacterial lysate solution and studied in artificial and real human urine at a volume ratio of 1:1 with 0.01 M PBS containing 1 mM Fe(CN)$_6^{3-/4-}$. Real human urine was obtained from a healthy 37-year-old woman, co-author of this publication. The analysis was carried out in a medical laboratory of Diagnostyka SA, Poland. The parameters of the urine tested are presented in the SI file, Table S1. The reference measurements (Au_ref) were carried out on the dsDNA functionalized electrode in the absence of the analyte. Each time, a control measurement (Au_ctrl) was also performed, admixing 1 CFU *E. coli* RNAP to the previously used solution, see Fig. 1e for experiment scheme. Prior to electrochemical measurements, the solution was heated to 37 °C using an Eppendorf ThermoMixer. By spiking the real human urine with 3 different concentrations of UPEC-57, and using above described, LOD was estimated using the median and standard deviation of the blank samples using the following equation (6):

$$\text{LOD} = \text{CFU}_{median} + 3 \times \text{SD}_{CFU} \tag{6}$$

2.4. Physicochemical analyses

X-ray photoelectron spectroscopy (XPS) analyses were carried out in the core-level binding energy range of *C 1s*, *Au 4f*, *O 1s* and *N 1s* to investigate the surface chemistry of the biosensor surface after consecutive functionalization steps, i.e. AuNC drop-casting at GCE and dsDNA grafting. These studies were carried out on an Escalab 250Xi (Thermo-Fisher Scientific), utilizing an AlKα X-ray source, spot diameter of 250 μm and pass energy of 20 eV. Low-energy electron and low-energy Ar$^+$ ion bombardment were used for charge compensation purposes. Avantage v5.9921(ThermoFisher Scientific) was used for deconvolution and peak calibration using adventitious carbon *C 1s* (284.6 eV).

Atomic force microscopy (AFM) studies were performed with NTgra Prima (NT-MDT) and using NSG30 probes with geometric parameters 125x40x4 μm, resonant frequency 320 kHz, and spring constant 40 N/m. A set of 25 approximation curves were made in a rectangular area (side – 3.5 μm) for statistical processing purposes. The static technique

was used. These measurements were conducted in the electrolyte used for the electrochemical studies, under a potentiostatic regime at three different polarization potentials, namely: -0.3 V, $+0.1$ V and $+0.5$ V vs Ag/AgCl, before and after RNAP exposure to dsDNA-functionalized AuNC at GCE. The scanning electron microscopy (SEM) analysis was performed using Quanta 250 FE-SEM (FEI), with the operating electron beam at a 20 kV accelerating voltage.

3. Results and discussion

3.1. dsDNA immobilization on gold nanocubes

The efficacy of consecutive electrode functionalization steps was verified directly by means of XPS analysis, and indirectly through impedimetric changes analysis. Fig. 1f and **g** reveal the high-resolution XPS spectra registered in the core-level binding energy range of the *Au 4f* and *C 1s* peaks, respectively. Following Fig. 1f, one can observe a strong *Au 4f$_{7/2}$* component at 84.7 eV, testifying the presence of AuNC at the GC surface. Two more peak doublets were identified, the one shifted at -1.5 eV is likely ascribed to an AuNC surface component
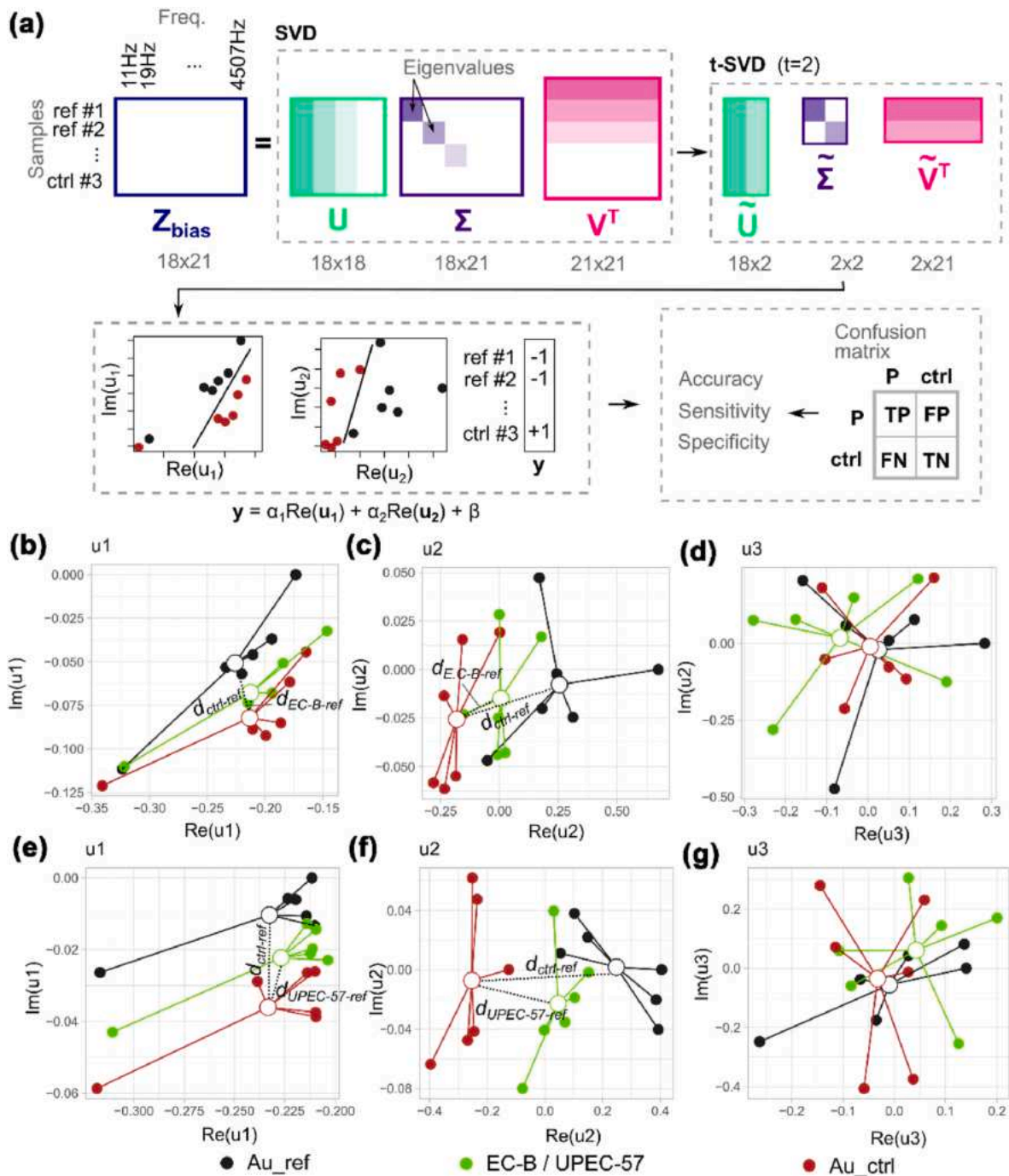

Fig. 2. (a) Schematic of the data elaboration, with an example for $N_p = 1760$ and $E_p = -0.28$ V; (b–g) Graphical representation of the first three columns of U: (b–d) for the EC-B, and (e–g) UPEC-57 datasets.

(Niedzialkowski et al., 2022; Passiu et al., 2020), while the one at +1.6 eV should be interpreted as Au-C moieties, thus testifying to Au complexing by surfactant, CTAB, as discussed in more detail in another report on AuNC chemistry (Niedzialkowski et al., 2022). Anchoring the thiol-functionalized oligonucleotide strand and hybridizing the complementary strand to obtain the dsDNA receptor led to an increase in the layer thickness, suppressing the Au signal. Notably, after surface functionalization, the primary constituent is the peak at 85.8 eV, which is characteristic of Au species involved in the Au-S bond (Laomeephol et al., 2020; Vitale et al., 2011). In the case of the GCE surface with drop-cast AuNCs, the major constituents of the *C 1s* spectra are the 284.8 and 285.6 eV peaks, attributed to aliphatic C-C and C-N/C-O bonds, respectively, from the presence of CTAB and adventitious carbons, with a smaller component from the sp^2-C within the GCE substrate (Dwivedi et al., 2015; Qu et al., 2019). Anchoring the dsDNA receptor significantly alters the surface chemistry of the sensor. The strongest signal originates from the C-O/C-N bonds and OC=O, NC=O bonds, present within the hydrocarbon chains in nucleic acid bases. This observation is typical of DNA anchored at electrode surfaces (Niedzialkowski et al., 2020; Silva-Moraes et al., 2018). A significant drop in the share of sp^2-C corroborates the increase in the functionalization layer.

Consecutive steps of surface functionalization, depicted in Fig. 1a, were routinely controlled by electrochemical impedance spectroscopy and cyclic voltammetry; see the data in the SI file, Fig. S1 and Table S2. As a general rule, the next functionalization steps lead to an increase in the thickness of the layer functionalized at the electrode surface, which successively increases the charge transfer resistance, R_{CT}.

3.2. Data analysis and RNA polymerase recognition in real bacteria cultures

The impedimetric data treatment is schematically reported in Fig. 2a. The first step in analyzing the data was to perform SVD for each polarization step. In the first part of the experiment, the recognition of real bacteria cultures was carried out in artificial urine. As an example, the real against the imaginary part of the first three columns of **U** are

reported, for both the EC-B and UPEC-57 datasets, at $N_p = 1760$ ($E_p = -0.28$ V) in Fig. 2b–g, showing that the greatest separation between control and positive samples is given both by the real and imaginary part of the first component and by the real part of the second component. No distinction is provided by the third component (as also reported by the low explained variance). For this reason, the PLS-DA was conducted with truncated SVD (t-SVD), with r = 2. Moreover, the Euclidean distances $d_{ctrl-ref}$, $d_{E.coli-ref}$ and $d_{UPEC-ref}$ have been defined as the distance between the centroids. A similar observation can be made regardless of whether the analysis is done on suspended bacteria or bacterial lysate (see SI file, Fig. S2 for details). Since the first column, u_1, carries most of the dataset information, it is possible to see that the individual points are characterized by high dispersion, which may be related to the characteristics of the single electrode, which results from the fabrication steps. On the other hand, in u_2, the different tests are well-clustered, suggesting that this component may be connected to the bacteria identification, independently of the different electrode characteristics. Indeed, minor features that distinguish the different impedance measurements are common and will most likely be represented by components different from the first. This behavior can be observed for both the EC-B and UPEC-57 datasets.

By performing the SVD analysis reported above at all the 1850 polarization steps (N_p), it was possible to observe how the sample clustering varies with the application of a polarization potential (E_p). The variation of the specificity, accuracy, and sensitivity as a function of N_p is shown in Fig. 3a for EC-B and Fig. 3b for UPEC-57. It is possible to see, for EC-B, the more pronounced presence of some intervals in which a dramatic drop in the sensitivity is present, which corresponds with the second component, showing a slight increase of the explained variance (Fig. 3c and d). By computing the previously defined Euclidean distances between centroids, it is possible to see distances maximization occurring at negative potentials (Fig. 3e and f). Similarly, to highlight the polarization potential intervals (PPIs) at which the distinction between sample sensitivity, accuracy, and specificity is most noticeable were calculated as functions of E_p (Fig. 3g,i). In particular, it is possible to observe the presence of three different behaviors at different electrode polarization
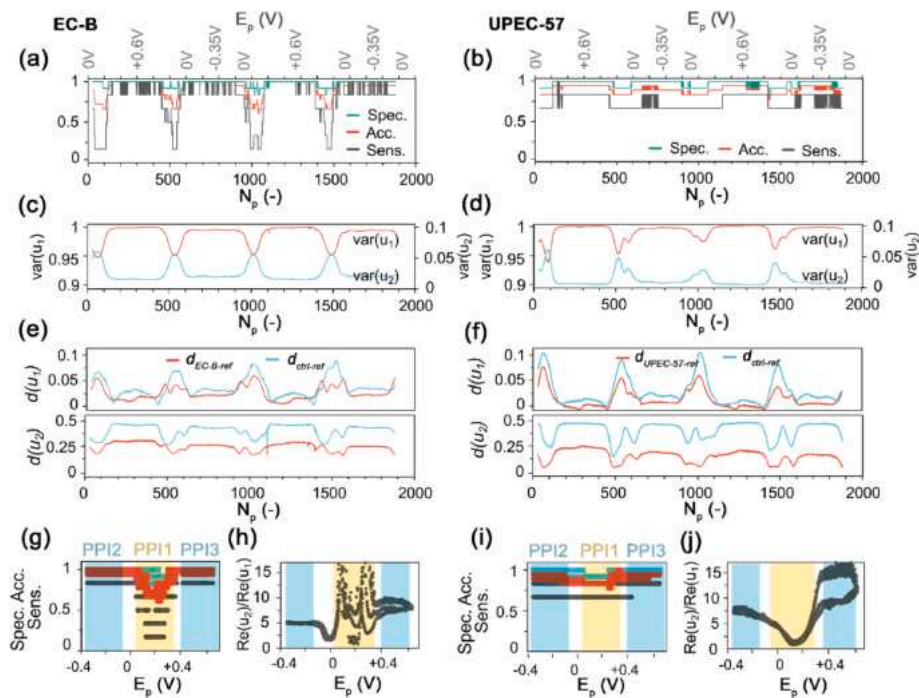
Fig. 3. Plot of specificity, accuracy and sensitivity as a function of N_p, for both (a) EC-B and (b) UPEC-57 datasets. Total variance explained by the first two columns of **U** for (c) EC-B and (d) UPEC-57. (e,f) Euclidean distance between the centroids given by the different test conditions, for u_1 and u_2. (g,i) plot of the specificity, accuracy and sensitivity as a function of E_p. (h,j) ratio between the real part of u_1 and u_2.

conditions:

1) **PPI1** (-0.1 V $< E_p < +0.3$ V). Interval in which the oxidation (or reduction) of the redox probe is not suitable for analyte detection.
2) **PPI2** ($E_p < -0.1$ V): Optimal interval for the bacteria detection, excluding the measurement performed close to the inversion potential. The Euclidean distance between the samples' (reference vs. control) centroids is slightly higher, suggesting better discrimination.
3) **PPI3** ($E_p > +0.4$ V): Suitable interval for the bacteria detection.

A conclusion may be drawn from the above analysis, suggesting that polarization with low overpotentials should be avoided due to its vicinity to the redox potential of the $[Fe(CN)]_6^{3-/4-}$ probe used in this study. The redox potentials may be subject to slight changes in-between particular experiments due to inevitable differences in the electric properties and, as an effect, the reversibility of the redox process at receptor-functionalized surfaces. This effect will exacerbate the accuracy and sensitivity drop of the biosensor when comparing results from many experiments. Identification of the decreased accuracy and sensitivity of the impedimetric analyses in **PPI1** is of paramount importance, since not only the redox potentials but also the formal potential E_F lies in the above interval. E_F is estimated based on anodic (E_a) and cathodic (E_c) voltammogram peaks, $E_F = (E_a - E_c)/2$ and is defined as the reduction potential applying to a half-reaction under a specific set of conditions, therefore it is typically considered to be electrode polarization conditions in the vast majority of impedimetric biosensor studies. The in-depth SVD analysis shown here suggests that the accuracy and sensitivity of EIS biosensors may be suboptimal at low overpotentials (**PPI1** polarization range). On the other hand, the necessity to meet the stationary condition in classic EIS studies makes it impossible to perform studies at higher anodic or cathodic overpotentials.

The cathodic (**PPI2**) or anodic (**PPI3**) overpotentials must be applied to efficiently distinguish between the control and positive samples. The detection may be related to diffusion-surface kinetic processes, since the contributions of frequencies in the low range are predominant (see SI file, Fig. S3, in particular the interval FI1 for frequencies below 20Hz), where studies by Settu et al. (2015) suggest a maximum relative changes measured at 10 Hz. At negative polarization potential, the same Re (u_2)/Re(u_1) ratio for both anodic and cathodic scan may suggests the existence of the same electrochemical behaviour, while, at positive polarization, the presence of an hysteresis loop may be indicator of two different behaviours for anodic and cathodic scans, as reported in Fig. 3h,j.

In light of the above considerations, Fig. 3e and f shows the distance between centroids for the first two columns of U, that the samples with real bacterial cultures find a place between the control and the reference. By using the same coefficients determined for the PLS-DA, the detection of UPEC-57 in artificial urine was performed, resulting in an averaged sensitivity, accuracy and specificity of 80, 90, 93% respectively, for the negative polarization interval (Fig. 3i). In general, the effect of electrode polarization potential on differentiating between the absence and presence of bacteria is more pronounced for EC-B than for UPEC-57. In particular, this is strongly penalized within the range bounded by the reduction and oxidation potentials of the redox probe; however, UPEC-57 is less affected (Fig. 3b). In conclusion, no significant differences in signal response were observed between EC-B and UPEC-57, which means that the proposed biosensor is not specific towards a given *E. coli* bacteria strain. Importantly, in the light of current diagnostic recommendations (Hay et al., 2016; Nicolle et al., 2019), the specificity of the method used to detect bacteria in the urine is not crucial. According to the medical dogma (Kass, 1962), the human urine of a healthy person should be sterile and UTI is typically thought to be caused by the presence of bacteria in the urine of a symptomatic patient.

3.3. UPEC-57 detection in real human urine

Detection in real media, such as human urine, is significantly more difficult compared to synthetic electrolytes, as it is characterized by chemical and biological diversity, containing up to 3000 different organic compounds and metabolites, including proteins, carbohydrates, and blood cells (Sarigul et al., 2019). To verify the utility of the developed methodology in the human urine environment, a procedure analogous to that described in the previous section was carried out. As expected, the studies in a real environment, with an unknown concentration of fouling agents, such as proteins and metabolites (Hanssen et al., 2016) led to a decrease in the averaged sensitivity, accuracy and specificity, now on the level of 83, 80 and 83%, respectively (averaged values at negative polarization potential) (Fig. 4a). When PLS regression was performed using t-SVD in real urine, **PPI2** was found to be superior to **PPI3** for UPEC-57 detection, see Fig. 4c and d, in the first polarization cycle, and that the sensing ability worsened with the increasing N_p. Indeed, after the first scan, it is possible to appreciate a loss in R^2, probably due to some irreversible processes taking place on the electrode surface (Fig. 4b).

The estimated LOD of UPEC-57 in human urine reaches 11.3 CFU/mL when studied at negative overpotentials of **PPI2** range. This result matches or surpasses most other available reports, while obtained using simple electrode surface architecture. A comparative study of different *E. coli* sensors in human urine is presented in Table 1, while electrochemical biosensors in other electrolytes are also given in the SI file, Table S3. Moreover, we have confirmed that the LOD of the method proposed here is 10x lower compared to the commonly used bacteria cultivation technique in which the detection of bacterial colonies is performed by plating of the bacterial solution onto Petri dishes with solid LA medium and overnight incubation. With this culture protocol, we were able to detect UPEC-57 bacteria in a solution that contained at least 10^2 bacterial cells per 1 mL (CFU/mL). The illustrative plates with bacterial colonies obtained by using the cultivation-based detection method are shown in Fig. 4f. For comparison, the proposed approach shows a limit of detection of 11.3 CFU/mL for the uropathogenic *E. coli* strain No. 57. Indeed, a similar LOD can be reached by using an enrichment procedure followed by molecular detection, however, this approach will take much more time (around 24 h) than the proposed by us method. On the other hand, our impedimetric analysis takes as little as 2 min, which results from polarization in the **PPI2** range (-0.35 to -0.10 V, with 2 mV/s), while no conditioning in real media was necessary.

It should be noted that, unlike in the artificial electrolyte, carrying out the analysis of several studied samples under deep anodic polarization have led to irreversible changes occurring at the biosensor surface. This process is associated with the accumulation of compounds present in urine (i.e. carbohydrates, proteins, and leukocytes) at the electrode surface, passivating it and blocking the electrode. In approx. 60% of these events, the surface passivation led to biosensor damage, as shown in Fig. 4e and SI file, Fig. S4. The voltammograms presented in the SI file, Fig. S5, reveal additional redox processes associated with the oxidation of uric acid. It should be noted that such behavior did not occur when the biosensor was subjected only to cathodic polarization in the **PPI2** range. Even when the passivation is incomplete, the above-described behavior explains the significantly lower biosensor accuracy when studied in the anodic polarization range, as shown in Fig. 4b, c and 4e.

The DEIS and PLS-DA approach provides valuable information about measurement conditions that could lead to electrode degradation, enabling users to take preventive measures. The analytical limits of any sensor can be adjusted to the individual needs by varying the applied polarization (in this case, **PPI2**) or frequency range. The utilization of adjusted frequency has been demonstrated to enhance sensor performance and improve the efficiency of machine learning algorithms, as previously observed (Kokabi et al., 2023; Xu and Hong, 2022). The
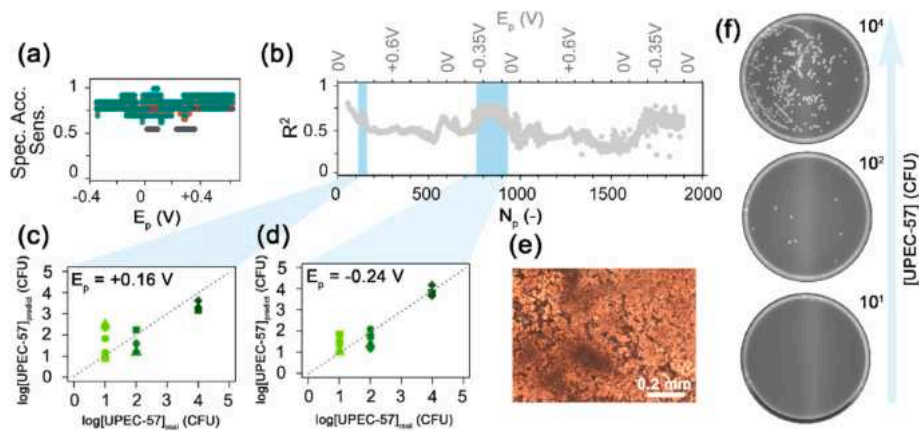
Fig. 4. Plot of (a) the specificity, accuracy and sensitivity and (b) R^2 as a function of E_p for UPEC-57 in real urine; difference between real and predicted values of UPEC-57 concentrations at (c) positive and (d) negative polarization potential; (e) optical microscope image of damaged surface; (f) illustrative plates with bacterial colonies obtained by using the cultivation-based detection method.

Table 1
E. coli LOD and detection time in real urine using different detection methods.

Detection method	Type of substrate	Detection time	LOD (CFU/ mL)	Ref.
Spectrofluorometry	Receptor-binding proteins on MNPs	1.5 h	$\sim10^7$	Costa et al. (2022)
PCR	Marker genes	1 h	10^4	Brons et al. (2020)
Bacteria cultivation	Bacterial colony number per 1 mL suspension	16–20 h	$\sim10^2$	This work
Electroporation	Segregation of nonreplicating plasmid pGTR902	22 min	10^2	Forsyth et al. (2018)
Microfluidic capillaric circuit	Antibody-functionalized microbeads	<7 min	120	Olanrewaju et al. (2017)
Fluorescence	Bacterial nuclease activity	1 h	<500	Flenker et al. (2017)
Fluorescence	Mannose-modified polyethyleneimine copolymer particles	$\sim$1 h[a]	265	Li et al. (2019)
CV-DPV	Au@MoS$_2$–PANI on GCE	30 min	10	Raj et al. (2021)
CV	PANI/AuNP composite on SPCE	$\sim$60 min[a]	4	Shoaie et al. (2018)
EIS	Interdigitated Au microelectrode	1–12 h	7	Settu et al. (2015)
LSV	Unspecified carbon electrode	35 min	24	Safavieh et al. (2012)
CV-DPV	rGO/ polyethyleneimine-modified Au	$\sim$35 min[a]	10	Jijie et al. (2018)
CV	Thionine dye (Th) on MWCNT/ chitosan coated on GCE	1 h	50	Gayathri et al. (2016)
MIDA	AuNC drop-cast on GCE	$\sim$2 min	11.3	This work

[a] information not available directly, the detection time is speculated based on the experimental steps provided.

utilization of Arduino microcontrollers enables the implementation of a multi-frequency approach, offering a user-friendly monitoring tool for therapy that can be easily operated by inexperienced individuals. (Merli et al., 2020; Murillo-Ortiz et al., 2020; Romero Coripuna et al., 2021; Wang, 2015).

A detailed understanding of the altered biosensor response depending on the applied overpotential is extremely difficult due to the complexity of the electrode surface, both in terms of the macromolecular structure and resultant, instantaneous surface charge distribution. To shed light on the role played by the charged-up electrode surface, we calculated the electrostatic potential based on the Poisson-Boltzmann equation for the macromolecules functionalized at the AuNC surface and conducted spectroscopic AFM studies of the proposed biosensors. Notably, neither the AuNC surface charge nor the solvent could be considered in these calculations. Fig. 5a shows a model of dsDNA attached covalently to AuNC and the RNAP. Since DNA bears a highly negative formal charge, due to the presence of negatively charged phosphate moieties linking neutral nucleosides, one can assume that upon oligonucleotide immobilization, the surface of the functionalized gold cubes becomes highly negative and remains negative upon DNA hybridization. On the other hand, RNAP is a complex system with some domains bearing a total negative and some positive charge, although most of the RNAP subunits have more negatively charged amino acids (D/E) than positively charged (K/R), resulting in a theoretical value of isoelectric points in the range of 4.5–5.2. In particular, the RNAP domain responsible for DNA binding is highly positive, so upon DNA binding, the DNA–protein complex is stabilized not only via specific van der Waals interactions and hydrogen bonds but also electrostatic interactions. Upon binding, the entire complex has an excess of negative charge and most of the protein domains binding DNA also become negatively charged due to the presence of dsDNA (Fig. 5b). However, our modeling predicts some RNAP domains (composed mostly of sub-unit alpha) that are positioned close to the gold surface, and that bear only a slightly negative electrostatic charge. As a result, upon RNAP binding, the electrostatic charge in the vicinity of the gold surface changes from highly negative to less negative/neutral, which is likely detected in the experimental setup.

The spectroscopic AFM mode is based on force imaging of the probe positioned on the sample surface, registering the change in the selected physical quantity. In this particular case, we registered the approach curves of the AFM probe to the functionalized electrode surface at electrode potentials falling in the **PPI1**, **PPI2** and **PPI3** range. The approach makes it possible to register the mechanical characteristics of dependence between the interaction force as a function of the probe–sample separation (Cappella and Dietler, 1999), where the process of transition between the non-contact and the contact mode of interaction can manifest via different shapes of the approach curves (Wu, 2010). In the first stage, the AFM probe approaches the surface, and when the attractive forces prevail over the spring constant of the lever, the probe jumps to a set-up position in the vicinity of the tested surface, marking the probe–sample distance, as illustrated in Fig. 5c. The AFM probe elongation, h, is inversely proportional to the thickness of the functionalized film. It should be noted, however, that neither the current
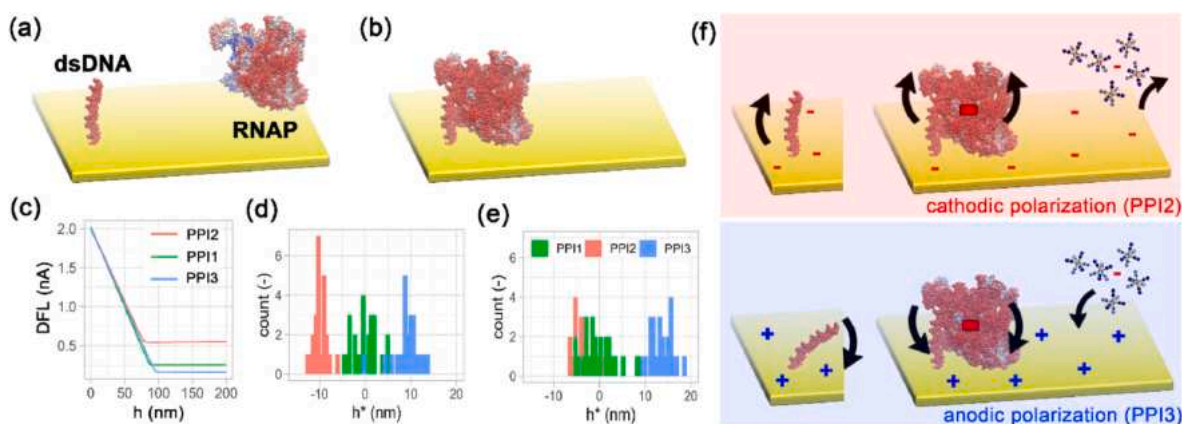
Fig. 5. (a) calculated electrostatic potential for DNA model on AuNC and RNAP sigma70 complex; and (b) RNAP-DNA complex model on AuNC. Red color corresponds to the negative electrostatic charge and blue color corresponds to the positive electrostatic charge; the more intensive the color, the stronger the negative/positive charge. (c) Exemplary AFM approach curve for the dsDNA functionalized Au_ref sample; piezoelectric elongation of: (d) Au_ref and (e) Au_ctrl at various electrode polarizations. (f,g) Scheme of coulombic forces between the functionalization film and the AuNC substrate, affecting charge transfer process at differently polarized electrode surface.

deflection of the AFM probe nor the current height of the sample at the contact point is known *a priori*, thus the approach curves provide only an indirect measure of changes in the conformation of the studied system depending on the applied polarization potential. Therefore, the probe–sample distance was normalized, setting the sample studied in the **PPI1** range as the reference ($h^* = 0$). The h^* value should be considered in terms of changes in the strength of interatomic interactions between the macromolecules and the atoms of the microscope tip. Fig. 5d shows the results of a statistical analysis from 25 approach curves to the Au_ref electrode surface. When these data are taken only in the context of changes in the conformation of the macromolecular film at the electrode surface, it can be concluded that polarization in the anodic **PPI2** range reduces the film thickness (compared to **PPI1**), while polarization in the cathodic direction (**PPI3**) causes the opposite effect. Similar changes in the orientation of dsDNA in the electric field were reported previously (Meunier et al., 2015; Niedzialkowski et al., 2020). The final effect on the macromolecule's conformation is visible upon RNAP interaction with the dsDNA at the electrode surface, as in Au_ctrl (Fig. 5e). The presence of coulombic repulsion between a negatively charged RNAP-DNA complex and the negatively charged electrode surface (**PPI2**) produces a similar effect to the one discussed above, but the h^* decrease is much smaller, possibly due to the steric hindrance effects by the RNAP-DNA complex.

The processes discussed may have a multidimensional influence on the measured impedimetric parameters. The most commonly used indicator, R_{CT}, will notably increase upon RNAP-DNA interaction, developing the functionalized layer thickness, and hindering the diffusion of the negatively charged ferrocyanide redox probe. It should also be noted that the higher the functionalized layer thickness, the smaller the measured capacitance. The change in electrode conformation has an immediate effect on the frequency dispersion of the capacitance, as previously discussed (Niedzialkowski et al., 2020). The effect of electrode polarization under **PPI2** and **PPI3** conditions is schematically illustrated in Fig. 5f, suggesting a possible mechanism of molecular interactions in the electric field that allows one to distinguish the impedimetric signal in the presence and in the absence of the RNAP. Due to the complexity of the studied interphase, however, any experimental or simulation technique will provide an impaired and incomplete interpretation of the studied process. Nevertheless, the combined DEIS with PLS-DA approach makes it possible to effectively identify the unique impedimetric fingerprint of the biosensor studied.

4. Conclusions

We proposed a new methodology for biosensor operation, which utilizes real-time impedimetric monitoring combined with partial least squares discriminant analysis. The principle of its operation is to distinguish the presence of the analyte not only by strong intermolecular forces but also by weak coulombic forces, when measured under different polarization conditions, to obtain the explicit impedimetric fingerprint of the macromolecular interactions.

As a proof-of-concept of the methodology, we selected the aptameric recognition of RNAP for two different *E. coli* strains, including uropathogenic UPEC-57. The approach discriminates the presence of the analyte at very low concentrations directly in the real human urine environment, despite the presence of an unknown amount and concentration of fouling agents. The impedimetric analysis was carried out on raw data, without fitting with electric equivalent circuits. The study revealed that the detection is most accurate at negative overpotentials (-0.35 to -0.10 V vs Ag/AgCl), where the interaction between negatively charged $[Fe(CN)]_6^{3-/4-}$ species and negatively charged RNAP-DNA complexes at AuNC should result in the increase of charge transfer resistance and introduce frequency dispersion of capacitance effects. Our study shows the capability of UPEC-57 identification with a LOD reaching 11.3 CFU/mL after only 2 min and using a simple glassy carbon electrode architecture with drop-cast, self-organizing Au nanocube patterns. Although there are differences between the data collected for EC-B and UPEC-57, the biosensor is not capable of distinguishing between two strains of *E. coli*.

CRediT authorship contribution statement

Adrian Koterwa: Validation, Formal analysis, Investigation, Data curation. **Mattia Pierpaoli:** Methodology, Software, Validation, Formal analysis, Investigation, Data curation, Writing – original draft, Visualization. **Bożena Nejman-Faleńczyk:** Methodology, Writing – original draft, Writing – review & editing. **Sylwia Bloch:** Validation, Investigation, Writing – original draft. **Artur Zieliński:** Investigation, Writing – original draft. **Wioletta Adamus-Białek:** Resources, Writing – review & editing. **Zofia Jeleniewska:** Investigation, Writing – original draft. **Bartosz Trzaskowski:** Formal analysis, Writing – original draft, Writing – review & editing, Visualization. **Robert Bogdanowicz:** Conceptualization, Writing – original draft, Writing – review & editing. **Grzegorz Węgrzyn:** Resources, Writing – review & editing. **Paweł Niedziałkowski:** Methodology, Investigation, Resources, Writing – original draft, Writing – review & editing, Supervision. **Jacek Ryl:** Conceptualization,

Methodology, Investigation, Writing – original draft, Writing – review & editing, Visualization, Supervision, Funding acquisition.

Declaration of competing interest

The authors declare that they have no known competing financial interests or personal relationships that could have appeared to influence the work reported in this paper.

Data availability

Data will be made available on request.

Appendix A. Supplementary data

Supplementary data to this article can be found online at https://doi.org/10.1016/j.bios.2023.115561.

References

Abedi, R., Bakhsh Raoof, J., Bagheri Hashkavayi, A., Asghary, M., 2021. Highly sensitive and label-free electrochemical biosensor based on gold nanostructures for studying the interaction of prostate cancer gene sequence with epirubicin anti-cancer drug. Microchem. J. 170, 106668 https://doi.org/10.1016/j.microc.2021.106668.

Aitekenov, S., Gaipov, A., Bukasov, R., 2021. Review: detection and quantification of proteins in human urine. Talanta 223, 121718. https://doi.org/10.1016/j.talanta.2020.121718.

Ali, M.R., Bacchu, M.S., Setu, M.A.A., Akter, S., Hasan, M.N., Chowdhury, F.T., Rahman, M.M., Ahommed, M.S., Khan, M.Z.H., 2021. Development of an advanced DNA biosensor for pathogenic Vibrio cholerae detection in real sample. Biosens. Bioelectron. 188, 113338 https://doi.org/10.1016/j.bios.2021.113338.

Bae, B., Feklistov, A., Lass-Napiorkowska, A., Landick, R., Darst, S.A., 2015. Structure of a bacterial RNA polymerase holoenzyme open promoter complex. Elife 4, e08504. https://doi.org/10.7554/eLife.08504.

Bhattacharjee, G., Majumder, S., Senapati, D., Banerjee, S., Satpati, B., 2020. Core-shell gold @silver hollow nanocubes for higher SERS enhancement and non-enzymatic biosensor. Mater. Chem. Phys. 239, 122113 https://doi.org/10.1016/j.matchemphys.2019.122113.

Brodowski, M., Pierpaoli, M., Janik, M., Kowalski, M., Ficek, M., Slepski, P., Trzaskowski, B., Swain, G., Ryl, J., Bogdanowicz, R., 2022. Enhanced susceptibility of SARS-CoV-2 spike RBD protein assay targeted by cellular receptors ACE2 and CD147: multivariate data analysis of multisine impedimetric response. Sensor. Actuator. B Chem. 370, 132427 https://doi.org/10.1016/j.snb.2022.132427.

Brons, J.K., Vink, S.N., de Vos, M.G.J., Reuter, S., Dobrindt, U., van Elsas, J.D., 2020. Fast identification of Escherichia coli in urinary tract infections using a virulence gene based PCR approach in a novel thermal cycler. J. Microbiol. Methods 169, 105799. https://doi.org/10.1016/j.mimet.2019.105799.

Cappella, B., Dietler, G., 1999. Force-distance curves by atomic force microscopy. Surf. Sci. Rep. 34, 1–104. https://doi.org/10.1016/S0167-5729(99)00003-5.

Chapman, C.A.R., Chen, H., Stamou, M., Biener, J., Biener, M.M., Lein, P.J., Seker, E., 2015. Nanoporous gold as a neural interface coating: effects of topography, surface chemistry, and feature size. ACS Appl. Mater. Interfaces 7, 7093–7100. https://doi.org/10.1021/acsami.5b00410.

Chen, F., Tang, Q., Ma, T., Zhu, B., Wang, L., He, C., Luo, X., Cao, S., Ma, L., Cheng, C., 2022. Structures, properties, and challenges of emerging 2D materials in bioelectronics and biosensors. InfoMat 4. https://doi.org/10.1002/inf2.12299.

Cimafonte, M., Fulgione, A., Gaglione, R., Papaianni, M., Capparelli, R., Arciello, A., Bolletti Censi, S., Borriello, G., Velotta, R., Della Ventura, B., 2020. Screen printed based impedimetric immunosensor for rapid detection of Escherichia coli in drinking water. Sensors 20, 274. https://doi.org/10.3390/s20010274.

Clock, S.A., Planet, P.J., Perez, B.A., Figurski, D.H., 2008. Outer membrane components of the tad (tight adherence) secreton of Aggregatibacter actinomycetemcomitans. J. Bacteriol. 190, 980–990. https://doi.org/10.1128/JB.01347-07.

Costa, S.P., Cunha, A.P., Freitas, P.P., Carvalho, C.M., 2022. A phage receptor-binding protein as a promising tool for the detection of Escherichia coli in human specimens. Front. Microbiol. 13, 871855 https://doi.org/10.3389/fmicb.2022.871855.

Davenport, M., Mach, K.E., Shortliffe, L.M.D., Banaei, N., Wang, T.-H., Liao, J.C., 2017. New and developing diagnostic technologies for urinary tract infections. Nat. Rev. Urol. 14, 296–310. https://doi.org/10.1038/nrurol.2017.20.

Deshmukh, R., Prusty, A.K., Roy, U., Bhand, S., 2020. A capacitive DNA sensor for sensitive detection of Escherichia coli O157:H7 in potable water based on the z3276 genetic marker: fabrication and analytical performance. Analyst 145, 2267–2278. https://doi.org/10.1039/C9AN02291K.

Dwivedi, N., Yeo, R.J., Satyanarayana, N., Kundu, S., Tripathy, S., Bhatia, C.S., 2015. Understanding the role of nitrogen in plasma-assisted surface modification of magnetic recording media with and without ultrathin carbon overcoats. Sci. Rep. 5, 7772. https://doi.org/10.1038/srep07772.

Emilsson, G., Schoch, R.L., Feuz, L., Höök, F., Lim, R.Y.H., Dahlin, A.B., 2015. Strongly stretched protein resistant poly(ethylene glycol) brushes prepared by grafting-to. ACS Appl. Mater. Interfaces 7, 7505–7515. https://doi.org/10.1021/acsami.5b01590.

Felix, F.S., Angnes, L., 2018. Electrochemical immunosensors – a powerful tool for analytical applications. Biosens. Bioelectron. 102, 470–478. https://doi.org/10.1016/j.bios.2017.11.029.

Flenker, K.S., Burghardt, E.L., Dutta, N., Burns, W.J., Grover, J.M., Kenkel, E.J., Weaver, T.M., Mills, J., Kim, H., Huang, L., Owczarzy, R., Musselman, C.A., Behlke, M.A., Ford, B., McNamara, J.O., 2017. Rapid detection of urinary tract infections via bacterial nuclease activity. Mol. Ther. 25, 1353–1362. https://doi.org/10.1016/j.ymthe.2017.03.015.

Flores-Mireles, A.L., Walker, J.N., Caparon, M., Hultgren, S.J., 2015. Urinary tract infections: epidemiology, mechanisms of infection and treatment options. Nat. Rev. Microbiol. 13, 269–284. https://doi.org/10.1038/nrmicro3432.

Forsyth, V.S., Armbruster, C.E., Smith, S.N., Pirani, A., Springman, A.C., Walters, M.S., Nielubowicz, G.R., Himpsl, S.D., Snitkin, E.S., Mobley, H.L.T., 2018. Rapid growth of uropathogenic Escherichia coli during human urinary tract infection. mBio 9, e00186. https://doi.org/10.1128/mBio.00186-18. -18.

Frimodt-Møller, N., 2019. The urine microbiome – contamination or a novel paradigm? EBioMedicine 44, 20–21. https://doi.org/10.1016/j.ebiom.2019.05.016.

Gayathri, C.H., Mayuri, P., Sankaran, K., Kumar, A.S., 2016. An electrochemical immunosensor for efficient detection of uropathogenic E. coli based on thionine dye immobilized chitosan/functionalized-MWCNT modified electrode. Biosens. Bioelectron. 82, 71–77. https://doi.org/10.1016/j.bios.2016.03.062.

Glyde, R., Ye, F., Darbari, V.C., Zhang, N., Buck, M., Zhang, X., 2017. Structures of RNA polymerase closed and intermediate complexes reveal mechanisms of DNA opening and transcription initiation. Mol. Cell 67, 106–116.e4. https://doi.org/10.1016/j.molcel.2017.05.010.

Grine, G., Lotte, R., Chirio, D., Chevalier, A., Raoult, D., Drancourt, M., Ruimy, R., 2019. Co-culture of Methanobrevibacter smithii with enterobacteria during urinary infection. EBioMedicine 43, 333–337. https://doi.org/10.1016/j.ebiom.2019.04.037.

Gui, A.L., Luais, E., Peterson, J.R., Gooding, J.J., 2013. Zwitterionic phenyl layers: finally, stable, anti-biofouling coatings that do not passivate electrodes. ACS Appl. Mater. Interfaces 5, 4827–4835. https://doi.org/10.1021/am400519m.

Güner, A., Çevik, E., Şenel, M., Alpsoy, L., 2017. An electrochemical immunosensor for sensitive detection of Escherichia coli O157:H7 by using chitosan, MWCNT, polypyrrole with gold nanoparticles hybrid sensing platform. Food Chem. 229, 358–365. https://doi.org/10.1016/j.foodchem.2017.02.083.

Hanssen, B.L., Siraj, S., Wong, D.K.Y., 2016. Recent strategies to minimise fouling in electrochemical detection systems. Rev. Anal. Chem. 35, 1–28. https://doi.org/10.1515/revac-2015-0008.

Hay, A.D., Birnie, K., Busby, J., Delaney, B., Downing, H., Dudley, J., Durbaba, S., Fletcher, M., Harman, K., Hollingworth, W., Hood, K., Howe, R., Lawton, M., Lisles, C., Little, P., MacGowan, A., O'Brien, K., Pickles, T., Rumsby, K., Sterne, J.A., Thomas-Jones, E., Van Der Voort, J., Waldron, C.-A., Whiting, P., Wootton, M., Butler, C.C., on behalf of the DUTY team, 2016. The Diagnosis of Urinary Tract infection in Young children (DUTY): a diagnostic prospective observational study to derive and validate a clinical algorithm for the diagnosis of urinary tract infection in children presenting to primary care with an acute illness. Health Technol. Assess. 20, 1–294. https://doi.org/10.3310/hta20510.

Jijie, R., Kahlouche, K., Barras, A., Yamakawa, N., Bouckaert, J., Gharbi, T., Szunerits, S., Boukherroub, R., 2018. Reduced graphene oxide/polyethylenimine based immunosensor for the selective and sensitive electrochemical detection of uropathogenic Escherichia coli. Sensor. Actuator. B Chem. 260, 255–263. https://doi.org/10.1016/j.snb.2017.12.169.

Kass, E.H., 1962. Pyelonephritis and bacteriuria: a major problem in preventive medicine. Ann. Intern. Med. 56, 46. https://doi.org/10.7326/0003-4819-56-1-46.

Klein, R.D., Hultgren, S.J., 2020. Urinary tract infections: microbial pathogenesis, host–pathogen interactions and new treatment strategies. Nat. Rev. Microbiol. 18, 211–226. https://doi.org/10.1038/s41579-020-0324-0.

Kokabi, M., Sui, J., Gandotra, N., Pournadali Khamseh, A., Scharfe, C., Javanmard, M., 2023. Nucleic acid quantification by multi-frequency impedance cytometry and machine learning. Biosensors 13, 316. https://doi.org/10.3390/bios13030316.

Laomeephol, C., Ferreira, H., Yodmuang, S., Reis, R.L., Damrongsakkul, S., Neves, N.M., 2020. Exploring the gelation mechanisms and cytocompatibility of gold (III)-Mediated regenerated and thiolated silk fibroin hydrogels. Biomolecules 10, 466. https://doi.org/10.3390/biom10030466.

Li, J., Li, B., Liu, M., 2019. One-step synthesis of mannose-modified polyethyleneimine copolymer particles as fluorescent probes for the detection of Escherichia coli. Sensor. Actuator. B Chem. 280, 171–176. https://doi.org/10.1016/j.snb.2018.10.018.

Lu, M., Cao, C., Wang, F., Liu, G., 2021. A polyethyleneimine reduced graphene oxide/gold nanocubes based electrochemical aptasensor for chloramphenicol detection using single-stranded DNA-binding protein. Mater. Des. 199, 109409 https://doi.org/10.1016/j.matdes.2020.109409.

Merli, P., Furnari, R., Fadda, M., De Francesco, A., McConnell, R., Massazza, G., 2020. Role of bioelectrical impedance analysis in the evaluation of patients with upper limb lymphedema. Lymphatic Res. Biol. 18, 555–559. https://doi.org/10.1089/lrb.2019.0085.

Meunier, A., Triffaux, E., Bizzotto, D., Buess-Herman, C., Doneux, T., 2015. In situ fluorescence microscopy study of the interfacial inhomogeneity of DNA mixed self-assembled monolayers at gold electrodes. Chemelectrochem 2, 434–442. https://doi.org/10.1002/celc.201402273.

Murillo-Ortiz, B., Hernández-Ramírez, A., Rivera-Villanueva, T., Suárez-García, D., Murguía-Pérez, M., Martínez-Garza, S., Rodríguez-Penin, A., Romero-Coripuna, R., López-Partida, X.M., 2020. Monofrequency electrical impedance mammography (EIM) diagnostic system in breast cancer screening. BMC Cancer 20, 876. https://doi.org/10.1186/s12885-020-07283-5.

Nicolle, L.E., Gupta, K., Bradley, S.F., Colgan, R., DeMuri, G.P., Drekonja, D., Eckert, L.O., Geerlings, S.E., Köves, B., Hooton, T.M., Juthani-Mehta, M., Knight, S.L., Saint, S., Schaeffer, A.J., Trautner, B., Wullt, B., Siemieniuk, R., 2019. Clinical practice guideline for the management of asymptomatic bacteriuria: 2019 update by the infectious diseases society of americaa. Clin. Infect. Dis. https://doi.org/10.1093/cid/ciy1121.

Niedzialkowski, P., Koterwa, A., Olejnik, A., Zielinski, A., Gornicka, K., Brodowski, M., Bogdanowicz, R., Ryl, J., 2022. Deciphering the molecular mechanism of substrate-induced assembly of gold nanocube arrays toward an accelerated electrocatalytic effect employing heterogeneous diffusion field confinement. Langmuir 38, 9597–9610. https://doi.org/10.1021/acs.langmuir.2c01001.

Niedzialkowski, P., Slepski, P., Wysocka, J., Chamier-Cieminska, J., Burczyk, L., Sobaszek, M., Wcislo, A., Ossowski, T., Bogdanowicz, R., Ryl, J., 2020. Multisine impedimetric probing of biocatalytic reactions for label-free detection of DEFB1 gene: how to verify that your dog is not human? Sensor. Actuator. B Chem. 323, 128664 https://doi.org/10.1016/j.snb.2020.128664.

Olanrewaju, A.O., Ng, A., DeCorwin-Martin, P., Robillard, A., Juncker, D., 2017. Microfluidic capillaric circuit for rapid and facile bacteria detection. Anal. Chem. 89, 6846–6853. https://doi.org/10.1021/acs.analchem.7b01315.

Pandey, C.M., Tiwari, I., Singh, V.N., Sood, K.N., Sumana, G., Malhotra, B.D., 2017. Highly sensitive electrochemical immunosensor based on graphene-wrapped copper oxide-cysteine hierarchical structure for detection of pathogenic bacteria. Sensor. Actuator. B Chem. 238, 1060–1069. https://doi.org/10.1016/j.snb.2016.07.121.

Park, J.-E., Lee, Y., Nam, J.-M., 2018. Precisely shaped, uniformly formed gold nanocubes with ultrahigh reproducibility in single-particle scattering and surface-enhanced Raman scattering. Nano Lett. 18, 6475–6482. https://doi.org/10.1021/acs.nanolett.8b02973.

Passiu, C., Rossi, A., Weinert, M., Tysoe, W., Spencer, N.D., 2020. Probing the outermost layer of thin gold films by XPS and density functional theory. Appl. Surf. Sci. 507, 145084 https://doi.org/10.1016/j.apsusc.2019.145084.

Pierpaoli, M., Lewkowicz, A., Dec, B., Nadolska, M., Bogdanowicz, R., 2022. Impedimetric sensing of α-amino acids driven by micro-patterned 1,8-Diazafluoren-9-one into titania- boron- doped maze-like nanocarbons. Sensor. Actuator. B Chem. 371, 132459 https://doi.org/10.1016/j.snb.2022.132459.

Price, T.K., Dune, T., Hilt, E.E., Thomas-White, K.J., Kliethermes, S., Brincat, C., Brubaker, L., Wolfe, A.J., Mueller, E.R., Schreckenberger, P.C., 2016. The clinical urine culture: enhanced techniques improve detection of clinically relevant microorganisms. J. Clin. Microbiol. 54, 1216–1222. https://doi.org/10.1128/JCM.00044-16.

Qu, J., Yuan, J., Wang, C., Wang, A., Liu, X., Wei, B., Wen, Y., 2019. Enhancing the redispersibility of TEMPO-mediated oxidized cellulose nanofibrils in N,N-dimethylformamide by modification with cetyltrimethylammonium bromide. Cellulose 26, 7769–7780. https://doi.org/10.1007/s10570-019-02655-y.

Raj, P., Oh, M.H., Han, K., Lee, T.Y., 2021. Label-Free electrochemical biosensor based on Au@MoS₂–PANI for Escherichia coli detection. Chemosensors 9, 49. https://doi.org/10.3390/chemosensors9030049.

Romero Coripuna, R., Hernandez Farias, D.I., Murillo Ortiz, B.O., Padierna, L.C., Fraga, T.C., 2021. Machine learning for the analysis of conductivity from mono frequency electrical impedance mammography as a breast cancer risk factor. IEEE Access 9, 152397–152407. https://doi.org/10.1109/ACCESS.2021.3122948.

Russo, M.J., Han, M., Desroches, P.E., Manasa, C.S., Dennaoui, J., Quigley, A.F., Kapsa, R.M.I., Moulton, S.E., Guijt, R.M., Greene, G.W., Silva, S.M., 2021. Antifouling strategies for electrochemical biosensing: mechanisms and performance toward point of care based diagnostic applications. ACS Sens. 6, 1482–1507. https://doi.org/10.1021/acssensors.1c00390.

Safavieh, M., Ahmed, M.U., Tolba, M., Zourob, M., 2012. Microfluidic electrochemical assay for rapid detection and quantification of Escherichia coli. Biosens. Bioelectron. 31, 523–528. https://doi.org/10.1016/j.bios.2011.11.032.

Sarigul, N., Korkmaz, F., Kurultak, İ., 2019. A new artificial urine protocol to better imitate human urine. Sci. Rep. 9, 20159 https://doi.org/10.1038/s41598-019-56693-4.

Settu, K., Chen, C.-J., Liu, J.-T., Chen, C.-L., Tsai, J.-Z., 2015. Impedimetric method for measuring ultra-low E. coli concentrations in human urine. Biosens. Bioelectron. 66, 244–250. https://doi.org/10.1016/j.bios.2014.11.027.

Shah Utsav, S., Subramaniam, V., Tamhankar Ashwin, S., 2021. Microbiome studies in urology- where do we stand and where can we reach? Indian J. Med. Microbiol. 39, 98–103. https://doi.org/10.1016/j.ijmmb.2020.10.009.

Shahrokhian, S., Ranjbar, S., 2018. Aptamer immobilization on amino-functionalized metal–organic frameworks: an ultrasensitive platform for the electrochemical diagnostic of Escherichia coli O157:H7. Analyst 143, 3191–3201. https://doi.org/10.1039/C8AN00725J.

Sharifi, M., Avadi, M.R., Attar, F., Dashtestani, F., Ghorchian, H., Rezayat, S.M., Saboury, A.A., Falahati, M., 2019. Cancer diagnosis using nanomaterials based electrochemical nanobiosensors. Biosens. Bioelectron. 126, 773–784. https://doi.org/10.1016/j.bios.2018.11.026.

Shoaie, N., Forouzandeh, M., Omidfar, K., 2018. Voltammetric determination of the Escherichia coli DNA using a screen-printed carbon electrode modified with polyaniline and gold nanoparticles. Microchim. Acta 185, 217. https://doi.org/10.1007/s00604-018-2749-y.

Silva-Moraes, M.O., Garcia-Basabe, Y., de Souza, R.F.B., Mota, A.J., Passos, R.R., Galante, D., Fonseca Filho, H.D., Romaguera-Barcelay, Y., Rocco, M.L.M., Brito, W.R., 2018. Geometry-dependent DNA-TiO2 immobilization mechanism: a spectroscopic approach. Spectrochim. Acta Mol. Biomol. Spectrosc. 199, 349–355. https://doi.org/10.1016/j.saa.2018.03.081.

Singhal, C., Dubey, A., Mathur, A., Pundir, C.S., Narang, J., 2018. Paper based DNA biosensor for detection of chikungunya virus using gold shells coated magnetic nanocubes. Process Biochem. 74, 35–42. https://doi.org/10.1016/j.procbio.2018.08.020.

Sun, Q., Yan, F., Yao, L., Su, B., 2016. Anti-biofouling isoporous silica-micelle membrane enabling drug detection in human whole blood. Anal. Chem. 88, 8364–8368. https://doi.org/10.1021/acs.analchem.6b02091.

Van Stralen, K.J., Stel, V.S., Reitsma, J.B., Dekker, F.W., Zoccali, C., Jager, K.J., 2009. Diagnostic methods I: sensitivity, specificity, and other measures of accuracy. Kidney Int. 75, 1257–1263. https://doi.org/10.1038/ki.2009.92.

Velayudham, J., Magudeeswaran, V., Paramasivam, S.S., Karruppaya, G., Manickam, P., 2021. Hydrogel-aptamer nanocomposite based electrochemical sensor for the detection of progesterone. Mater. Lett. 305, 130801 https://doi.org/10.1016/j.matlet.2021.130801.

Vitale, F., Fratoddi, I., Battocchio, C., Piscopiello, E., Tapfer, L., Russo, M.V., Polzonetti, G., Giannini, C., 2011. Mono- and bi-functional arenethiols as surfactants for gold nanoparticles: synthesis and characterization. Nanoscale Res. Lett. 6, 103. https://doi.org/10.1186/1556-276X-6-103.

Wang, H., Zhao, Y., Bie, S., Suo, T., Jia, G., Liu, B., Ye, R., Li, Z., 2019. Development of an electrochemical biosensor for rapid and effective detection of pathogenic Escherichia coli in licorice extract. Appl. Sci. 9, 295. https://doi.org/10.3390/app9020295.

Wang, J., 2015. Design and Implementation of an Impedance Analyzer Based on Arduino Uno.

Wang, R., Lum, J., Callaway, Z., Lin, J., Bottje, W., Li, Y., 2015. A label-free impedance immunosensor using screen-printed interdigitated electrodes and magnetic nanobeads for the detection of E. coli O157:H7. Biosensors 5, 791–803. https://doi.org/10.3390/bios5040791.

Wang, Y., Fewins, P.A., Alocilja, E.C., 2015. Electrochemical immunosensor using nanoparticle-based signal enhancement for Escherichia coli O157:H7 detection. IEEE Sensor. J. 15, 4692–4699. https://doi.org/10.1109/JSEN.2015.2396036.

Wu, J.-J., 2010. The jump-to-contact distance in atomic force microscopy measurement. J. Adhes. 86, 1071–1085. https://doi.org/10.1080/00218464.2010.519256.

Wu, S., Su, F., Dong, X., Ma, C., Pang, L., Peng, D., Wang, M., He, L., Zhang, Z., 2017. Development of glucose biosensors based on plasma polymerization-assisted nanocomposites of polyaniline, tin oxide, and three-dimensional reduced graphene oxide. Appl. Surf. Sci. 401, 262–270. https://doi.org/10.1016/j.apsusc.2017.01.024.

Xiao, T., Huang, J., Wang, D., Meng, T., Yang, X., 2020. Au and Au-Based nanomaterials: synthesis and recent progress in electrochemical sensor applications. Talanta 206, 120210. https://doi.org/10.1016/j.talanta.2019.120210.

Xu, J., Hong, Z., 2022. Low power bio-impedance sensor interfaces: review and electronics design methodology. IEEE Rev. Biomed. Eng. 15, 23–35. https://doi.org/10.1109/RBME.2020.3041053.

Xu, M., Wang, R., Li, Y., 2016. Rapid detection of Escherichia coli O157:H7 and Salmonella Typhimurium in foods using an electrochemical immunosensor based on screen-printed interdigitated microelectrode and immunomagnetic separation. Talanta 148, 200–208. https://doi.org/10.1016/j.talanta.2015.10.082.

Yang, D., Wang, J., Cao, Y., Tong, X., Hua, T., Qin, R., Shao, Y., 2023. Polyaniline-based biological and chemical sensors: sensing mechanism, configuration design, and perspective. ACS Appl. Electron. Mater. 5, 593–611. https://doi.org/10.1021/acsaelm.2c01405.

Zhou, M., Zhai, Y., Dong, S., 2009. Electrochemical sensing and biosensing platform based on chemically reduced graphene oxide. Anal. Chem. 81, 5603–5613. https://doi.org/10.1021/ac900136z.

Supporting information

for

Discriminating Macromolecular Interactions Based on an Impedimetric Fingerprint Supported by Multivariate Data Analysis for Rapid and Label-free *Escherichia coli* Recognition in Human Urine

Adrian Koterwa[1,#], Mattia Pierpaoli[2,#], Bożena Nejman-Faleńczyk[3], Sylwia Bloch[3], Artur Zieliński[4], Wioletta Adamus-Białek[5], Zofia Jeleniewska[6], Bartosz Trzaskowski[7], Robert Bogdanowicz[2], Grzegorz Węgrzyn[3], Paweł Niedziałkowski[1,*], Jacek Ryl[6,*]

[1] Department of Analytic Chemistry, University of Gdańsk, Wita Stwosza 63, 80-308 Gdańsk, Poland

[2] Department of Metrology and Optoelectronics, Gdańsk University of Technology, Narutowicza 11/12, 80-233 Gdańsk, Poland

[3] Department of Molecular Biology, Faculty of Biology, University of Gdansk, Wita Stwosza 59, 80-308, Poland

[4] Faculty of Chemistry, Gdańsk University of Technology, Narutowicza 11/12, 80-233 Gdańsk, Poland

[5] Institute of Medical Sciences, Jan Kochanowski University, IX Wieków Kielc 19a, 25-516 Kielce, Poland.

[6] Division of Electrochemistry and Surface Physical Chemistry, Faculty of Applied Physics and Mathematics, Gdańsk University of Technology, Narutowicza 11/12, Gdańsk, 80-233, Poland

[7] Centre of New Technologies, University of Warsaw, Banach 2c, 02-097 Warsaw, Poland

* Corresponding authors: jacek.ryl@pg.edu.pl (J.R.) pawel.niedzialkowski@ug.edu.pl (P.N.)

# These authors contributed equally to this work

1. The AuNCs synthesis procedure.

The synthesis of AuNCs consists of two independent processes, the first involves the synthesis of Au nanoparticles (Au seeds), while the second process is the AuNCs growth. The Au nanoparticles were obtained in a round bottom flask, where initially 0.125 mL of 0.01 M $HAuCl_4 \cdot 4H_2O$ in 3.75 mL of 0.1 M CTAB was dissolved. Then 0.3 mL of 0.01 M $NaBH_4$ was added. The solution was stirred at room temperature for 12 h before use.

In the second step, the AuNCs were grown. This was achieved adding 6.4 mL of 0.1 M CTAB, 0.8 mL of 0.01 M $HAuCl_4 \cdot 4H_2O$, and 3.8 mL of 0.1 M ascorbic acid. Next, 30 µL of previously obtained Au seeds was added and diluted 10-fold. Next, the solution was mixed using a vortex mixer for 30 s, and left overnight. The obtained AuNCs were twice centrifuged (5000 rpm, 20 min) before use and dissolved in a 0.001 M CTAB solution. The obtained AuNCs were stored in a room temperature in 0.001 M CTAB solution.

2. Detail on bacterial strain growth conditions and preparation of bacterial suspension

The antibiogram report indicates that strain UPEC-57 is resistant to five agents: ampicillin, ampicillin with sulbactam, amoxicillin with clavulanic acid, piperacillin-tazobactam, and cefuroxime and, in turn, sensitive to ceftazidime, cefotaxime, cefepime, meropenem, ertapenem, imipenem, aztreonam, norfloxacin, tobramycin, ciprofloxacin, nitrofurantoin, trimethoprim-sulfamethoxazole. Furthermore, a test result indicates an intermediate susceptibility of the UPEC-57 strain to amikacin and gentamicin. Moreover, the strain has all tested virulence factors, the CRISPR3, and CRISPR4 regions, and belongs to the B2 phylogenetic group. The detection of CRISPR regions 1-4 was performed according to the protocol described elsewhere (Dang et al., 2013). Briefly, multiplex-PCRs were performed with bacterial DNA (approx. 20 ng) in a 25 µl reaction mixture containing a 12.5 µl DreamTaq™ Green DNA Polymerase Master Mix (2x) (ThermoFisher Scientific™) and 10 pmol of each primer (oligo.pl) and refilled with MiliQ water. After electrophoresis on 2% agarose gel, the PCR products were visualized under UV light. The six virulence factor genes: *papC sfaD/sfaE*, *cnf1*, *usp*, *fimG/H*, *hlyA* coding for respectively: the chaperon usher protein pyelonephritis-associated pili, S fimbrial adhesins, cytotoxic necrotizing factor, uropathogenic-specific protein Usp, type 1 fimbrin D-mannose specific adhesin and α-hemolysin, were identified according to the protocol described by Adamus-Bialek et al

(Adamus-Bialek et al., 2009). The analysis of the phylogenetic groups (A, B1, B2, D, F, C, E, and other clades) was performed according to the method of Clermont et al. (Clermont et al., 2013).

Overnight cultures of the EC-B and UPEC-57 strains were 100-fold diluted in fresh LB medium and cultivated with shaking at 37°C to an OD_{600} of 0.2. Then, 10 mL of each bacterial culture was centrifuged at 2000 g for 20 min to remove the medium and washed with 1 x PBS buffer (EPRO, Poland) twice. In the next step, the bacterial pellets were suspended in 10 mL of Surine™ Negative Urine Control (MERCK, Germany) or the real human urine that was filtered prior to use through 0.22 μm SFCA membrane filter. In the next step, the suspensions were divided into two aliquots of 5 mL. To obtain the bacterial lysate in which the bacterial cells were subjected to mechanical lysis, one of the samples was passed through the filter with a 0.22-μm-pore size SFCA membrane (Nalgene, USA). The second was a variant without filtration that contained intact bacterial cells suspended in synthetic or real human urine. The enumeration of bacterial cells in both prepared samples was performed by plate-count techniques and expressed in the number of bacterial cells per mL (CFU/mL) as previously described (Topka et al., 2019). To estimate the CFU/mL, 0.01 mL of the bacterial suspension or cell-free bacterial lysate was 10-fold diluted in 0.85% sodium chloride (Chempur, Poland). Then 0.04 mL of the appropriate dilution was spread onto a LA agar plate. After overnight incubation at 37°C, the bacterial colonies were counted, and the CFU/mL was determined according to the formula: CFU/mL = (No. of colonies × Total dilution factor)/Volume of culture plated in mL.

3.   **Results of the human urine analysis, used in this study**

Table S1 – results of the human urine test

Analyte (unit)	Result (Reference range or value)
Appearance/Clarity	clear
Color	dark yellow
Specific gravity (kg/l)	1.026 (1.015-1.030)
pH	7.0
Glucose	negative
Ketones	negative
Urobilinogen (mg/dl)	normal range (0-1)
Bilirubin	negative
Protein	negative
Nitrites	negative
Erythrocytes	negative
Leukocytes	small

4. Electrochemical analysis to monitor successful electrode functionalization steps
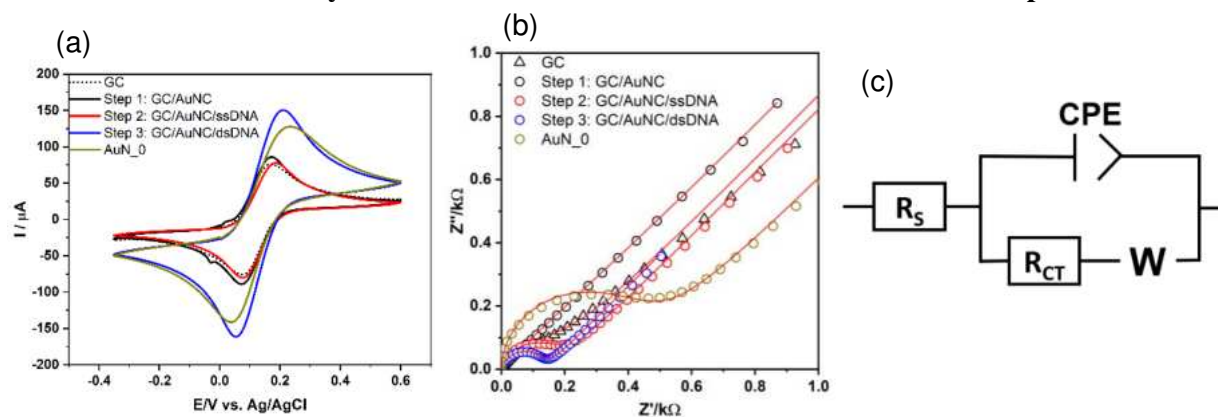

Figure S1 – exemplary a) CV and b) EIS spectra registered after consecutive functionalization steps: (step1) AuNC drop-casting, (step2) ssDNA anchoring by thiol, (step3) dsDNA hybridization, AuNC_0 marks the change under exposure to RNAP. c) the electric equivalent circuit used to deconvolute impedance data presented in Table S2.

The impedance data presented in **Fig. S1b** were fitted using electric equivalent circuit $R_S(Q(R_{CT}W))$, depicted in **Fig. S1c**. It is a modification of Randles circuit, with series (electrolyte) resistance R_S, charge transfer resistance R_{CT} and Warburg diffusion impedance W. The CPE stands for the constant phase element, used to represent electric heterogeneity of the electrode. The CPE impedance may be described with the following equation: $Z_{CPE} = [Q(j\omega)^n]^{-1}$, where Q is the *quasi*-capacitance and CPE exponent n marks the degree of heterogeneity (for n = 1, CPE represents ideal capacitor behavior).

Table S2 – The EIS data from fitting with $R_S(Q(R_{CT}W))$ EEC. The Rs is a solution resistance, CPE is a constant phase element defined by Q – *quasi*-capacitance and exponent n, R_{CT} is charge transfer resistance and W is a Warburg resistance. All measurements were performed in 0.01 M PBS, pH 7.4, containing 1 mM $Fe(CN)_6^{3-/4-}$ and frequency range from 10 kHz to 0.1 Hz.

Electrode	R_{CT} / kΩ	CPE		W / $\mu Ss^{1/2}$	Chi^2 / -
		Q / μSs^n	n / -		
GC	154.1	34.93	0.81	828.9	2.99×10^{-2}
GC/AuNC	4.9	3.77	0.99	1042	6.73×10^{-2}
GC/AuNC/ssDNA	181.5	9.15	0.89	1056	8.87×10^{-3}
GC/AuNC/dsDNA	132.8	7.69	0.91	2407	4.55×10^{-3}
AuNC_0	427.6	4.62	1.00	621	4.34×10^{-3}

5.   The SVD results obtained for suspended bacteria and bacterial lysate
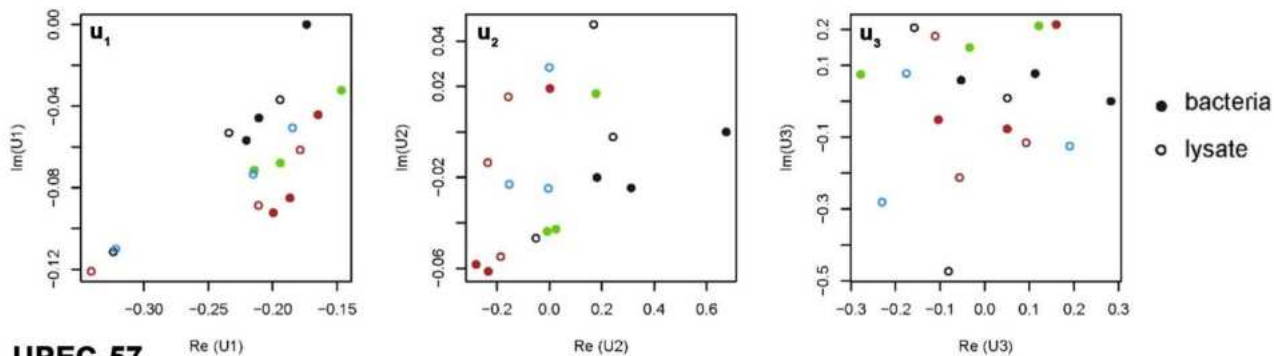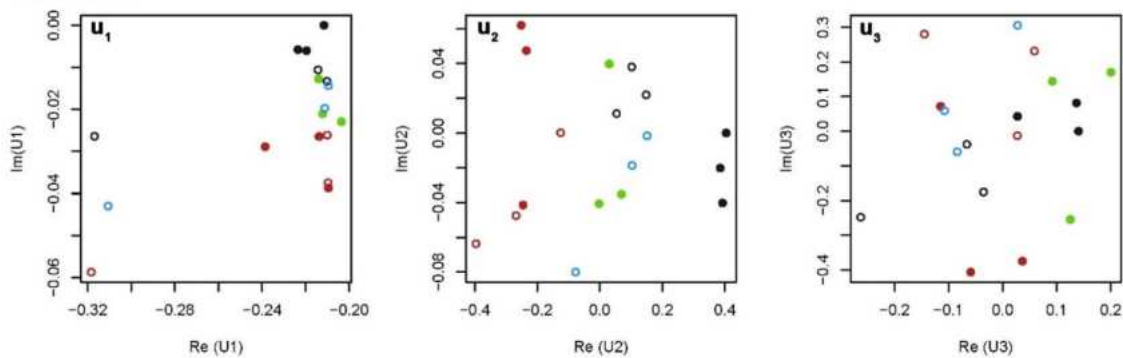
Figure S2 – The graphical representation of the first three components of U with differences between the lysate and bacteria

6. Analytical importance of the impedimetric data collected at various frequencies

Linear regression was performed by SVD, on the original transposed dataset, using y as the same response variable. By reporting the weighting X that relates the impedance spectra at a specific applied potential to the dummy response variable, y, Figure S3 are obtained. On the left, PLS regression was performed using a truncated SVD with t=2, while, on the right, with t =3. It is interesting to notice the appearance of an interval of frequency of interest (FI2), only for t=3, between 40-100 Hz, at the polarization potential related to the oxidation-reduction potential of the redox pair.

Figure S3 – Differences between the t-SVD for t=2 (left) and t=3 (right).

7. Literature review of different electrochemical *E-coli* biosensors in different environments

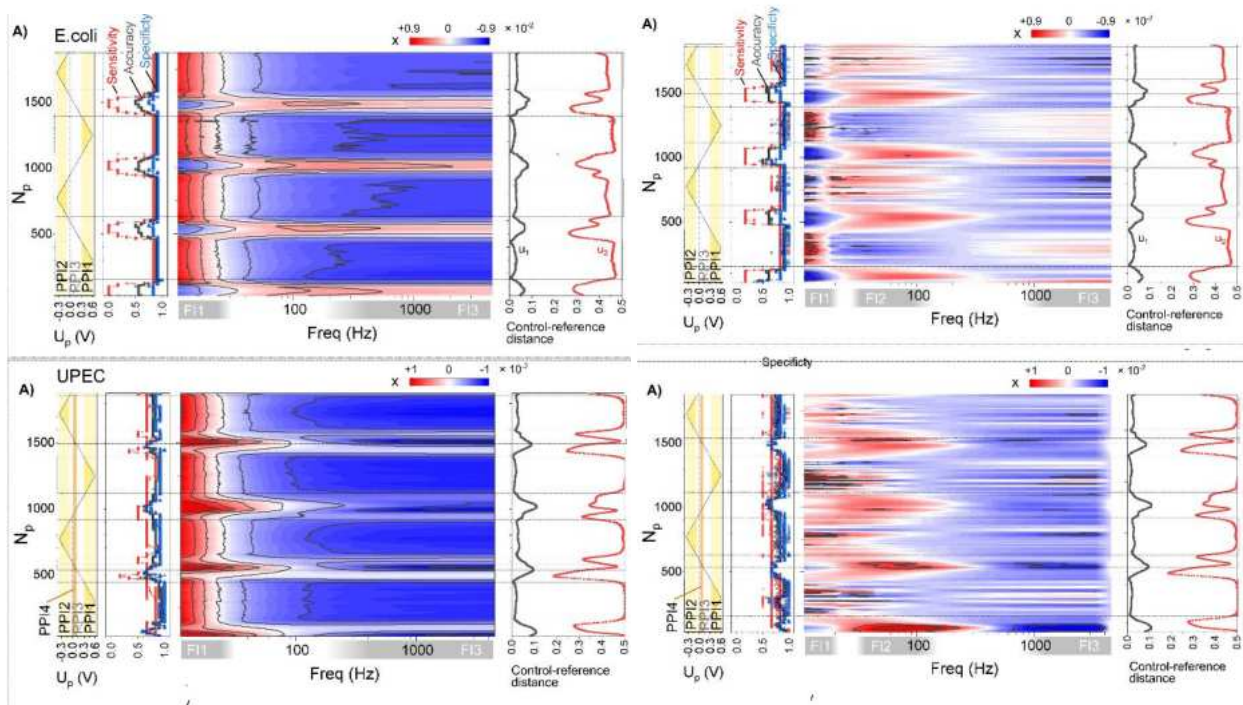Table S3 – Electrochemical *E.coli* biosensors with offered LOD.

Detection method	Type of substrate	Medium	Detection time	LOD (CFU/mL)	Ref.
CV	PPy/AuNP/MWCNT/Chi 25 hybrid bionanocomposite modified graphite	PBS	< 1 h*	30	(Güner et al., 2017)
EIS	ITO electrode	PBS	~2.5 h*	1	(Barreiros dos Santos et al., 2015)
DPV	Sandwich MNP-target-AuNP on a screen printed carbon electrode	PBS	~1 h*	1	(Wang and Alocilja, 2015)
EIS	G–PEDOT–AuNPs composites modified glass carbon electrode	Milk	~2.5 h	34	(Guo et al., 2015)
DPV	Gold electrode in aptamer-based biosensor	Licorice extract	2.5 h	80	(Wang et al., 2019)
EIS	Screen printed gold electrode	Drinking water	1 h	3	(Cimafonte et al., 2020)
EIS	rGO-CysCu molecules on gold electrode	PBS		3. 8	(Pandey et al., 2017)
EIS	SP-IDME electrode	Ground beef	< 2 h	10^3	(Xu et al., 2016)
EIS	Gold electrode	River water	1 h*	50	(Geng et al., 2008)
CV-DPV	SWCNT modified SPE	Tap water	< 45 min*	17	(Housaindokht et al., 2018)
Impedimetric fingerprint	AuNC drop-casted at GCE	Human urine	2 min	11.3	This work

* information not available directly, the detection time is speculated based on the experimental steps provided

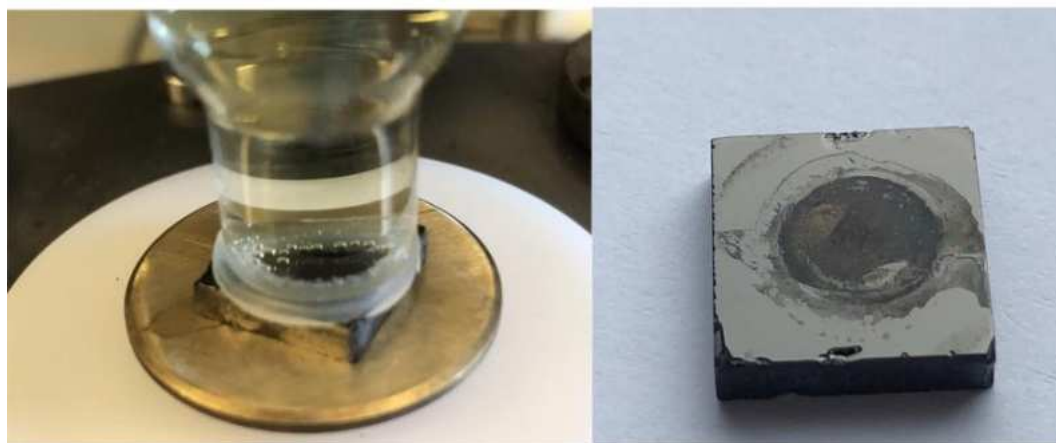**8. The electrode degradation during real urine analysis**

Figure S4 – A visual documentation of the electrode degradation in real urine under anodic polarization

9. Exemplary cyclic voltammetry analyses after sensor exposure to UPEC in real urine
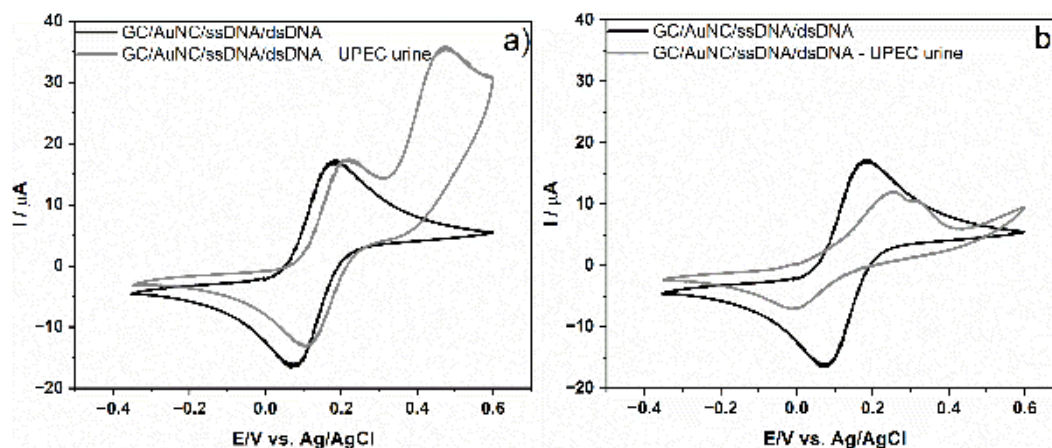

Figure S5 – CV scans (at 2 mV/s) in UPEC lysate detection in real human urine in concentrations a) 100 CFU/mL and b) 10^5 CFU/mL.

10. References:

Adamus-Bialek, W., Wojtasik, A., Majchrzak, M., Sosnowski, M., Parniewski, P., 2009. (CGG) $_4$ -Based PCR as a Novel Tool for Discrimination of Uropathogenic *Escherichia coli* Strains: Comparison with Enterobacterial Repetitive Intergenic Consensus-PCR. J Clin Microbiol 47, 3937–3944. https://doi.org/10.1128/JCM.01036-09

Barreiros dos Santos, M., Azevedo, S., Agusil, J.P., Prieto-Simón, B., Sporer, C., Torrents, E., Juárez, A., Teixeira, V., Samitier, J., 2015. Label-free ITO-based immunosensor for the detection of very low concentrations of pathogenic bacteria. Bioelectrochemistry 101, 146–152. https://doi.org/10.1016/j.bioelechem.2014.09.002

Cimafonte, M., Fulgione, A., Gaglione, R., Papaianni, M., Capparelli, R., Arciello, A., Bolletti Censi, S., Borriello, G., Velotta, R., Della Ventura, B., 2020. Screen Printed Based Impedimetric Immunosensor for Rapid Detection of Escherichia coli in Drinking Water. Sensors 20, 274. https://doi.org/10.3390/s20010274

Clermont, O., Christenson, J.K., Denamur, E., Gordon, D.M., 2013. The Clermont *Escherichia coli* phylo-typing method revisited: improvement of specificity and detection of new phylo-groups: A new *E. coli* phylo-typing method. Environmental Microbiology Reports 5, 58–65. https://doi.org/10.1111/1758-2229.12019

Dang, T.N.D., Zhang, L., Zöllner, S., Srinivasan, U., Abbas, K., Marrs, C.F., Foxman, B., 2013. Uropathogenic Escherichia coli are less likely than paired fecal E. coli to have CRISPR loci. Infection, Genetics and Evolution 19, 212–218. https://doi.org/10.1016/j.meegid.2013.07.017

Geng, P., Zhang, X., Meng, W., Wang, Q., Zhang, W., Jin, L., Feng, Z., Wu, Z., 2008. Self-assembled monolayers-based immunosensor for detection of Escherichia coli using electrochemical impedance spectroscopy. Electrochimica Acta 53, 4663–4668. https://doi.org/10.1016/j.electacta.2008.01.037

Güner, A., Çevik, E., Şenel, M., Alpsoy, L., 2017. An electrochemical immunosensor for sensitive detection of Escherichia coli O157:H7 by using chitosan, MWCNT, polypyrrole with gold nanoparticles hybrid sensing platform. Food Chemistry 229, 358–365. https://doi.org/10.1016/j.foodchem.2017.02.083

Guo, Y., Wang, Y., Liu, S., Yu, J., Wang, H., Cui, M., Huang, J., 2015. Electrochemical immunosensor assay (EIA) for sensitive detection of E. coli O157:H7 with signal amplification on a SG–PEDOT–AuNPs electrode interface. Analyst 140, 551–559. https://doi.org/10.1039/C4AN01463D

Housaindokht, M.R., Sheikhzadeh, E., Pordeli, P., Rouhbakhsh Zaeri, Z., Janati-Fard, F., Nosrati M. Mashreghi, M., Nakhaeipour, A., A. Esmaeili, A., Solimani, S., 2018. A sensitive electrochemical aptasensor based on single wall carbon nanotube modified screen printed electrode for detection of Escherichia coli O157:H7. Adv. Mater. Lett. 9, 369–374. https://doi.org/10.5185/amlett.2018.1701

Pandey, C.M., Tiwari, I., Singh, V.N., Sood, K.N., Sumana, G., Malhotra, B.D., 2017. Highly sensitive electrochemical immunosensor based on graphene-wrapped copper oxide-cysteine hierarchical structure for detection of pathogenic bacteria. Sensors and Actuators B: Chemical 238, 1060–1069. https://doi.org/10.1016/j.snb.2016.07.121

Topka, G., Bloch, S., Nejman-Faleńczyk, B., Gąsior, T., Jurczak-Kurek, A., Necel, A., Dydecka, A., Richert, M., Węgrzyn, G., Węgrzyn, A., 2019. Characterization of Bacteriophage vB-EcoS-95, Isolated From Urban Sewage and Revealing Extremely Rapid Lytic Development. Front. Microbiol. 9, 3326. https://doi.org/10.3389/fmicb.2018.03326

Wang, H., Zhao, Y., Bie, S., Suo, T., Jia, G., Liu, B., Ye, R., Li, Z., 2019. Development of an Electrochemical Biosensor for Rapid and Effective Detection of Pathogenic Escherichia coli in Licorice Extract. Applied Sciences 9, 295. https://doi.org/10.3390/app9020295

Wang, Y., Alocilja, E.C., 2015. Gold nanoparticle-labeled biosensor for rapid and sensitive detection of bacterial pathogens. J Biol Eng 9, 16. https://doi.org/10.1186/s13036-015-0014-z

Xu, M., Wang, R., Li, Y., 2016. Rapid detection of Escherichia coli O157:H7 and Salmonella Typhimurium in foods using an electrochemical immunosensor based on screen-printed interdigitated microelectrode and immunomagnetic separation. Talanta 148, 200–208. https://doi.org/10.1016/j.talanta.2015.10.082

RESEARCH ARTICLE

An electrochemical biosensor for the determination of hormone Human Chorionic Gonadotropin (hCG) in human serum

Adrian Koterwa[1] | Magdalena Bojko[2] | Jacek Ryl[3] | Krzysztof Łukaszuk[4, 5] |
Kornelia Kozłowska[1] | Wiktor Sieklicki[6] | Sylwia Rodziewicz-Motowidło[2] |
Paweł Niedziałkowski[1]

[1]Department of Analytical Chemistry, Faculty of Chemistry, University of Gdansk, Gdansk, Poland

[2]Department of Biomedical Chemistry, Faculty of Chemistry, University of Gdansk, Gdansk, Poland

[3]Institute of Nanotechnology and Materials Engineering and Advanced Materials Center, Gdansk University of Technology, Gdansk, Poland

[4]INVICTA Research and Development Center Fertility and Reproductive Center, Gdansk, Poland

[5]Department of Obstetrics and Gynecological Nursing, Faculty of Health Sciences, Medical University of Gdansk, Gdansk, Poland

[6]Faculty of Mechanical Engineering, Gdansk University of Technology, Gdańsk, Poland

Correspondence

Paweł Niedziałkowski, Department of Analytical Chemistry, Faculty of Chemistry, University of Gdansk, Wita Stwosza 63, 80-308 Gdansk, Poland.
Email: pawel.niedzialkowski@ug.edu.pl

Abstract

This work describes the modification of a gold electrode to create an electrochemical biosensor capable of detecting human chorionic gonadotropin (hCG). The biosensor was obtained by modifying the gold electrode with cysteamine and oligopeptide (PPLRINRHILTR). The modification steps of the gold electrode were confirmed by cyclic voltammetry (CV) and impedance electrochemical spectroscopy (EIS) measurements. The conducted EIS experiments in 0.01 M PBS, pH 7.4 confirm that the biosensor exhibits sensitivity towards hCG in a range of concentrations from 1×10^{-12} to 1×10^{-7} M (0.5 mIU/mL – 50 000 mIU/mL) to solutions with a detection limit of 1.91×10^{-14} M (0.0095 mIU/mL). The effectiveness of the investigated biosensor was also investigated in human serum. The EIS comparative investigations were performed in human serum containing a concentration of 1×10^{-12} M (0.5 mIU/mL) hCG and in human serum where the hCG was added. The obtained results indicate that the investigated biosensor is selective for the presence of hCG hormone in the human serum.

KEYWORDS

electrochemical detection, gold electrode functionalization, human Chorionic Gonadotropin (hCG), human serum

1 | INTRODUCTION

Human chorionic gonadotropin (hCG) is a 37 kDa glycoprotein hormone consisting of two combined, dissimilar subunits designated alpha (common to other glycoprotein pituitary hormones - LH, FSH, TSH) and beta, which are specific for hCG [1] It has 8 sites of glycosylation −4 N and 4 O; because of their different glycosylation their weight varies from 27.6 to 42.8 kDa [2]. There are at least 18 different isomers or degradation

products which are biologically active. The hCG is the most glycosylated hormone in humans – the percentage of the sugars'weight varies from 28 to 42% [3]. The consequence of such a high sugar component is a very long half-life in human blood which could last 36 hours [4].

hCG is the essential pregnancy hormone, necessary for syncytiotrophoblast formation, embryo implantation, placental development and pregnancy maintenance. It stimulates progesterone production, causes quiescence of the myometrium and angiogenesis. Production of the hCG starts before implantation probably during the blastocyst formation [5].

Early hCG secretion is a marker of good embryonic development and indicates a good prognosis for the development of the pregnancy. It is therefore important to be able to accurately measure hCG as early in pregnancy as possible, when its levels are very low. The average serum level of hCG in a healthy pregnancy in the third week is about 0.26 ng/ml and in the peak period of its secretion it exceeds 10000 ng/ml [4]. hCG is also a factor involved in the pathomechanism of many pregnancy complications.

The deficiency of hyperglycosylated hCG (the main form of hCG in early pregnancy) is considered to be the main factor of hypertensive pregnancy [6], pre-eclampsia, or the development of pregnancy induced hypertension (PIH), but also predicts poor hemochorial placentation growth or nutritional deficiency. The hCG level is also used in prenatal diagnostics for Down syndrome pregnancies risk estimation [7].

Attempts to determine hCG levels have been made since its role was first understood. Biological tests have been carried out since 1927 – using urine injected into mice (1927), rabbits (1931), toads (1934) or rats (1941) [8].

Electrochemical determination of the hCG hormone is most often performed using antibodies on modified electrodes [2, 9–14]. There are some literature reports where instead of expensive antibodies, oligopeptide was used that interacts with hCG. The above works are mainly based on the short oligopeptide sequence (PPLRINRHILTR), which was selected from a phage library after five rounds of screening reported by Ding and Yang [11]. The above oligopeptide was previously used for the detection of hCG. Based on the mechanism of the catalytic properties of gold nanoparticles (AuNPs) with described peptide, however, a label-free colorimetric assay was designed for the detection of hCG [15]. The graphene oxide (GO) with a oligopeptide modified by fluorescein isothiocyanate was employed for the detection of the hCG [16]. GO sheets modified by oligopeptides placed on the modified gold were also applied for an ultra-high hGC sensitive biosensor based on surface plasmon resonance (SPR) changes [17]. The oligopeptide used for the hGC detection also utilized silver nanoparticles (AgNPs) as redox reporters employing linear-sweep voltammetry (LSV) [18].

Furthermore, one of the most commonly used methods for the detection of hCG is the application of hormone-specific anti-hCG antibodies. Modifications with anti-hCG usually can be performed on a GC electrode modified with Pt nanoparticles and graphene ionic liquid chitosan nanocomposite [19], modified with silver nanoparticles and a nanocomposite composed of graphene, chitosan and ionic liquid, using riboflavin as a redox probe [20] and a GC electrode modified by gold nanoparticles and cysteamine [21].

In this work, we demonstrate a new approach of the (PPLRINRHILTR) oligopeptide to obtain a novel, modified gold electrode sensitive to the presence of hCG both in a phosphate buffer solution (PBS) used as a reference solution and in a human serum solution. The sensitivity of the prepared gold electrode was investigated in a 0.01 M PBS solution in a concentration range from 1×10^{-12} to 1×10^{-7} M (0.5 mIU/mL–50 000 mIU/mL) using the (EIS) method. The efficiency of the obtained electrodes was also tested in human serum. The comparative hCG detection was performed in a human serum of the concentration 1×10^{-12} M (0.5 mIU/mL) and in human serum where the hCG was added. The obtained results demonstrate that the obtained biosensor is sensitive for hCG in the PBS solution and human serum samples. The hCG detection is extremely important in the assessment of the normal course of a pregnancy and the diagnosis of many cancers including trophoblastic and non-trophoblastic cancers such as gynaecological cancers, testicular cancers or biliary and pancreatic cancer and many others [1, 22, 23]. The invention of a biosensor that works in a variety of media including human serum is very crucial.

2 | EXPERIMENTAL

2.1 | Materials and reagents

All of the chemicals were of an analytical grade. N-hydroxysuccinimide (NHS), 1-ethyl-3-(3-dimethylaminopropyl) carbodiimide (EDC), piperidine, N,N-Diisopropylethylamine) (DIPEA), N,N′-Diisopropylcarbodiimide (DIC) Ethyl (hydroxyimino) cyanoacetate (Oxyma), Trifluoroacetic acid (TFA), Triisopropyl silane (TIPSI), Acetonitrile (ACN) cysteamine, bovine serum albumin (BSA), $K_3[Fe(CN)_6]$, and $K_4[Fe(CN)_6]$ were purchased from Sigma-Aldrich. 0.01 M PBS, pH 7.4 was obtained from tablets purchased from Sigma-Aldrich. 0.02 M PBS,

pH 5.15 was obtained from (2.72 g KH_2PO_4, adjusted to suitable pH by KOH in 1000 mL). Alumina powders of 0.03 µm and 0.05 µm and microcloth pads were purchased from Buehler (USA). Ethanol, N, and N-dimethyloformdamide (DMF), were purchased from POCh (Poland).

2.2 | Peptide synthesis (PPLRINRHILTR)

The (PPLRINRHILTR) (Pro-ProLeu-Arg-Ile-Asn-Arg-His-Ile-Leu-Thr-Arg) oligopeptide was synthesised applying the standard solid-phase peptide synthesis (SPPS) protocol using Fmoc/tBu chemistry on an automated microwave synthesizer, Liberty BlueTM (CEM Corporation, USA). The oligopeptide used for electrode surface modification was obtained with the Fmoc protecting group at the N-terminus of amino acid. Synthesis was performed on a 2-chlorotrityl chloride resin with the capacity of 1.0–1.6 mmol/g (Lipopharm, Poland) using standard amino acids derivatives. The coupling of the C-terminal arginine residue was performed manually prior to synthesis on the Liberty BlueTM with a two fold excess of N-Fmoc protected arginine with the addition of a four fold excess of DIPEA (N,N-Diisopropylethylamine). Fmoc protecting groups were removed by the use of a 20% piperidine solution in DMF. The coupling reactions run on the Liberty BlueTM were performed with a 0.5 M DIC solution in DMF with a 1 M solution of Oxyma pure in DMF. The cleaved processes were run with the simultaneous removal of amino acids side chains protecting groups in the mixture of 88% TFA/5% phenol/5% H_2O/2% TIPSI. The crude peptide was purified using the reverse-phase high performance liquid chromatography (RP-HPLC) technique on a semi-preparative column – Luna C8 (2) (250 mm×20 mm, 5 µm) from Phenomenex (Torrance, USA), in an ambient temperature using an appropriate H_2O/ACN gradient with 0.1% of TFA. The purity of the final product was confirmed by RP-HPLC using the analytical column Kromasil C8 (250 mm×4.6 mm, 5 µm) and mass spectrometry.

2.3 | Preparation of the hCG electrochemical biosensor

The hCG electrochemical biosensor presented in this paper is based on a chemical modification of the gold electrode. In the first step, the gold electrodes were modified by immobilization by covalent linkage via cysteamine, performed according to the literature procedure [24]. The 18 mM cysteamine solution in ethanol, during 12 h

was used to obtain a self-assembled monolayer (SAM) on the electrode's surface.

In the second step, the oligopeptide (PPLRINR-HILTR) was attached to the amino groups present on the gold electrode using the EDC/NHS mixture solution as coupling agents. The cysteamine modified electrodes were placed in a 0.02 M PBS solution of pH 5.15 containing 1.5 mM of oligopeptide in a form of (Fmoc-PPLRINRHILTR), containing the Fmoc group as a protecting group of the N-chain and 100 mM EDC and 50 mM NHS. The reaction was performed in room temperature in a 200 µl vessel over 16 h. Then the electrodes were placed in a 200 µl vessel containing a 20% solution of piperidine in DMF during 30 min to remove the Fmoc group. The Fmoc group removal reaction was repeated twice.

Next the electrodes were rinsed with 0.01 M PBS, pH 7.4 and deionized water, and incubated in 10 µL of a 0.1% (BSA) solution for 45 min to block the unreacted and non-specific sites. The electrodes obtained in such a manner were subsequently applied for the detection of the (hCG). The detection of the (hCG) hormone was performed (0.01 M (PBS) buffer, pH 7.4, and human serum) by applying 10 µL on the electrode's surface for 45 minutes. The sensitivity of the gold electrodes to hCG in different concentrations were evaluated by EIS measurements.

2.4 | Serum extraction

Human serum was obtained from anonymized patient samples collected for routine clinical analysis. These were human serum samples from subjects gestation period with known hCG levels established by an electrochemiluminescence assay on roche cobas performed on Elecsys total HCG cobas, (Roche Switzerland).

3 | RESULTS AND DISCUSSION

3.1 | Functionalization of the gold electrode for the hCG detection

The structures of both bovine serum albumin (BSA) and hCG presented in papers [25, 26], were used to schematically represent the various steps of the electrode modification. A chemical modification scheme for the gold electrode is shown in Figure 1.

The first modification of the gold electrode was carried out in an 18 mM solution of cysteamine in anhydrous ethanol over 12 h, applying the procedure described elsewhere [24]. The monolayer based on the
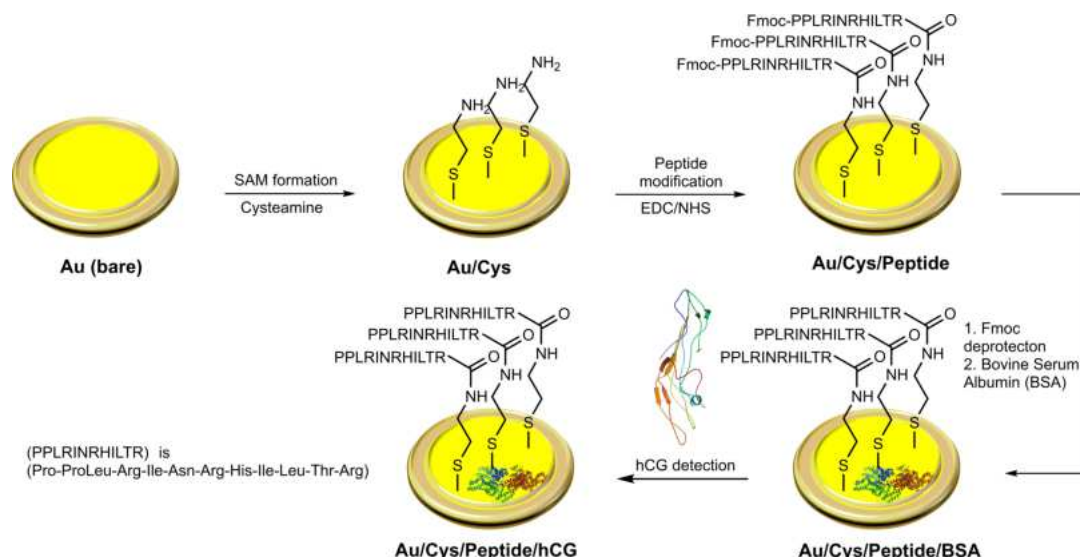
FIGURE 1 The functionalization scheme of a gold electrode as an electrochemical biosensor for hCG detection.

cysteamine in ethanolic solution is a commonly used technique in the preparation of biosensors and allows for the gold's modification [27, 28].

The application of (SAM) allows for the coating of a surface that can be further chemically modified to obtain biosensors [29]. The usage of cysteamine allows for the amino groups presence on the electrode's surface. The oligopeptide was ahnored on the gold electrode through the activation of carboxyl groups in the presence of a mixture of EDC/NHS. The reaction was performed in a phosphate buffer solution pH 5.15, due to the fact that the EDC/NHS reaction is the most efficient in the pH range of 4.5 to 7.2 [30].

Then the electrodes were placed in a solution of 0.1 % of BSA which is used to prevent non-specific adsorption on the surface of the electrode and to block non-specific binding sites [31]. The sensitivity of the obtained electrochemical biosensors were examined to detect the hCG hormone in the PBS solution in various concentrations from 1×10^{-12} to 1×10^{-7} M (0.5 mIU/mL–50 000 mIU/mL) used as the standard solution as well as in human serum containing a known concentrattion of hCG (1×10^{-12} M) (0.5 mIU/mL) and in human serum with the addition of hCG. The electrochemical changes of electrodes during the functionalizastion process were measured by the CV and EIS methods, while in the presence of hCG involved different media were monitored using the EIS techniques.

3.2 | Electrochemical investigations of the electrode during the biosensor formation

3.2.1 | Cyclic voltammetry

CV and EIS measurements were performed after each gold electrode's functionalization step were carried out in a 0.01 M PBS solution containing 1 mM of ([Fe-$(CN)_6]^{3-}$/[Fe$(CN)_6]^{4-}$ used as redox couples. This redox mediator belongs to inner-sphere electrochemical redox probes sensitive to electrode surface changes [32, 33]. Figure 2a shows the CV's obtained for the bare gold electrode, modified with cysteamine, peptide, and the response of the electrode in the presence of hCG in the concentration of 1×10^{-7} M (50 000 mIU/mL).

The quasi-reversible redox process is observed for the bare Au electrode with peak to peak separation $\Delta E = 90$ mV. For the modified electrode with the cysteamine, the peak to peak separation decreased to 74 mV. This indicates the self-assembly monolayers (SAM's) formation on the electrode's surface. The presence of protonated amine groups on the surface enhances the transfer of electrons [34], which interact with the applied redox probes [35].

The presence of oligopeptide on the electrode's surface slightly influence the electrode's response. The modification by oligopeptide does not affect the observed
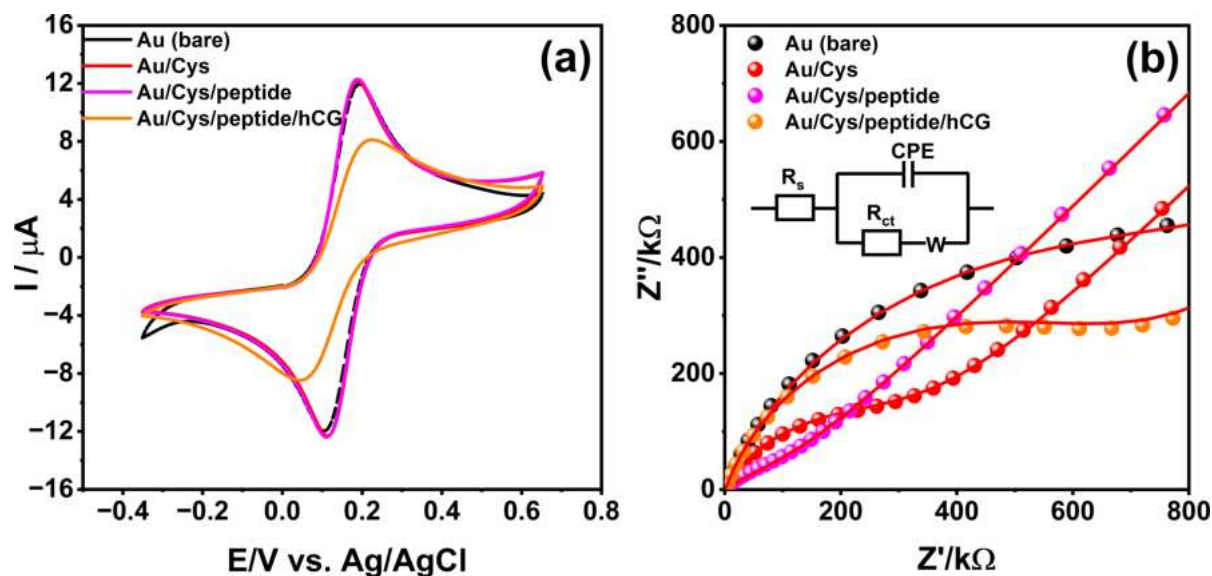
FIGURE 2 a) CV, b) EIS curves obtained for: Au bare, Au modified with cysteamine, Au modified with cysteamine and oligopeptide and response of obtained electrodes in the presence of hCG in concentration of 1×10^{-7} M (50 000 mIU/mL) in 0.01 M PBS, pH 7.4 containing 1 mM $Fe[(CN)_6]^{3-/4-}$.

voltammetric currents, but the peak to peak separation also increases from 74 mV to 81 mV.

This is probably attributed to the chemical structure of the attached oligopeptide, which processes positively charged amino acids in the structure.

The electrochemical response of the investigated biosensor was tested in a 0.01 M PBS solution containing 1×10^{-7} M (50 000 mIU/mL) of hCG by CV which resulted in the peak-to-peak separation increasing from 81 mV to 179 mV; moreover, a significant decrease of the height currents were observed on cyclic voltammeters (see Figure 2a).

3.2.2 | Electrochemical impedance spectroscopy

The EIS measurements were performed both for the characterization of the electrodes at each stage of their functionalization and for the hCG detection. EIS is a high-sensitivity measurement method frequently used to characterise the various steps of the electrode modification of biosensors including the (SAM's) formation [39]. The EIS measurement method gives information that cannot be achieved by CV. Therefore, EIS studies are often used to investigate the phenomena occurring at the electrode's surface during the binding of the analytes of many biosensors [37].

All of the obtained impedance spectra in this paper were fitted using the modified Randles equivalent circuit consisting of: solution resistance (R_s), constant phase element (CPE), electron transfer resistance (R_{ct}) and Warburg impedance element (W) (see inset of Figure 2b).

The CPE in the applied equivalent circuit model, including irregularity of the electrode's surface and inhomogeneity of the current distribution, was used instead of double layer capacitance [38]. The description of CPE including impedance analysis of electrode materials and biosensors is described in many papers [39–42].

The obtained EIS measurement data here are presented as points, while lines show the fitted data. The calculated value from the fittings for all the obtained experimental data are presented in Tables S1, S2 and S4, where it can be seen that the applied equivalent electrical circuits were well fitted, as indicated by the Chi^2 parameter.

The impedance spectra for all the steps of the modification of the gold electrode are shown in Figure 2b. The calculated R_{ct} value for the bare Au electrode is 986.9 Ω. This value decreases to 337.8 Ω after the (SAM's) formation. The presence of the positively charged amino group on the electrode's surface which interacts with negatively charged redox probes caused the increases of the charge transfer to the electrode [43].

The immobilization reaction of oligopeptide containing the Fmoc group resulted in a decrease of R_{ct} value to

305.2 Ω. The removal of the Fmoc group from and incubation in 0.1% BSA solution caused the decrease of the R_{ct} value to 289.9 Ω indicating a slight effect of BSA on the electrode's surface.

The obtained electrode was utilized to 1×10^{-7} M (50 000 mIU/mL) hCG detection in the PBS solution (see Figure 2b). The incubation in this solution caused the appearance of a semicircle in the impedance spectra and increased the R_{ct} value to 1014.0 Ω indicating an inhibition of electron transfer. The presence of hCG results in an increase of R_{ct} by 3.5 times.

The analysis of the EIS data also reveals very interesting changes in the α parameter. The parameter α for the cysteamine modified electrode is about 0.8, which indicates a certain roughness (for the smooth electrode α = 1 [44]) or inhomogeneity of the charge distribution [45, 46]. The attachment of an oligopeptide to the electrode causes a change in roughness and a decrease of parameter α to 0.49. Nevertheless, the attachment of the hCG hormone causes an increase in the α parameter to about 0.87 for the hCG concentration of 1×10^{-7} M (50 000 mIU/mL). Further investigated hCG concentrations in the range from 1×10^{-12} to 1×10^{-7} M (0.5 mIU/mL–50 000 mIU/mL) result in a linear decrease of the α parameter from 0.87 to 0.82 respectively. The detailed results of EIS analysis are presented in Table S1

3.3 | Electrochemical hCG hormone detection in PBS solution

The sensitivity of the obtained biosensor was tested in a 0.01 M PBS, pH 7.4 used as a standard solution in hCG concentrations of from 1×10^{-12} to 1×10^{-7} M (0.5 mIU/mL–50 000 mIU/mL). The electrodes were incubated at the biosensor's surface for 45 min in solution, then the EIS measurements were performed (see Figure 3a).

The obtained R_{ct} values indicate that the R_{ct} increases according to the hCG concentration increase after incubation (see Table S2). The ΔR_{ct} was calculated for equations of the R_{ct} value of the electrode after incubation in suitable human hCG concentration and the R_{ct} of the electrode after incubation in BSA. Based on the dependence of ΔR_{ct} on the logarithm of the hCG concentration (Figure 3b), two linear regression equations were observed from 1×10^{-12} to 1×10^{-9} M (0.5 mIU/mL–500 mIU/mL) and 1×10^{-9} to 1×10^{-7} M (500 mIU/mL–50 000 mIU/mL) with the following equations: $\Delta Rct = 64.50 \log C(hCG) (M) + 778.99$ with $R^2 = 0.987$ and $\Delta Rct = 216.41 \log C(hCG) (M) + 2199.34$ with $R^2 = 0.991$ respectively.

The calculated detection limit (LOD) of the hCG biosensor is 1.91×10^{-14} M (0.0095 mIU/mL), estimated on the basis of the detection analysis limit, presented elsewhere [47, 48].
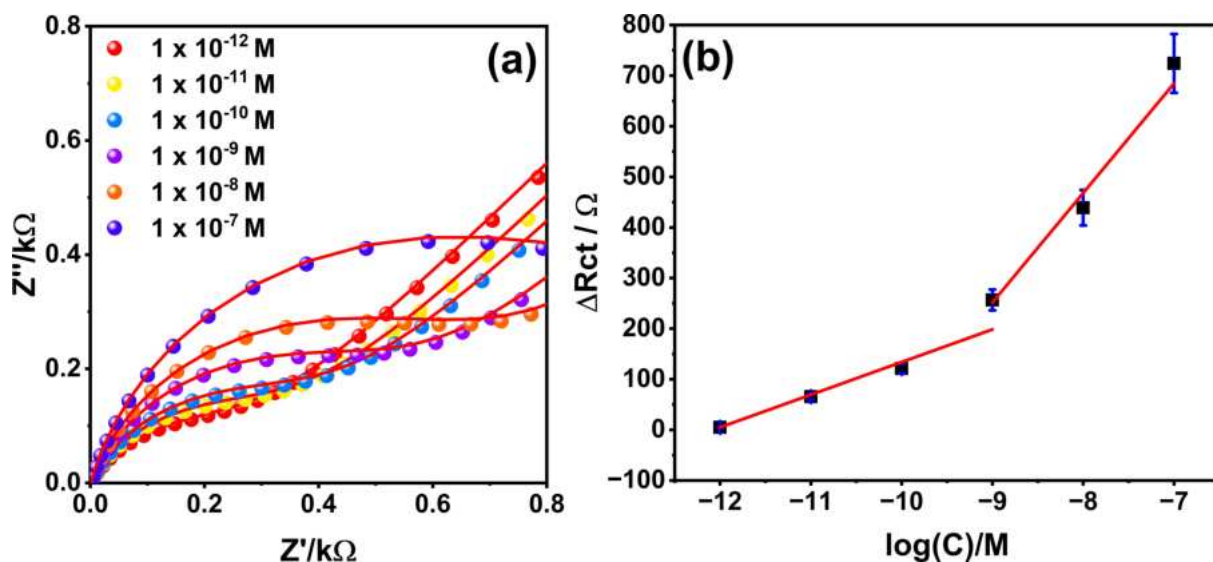

FIGURE 3 a) Electrochemical impedance spectroscopy curves obtained after incubation at a concentration of hCG hormone ranging from 1×10^{-12} to 1×10^{-7} M (0.5 mIU/mL–50 000 mIU/mL) in 0.01 M PBS. b) Dependence between the calculated ΔR_{ct} and hCG concentrations.

The detection limit of the hCG of the sensors based on the described oligopeptide were: 0.065 nM for SPR [17], 15 mIU/ml and 25 mIU/ml for colorimetric assay [15], [18], 20 mIU/ml for fluorescent measurement [16] and 1 IU/ml for liquid crystals [11]. The results obtained for the described biosensor allows for the hCG detection at comparable or lower concentrations. Due to the fact that 1 IU/mL is 2 nM [11], the limit of the detection of hCG determination is 1.91×10^{-14} M (0.0095 mIU/mL). Additionally the above method of hCG detection with others based on electrochemical techniques including the synthetic oligopeptide usage [49–52] are compared in Table S3.

3.4 | Detections of hCG hormone in human serum

The investigated biosensor has been also investigated in human serum which was selected due to the fact that clinical assays for hCG determination are usually performed in this medium. The EIS investigations were performed in human serum containing hCG ranging from 1×10^{-13} to 1×10^{-11} M (0.05 mIU/mL–5 mIU/mL). Only the results for the 1×10^{-12} M (0.5 mIU/mL) are presented in this work due to the fact that the lower concentrations of hCG were not possible to detect.

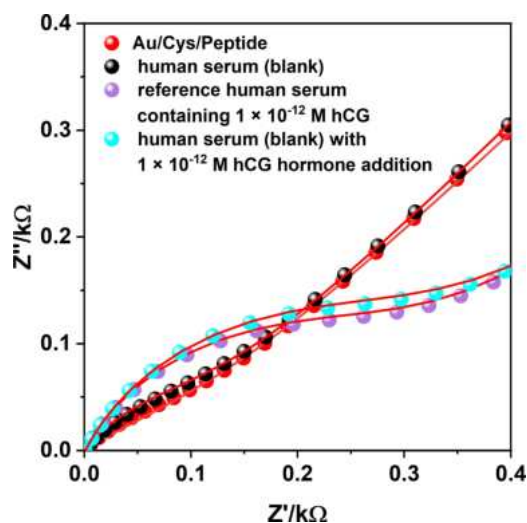The obtained EIS spectra shows the biosensor response recorded in solutions of: human serum without

FIGURE 4 Electrochemical impedance spectroscopy curves obtained for the tested biosensor after incubation in human serum (blank), reference human serum containing 1×10^{-12} M (0.5 mIU/mL) hCG, and human serum with 1×10^{-12} M (0.5 mIU/mL) hCG hormone addition.

hCG hormone (blank solution), reference human serum containing 1×10^{-12} M (0.5 mIU/mL) hCG and human serum (blank solution) with 1×10^{-12} M (0.5 mIU/mL) hCG addition (see Figure 4). The detailed results of the EIS analysis spectra are presented in Table S4 in (SI).

The obtained R_{ct} value for the biosensor after incubation in human serum used as a blank solution was equal to 140,6 Ω, while the R_{ct} value for the human serum containing 1×10^{-12} M (0.5 mIU/mL) hCG increased to 328.1 Ω.

In order to confirm the hGC detection effectiveness of the tested biosensor the electrode was incubated in human serum (previously used as a blank solution) where the 1×10^{-12} M hCG (0.5 mIU/mL) was added. The R_{ct} value calculated for the biosensor in this solution is equal to 349.1 Ω, which is close to the R_{ct} value calculated for the biosensor response in the solution containing the same concentration of hCG which is equal to 328.1 Ω.

This experiment shows that the obtained biosensor is able to detect the hCG hormone in human serum by the EIS method.

4 | CONCLUSIONS

In this study the oligopeptide (PPLRINRHILTR) was used to create a new electrochemical biosensor tested by the EIS method. The aforementioned oligopeptide has been used in other work for hCG detection, but in this work the EIS method was used for the first time, based on a modified gold electrode. Each modification step was confirmed by electrochemical investigations. The obtained biosensor exhibits sensitivity towards hCG in a range of concentrations from 1×10^{-12} to 1×10^{-7} M (0.5 mIU/mL–50 000 mIU/mL) in 0.01 M PBS solution with detection limit of 1.91×10^{-14} M (0.0095 mIU/mL). The effectiveness of the investigated biosensor was also tested in human serum.

The performed comparative studies in human serum of a known concentration of hCG in human serum where the hCG was added, allow to conclude that the tested biosensor was selective at the hCG concentration of 1×10^{-12} M (0.5 mIU/mL). The use of new electrochemical biosensors may in the future contribute to the rapid determination of hCG with high sensitivity, which can have practical applications in clinical analysis.

CONFLICT OF INTEREST

The authors declare that they have no known competing financial interests or personal relationships that could have appeared to influence the work reported in this paper.

DATA AVAILABILITY STATEMENT

Research data are not shared.

REFERENCES

1. C. Nwabuobi, S. Arlier, F. Schatz, O. Guzeloglu-Kayisli, C. J. Lockwood, U. A. Kayisli, *Int. J. Mol. Sci.* **2017**, *18*, 2037.
2. M. Roushani, A. Valipour, M. Valipour, *Mater. Sci. Eng. C* **2016**, *61*, 344–350.
3. T. Fournier, *Annales d'Endocrinologie* **2016**, *77*, 75–81.
4. M. D. Damewood, W. Shen, H. A. Zacur, W. D. Schlaff, J. A. Rock, E. E. Wallach, *Fertil. Steril.* **1989**, *52*, 398–400.
5. A. Jurisicova, M. Antenos, K. Kapasi, J. Meriano, R. F. Casper, *Hum. Reprod.* **1999**, *14*, 1852–1858.
6. L. A. Cole, *Placenta* **2010**, *31*, 653–664.
7. R. Räty, U. Ekblad, L. Anttila, A. Virtanen, P. Koskinen, P. Laitinen, A. Tiitinen, *Fertil. Steril.* **2001**, *76*, 1075–1077.
8. B. Lunenfeld, W. Bilger, S. Longobardi, V. Alam, T. D'Hooghe, S. K. Sunkara, *Front. Endocrinol.* **2019**, *10*, 429.
9. P. Li, B. Ge, L. Ou, Z. Yao, H.-Z. Yu, *Sensors* **2015**, *15*, 20543–20556.
10. I. R. Suhito, K.-M. Koo, T.-H. Kim, *Biomedicine* **2020**, *9*, 15.
11. X. Ding, K.-L. Yang, *Anal. Chem.* **2013**, *85*, 10710–10716.
12. N. X. Viet, N. X. Hoan, Y. Takamura, *Mater. Chem. Phys.* **2019**, *227*, 123–129.
13. M. Rizwan, M. Hazmi, S. A. Lim, M. U. Ahmed, *J. Electroanal. Chem.* **2019**, *833*, 462–470.
14. S. Damiati, C. Haslam, S. Sopstad, M. Peacock, T. Whitley, P. Davey, S. A. Awan, *IEEE Access* **2019**, *7*, 94048–94058.
15. C.-C. Chang, C.-P. Chen, C.-H. Lee, C.-Y. Chen, C.-W. Lin, *Chem. Commun.* **2014**, *50*, 14443–14446.
16. N. Xia, X. Wang, L. Liu, *Sensors* **2016**, *16*, 1699.
17. N.-F. Chiu, C.-T. Kuo, T.-L. Lin, C.-C. Chang, C.-Y. Chen, *Biosens. Bioelectron.* **2017**, *94*, 351–357.
18. N. Xia, Z. Chen, Y. Liu, H. Ren, L. Liu, *Sens. Actuators B* **2017**, *243*, 784–791.
19. M. Roushani, A. Valipour, *Sens. Actuators B* **2016**, *222*, 1103–1111.
20. M. Roushani, A. Valipour, *Microchim. Acta* **2016**, *183*, 845–853.
21. M. Roushani, A. Valipour, M. Valipour, *Mater. Sci. Eng. C* **2016**, *61*, 344–350.
22. U.-H. Stenman, H. Alfthan, K. Hotakainen, *Clin. Biochem.* **2004**, *37*, 549–561.
23. U.-H. Stenman, A. Tiitinen, H. Alfthan, L. Valmu, *Hum. Reprod. Update* **2006**, *12*, 769–784.
24. P. Niedziałkowski, M. Bojko, J. Ryl, A. Wcisło, M. Spodzieja, K. Magiera-Mularz, K. Guzik, G. Dubin, T. A. Holak, T. Ossowski, S. Rodziewicz-Motowidło, *Bioelectrochemistry* **2021**, *139*, 107742.
25. A. J. Lapthorn, D. C. Harris, A. Littlejohn, J. W. Lustbader, R. E. Canfield, K. J. Machin, F. J. Morgan, N. W. Isaacs, *Nature* **1994**, *369*, 455–461.
26. K. A. Majorek, P. J. Porebski, A. Dayal, M. D. Zimmerman, K. Jablonska, A. J. Stewart, M. Chruszcz, W. Minor, *Mol. Immunol.* **2012**, *52*, 174–182.
27. M. G. R. Pimenta-Martins, R. F. Furtado, L. G. D. Heneine, R. S. Dias, M. de F. Borges, C. R. Alves, *J. Microbiol. Methods* **2012**, *91*, 138–143.
28. M. K. Sezgintürk, Z. O. Uygun, *Anal. Biochem.* **2012**, *423*, 277–285.
29. J. J. Gooding, D. B. Hibbert, *TrAC Trends Anal. Chem.* **1999**, *18*, 525–533.
30. N. Karoonuthaisiri, R. Charlermroj, M. J. Morton, M. Oplatowska-Stachowiak, I. R. Grant, C. T. Elliott, *Sens. Actuators B* **2014**, *190*, 214–220.
31. J. Y. Lichtenberg, Y. Ling, S. Kim, *Sensors* **2019**, *19*, 2488.
32. P. Chen, R. L. McCreery, *Anal. Chem.* **1996**, *68*, 3958–3965.
33. M. Janik, P. Niedziałkowski, K. Lechowicz, M. Koba, P. Sezemsky, V. Stranak, T. Ossowski, M. Śmietana, *Opt. Express* **2020**, *28*, 15934–15942.
34. H. Abdulkarim, M. Zourob, M. Siaj, *Sci. Rep.* **2020**, *10*, 10424.
35. F. Arduini, S. Guidone, A. Amine, G. Palleschi, D. Moscone, *Sens. Actuators B* **2013**, *179*, 201–208.
36. K. Siuzdak, P. Niedziałkowski, M. Sobaszek, T. Łęga, M. Sawczak, E. Czaczyk, K. Dziąbowska, T. Ossowski, D. Nidzworski, R. Bogdanowicz, *Sens. Actuators B* **2019**, *280*, 263–271.
37. M. Cimafonte, A. Fulgione, R. Gaglione, M. Papaianni, R. Capparelli, A. Arciello, S. Bolletti Censi, G. Borriello, R. Velotta, B. Della Ventura, *Sensors* **2020**, *20*, 274.
38. C. Tlili, E. Sokullu, M. Safavieh, M. Tolba, M. U. Ahmed, M. Zourob, *Anal. Chem.* **2013**, *85*, 4893–4901.
39. J.-B. Jorcin, M. E. Orazem, N. Pébère, B. Tribollet, *Electrochim. Acta* **2006**, *51*, 1473–1479.
40. J. S. Daniels, N. Pourmand, *Electroanalysis* **2007**, *19*, 1239–1257.
41. A. Koterwa, I. Kaczmarzyk, S. Mania, M. Cieslik, R. Tylingo, T. Ossowski, R. Bogdanowicz, P. Niedziałkowski, J. Ryl, *Appl. Surf. Sci.* **2022**, *574*, 151587.
42. P. Niedzialkowski, P. Slepski, J. Wysocka, J. Chamier-Cieminska, L. Burczyk, M. Sobaszek, A. Wcislo, T. Ossowski, R. Bogdanowicz, J. Ryl, *Sens. Actuators B* **2020**, *323*, 128664.
43. S. K. Arya, S. Bhansali, *Biosensors J.* **2012**, *1*, 1–7.
44. M. Samiei Foroushani, N. Niroumand, R. Karimi Shervedani, F. Yaghoobi, A. Kefayat, M. Torabi, *Bioelectrochemistry* **2019**, *130*, 107347.
45. B. Hirschorn, M. E. Orazem, B. Tribollet, V. Vivier, I. Frateur, M. Musiani, *Electrochim. Acta* **2010**, *55*, 6218–6227.
46. C. L. Alexander, B. Tribollet, M. E. Orazem, *Electrochim. Acta* **2015**, *173*, 416–424.
47. P. Van Hao, C. T. Xuan, P. D. Thanh, N.-T. Thuat, N. H. Hai, M. A. Tuan, *J. Sci. Adv. Mater. Devices* **2018**, *3*, 129–138.
48. P. Jakóbczyk, M. Kowalski, M. Brodowski, A. Dettlaff, B. Dec, D. Nidzworski, J. Ryl, T. Ossowski, R. Bogdanowicz, *Appl. Surf. Sci.* **2021**, *539*, 148286.
49. H. Li, T. Cai, Y. Ren, J. Huang, H. Jiang, Y. Hou, C. Tang, J. Yang, J. Zhao, P. Yu, *Anal. Methods* **2021**, *13*, 4442–4451.

50. M. Dąbrowski, A. Zimińska, J. Kalecki, M. Cieplak, W. Lisowski, R. Maksym, S. Shao, F. D'Souza, A. Kuhn, P. S. Sharma, *ACS Appl. Mater. Interfaces* **2019**, *11*, 9265–9276.

51. N. Xia, Z. Chen, Y. Liu, H. Ren, L. Liu, *Sens. Actuators B* **2017** *243*, 784–791.

52. X. Shen, Y. Ma, Q. Zeng, J. Huang, J. Tao, L. Wang, *ChemistrySelect* **2017**, *2*, 6549–6555.

SUPPORTING INFORMATION

Additional supporting information can be found online in the Supporting Information section at the end of this article.

ELECTROANALYSIS

Supporting Information

An electrochemical biosensor for the determination of hormone Human Chorionic Gonadotropin (hCG) in human serum

Adrian Koterwa[1] | Magdalena Bojko[2] | Jacek Ryl[3] | Krzysztof Łukaszuk[4, 5] |
Kornelia Kozłowska[1] | Wiktor Sieklicki[6] | Sylwia Rodziewicz-Motowidło[2] |
Paweł Niedziałkowski[1]

Supplementary Information

Electrochemical biosensor for the determination of hormone Human Chorionic Gonadotropin (hCG) in human serum

Adrian Koterwa,[a] Magdalena Bojko,[b] Jacek Ryl,[c], Krzysztof Łukaszuk,[d,e], Kornelia Kozłowska,[a] Wiktor Sieklicki,[f], Sylwia Rodziewicz-Motowidło,[b], Paweł Niedziałkowski,[a]*

a   Department of Analytical Chemistry, Faculty of Chemistry, University of Gdansk, Wita Stwosza 63, 80-308 Gdansk, Poland
b   Department of Biomedical Chemistry, Faculty of Chemistry, University of Gdansk, Wita Stwosza 63, 80-308 Gdansk, Poland
c   Institute of Nanotechnology and Materials Engineering and Advanced Materials Center, Gdansk University of Technology, Narutowicza 11/12, 80-233 Gdansk, Poland
d   INVICTA Research and Development Center Fertility and Reproductive Center, 80-850 Gdansk, Poland
e   Department of Obstetrics and Gynecological Nursing, Faculty of Health Sciences, Medical University of Gdansk, 80-210 Gdansk, Poland
f   Faculty of Mechanical Engineering, Gdansk University of Technology, ul. G. Narutowicza 11/12, 80-233 Gdańsk

*   e-mail: pawel.niedzialkowski@ug.edu.pl

Table S1. The results of the impedance analysis data with R(Q(RW)) applied as equivalent electrical circuits after each step of gold electrode modification.

Electrode	R_{ct} / Ω	Q / μSs^n	W / μSs$^{1/2}$	α /-	Chi^2
Au (bare)	986.9	4.52	169.8	0.79	1.61×10^{-04}
Au/Cys	337.8	2.42	165.4	0.82	5.34×10^{-05}
Au/Cys/Peptide	305.2	5.77	110.8	0.49	1.04×10^{-04}
Au/Cys/Peptide/hCG $C_{hCG} = 1 \times 10^{-7}$ (50 000 mIU/mL)	1014.00	1.36	170.4	0.87	7.71×10^{-05}

Table S2. The results of the impedance analysis data with R(Q(RW)) applied as equivalent electrical circuits in hCG hormone detection on electrochemical biosensor.

log ($C_{(hCG)}$ / M)	R_{ct} / Ω	Q / μSs^n	W / μSs$^{1/2}$	α /-	Chi^2
-14	294.80	2.79	170.30	0.81	6.49×10^{-05}
-13	355.40	2.30	171.00	0.83	6.90×10^{-05}
-12	411.00	2.13	169.70	0.83	5.83×10^{-05}
-11	546.50	1.72	171.70	0.85	8.71×10^{-05}
-10	687. 80	1.51	171.10	0.86	7.03×10^{-05}
-9	1014.00	1.36	170.4	0.87	7.71×10^{-05}

Table S3. Comparison of different method for detection of hCG based on the oligopeptide.

Modification	Method	Linear Range	LOD	Reference
Peptide aptametr/GO	SPR	8.32 - 0.065 nM	0.065 nM	[S1]
Peptide aptametr/AuNPs/4-nitrophenol	Colorimetry	15–750 mIU/mL	15 mIU/mL	[S2]
Peptide aptamer/AuNPs	Colorimetry	25–1000 mIU/mL	25 mIU/mL	[S3]
Peptide aptamer/GO	Fluorescence	0.05–20 IU/mL	20 mIU/mL	[S4]
Peptide aptametr	Liquid crystal	12.5-100 mIU/ml	1 IU/ml	[S5]
Au Electrode/AgNPs/Peptide aptametr /	LSV	1–200 mIU/mL	0.4 mIU/mL	[S6]
SPE/AuNPs/Peptide	EIS	5–1500 mIU/mL	5 mIU/mL	[S7]
Macroporous semi-covalently surface-imprinted MIP	Extended-gate field-effect transistors	0.8−50.6 fM	0.8 fM	[S8]
	Capacitive impedimetry	0.17−2.30 fM	0.17 fM	
MWCNTs based MIPs/GC Electrode	DPV	0.0005 – 250 ng/ml	0.000035 pg/mL	[S9]
Au Electrode /Peptide aptamer	EIS	1×10^{-12} to 1×10^{-9} M (0.5 mIU/mL – 500 mIU/mL)	1.91×10^{-14} M (0.0095 mIU/mL)	This work

Table S4. The results of the impedance analysis data with using R(Q(RW)) applied as equivalent electrical circuits after each step of hCG hormone detection in human serum using obtained biosensor.

Electrode	R_{ct} / Ω	Q / μSs^n	W / μSs$^{1/2}$	α /-	Chi^2
Au/Cys/Peptide	305.2	5.77	110.8	0.49	1.04×10^{-04}
Human serum (Blank)	140.6	2.82	162.5	0.83	1.10×10^{-04}
Reference Human serum containing 1×10^{-12} M (0.5 mIU/mL) hCG	328.1	1.43	164.5	0.80	7.71×10^{-05}
Human serum (blank) with 1×10^{-12} M (0.5 mIU/mL) hCG hormone addition	349.1	1.56	163.8	0.80	5.74×10^{-04}

Reference

[S1] N.-F. Chiu, C.-T. Kuo, T.-L. Lin, C.-C. Chang i C.-Y. Chen, *Biosensors and Bioelectronics*, **2017**, 94, 351–357.

[S2] C.-C. Chang, C.-P. Chen, C.-H. Lee, C.-Y. Chen i C.-W. Lin, *Chem. Commun.*, **2014**, 50, 14443–14446.

[S3] C.-C. Chang, C.-Y. Chen, C.-P. Chen i C.-W. Lin, *Anal. Methods*, **2014**, 7, 29–33.

[S4] N. Xia, X. Wang i L. Liu, *Sensors*, **2016**, 16, 1699.

[S5] X. Ding i K.-L. Yang, *Anal. Chem.*, **2013**, 85, 10710–10716.

[S6] N. Xia, Z. Chen, Y. Liu, H. Ren i L. Liu, *Sensors and Actuators B: Chemical*, **2017**, 243, 784–791.

[S7] H. Li, T. Cai, Y. Ren, J. Huang, H. Jiang, Y. Hou, C. Tang, J. Yang, J. Zhao i P. Yu, *Anal. Methods*, **2021**, 13, 4442–4451.

[S8] M. Dąbrowski, A. Zimińska, J. Kalecki, M. Cieplak, W. Lisowski, R. Maksym, S. Shao, F. D'Souza, A. Kuhn i P. S. Sharma, *ACS Appl. Mater. Interfaces*, **2019**, 11, 9265–9276.

[S9] X. Shen, Y. Ma, Q. Zeng, J. Huang, J. Tao i L. Wang, *ChemistrySelect*, **2017**, 2, 6549–6555.

Full Length Article

The role of electrolysis and enzymatic hydrolysis treatment in the enhancement of the electrochemical properties of 3D-printed carbon black/poly(lactic acid) structures

Adrian Koterwa [a,1], Iwona Kaczmarzyk [b,1], Szymon Mania [c], Mateusz Cieslik [c,d], Robert Tylingo [c], Tadeusz Ossowski [a], Robert Bogdanowicz [b], Paweł Niedziałkowski [a], Jacek Ryl [d,*]

[a] Department of Analytical Chemistry, University of Gdansk, Wita Stwosza 63, 80-308 Gdansk, Poland
[b] Department of Metrology and Optoelectronics and Advanced Materials Center, Gdansk University of Technology, Narutowicza 11/12, 80-233 Gdansk, Poland
[c] Faculty of Chemistry, Gdansk University of Technology, Narutowicza 11/12, 80-233 Gdansk, Poland
[d] Institute of Nanotechnology and Materials Engineering and Advanced Materials Center, Gdansk University of Technology, Narutowicza 11/12, 80-233 Gdansk, Poland

ABSTRACT

Additive manufacturing, also known as 3D printing, is beginning to play an unprecedented role in developing many applications for industrial or personalized products. The conductive composite structures require additional treatment to achieve an electroactive surface useful for electrochemical devices. In this paper, the surfaces of carbon black/poly(lactic acid) CB-PLA printouts were activated by electrolysis or enzymatic digestion with proteinase K, or a simultaneous combination of both. The proposed modification protocols allow the tailoring of electrochemically active surfaces and electron transfer kinetics determined by electrochemical techniques (CV, EIS) by $[Fe(CN)_6]^{4-/3-}$ redox probe. X-ray photon spectroscopy and SEM imaging were applied to determine the delivered surface chemistry. CB-PLA hydrolysis under alkaline conditions and anodic polarization greatly impacted the charge transfer kinetics. The enzymatic hydrolysis of PLA with proteinase K led to highly efficient results, yet requires an unsatisfactory prolonged activation duration of 72 h, which can be efficiently reduced by electrolysis carried out in the presence of the enzyme. Our studies hint that the activation protocol originates from surface electropolymerization rather than a synergistic interaction between the electrolysis and enzymatic hydrolysis. The detailed mechanism of CB-PLA hydrolysis supported by electrolysis is a promising new route to achieve time-efficient and environmentally-friendly activation procedure.

1. Introduction

The advent of Additive Manufacturing (AM), also known as 3D printing, has an unprecedented impact on development in various fields, including science, engineering and industry. As a result, affordable desktop three-dimensional printers, based on fused deposition modeling (FDM), have become a popular tool for fabricating personalized consumer products. Fused deposition modeling or fused filament fabrication (FFF) are the most commonly utilized and commercially successful methods due to their low cost, easy-to-use interface and graphic software. Furthermore, the expiration of the original FDM patents has led to a growing market in extrusion-based printers. The development of desktop extrusion-based printers opens up ways to approach new areas, including biomedical sensors [1], electronics, chemistry [2], pharmaceutics [3] and medicine [4], partly because they are inexpensive to own and operate. Furthermore, they are eco-friendly, encourage fast prototyping, and give the possibility to design objects featuring specific shapes.

Polylactic acid (PLA) is one of the most promising materials used nowadays. It is biodegradable, recyclable, highly processable, and degrades into non-toxic products [5,6]. High conductive fillers such as graphene, carbon black (CB) and carbon nanotubes (CNT), dispersed in the thermoplastic polymer matrix, are used to achieve electrically conductive filaments. Developments in FFF and commonly available conductive filaments allow the fabrication of sensors for various applications, flow cells [7], and microfluidic devices [8]. 3D printed

---

* Corresponding author.
  E-mail address: jacek.ryl@pg.edu.pl (J. Ryl).
[1] These authors contributed equally to the manuscript.

electrodes have been used for numerous electrochemical applications, including sensing dopamine, catechol, 2,5,6-trinitrotoluene (TNT) [9] and glucose, the simultaneous determination of uric acid and nitrite [10], energy storage devices [11], etc. Among the various available materials, one of the most popular is carbon black/PLA (CB-PLA) conductive composite. Carbon Black is a material made of finely divided carbons produced by the thermal decomposition of a hydrocarbon. Conductive carbon particles in CBs are chemically bound and form agglomerates by weak Van der Waals interactions [12]. The conductivity of CB-PLA is dominated by percolation, which means that the addition of conductive fillers has little effect until enough filler is present to form a continuous particle pathway through the material. Recent research indicate that 3D-printed CB/PLA electrodes have promising applications as electrochemical sensors, including fuel electroanalysis [13], electrochemical cells for detection of mercury ions [14], caffeine and glucose [15], simultaneous determination of cadmium and lead ions in biological fluids [16], etc.

New carbon/polymer 3D-printout electrodes present poor electrochemical properties prior to the application of a surface activation treatment. The activation treatments remove the excess polymeric matrix to expose conductive fillers at the electrode surface. It has been well documented that the chemical activation of carbon/polymer electrodes improves the efficiency of electrochemical processes. Manzanares-Palenzuela et al. reported the surface treatment of graphene-PLA (G-PLA) by immersion in dimethylformamide (DMF) for 10 min exposed the graphene fillers [31] successfully. However, the most commonly used DMF has a negative impact on the environment. Therefore, other activation surface treatments are being investigated. One of them is electrochemical treatment in NaOH, which has highly improved the electrochemical response significantly. For example, Rocha et al. [16] studied the electron transfer after surface treatment in 0.5 mol L^{-1} NaOH by applying a constant potential of 1.4 V for 200 s and then −1.0 V for 200 s. The proposed electrochemical surface treatment by Richter et al. was used in a fully additively manufactured electrochemical sensing platform [17]. Furthermore, Browne et al. demonstrated that a combined DMF treatment and electrochemical activation process improves the activity of the 3D-printed G-PLA electrodes. Solvent treatments were performed by soaking the 3D-printed electrodes in DMF for 10 min, which was completed prior to electrochemical activation. Next, electrochemical activation of the 3D electrodes was carried out in a phosphate buffer solution (pH 7.2) using a chronoamperometry method at high oxidizing potentials for a range of times [18]. PLA, belonging to the aliphatic polyester group, is usually hydrolyzed by esterases, lipases or proteases. Acid and neutral proteases have little or no activity, but some alkaline proteases are able to form appreciable amounts of lactic acid from PLA [19]. The hydrolytic activity of enzymes depends on many factors, including pH and temperature. Successful Proteinase K-catalyzed G-PLA digestion was recently reported by Manzanares-Palenzuela et al. [20], opening a new environmentally friendly and reproducible alternative to the surface activation procedure of PLA-based 3D printed electrodes. Solvent-free activation by laser ablation was recently proposed by Glowacki et al. [21]. Further examples of post-treatment procedures for 3D-printed surfaces for electrochemical applications are presented in an interesting mini-survey by Rocha et al. [22].

This work aims to present and understand the electrochemically active surface area development of CB-PLA through controlled electrolysis, with the goal of increasing the electrode's utility as an electrochemical sensor platform.

Various polarization protocols were studied to evaluate the optimum conditions for CB-PLA activation. First, the anodic and cathodic polarization depth were evaluated for PLA electrolysis carried out in acidic and alkaline media, discussing the resultant modification to the surface chemistry and the activation mechanism. A separate study was conducted to develop the CB-PLA activation protocol by proteinase K enzymatic interaction. Finally, the efficiency of the synergistic

interaction of enzymatic hydrolysis and electrolysis were reported. To the authors best knowledge, this is the first attempt to explore activation potential through both of these processes, carried out simultaneously.

2. Experimental

3D printout electrodes: Flat electrodes with the dimensions 10x10x2 mm were 3D-printed from conductive, commercially available PLA, Proto-Pasta, on an Ender 3 Pro 3D printer (Ender, China). The electrodes were horizontally printed with the parallelly-oriented layers versus the load direction. The printing temperature was 200 °C. According to the thermogravimetric analysis (presented in the **Supplementary Information file, Section S1**), the CB-PLA filament contained 26.4 wt% carbon filler, which resulted in 30 Ωcm electric resistivity. The filament, as well as the electrodes, were stored under atmospheric conditions.

Activation protocols: The activation procedure was started immediately after the printing process. Chemical, electrochemical and enzymatic activation protocols were investigated. The electrochemical activation was carried out in acidic (1 M HCl solution, pH = 0) and alkaline (1 M NaOH solution, pH = 14) media. The activation was performed by potentiodynamic polarization scan at a constant rate of 50 mV/s for various polarization ranges. Each electrode was subjected to a total of 10 polarization cycles. The chemical and enzymatic activation treatments simply involved soaking the electrode in the target electrolyte. Solvent treatments were performed by soaking the 3D-printed electrodes in one of the studied electrolytes for 24 h. For determination of the effect of enzyme activity on the CB-PLA, two tests were performed. For the first, each 3D-printed specimen was immersed in a 0.6 mg /mL proteinase K solution prepared in a Tris-HCl buffer (Tris 100 mM, $CaCl_2$ 1 mM, pH = 8.0) and incubated at 37 °C for 24 h, 48 h, 72 h and 96 h. For the second, each 3D-printed specimen was immersed in a proteinase K solution with 0.2 mg/mL, 0.4 mg/mL, 0.6 mg/mL and 0.8 mg/mL prepared in Tris-HCl buffer (Tris 100 mM, $CaCl_2$ 1 mM, pH = 8.0) and incubated at 37 °C for 72 h. The enzyme/buffer was replaced every 24 h to restore enzymatic activity, avoiding pH value decrease. After CB-PLA electrochemical activation was finished, the samples were rinsed thoroughly with distilled water at 4 °C to stop further degradation, and then dried to achieve a constant mass. The mass loss (%) was calculated according to $(m_0 - m_t)/m_0$, where m_0 and m_t represent the dry weights of the specimens before and after degradation, respectively.

Electrochemical studies: All the electrochemical measurements, including electrochemical activation and the electrochemically active surface area (EASA) determination of the electrode, were carried out in a three-electrode setup with the 3D-printed working electrode, Ag|AgCl as the reference electrode and platinum wire as the counter electrode. The electrochemical measurements were made using a Reference 600 + potentiostat/galvanostat (Gamry Instruments, USA), controlled by Gamry Framework software.

Determination of the surface activation efficiency was based on evaluation of charge transfer kinetics in an electrolyte composed of 2.5 mM $[Fe(CN)_6]^{4-}$ and 2.5 mM $[Fe(CN)_6]^{3-}$ as the electroactive redox species dissolved in 0.5 M Na_2SO_4. Studies were performed in 5 mL electrochemical cells in naturally aerated electrolytes. Two techniques were used, namely electrochemical impedance spectroscopy (EIS) and cyclic voltammetry (CV). The EIS experiment was carried out under open circuit potential (OCP) conditions (0.25 ± 0.04 V vs Ag|AgCl), with a voltage perturbation amplitude of 10 mV, and for the frequency range of 100 000 to 0.1 Hz, 10 points per frequency decade. The CV experiments were done at a scan rate of 50 mV/s. The $[Fe(CN)_6]^{4-/3-}$ species were used as the most commonly referred redox-active probe. Moreover, the inner sphere electron transfer (ISET) mechanism of the ferrocyanides is known to be largely dependent on the electrode surface chemistry [23,24]. Thus, we found this redox probe to be particularly valuable in differentiating the efficiency of the surface activation protocols.

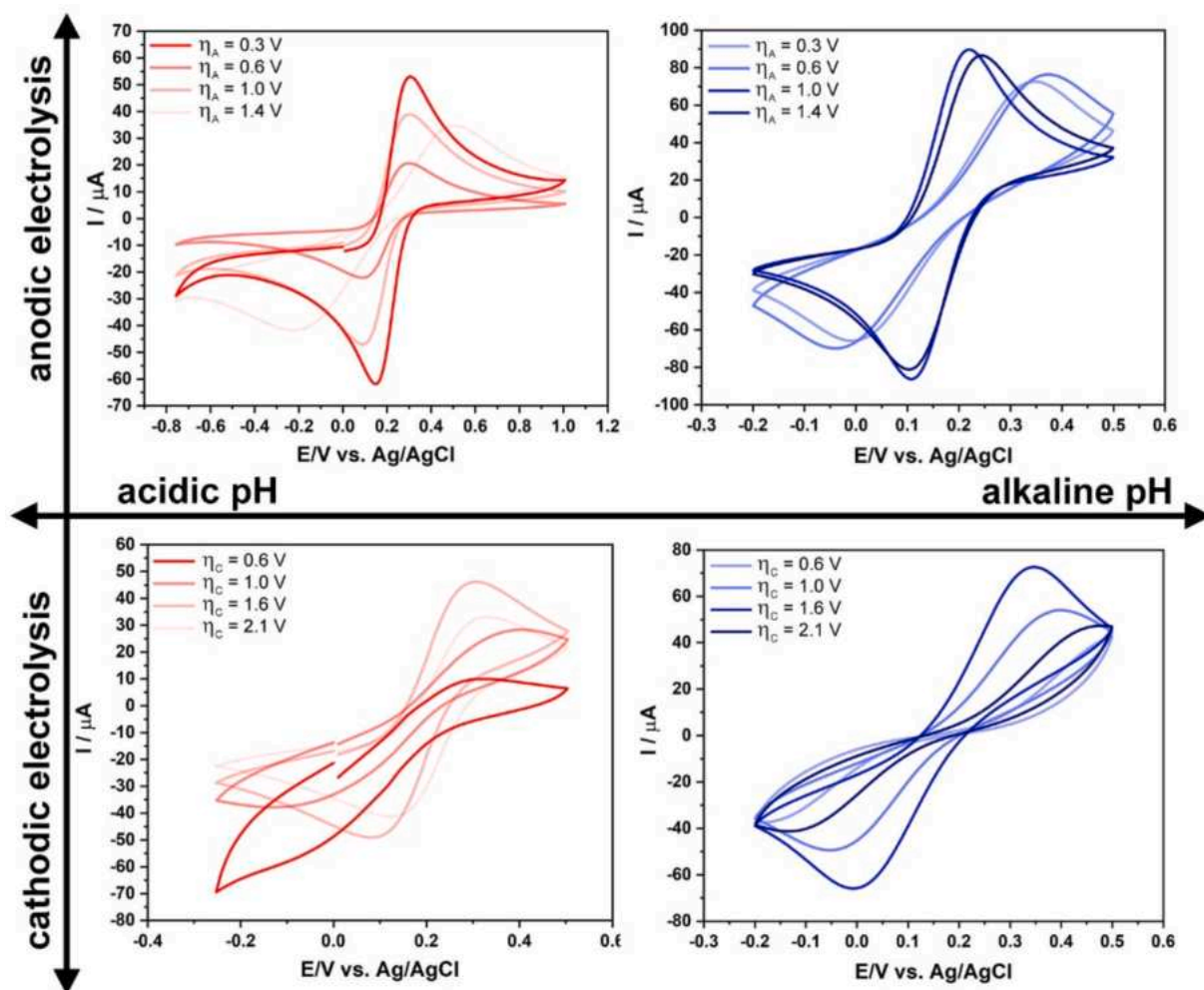The standard heterogeneous rate constant k^0 was estimated from the

Fig. 1. a) CV curves reflecting charge transfer kinetics through the electro-activated CB-PLA electrode depending on the direction and depth of electrochemical polarization, carried out in an electrolyte with acidic (1 M HCl) and alkaline (1 M NaOH) media. Electrolyte: 0.5 M Na_2SO_4 + 5 mM $[Fe(CN)_6]^{4-/3-}$. Polarization scan rate 50 mV/s.

CV studies at a scan rate of 50 mV/s or 10 mV/s (when the electron transfer was found irreversible at higher scan rates), using the Nicholson approach, with Eq. (1) [25,26]:

$$k^0 = \psi \left(\pi D_0 \frac{nFv}{RT} \right)^{1/2} \tag{1}$$

where ψ is the dimensionless kinetic parameter estimated from the literature based on peak potential separation ΔE_P [25], D_0 is the diffusion coefficient (6.67×10^{-6} cm^2/s), n is the number of electrons transferred, v is the applied scan rate, R is the gas constant, F is the Faradaic constant and T is the temperature.

Physicochemical studies: The X-Ray photoelectron spectroscopy (XPS) studies were carried out with an Escalab 250Xi multispectroscope (Thermo Fisher Scientific, USA), equipped with a monochromatic AlKα source (spot diameter 650 μm). The high-resolution spectra of CB-PLA electrodes after various surface activation routes were collected in the core-level binding energy range of the *C 1s* and *O 1s* peaks. The pass energy was 15 eV. Charge compensation was controlled through a low-energy electron and low-energy Ar$^+$ flow. Next, the scanning electron microscopy (SEM) examination of the surface activated samples was carried out using an S-3400N VP-SEM microscope (Hitachi, Japan), using the secondary electron mode and 20 kV accelerating voltage. Prior to the examination, the CB-PLA electrodes were sputtered with a 10 nm gold layer.

3. Results and discussion

3.1. The CB-PLA electro-activation by PLA electrolysis

The efficiency of the electrochemical activation of each CB-PLA electrode, illustrated through CV curves, is shown in Fig. 1. The CB-PLA electrodes were subjected to potentiodynamic polarization treatment under various applied anodic (η_A) or cathodic (η_C) overpotentials, with the aim of evaluating the effect of the electrolysis on the surface electro-activation efficiency.

The results displayed in Fig. 1 confirm that the electrochemical treatment significantly enhances the charge transfer kinetics at the electrode interface, proving their successful activation, both in acidic and alkaline environments. Moreover, the charge transfer is strongly affected by the polarization direction and the polarization depth. In comparing the efficiency of the ferrocyanide/ferricyanide ion oxidation/reduction process, it should be concluded that exceptionally high efficiency is obtained by applying anodic overpotential at the electrode surface.

Ferrocyanide oxidation proceeded more efficiently at the CB-PLA electrode activated in the alkaline media than in the acidic media. The electrochemical surface area development in alkaline media was testified by the significant increase in measured redox currents ($i_A = 86.3$ vs 57.5 μA for alkaline vs acidic media, scan rate 50 mV/s). The charge transfer reversibility improved as well after activation in NaOH, testified

Table 1
The CV characteristics of the $[Fe(CN)_6]^{4-/3-}$ redox at the CB-PLA electrodes, obtained after various polarization treatments in 1 M HCl or 1 M NaOH electrolyte.

	1 M HCl				1 M NaOH			
η_A/V	**0.3**	**0.6**	**1.0**	**1.4**	**0.3**	**0.6**	**1.0**	**1.4**
ΔE_p/mV	443	282	192	151	356	413	112	140
i_A/μA	37.8	42.6	23.2	57.5	65.9	69.9	86.3	81.2
i_A:i_C/-	1.01	1.00	0.90	0.95	0.91	0.91	0.96	0.94
k^0/cm/s	$3.2 \cdot 10^{-4}$	$5.1 \cdot 10^{-3}$	$9.6 \cdot 10^{-4}$	$1.4 \cdot 10^{-3}$	$3.8 \cdot 10^{-4}$	$3.2 \cdot 10^{-4}$	$2.7 \cdot 10^{-3}$	$1.6 \cdot 10^{-3}$
η_C/V	**0.6**	**1.1**	**1.6**	**2.1**	**0.6**	**1.1**	**1.6**	**2.1**
ΔE_p/mV	–	390	159	180	687	447	356	615
i_A/μA	12.2	27.3	46.2	33.7	37.5	49.4	65.9	41.3
i_A:i_C/-	–	0.74	0.90	0.80	0.88	0.91	0.91	0.87
k^0/cm/s	–	$3.8 \cdot 10^{-4}$	$1.3 \cdot 10^{-3}$	$9.6 \cdot 10^{-4}$	$1.9 \cdot 10^{-4}$	$3.2 \cdot 10^{-4}$	$3.8 \cdot 10^{-4}$	$1.9e \cdot 10^{-4}$

by $\Delta E_p = 112$ mV and i_A:$i_C = 0.96$ ($\eta_A = 1.0$ V, scan rate 50 mV/s). Given the CB-PLA activation was carried out at sufficiently high anodic polarization, the electrolysis led to higher values of k^0 and more effective redox kinetics. This effect was observable in particular at η_A exceeding 0.6 V, when the observable value of k^0 increased by an order of magnitude, peaking at 0.003 cm/s, the exact values can be found in Table 1. The considerable improvement in electron charge transfer was probably due to removing the polylactide matrix and exposing conductive CB fillers at the electrode surface. The efficiency of the activation process was more evident in alkaline media, where the oxidation peak current reached 90 μA after CB-PLA activation at the highest studied η_A. However, even when the activation was carried out at much smaller potentials, not exceeding + 0.5 V vs. Ag|AgCl, the redox process kinetics was considerable, with $i_A = 66$ μA.

The highest value of the heterogeneous rate constant k^0 after activation in acidic media was only half that, and achieved after activation at the highest anodic overpotentials applied during the activation process, with oxidation peak current i_A reaching 57.5 μA (at 50 mV/s scan rate). Nevertheless, the peak separation potential at the most efficient studied η_A was $\Delta E_P = 151$ mV, which, together with a slightly unbalanced anodic-to-cathodic current ratio i_A:$i_C = 0.95$, hints at the irreversibility of the electrochemical process. Notably, the activation performed in both studied electrolytes may lead to obtaining the quasi-reversibility regime of the redox process [27].

A key observation should also be made based on the analyses of these results. The CB-PLA electrodes should be handled with great care since the polarization regime of commonly used CV procedures when using the most popular redox probes often exceed the polarization limits sufficient for CB-PLA surface modification throughout the measurement. On the other hand, most research groups dealing with 3D printed electrodes study the electron charge transfer using potassium hexacyanoferrate(II) as the redox probe [16,18]. The impedimetric measurements may be found to be a more suitable approach to investigating the electrochemical response of 3D-printed PLA-based electrodes, which is due to the mV polarization range of the perturbation amplitude.

The polarization curves registered during the surface activation treatment are given in the Supplementary Information file, Section S2. The sole action of the studied electrolyte, in the absence of electrode polarization, is given in the Supplementary Information file, Section S3. The obtained results indicate that surface activation by PLA hydrolysis in the absence of the polarization component is also the most effective when hydrolysis in carried out in the alkaline environment, assuming a well-developed EASA and electron transfer rate. On the other hand, with very slow electron transfer kinetics of only partially-surface activated electrodes in the acidic and neutral pH environments, the obtained results were poor, without defined redox peaks. The increased PLA susceptibility to saponification in alkaline solution could be explained by more effective PLA hydrolysis under these conditions and thus better exposure of the conductive CB nanoparticles at the electrode surface. Most notably, the surface activation in 1 M NaOH under cyclic
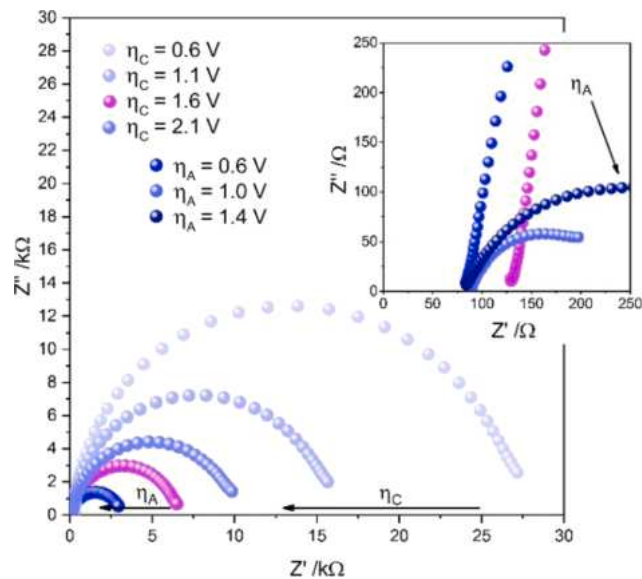

Fig. 2. EIS spectra for CB-PLA electrodes electrochemically activated under different potentiodynamic polarization conditions, in 1 M NaOH. Studies carried out in 0.5 M Na_2SO_4 + 5 mM $[Fe(CN)_6]^{4-/3-}$.

polarization conditions was found to be a time-efficient and environmentally-friendly alternative to etching in aprotic solvents such as DMF.

While anodic activation treatment leads to the pronounced CB-PLA EASA development, performing the activation process at cathodic polarization to a certain extent increases the faradaic charge transfer. However, the activation efficiency is dramatically lower, and the resultant heterogeneous rate constant barely competes with the k^0 value obtained after activation at the lower studied anodic polarization (see Supplementary Information file, Section S4 for a graphical representation). These results prove the smaller utility of cathodic polarization treatment as a part of the 3D-printed electrode activation protocol [17,28]. Overall, the optimum electrochemical activation polarization range was determined to be from −1.4 V to +1.2 V vs. Ag/AgCl, where the smallest peak-to-peak separation and the highest redox probe faradaic current were achieved. The voltammetric EASA estimation for the optimal conditions of the electro-activation protocol is given in Supplementary Information file, Section S5. The obtained EASA value of 0.204 cm^2 is nearly the same as the electrolyte-exposed CB-PLA geometric surface, suggesting successful activation, where evenly distributed CB nanoparticles produce heavily overlapping diffusion layers [29].

A similar observation regarding the CB-PLA EASA development efficiency was made based on the electrochemical impedance spectroscopy measurements of the studied electrodes. These results were carried

Table 2
The electric parameters obtained for CB-PLA electro-activation in 1 M NaOH for each studied electrochemical polarization condition.

	η/V	R_{CT}/kΩ	Q/μSs^n	α/-
$η_C$	0.6	27.41	2.47	0.93
	1.1	15.85	4.08	0.94
	1.6	6.41	5.57	0.95
	2.1	9.92	4.97	0.93
$η_A$	0.3	6.41	5.57	0.95
	0.6	3.05	5.81	0.93
	1.0	0.16	43.92	0.80
	1.4	0.34	46.45	0.70

out in a 1 M NaOH solution, which was found highly effective for the activation process. The Nyquist plots are given in Fig. 2.

The impedance data were analyzed using an R(QR) electric equivalent circuit (EEC) built of a series resistance R_S (sum of the resistances of electrolyte, electrode, wires etc.) and a parallel connection of a charge transfer resistance (R_{CT}) and constant phase element (CPE) representing the electric double-layer capacitance of a heterogeneous electrode. The impedance of the CPE may be defined with Eq. (2) [30].

$$Z_{CPE} = \frac{1}{Q(j\omega)^\alpha} \tag{2}$$

where Q is the quasi-capacitance, j is the imaginary number, and ω is the angular frequency. For α = 1, the CPE represents the ideal capacitor, and lower α values are introduced by frequency dispersion of capacitance due to heterogeneous charge transfer at the electrode/electrolyte interface [30,31]. The electric parameters from the fitting procedure with the selected EEC are given in Table 2.

Altering the cathodic polarization potentials during the electrochemical activation of CB-PLA electrodes influences the charge transfer resistance. Compared with the previously presented untreated CB-PLA electrode (R_{CT} = 326 kΩ), the R_{CT} parameter drops by one order of magnitude yet does not fall below 6 kΩ (98% efficiency) regardless of the applied cathodic polarization depth limit. On the other hand, the deeper the anodic polarization range, the lower the R_{CT} value. In particular, for $η_A$ > 0.6 V, the R_{CT} drops by another order of magnitude to 160.3 Ω at $η_A$ = 1.0 V, which exceeds 99.9% activation efficiency. Notably, the EIS-measured R_{CT} characteristic of the surface-activated CB-PLA electrodes corroborates the CV-measured i_A and k^0. An interesting feature was observed when analyzing the CPE-exponent α changes, suggesting that the electric heterogeneity of each cathodically-activated CB-PLA electrode surface was similar and only decreased if the activation procedure was carried out with deep anodic polarization limits ($η_A$ > 0.6 V). There are few possible explanations of such characteristics. Most likely, highly efficient uncovering of the conductive CB particles leads to the appearance of the surface distribution of the time-constant dispersion, falling in the mechanism of heavily overlapping diffusion layers at spatially heterogeneous electrodes [29,32]. The second plausible cause is the introduction of the normal distribution of the time constants through the appearance of the porous electrode surface.

The high-resolution XPS spectra were recorded in the *C 1s* (Fig. 3a) and *O 1s* (Fig. 3b) core-level binding energy range to determine the CB-PLA surface chemistry resulting from various electro-activation protocols and PLA etching. The untreated, 3D printed CB-PLA electrode was also studied for comparison purposes.

The polylactide chemistry includes three different carbon chemical states, namely C-C, C-O, and C = O. These three types of chemical bonds are commonly identified in the *C 1s* spectra as signals peaking at a binding energy of 284.6 eV (C2), 286.0 (C3), and 288.1 eV (C4),
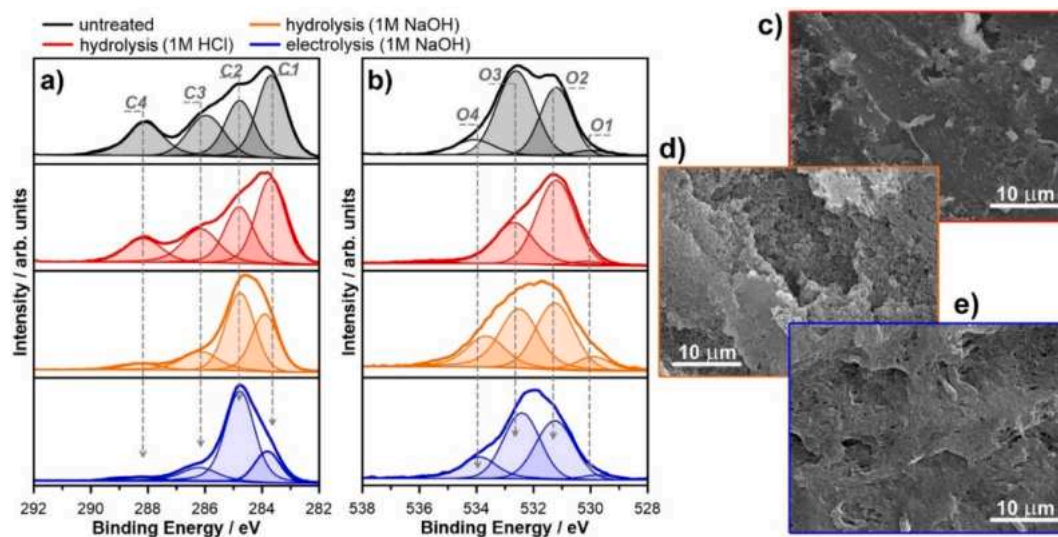

Fig. 3. a,b) XPS spectra registered in a) C 1s and b) O 1s binding energy range for the untreated CB-PLA electrode and after its electro-activation using various protocols, c-e) SEM micrographs of the CB-PLA electrode surface after hydrolysis in c) 1 M HCl and d) 1 M NaOH, and e) electrolysis in 1 M NaOH (−1.4 to +1.2 V vs. Ag|AgCl polarization range).

Table 3
The CB-PLA surface chemistry (in at.%) in terms of various chemical states of carbon and oxygen, based on XPS analysis with the deconvolution model.

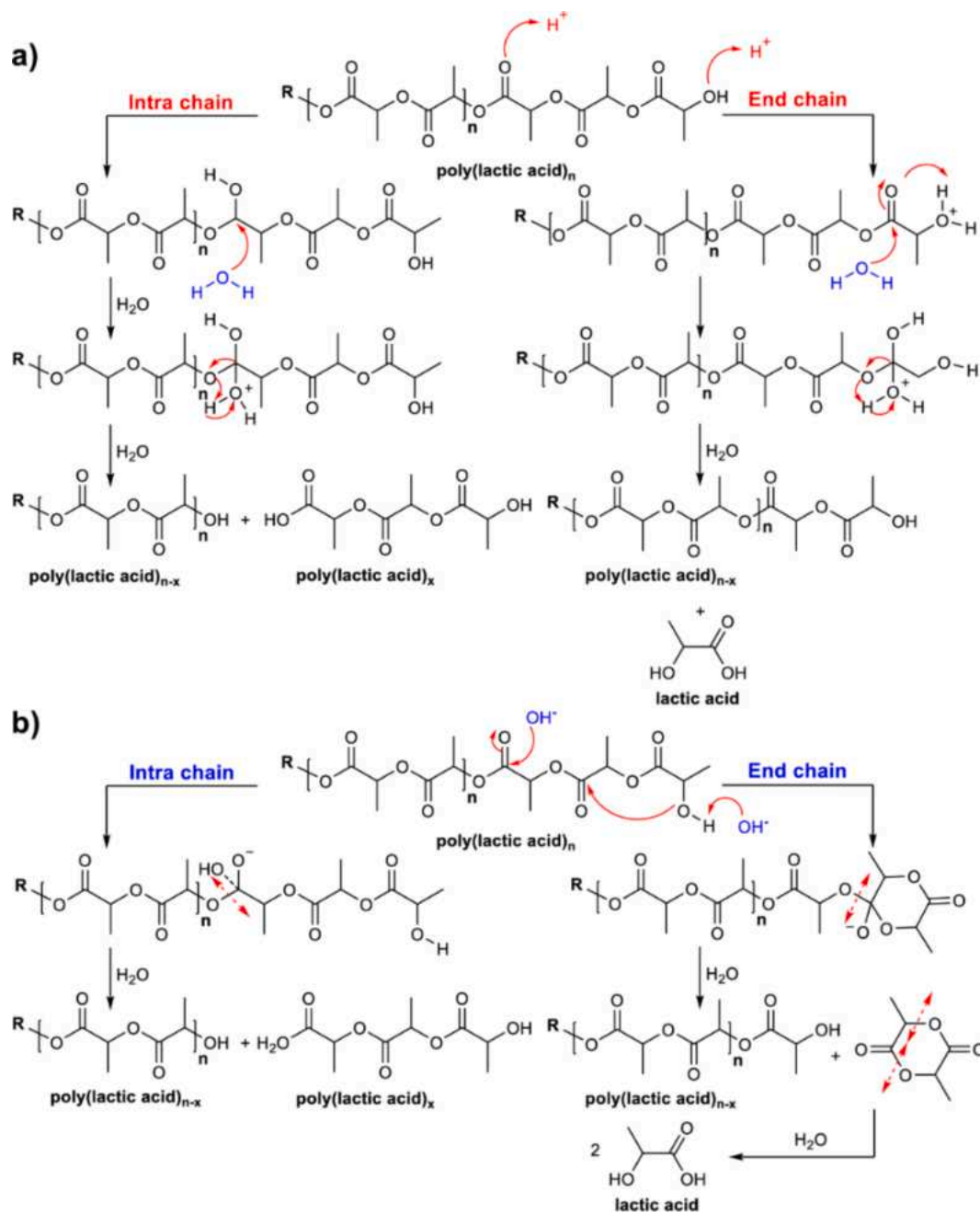|		*C 1s*				*O 1s*			
		C1	C2	C3	C4	O1	O2	O3	O4
BE/ eV		283.7	284.6	286.0	288.1	529.9	531.2	532.7	534.1
Untreated		27.0	18.6	15.9	14.6	1.0	8.4	12.2	2.4
Hydrolysis	HCl	26.5	18.0	13.9	9.1	0.9	19.8	11.3	0.5
	NaOH	29.2	41.4	14.4	4.2	0.9	4.0	3.9	2.1
Electrolysis	NaOH	16.0	55.6	11.1	2.7	0.5	5.7	6.2	2.3

Fig. 4. The mechanism PLA hydrolysis in an a) acidic, b) alkaline environment.

respectively [21,33,34]. Furthermore, their expected ratio for PLA matrix should be 1:1:1. A similar ratio of C2:C3:C4 components was found for the untreated sample. The aliphatic C-C bonds (C2) dominated due to the simultaneous detection of surface adventitious carbon contaminants from atmospheric exposure [35]. The most prominent component (C1) recorded in the untreated PLA *C 1s* spectra lies in the energy range characteristic to the sp²-carbon in CB [21,36,37], revealing that the approx. 27 at.% signal originates from the composite filler, corroborating the thermogravimetric analysis. The data are presented in Table 3. The oxygen chemistry analyzed for the untreated sample may also be divided to four different types of interactions. The dominant two, O2 and O3, are characteristic of C = O and C-O bonds, respectively, originating primarily from the polylactide matrix. Two minor oxygen components were also identified, first the O1 at 529.9 eV, a value typical for metal oxides, impurities to commercially available PLA filaments originating from thermal stabilizers and plasticizers [38]. Finally,

oxygen in chemisorbed water molecules may result in the signal appearing at approx. 534 eV, identified as O4 [34,39].

Both carbon and oxygen chemistry are significantly affected by the applied CB-PLA surface activation protocols, yet the mechanism of the interaction based on the obtained XPS results is complex and possibly different in each case. The hydrolysis process, carried out in an aqueous 1 M hydrochloric acid solution, appears to lead to a significant increase in the share of oxygen content of 24 at.% for the untreated CB-PLA electrode up to 32.3 at.%. On the other hand, due to the PLA treatment in the alkaline environment, the amount of surface oxygen atoms is halved. This observation is visible with and without activation by electrolysis. Other XPS studies on the CB-PLA activation reveal similar effects, where a significant share of oxide groups is found for O₂ plasma compared with CO₂ [40] as well as laser ablation in air compared with a He atmosphere [21]. The above-described change is primarily recognized as the increase of C-O and C = O interactions, while the share of
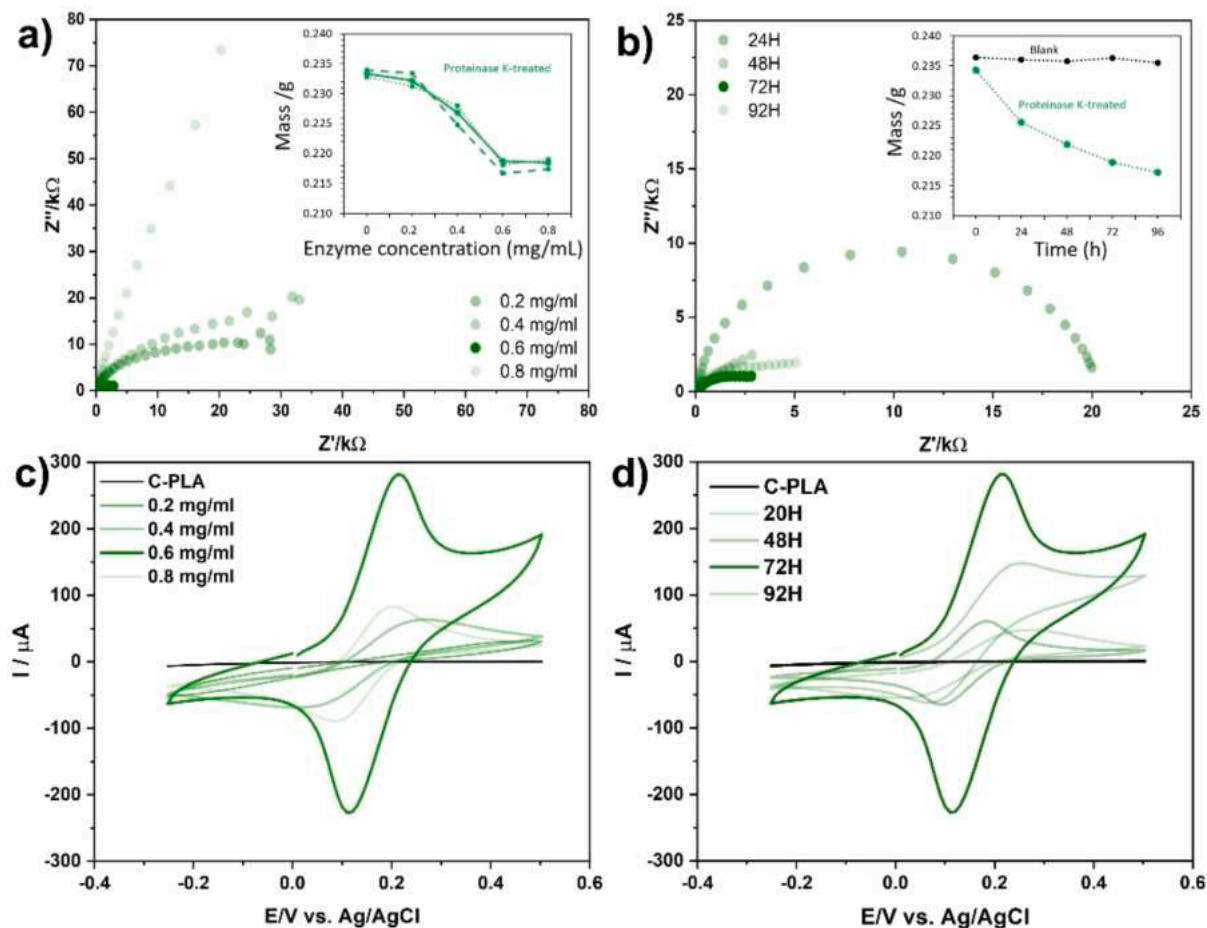
Fig. 5. a,b) CV curves and c,d) EIS spectra reflecting alteration of charge transfer kinetics, depending on various studied proteinase-K digestion conditions, i.e. a,c) enzyme concentration and b,d) enzymatic hydrolysis time. Mass variation during CB-PLA electro-activation in the inset: a) 72 h activation, b) 0.6 mg/mL proteinase-K concentration.

O1 and O4 components is negligibly affected by the chemical oxidation process and does not exceed 1.4 and 2.4 at.%, respectively. This effect will be discussed later.

The exposure of the electrically conductive carbon black filler at the CB-PLA surface is evident based on the increase in charge transfer kinetics through the activated electrode. However, this observation is not confirmed by the rise in *C 1s* carbon black nanofiller C1 component share. This is an important yet unexpected observation, confirmed by each studied activation procedure, either through PLA hydrolysis or electrolysis. One possible explanation of this mechanism may originate from partial oxidation of the sp²-carbon filler material. The excessive oxidation of the electrode surface during the electrolysis process was presumably the cause of the more irreversible charge transfers observed after anodic electrochemical activation of 3D printed CB-PLA electrodes by Vaněčková et al. [41]. According to this hypothesis, the amount of CB exposed at the electrode surface increases, yet its oxidation leads to a positive binding energy shift towards energies characteristic for the C2 or even C3 components, superimposing with the PLA-based features. A possible confirmation of the above-presented explanation may be found in our recent XPS examination of the surface PLA treatment by laser ablation in an air and helium atmosphere, leading to CB-PLA electrochemical activation. Laser ablation in an air atmosphere is characterized by a nearly 25% decrease of C1 with a similar increase in C2 peak share. On the other hand, the noble gas matrix does not lead to CB oxidation, resulting in an over 20% C1 increase and only a 7% C2 increase compared with the results of the untreated CB-PLA electrode [21].

An optional explanation of the above phenomenon is the rapid surface area development of the CB-PLA electrode due to PLA hydrolysis

process, leading to breaking of the ester bond and an increase in the amount of aliphatic C-C bonds at the surface, confirmed by a rapid decrease of C = O bonds (C4, O2 peaks), in particular in an alkaline environment. The development of the surface area will also result in an increased amount of surface-adsorbed adventitious carbons. Surface area development is visible on SEM micrographs, see Fig. 3c-e. A possible mechanism for the PLA hydrolysis is presented in Fig. 4. The decrease in C1 share may also be attributed to the detaching of loosely linked conductive carbon nanoparticles by PLA hydrolysis or a binding energy shift resulting from the disappearance of C-C bonds between the CB and the polymer [42]. Notably, the above-proposed hypotheses do not exclude each other, and both may co-occur, although verification requires independent studies.

The hydrolysis of the PLLA (poly(L-lactic acid) ester bonds occurs in acidic and alkaline environments. It is well known that the hydrolytic degradation of ester bonds is slow in aqueous conditions, while it is much faster in alkaline environments than in acidic ones [43]. The efficiency of PLLA hydrolysis is very slow in neutral pH and moderate acidic and alkaline solutions. Therefore, the activation of the CB-PLA surface was performed in strongly acidic (pH = 0) and alkaline (pH = 14) media, with the hydrolytic degradation being much faster in the latter. The mechanism of PLA hydrolysis previously proposed by Lucas et al. [44] involves two paths of degradation by intrachain or end chain of the PLA regardless of the environment.

The mechanism of PLA hydrolysis performed in an acidic solution involves the protonation of the hydroxyl groups end groups, which leads to the formation of intramolecular hydrogen bonds and contributes to the hydrolysis reaction and the formation of free lactic acid, causing the

Table 4

CV characteristics of the $[Fe(CN)_6]^{4-/3-}$ redox at the CB-PLA electrodes, obtained at various proteinase K digestion conditions, measured at polarization at a scan rate of 50 mV/s.

η_A/V	Concentration/mg/mL				Activation time/h			
	0.2	0.4	0.6	0.8	20	48	72	92
ΔE_P/mV	–	201	91	111	221	250	91	141
i_A/μA	–	54.5	222.4	87.0	44.4	60.2	222.4	80.9
$i_A{:}i_C$/-	–	1.04	0.96	1.04	1.06	1.01	0.96	1.00
k^0/cm/s	–	$7.7 \cdot 10^{-4}$	$4.8 \cdot 10^{-3}$	$2.9 \cdot 10^{-3}$	$5.8 \cdot 10^{-4}$	$5.4 \cdot 10^{-4}$	$4.8 \cdot 10^{-3}$	$1.6 \cdot 10^{-3}$

decrease in length of PLA. On the other hand, the acidic conditions lead to the random protonation of the carbonyl group and the PLA oxygen leads to the intramolecular hydrolysis of the ester bonds in the PLA chain. This reaction causes the degradation of the polymer and the formation of PLA chains consisting of lower molecular weights (Fig. 4a). The hydrolytic degradation of PLA also occurs in a strongly alkaline solution, where it involves intramolecular degradation and a reaction at the polymer end groups. One possible mechanism of end chain PLA degradation, including intramolecular transesterification, is suggested by Jong [45] (Fig. 4b). In alkaline conditions, the nucleophilic attack of the hydroxyl end group on the carbonyl group causes the formation of a six-membered ring as an intermediate. The newly formed free lactide hydrolyzes into two species of lactic acid. However, the intramolecular chain is randomly hydrolyzed as a hydroxide ion attacks the carbonyl groups of esters leading to hydrolysis. In this reaction path, two new molecules are formed.

The results of the XPS studies confirm that during the electro-chemical degradation in an acidic solution, the significant increase in the share of oxygen content, from approx. 24 at.% for the untreated CB-PLA electrode up to 32.3 at.% can be observed, which can be a consequence of both the intramolecular hydrolysis and hydrolysis occurring at the end groups. Furthermore, the hydrolysis performed in an alkaline solution causes the share of surface oxygen atoms to be half that, which suggests that intramolecular hydrolysis is preferred.

The alteration of the electrode polarization causes the alkalization of the electrode surface in the anode area and acidification in the cathode area. Additionally, the solution pH has a significant influence on the alkalization or acidification at the electrode surface. The total effect, dependent on the implementation of electrochemical process conditions, can lead to a local pH change towards effective acidic or alkaline hydrolysis of PLA. Therefore, the overall efficiency depends on the sum of both overlapping processes. Thus, the applied polarization significantly influences the PLA hydrolysis, as shown in Fig. 1.

3.2. CB-PLA electro-activation by synergistic electrolysis and enzymatic hydrolysis interaction

Proteinase K is an enzyme used to catalyze the hydrolysis of PLLA (poly(L-lactic acid) since the structure of the PLLA monomer is similar to alanine [46]. The hydrolytic activity of enzymes depends on many factors, including pH and temperature. The critical parameter is also the chirality of the lactide unit, which exists in three diastereoisomeric forms: L-lactide (PLLA), D-lactide (PDLA) and meso-lactide [47]. Both PLLA and PDLA are enzymatically hydrolyzed by two different classes of enzymes: proteases and lipases. One of the best known efficiently hydrolyzing PLA alkaline proteases is proteinase K. A successful Proteinase K-catalyzed G-PLA digestion was recently reported by Manzanares-Palenzuela et al. [20], opening a new environmentally friendly and reproducible alternative for the surface activation procedure of PLA-based 3D printed electrodes. These significant studies indicate the possibility of CB-PLA activation through enzymatic hydrolysis; however, the prolonged treatment duration hinders the potential laboratory applications of this approach.

Due to the reported long time required for enzymatic hydrolysis, we have decided to verify the possibility of achieving the synergistic

interaction between enzymatic and electrochemical PLA surface activation for a more time-efficient protocol. In order to do so, first we studied the enzymatic-driven surface activation of the carbon black-PLA electrodes, achieving tailorable electrode performance, dependent on the Proteinase K digestion conditions. The results of the enzymatic hydrolysis on the CB-PLA electrode are summarized in Fig. 5.

Increasing the proteinase K concentration from 0.2 mg/mL to 0.6 mg/mL improved the electrode surface activation effect. The peak separation of the ferrocyanide redox probe was reported as 91 mV at 0.6 mg/mL proteinase K concentration, allowing the estimation of the heterogeneous rate constant k^0 at 0.05 cm/s, almost twice the value obtained previously, in the case of the most effective electrochemical activation protocol. Likewise, the faradaic oxidation currents i_A significantly exceeded the CB-PLA values after the electrochemical activation protocol (86.3 μA), reaching 222 μA (at 50 mV/s scan rate) for a proteinase K concentration of 0.6 mg/mL. These parameters are reported in Table 4. However, at higher concentrations (0.8 mg/mL), the reaction will no longer speed up since the amount of substrate was available at all the enzyme active sites at the electrode surface, reaching the rate-limiting factor. Thus, the optimal concentration of the enzyme in the tested system was 0.6 mg/mL. Increasing the enzyme concentration will speed up the reaction. However, once all substrates are bound, the reaction will no longer speed up since there will be nothing on which the enzymes may bind [48].

The CV studies find confirmation in the shape of the impedimetric spectra. At the lowest proteinase K concentration, the R_{CT} exceeded 300 kΩ and dropped significantly, with the enzyme concentration increase reaching 20.3 kΩ at 0.6 mg/mL. However, the shape of the impedance spectra after enzymatic activation was more complex than previously reported for electrochemical treatment, revealing a second time-constant most likely originating from the surface-adsorbed proteinase K layer. These results corroborate the mass loss measurement presented in the inset of Fig. 5a, where the maximum mass loss of about 170 mg after 72 h exposure was consistently reported after digestion in a 0.6 mg/mL proteinase K concentration, with the plateau observable as a result of PLA digestion at higher enzyme concentrations.

The CB-PLA mass-loss studies after enzymatic action in Fig. 5d reveal the PLA digestion rate over the exposure duration. Notably, the highest mass loss was observed during the first day of activation and then slowly reaching a plateau at higher exposure times. Nevertheless, even after 72 h of exposure, further digestion is still observable. This result provides another proof of different 3D printed PLA-based electrode surface activations by proteinase K depending on the conductive carbon filler since in the original studies the longer digestion times (72 h) disintegrated the 3D-printed electrodes [49]. In the case of CB-PLA, no such behavior was observed. On the contrary, the highest surface activation efficiency measured with the heterogeneous rate constant k^0 and faradaic oxidation current i_A values was incomparably smaller in the case of smaller activation durations.

The short, one-day-long activation procedure as reported by Manzanares-Palenzuela et al. [49] was found of little efficiency in the case of CB-PLA. Even at 72 h exposure, the reported proteinase K concentration of 0.2 mg/mL was insufficient to reveal the faradaic currents originating from the redox probe, suggesting that the CB-PLA composite shows significantly lower activation efficiency than the originally used
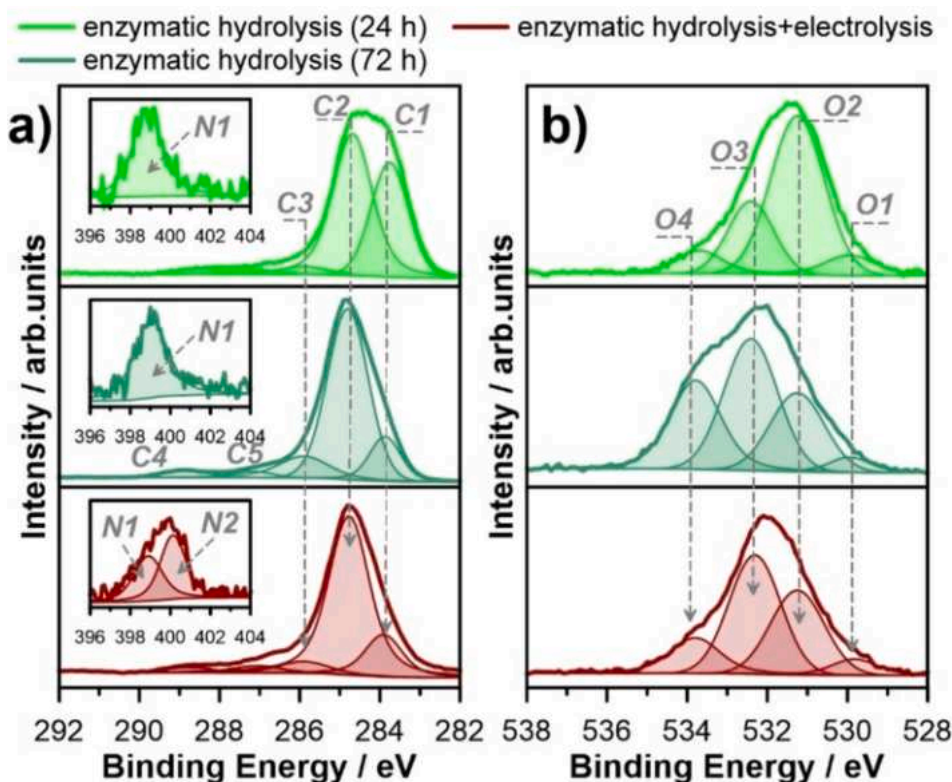
Fig. 6. XPS spectra registered in a) C 1s and b) O 1s binding energy range for the CB-PLA electrode after activation in proteinase K for 24 and 72 h, and after the combined action of electrolysis (−1.4 to +1.2 V vs Ag|AgCl polarization range) and enzymatic hydrolysis. The N 1s spectra in the inset.

Table 5
The CB-PLA surface chemistry (in at.%) after enzymatic hydrolysis in terms of various chemical states of carbon, oxygen and nitrogen, based on the XPS analysis with the deconvolution model.

		C 1s					*O 1s*			*N 1s*		
		C1	C2	C3	C5	C4	O1	O2	O3	O4	N1	N2
BE/ eV		283.7	284.6	286.0	287.2	288.5	529.9	531.2	532.7	533.8	399.0	400.1
Enzymatic hydrolysis	24 h	31.8	43.5	6.0	2.2	1.8	1.1	7.8	3.0	1.2	1.5	–
	72 h	14.0	62.1	9.3	2.1	2.8	0.4	2.2	3.6	2.5	1.1	–
Synergistic action		14.1	57.9	5.4	3.2	1.9	0.9	4.8	6.5	2.2	1.4	1.7

G-PLA. The proteinase K-catalyzed degradation rate is determined by the type, concentration, shape, dimension, dispersion, and adhesion of the fillers [50]. For example, fullerene and carbon nanotubes accelerated the enzymatic degradation due to the creation of large gaps between the PLA phase and facilitation of the proteinase K diffusion into the material (inside and surface cleaving). Because of the lack of adhesiveness of the fillers mentioned above to the PLA phase, they should have been readily released from the film surface, forming a porous structure increasing the surface area for the action of the enzyme (facile release). They also confirmed that conventional carbons have minimal effects on the enzymatic degradation rate [50]. Thus, carbon black probably forms small gaps in the PLA matrix and releases poorly from its surface.

The XPS analysis (Fig. 6) reveals the progressive digestion of the PLA by the proteinase K. One can notice that enzymatic hydrolysis duration leads to the decreased share of the CB NP's (C1 component), reaching 14 at.% at the end of a 72 h digestion process, a similar trend to the one presented for the most efficient alkaline electrolysis experiment. This effect is assisted by a significantly decreased share of the oxidized carbon bonds, C-O (C3, O3), C = O (C4, O2). Moreover, the exposition to proteinase K leads to a small share of C-N bonds at the electrode surface, labeled as C 1s C5 peak at 287.2 eV and N 1s N1 peak at 399.0 eV. These

peaks were ascribed to sp^2 hybridized N bonded to three atoms, C-N(-C)-C or C-N(-H)-C [51,52]. The total share of these species based on the C5 + N1 sum peaks at 3.5 at.% and is independent of the studied proteinase K digestion duration. It was confirmed that the enzymatic action does not lead to excessive surface oxidation as the combined share of C3, C4, C5, O2, O3 peaks does not exceed 21 at.% compared to 26 at.% for activation in alkaline media (either through electrolysis or hydrolysis) and over 54 at.% for hydrolysis in acidic media. Thus, it is most plausible that the rapid increase in C2 peak share after successful surface activation is due to the surface area development rather than conductive carbon oxidation. The complete XPS analysis is summarized in Table 5.

The primary mechanism of proteinase K digesting of PLA polymer involves the use of a nucleophilic residue to cleave an ester bond. Serine proteases use an active serine to perform a nucleophilic attack on carbon of the ester group. Proteinase K degraded the amorphous and homo crystalline regions of PLA films to produce oligo(lactic acid)s consisting mainly of linear ones and including small amounts of cyclic forms [53,54]. The enzymatic degradation mechanism depends on the enzyme's ability to recognize protein homologs, e.g. the lactic acid analogy in PLLA polymer to the L-alanine abundant in silk fibroins. Moreover, it is known that proteases can hydrolyze n-butyl or ethyl-D- and L-lactate but cannot PDLA, which is probably due to the problem with PDLA
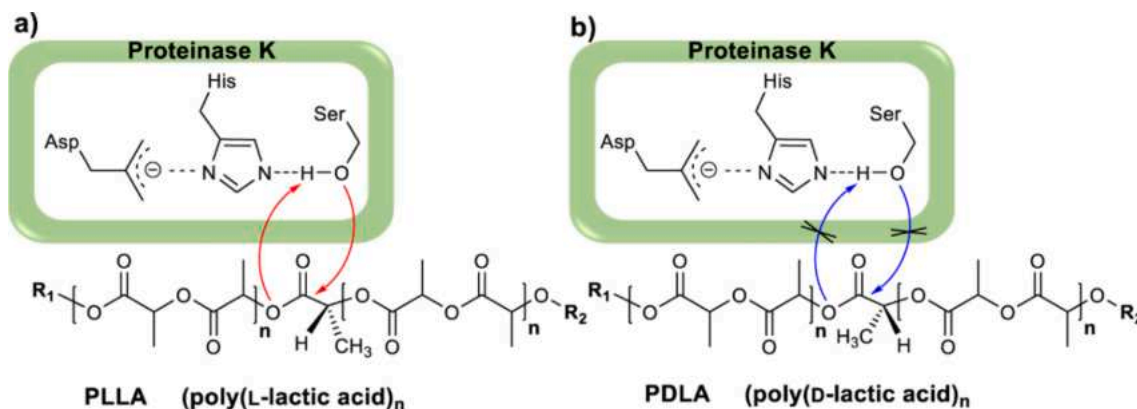
Fig. 7. The mechanism of Proteinase K action in the presence of a) PLLA and b) PDLA.
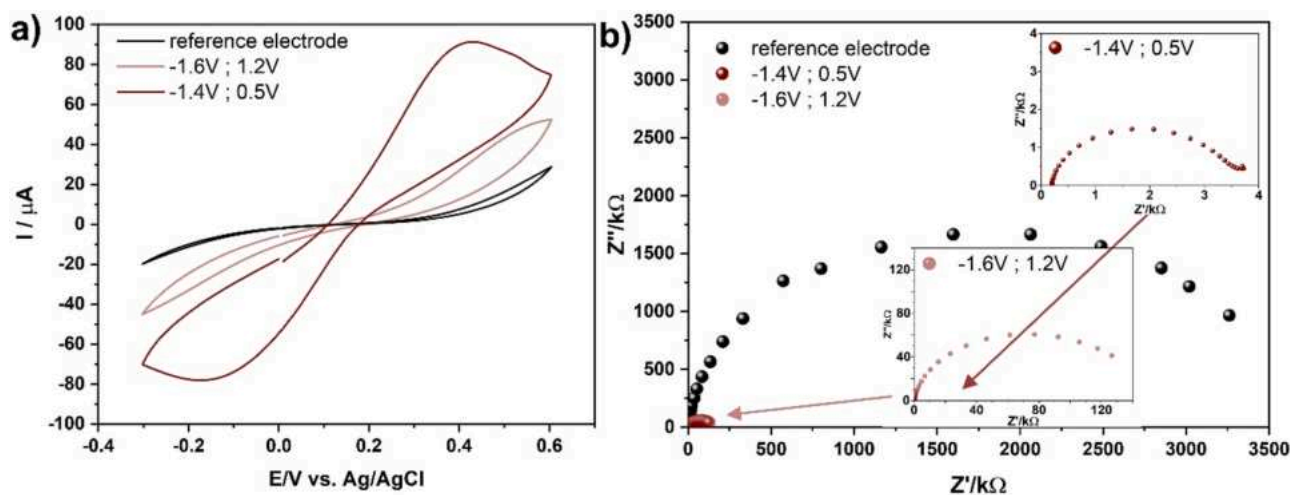

Fig. 8. The results obtained for the CB-PLA electrode subjected to electrolysis in the presence of proteinase K: a) CV curves (50 mV/s scan rate) and b) EIS spectra reflecting the charge transfer at the CB-PLA electrode for the narrow and wide polarization ranges.

accommodation in the active site or making an acyl-enzyme intermediate. In PLLA the free electron pair present on the serine oxygen can interact with the carbon of the ester group and induce digestion. In the PDLA isomer, the methyl group creates a steric hindrance that blocks the substrate from accessing the enzyme's active site [55].

The proposed mechanism was previously described by Kawai [36] and lead to the random cleavage of ester bonds in PLLA in a relatively short time (Fig. 7a), while this process is not observed in the presence of PDLA (Fig. 7b). Proteinase K is a serine protease with the classic catalytic triad of Asp^{39}-His^{69}-Ser^{224} at its active site [56]. In the presented mechanism (Ser) is the primary nucleophile, while (His) plays a dual role both as a proton acceptor and donor at different steps in the reaction. The primary function of (Asp) is based on bringing the (His) residue to the correct orientation to facilitate nucleophilic attack by (Ser) [57]. The lack of hydrolysis observed in the PDLA results from the stereochemistry mismatch of the catalytic triad and PDLA (poly(D-lactic acid) or the impossibility of making an acyl-enzyme intermediate.

The prolonged activation duration of CB-PLA electrodes under proteinase K digestion is unattractive when considering the effective use of this activation protocol in laboratory studies. Therefore, we have verified the applicability of an electrochemically-catalyzed enzymatic action to shorten the activation duration. Due to their chemical structure, enzymes are proteins. Like other proteins, they are endowed with a net charge, which is determined by the quantitative and qualitative composition of amino acids in the primary structure, spatial arrangement in the higher-order structures, and the conditions of the

environment in which they are located. The action of an electric field in an enzyme solution may cause the conformational change of the active site, the inhibition of the binding of substrate to protein, and the destabilization of the protein structure, which ultimately decreases the protein's activity [58].

The synergistic action of enzymatic hydrolysis and electrolysis on CB-PLA etching was studied at an elevated temperature (37 °C) and in Tris-HCl buffer (pH = 8), necessary for successful enzyme incubation. The results of this treatment are shown in Fig. 8. In addition, the effect of the electrochemical CB-PLA activation in Tris-HCl buffer at room temperature and at 37 °C was studied, and the results presented in the **Supplementary Information** file, **Section S6**. In the absence of proteinase K, the electrolysis process gave sub-optimal surface activation efficiency, with barely distinguishable redox processes and a negligible effect of temperature increase.

The enzymatic hydrolysis under the previously optimized polarization regime negligibly affected the very poor CB-PLA electrode kinetics. Although the nonlinear Butler-Volmer characteristics were now observable in the CV studied polarization range, the redox probe process was still indistinguishable, assisted by a decrease in the charge transfer resistance to approx. 150 kΩ. Oxidation and reduction peaks appear on the potentiodynamic polarization scan during the activation process (**Supplementary Information** file, **Fig. S7a**). The reduction peak at −1.2 V vs. Ag|AgCl may be explained by immobilizing the proteinase K on the CB-PLA surface [59]. In contrast, the surface modification is oxidized at +0.9 V. Since the process is irreversible, the corresponding

Table 6
Optimized CV characteristics of the CB-PLA electrodes after various applied activation protocols.

Filament	Activation protocol	Redox probe	ΔE_P/mV	R_{CT}/Ω	k^0/cm/s	Ref.
CNT-PLA CB-PLA	Electrochemical activation CV: −0.1 V and + 3.1 V in PBS (DMF treated)	4 mM $[Fe(CN)_6]^{4-}$ in 0.5 M KCl	251	n/a	$5.0 \cdot 10^{-4}$	[60]
G-PLA	Electrochemical activation +1.8 V in 0.1 M PBS (pH 7.4) and 1 M NaOH	5 mM $[Ru(NH_3)_6]^{3+}$ in 0.1 M KCl	115	280	$1.5 \cdot 10^{-3}$	[28]
CB-PLA	Electrochemical, 1 M NaOH CV: −1.4 ÷ +1.2 V	5 mM $[Fe(CN)_6]^{4-/3-}$ in 0.5 M Na_2SO_4	112	160	$2.7 \cdot 10^{-3}$	This work
CB-PLA	Polishing + electrochemical in 0.5 M NaOH; CV ± 1.2 V	2 mM $[Fe(CN)_6]^{4-}$ in 0.1 M KCl	150*	2050	n/a	[61]
CB-PLA	Polishing + electrochemical in 0.5 M NaOH: +1.4 and −1.0 V (200 s each)	1 mM $[Fe(CN)_6]^{4-}$ in 0.1 M KCl	297	n/a	$8.3 \cdot 10^{-3}$	[16]
CB-PLA	Polishing + electrochemical in 0.5 M NaOH: 1. + 1.4 V for 200 s 2. −1.0 V for 200 s	1 mM $[Ru(NH_3)_6]^{3+}$ in 0.1 M PBS and 1 M KCl	1. n/a 2. 150*	n/a	$9.9 \cdot 10^{-3}$	[17]
CB-PLA	Electrochemical, 1 M HCl CV: −1.4 ÷ +1.2 V	5 mM $[Fe(CN)_6]^{4-/3-}$ in 0.5 M Na_2SO_4	151	n/a	$1.4 \cdot 10^{-3}$	This work
G-PLA	Enzymatic in proteinase K	1 mM $[Fe(CN)_6]^{4-}$ in 0.1 M KCl	350	n/a	n/a	[20]
CB-PLA	Enzymatic, 72 h, proteinase K (0.6 mg/mL)	5 mM $[Fe(CN)_6]^{4-/3-}$ in 0.5 M Na_2SO_4	91	~2300	$4.8 \cdot 10^{-3}$	This work
CB-PLA	Electrografting, proteinase K (0.6 mg/mL), CV: −1.6 ÷ +0.5 V	5 mM $[Fe(CN)_6]^{4-}$ in 0.5 M Na_2SO_4	632	~3500	$4.0 \cdot 10^{-5}$	This work
CB-PLA	Laser ablation in: 1. He, 2. air	1 mM $[Ru(NH_3)_6]^{3+}$ in 0.1 M KCl	1. 161 2. 141	1. 250* 2. 285*	1. $2.8 \cdot 10^{-3}$ 2. $2.4 \cdot 10^{-3}$	[21]
CB-PLA	Plasma-treated in: 1. CO_2 2. O_2	1 mM $[Fe(CN)_6]^{4-}$ in 0.1 M KCl	1. 301 2. 156	1. 1915 2. 394	1. $4.1 \cdot 10^{-4}$ 2. $2.0 \cdot 10^{-3}$	[40]
G-PLA	Annealing in vacuum at 350 °C (3 h, N_2)	10 mM $[Fe(CN)_6]^{4-}$ in 1 M KCl	255	11.1	$1.7 \cdot 10^{-4}$	[62]

*Data estimated from the plots in the articles. The authors did not provide exact values

faradaic currents develop with consecutive polarization scans.

A second experimental approach was carried out in a narrower potentiodynamic polarization range with the anodic overpotentials not exceeding the value of the anodic polarization peak (CV scans upon η_A = 0.3 V, seen in the **Supplementary Information** file, **Fig. S7**b) to avoid removal of the proteinase K-functionalized layer. Performing the polarization in these conditions allowed us to observe prominent oxidation/reduction peaks from the ferrocyanide redox probe. The measured ΔE_P = 632 mV (scan rate 50 mV/s) hints at the irreversibility of the electrochemical process with the heterogeneous rate constant of approximately $4.0 \cdot 10^{-5}$ cm/s. Nevertheless, the irreversible electrode kinetics and the electrochemically active surface area (EASA) by carbon black is well-developed under proteinase K digestion with electrolysis co-occurrence. The direct proof of significant EASA development is the high value of the oxidation faradaic current i_A, exceeding 90 μA at the studied scan rate, similar to surface activation in 1 M NaOH electrolyte. The charge transfer resistance measured in the optimized enzymatic-electrochemical activation conditions was not less than 3.5 kΩ. The conclusion should be drawn, attributing the enhancement of the ferrocyanide kinetics and CB-PLA EASA development to the surface modification during proteinase K electrografting [59].

The XPS analysis was carried out to study the surface chemistry of the sample after the combined enzymatic hydrolysis and electrolysis (η_A = 0.3 V). The surface carbon chemistry revealed a high resemblance to the previously studied electrodes after enzymatic hydrolysis (72 h) and alkaline electrolysis due to the similar electrochemical surface area development level, as testified by the electrochemical EASA examination. The essential differences observed were the decreased share of the C–O bonds (C3 drops by a factor of two, down to 5.4 at.%) and an increased amount of C–N species (C5 + N1 increased by half, reaching 4.6 at.%). Moreover, another form of nitrogen appeared, N2, peaking at 400.1 eV, attributed to hydrogen-bonded/protonated NH_2/NH_3^+ amine species [51]. The total nitrogen share grew twice. All the above observations hint at the electrodeposition by proteinase K.

The studies carried out on the combined enzymatic and electrolysis action towards the increase of CB-PLA electrochemical activation

confirm the simultaneous activation of the CB-PLA electrodes vυ and that this modification route may be a new and invaluable direction of enhancing enzyme activity, which requires a separate research path.

4. Final remarks

The CB-PLA electrolysis by potentiodynamic polarization is the most efficient when carried out in an alkaline environment, delivering higher EASA and an improved electron transfer rate. In particular, for anodic overpotentials reaching η_A = 1.2 V the oxidation peak current i_A of 86.3 μA (at 50 mV/s scan rate) and the peak-to-peak separation of ΔE_P = 112 mV were recorded. At the same time, the surface chemistry analysis by XPS revealed a significant decrease in oxygen content down to 12% when compared with the untreated surface (32.3 at.%). However, the surface activation is less affected when the cathodic polarization range is modified, with the most efficient activation achieved at η_C = 1.6 V. The solution pH significantly influences the alkalization or acidification of the electrode surface, which is further enhanced by changes in electrode polarization. The total effect, dependent on the implementation of electrochemical process conditions, can lead to a local pH change towards effective acidic or alkaline hydrolysis of PLA. The hydrolytic decomposition mechanism of PLA in strong alkaline conditions was attributed to the end chain degradation by intramolecular transesterification.

The enzymatic hydrolysis by proteinase K is less efficient for CB-PLA than in the case of the previously reported G-PLA composite. The difference most likely originates from small gaps between the CB and PLA phases, hindering proteinase K diffusion. The optimized digestion conditions were as follows: 72 h exposure at a 0.6 mg/mL proteinase K concentration, which resulted in very high ferrocyanide oxidation currents, i_A = 222 μA, and higher reversibility (ΔE_P = 91 mV). Our results suggest enzymatic hydrolysis to be a significantly more effective protocol for CB-PLA electrochemical activation than electrolysis in either 1 M NaOH or 1 M HCl. However, prolonged treatment duration hinders potential laboratory applications of this approach.

Finally, we have demonstrated the novel strategy of electro-

activation of 3D-printed carbon black/poly(lactic acid) electrodes based on simultaneous surface treatment by electrolysis and enzymatic hydrolysis with proteinase K. This allows a unique synergistic interaction for tailoring of electrolysis and enzymatic hydrolysis, both for the electrochemically active surface area and electron transfer kinetics. This activation protocol has led to EASA development comparable to alkaline electrolysis activation (i_A = 90 μA), yet providing irreversible electron transfer kinetics. Furthermore, the XPS analysis reveals a high resemblance of the CB-PLA electrodes after enzymatic hydrolysis (72 h) and alkaline electrolysis, thanks to the analogous electrochemical surface areas. The enhanced charge transfer kinetics were attributed to proteinase K electro-polymerization under the cathodic currents. It should be noted that the electro-polymerization introduces surface modification rather than just uncovering conductive CB particles, as in the case of other protocols.

The optimized values of the electrochemical parameters obtained for each studied activation protocol together with recent literature findings for various electro-activation protocols were summarized in Table 6.

It may be concluded that the lowest ΔE_P and highly competitive k^0 values were found for our CB-PLA electrode activated by enzymatic hydrolysis in proteinase K, with time- and cost-efficient electrolysis in 1 M NaOH being only slightly inferior.

CRediT authorship contribution statement

Adrian Koterwa: Investigation, Writing – original draft, Visualization, Data curation. **Iwona Kaczmarzyk:** Investigation, Writing – original draft, Visualization, Data curation. **Szymon Mania:** Investigation, Writing – original draft, Methodology. **Mateusz Cieslik:** Investigation, Writing – original draft. **Robert Tylingo:** Writing – review & editing. **Tadeusz Ossowski:** Writing – review & editing. **Robert Bogdanowicz:** Writing – review & editing, Funding acquisition. **Paweł Niedziałkowski:** Writing – original draft, Writing – review & editing, Conceptualization. **Jacek Ryl:** Investigation, Writing – original draft, Writing – review & editing, Conceptualization, Methodology, Funding acquisition, Visualization.

Declaration of Competing Interest

The authors declare that they have no known competing financial interests or personal relationships that could have appeared to influence the work reported in this paper.

Acknowledgements

Appendix A. Supplementary data

Supplementary data to this article can be found online at https://doi.org/10.1016/j.apsusc.2021.151587.

References

[1] T. Han, S. Kundu, A. Nag, Y. Xu, 3D printed sensors for biomedical applications: a review, Sensors 19 (2019) 1706, https://doi.org/10.3390/s19071706.

[2] M.D. Symes, P.J. Kitson, J. Yan, C.J. Richmond, G.J.T. Cooper, R.W. Bowman, T. Vilbrandt, L. Cronin, Integrated 3D-printed reactionware for chemical synthesis and analysis, Nat. Chem. 4 (5) (2012) 349–354, https://doi.org/10.1038/nchem.1313.

[3] A. Melocchi, F. Parietti, A. Maroni, A. Foppoli, A. Gazzaniga, L. Zema, Hot-melt extruded filaments based on pharmaceutical grade polymers for 3D printing by fused deposition modeling, Int. J. Pharm. 509 (1-2) (2016) 255–263, https://doi.org/10.1016/j.ijpharm.2016.05.036.

[4] M. Wang, P. Favi, X. Cheng, N.H. Golshan, K.S. Ziemer, M. Keidar, T.J. Webster, Cold atmospheric plasma (CAP) surface nanomodified 3D printed polylactic acid (PLA) scaffolds for bone regeneration, Acta Biomater. 46 (2016) 256–265, https://doi.org/10.1016/j.actbio.2016.09.030.

[5] L. Xiao, B. Wang, G. Yang, M. Gauthier, Poly(Lactic Acid)-Based Biomaterials: Synthesis, Modification and Applications, in: D.N. Ghista (Ed.), Biomedical Science, Engineering and Technology, InTech, 2012. https://doi.org/10.5772/23927.

[6] D. Garlotta, A literature review of poly(lactic acid), J. Polym. Environ. 9 (2001) 63–84, https://doi.org/10.1023/A:1020200822435.

[7] G.D. O'Neil, S. Ahmed, K. Halloran, J.N. Janusz, A. Rodríguez, I.M. Terrero Rodríguez, Single-step fabrication of electrochemical flow cells utilizing multi-material 3D printing, Electrochem. Commun. 99 (2019) 56–60, https://doi.org/10.1016/j.elecom.2018.12.006.

[8] G. Gaal, M. Mendes, T.P. de Almeida, M.H.O. Piazzetta, Â.L. Gobbi, A. Riul, V. Rodrigues, Simplified fabrication of integrated microfluidic devices using fused deposition modeling 3D printing, Sens. Actuators, B 242 (2017) 35–40, https://doi.org/10.1016/j.snb.2016.10.110.

[9] R.M. Cardoso, D.M.H. Mendonça, W.P. Silva, M.N.T. Silva, E. Nossol, R.A.B. da Silva, E.M. Richter, R.A.A. Muñoz, 3D printing for electroanalysis: From multiuse electrochemical cells to sensors, Anal. Chim. Acta 1033 (2018) 49–57, https://doi.org/10.1016/j.aca.2018.06.021.

[10] R.M. Cardoso, P.R.L. Silva, A.P. Lima, D.P. Rocha, T.C. Oliveira, T.M. do Prado, E.L. Fava, O. Fatibello-Filho, E.M. Richter, R.A.A. Muñoz, 3D-printed graphene/polylactic acid electrode for bioanalysis: Biosensing of glucose and simultaneous determination of uric acid and nitrite in biological fluids, Sens. Actuators, B 307 (2020) 127621, https://doi.org/10.1016/j.snb.2019.127621.

[11] C.W. Foster, M.P. Down, Y. Zhang, X. Ji, S.J. Rowley-Neale, G.C. Smith, P.J. Kelly, C.E. Banks, 3D printed graphene based energy storage devices, Sci. Rep. 7 (2017) 42233, https://doi.org/10.1038/srep42233.

[12] R. Gómez-Hernández, Y. Panecatl-Bernal, M.Á. Méndez-Rojas, High yield and simple one-step production of carbon black nanoparticles from waste tires, Heliyon. 5 (7) (2019) e02139, https://doi.org/10.1016/j.heliyon.2019.e02139.

[13] A.F. João, A.L. Squissato, E.M. Richter, R.A.A. Muñoz, Additive-manufactured sensors for biofuel analysis: copper determination in bioethanol using a 3D-printed carbon black/polylactic electrode, Anal. Bioanal. Chem. 412 (12) (2020) 2755–2762, https://doi.org/10.1007/s00216-020-02513-y.

[14] V. Katseli, N. Thomaidis, A. Economou, C. Kokkinos, Miniature 3D-printed integrated electrochemical cell for trace voltammetric Hg(II) determination, Sens. Actuators, B 308 (2020) 127715, https://doi.org/10.1016/j.snb.2020.127715.

[15] V. Katseli, A. Economou, C. Kokkinos, Single-step fabrication of an integrated 3D-printed device for electrochemical sensing applications, Electrochem. Commun. 103 (2019) 100–103, https://doi.org/10.1016/j.elecom.2019.05.008.

[16] D.P. Rocha, A.L. Squissato, S.M. da Silva, E.M. Richter, R.A.A. Munoz, Improved electrochemical detection of metals in biological samples using 3D-printed electrode: Chemical/electrochemical treatment exposes carbon-black conductive sites, Electrochim. Acta 335 (2020) 135688, https://doi.org/10.1016/j.electacta.2020.135688.

[17] E.M. Richter, D.P. Rocha, R.M. Cardoso, E.M. Keefe, C.W. Foster, R.A.A. Munoz, C.E. Banks, Complete additively manufactured (3D-printed) electrochemical sensing platform, Anal. Chem. 91 (20) (2019) 12844–12851, https://doi.org/10.1021/acs.analchem.9b02573.10.1021/acs.analchem.9b02573.s001.

[18] M.P. Browne, F. Novotný, Z. Sofer, M. Pumera, 3D printed graphene electrodes' electrochemical activation, ACS Appl. Mater. Interfaces 10 (46) (2018) 40294–40301, https://doi.org/10.1021/acsami.8b1470110.1021/acsami.8b14701.s001.

[19] S.H. Lee, W.S. Song, Enzymatic hydrolysis of polylactic acid fiber, Appl. Biochem. Biotechnol. 164 (1) (2011) 89–102, https://doi.org/10.1007/s12010-010-9117-7.

[20] C.L. Manzanares-Palenzuela, S. Hermanova, Z. Sofer, M. Pumera, Proteinase-sculpted 3D-printed graphene/polylactic acid electrodes as potential biosensing platforms: towards enzymatic modeling of 3D-printed structures, Nanoscale. 11 (25) (2019) 12124–12131, https://doi.org/10.1039/C9NR02754H.

[21] M.J. Glowacki, M. Cieslik, M. Sawczak, A. Koterwa, I. Kaczmarzyk, R. Jendrzejewski, L. Szynkiewicz, T. Ossowski, R. Bogdanowicz, P. Niedzialkowski, J. Ryl, Helium-assisted, solvent-free electro-activation of 3D printed conductive carbon-polylactide electrodes by pulsed laser ablation, Appl. Surf. Sci. 556 (2021) 149788, https://doi.org/10.1016/j.apsusc.2021.149788.

[22] D.P. Rocha, R.G. Rocha, S.V.F. Castro, M.A.G. Trindade, R.A.A. Munoz, E.M. Richter, L. Angnes, Posttreatment of 3D-printed surfaces for electrochemical applications: A critical review on proposed protocols, Electrochem. Sci. Adv. (2021), https://doi.org/10.1002/elsa.202100136.

[23] P. Chen, R.L. McCreery, Control of electron transfer kinetics at glassy carbon electrodes by specific surface modification, Anal. Chem. 68 (22) (1996) 3958–3965, https://doi.org/10.1021/ac960492r.

[24] M. Janik, P. Niedziałkowski, K. Lechowicz, M. Koba, P. Sezemsky, V. Stranak, T. Ossowski, M. Śmietana, Electrochemically directed biofunctionalization of a lossy-mode resonance optical fiber sensor, Opt. Express 28 (11) (2020) 15934, https://doi.org/10.1364/OE.390780.

[25] R.S. Nicholson, Theory and application of cyclic voltammetry for measurement of electrode reaction kinetics, Anal. Chem. 37 (11) (1965) 1351–1355, https://doi.org/10.1021/ac60230a016.

[26] J. Ryl, L. Burczyk, A. Zielinski, M. Ficek, A. Franczak, R. Bogdanowicz, K. Darowicki, Heterogeneous oxidation of highly boron-doped diamond electrodes and its influence on the surface distribution of electrochemical activity, Electrochim. Acta 297 (2019) 1018–1027, https://doi.org/10.1016/j.electacta.2018.12.050.

[27] J. Heinze, Cyclovoltammetrie — die „Spektroskopie" des Elektrochemikers, Angew. Chem. 96 (11) (1984) 823–840, https://doi.org/10.1002/(ISSN)1521-375710.1002/ange.v96:1110.1002/ange.19840961104.

[28] C. Kalinke, N.V. Neumsteir, G.d.O. Aparecido, T.V.d.B. Ferraz, P.L. dos Santos, B. C. Janegitz, J.A. Bonacin, Comparison of activation processes for 3D printed PLA-graphene electrodes: electrochemical properties and application for sensing of dopamine, Analyst. 145 (4) (2020) 1207–1218, https://doi.org/10.1039/C9AN01926J.

[29] T.J. Davies, C.E. Banks, R.G. Compton, Voltammetry at spatially heterogeneous electrodes, J. Solid State Electrochem. 9 (12) (2005) 797–808, https://doi.org/10.1007/s10008-005-0699-x.

[30] P. Niedziałkowski, M. Bojko, J. Ryl, A. Wcisło, M. Spodzieja, K. Magiera-Mularz, K. Guzik, G. Dubin, T.A. Holak, T. Ossowski, S. Rodziewicz-Motowidło, Ultrasensitive electrochemical determination of the cancer biomarker protein sPD-L1 based on a BMS-8-modified gold electrode, Bioelectrochemistry 139 (2021) 107742, https://doi.org/10.1016/j.bioelechem.2021.107742.

[31] P. Niedzialkowski, P. Slepski, J. Wysocka, J. Chamier-Cieminska, L. Burczyk, M. Sobaszek, A. Wcislo, T. Ossowski, R. Bogdanowicz, J. Ryl, Multisine impedimetric probing of biocatalytic reactions for label-free detection of DEFB1 gene: How to verify that your dog is not human? Sens. Actuators, B 323 (2020) 128664, https://doi.org/10.1016/j.snb.2020.128664.

[32] B. Hirschorn, M.E. Orazem, B. Tribollet, V. Vivier, I. Frateur, M. Musiani, Determination of effective capacitance and film thickness from constant-phase-element parameters, Electrochim. Acta 55 (21) (2010) 6218–6227, https://doi.org/10.1016/j.electacta.2009.10.065.

[33] M. Sobaszek, K. Siuzdak, M. Sawczak, J. Ryl, R. Bogdanowicz, Fabrication and characterization of composite TiO2 nanotubes/boron-doped diamond electrodes towards enhanced supercapacitors, Thin Solid Films 601 (2016) 35–40, https://doi.org/10.1016/j.tsf.2015.09.073.

[34] D.P. Rocha, V.N. Ataide, A. de Siervo, J.M. Gonçalves, R.A.A. Muñoz, T.R.L. C. Paixão, L. Angnes, Reagentless and sub-minute laser-scribing treatment to produce enhanced disposable electrochemical sensors via additive manufacture, Chem. Eng. J. 425 (2021) 130594, https://doi.org/10.1016/j.cej.2021.130594.

[35] S. Evans, Correction for the effects of adventitious carbon overlayers in quantitative XPS analysis, Surface and Interface, Analysis. 25 (1997) 924–930, https://doi.org/10.1002/(SICI)1096-9918(199711)25:12<924::AID-SIA317>3.0.CO;2-2.

[36] D. Pantea, H. Darmstadt, S. Kaliaguine, C. Roy, Electrical conductivity of conductive carbon blacks: influence of surface chemistry and topology, Appl. Surf. Sci. 217 (1-4) (2003) 181–193, https://doi.org/10.1016/S0169-4332(03)00550-6.

[37] P. Niedziałkowski, T. Ossowski, P. Zięba, A. Cirocka, P. Rochowski, S. J. Pogorzelski, J. Ryl, M. Sobaszek, R. Bogdanowicz, Poly-l-lysine-modified boron-doped diamond electrodes for the amperometric detection of nucleic acid bases, J. Electroanal. Chem. 756 (2015) 84–93, https://doi.org/10.1016/j.jelechem.2015.08.006.

[38] K. Ghosh, S. Ng, C. Iffelsberger, M. Pumera, Inherent impurities in graphene/polylactic acid filament strongly influence on the capacitive performance of 3D-printed electrode, Chem. Eur. J. 26 (67) (2020) 15746–15753, https://doi.org/10.1002/chem.v26.6710.1002/chem.202004250.

[39] J. Ryl, J. Wysocka, M. Cieslik, H. Gerengi, T. Ossowski, S. Krakowiak, P. Niedzialkowski, Understanding the origin of high corrosion inhibition efficiency of bee products towards aluminium alloys in alkaline environments, Electrochim. Acta 304 (2019) 263–274, https://doi.org/10.1016/j.electacta.2019.03.012.

[40] J.F.S. Pereira, R.G. Rocha, S.V.F. Castro, A.F. João, P.H.S. Borges, D.P. Rocha, A. de Siervo, E.M. Richter, E. Nossol, R.V. Gelamo, R.A.A. Muñoz, Reactive oxygen plasma treatment of 3D-printed carbon electrodes towards high-performance electrochemical sensors, Sens. Actuators, B 347 (2021) 130651, https://doi.org/10.1016/j.snb.2021.130651.

[41] E. Vaněčková, M. Bouša, Š. Nováková Lachmanová, J. Rathouský, M. Gál, T. Sebechlebská, V. Kolivoška, 3D printed polylactic acid/carbon black electrodes with nearly ideal electrochemical behaviour, J. Electroanal. Chem. 857 (2020) 113745, https://doi.org/10.1016/j.jelechem.2019.113745.

[42] Y. Yamada, J. Kim, S. Matsuo, S. Sato, Nitrogen-containing graphene analyzed by X-ray photoelectron spectroscopy, Carbon 70 (2014) 59–74, https://doi.org/10.1016/j.carbon.2013.12.061.

[43] J.H. Jung, M. Ree, H. Kim, Acid- and base-catalyzed hydrolyses of aliphatic polycarbonates and polyesters, Catal. Today 115 (1-4) (2006) 283–287, https://doi.org/10.1016/j.cattod.2006.02.060.

[44] N. Lucas, C. Bienaime, C. Belloy, M. Queneudec, F. Silvestre, J.-E. Nava-Saucedo, Polymer biodegradation: Mechanisms and estimation techniques – A review, Chemosphere 73 (4) (2008) 429–442, https://doi.org/10.1016/j.chemosphere.2008.06.064.

[45] S.J. de Jong, E.R. Arias, D.T.S. Rijkers, C.F. van Nostrum, J.J. Kettenes-van den Bosch, W.E. Hennink, New insights into the hydrolytic degradation of poly(lactic acid): participation of the alcohol terminus, Polymer 42 (7) (2001) 2795–2802, https://doi.org/10.1016/S0032-3861(00)00646-7.

[46] Q. Huang, M. Hiyama, T. Kabe, S. Kimura, T. Iwata, Enzymatic self-biodegradation of poly(L-lactic acid) films by embedded heat-treated and immobilized proteinase K, Biomacromolecules 21 (2020) 3301–3307, https://doi.org/10.1021/acs.biomac.0c00759.

[47] H. Tsuji, S. Miyauchi, Enzymatic hydrolysis of poly(lactide)s: effects of molecular weight, L -lactide content, and enantiomeric and diastereoisomeric polymer blending, Biomacromolecules 2 (2001) 597–604, https://doi.org/10.1021/bm010048k.

[48] W. Saenger, K. Proteinase, Handbook of Proteolytic Enzymes, Elsevier (2013) 3240–3242, https://doi.org/10.1016/B978-0-12-382219-2.00714-6.

[49] C. Lorena Manzanares Palenzuela, Filip Novotný, Petr Krupička, Zdeněk Sofer, Martin Pumera, 3D-printed graphene/polylactic acid electrodes promise high sensitivity in electroanalysis, Anal. Chem. 90 (9) (2018) 5753–5757, https://doi.org/10.1021/acs.analchem.8b0008310.1021/acs.analchem.8b00083.s001.

[50] Hideto Tsuji, Yoshio Kawashima, Hirofumi Takikawa, Saburo Tanaka, Poly(l-lactide)/nano-structured carbon composites: Conductivity, thermal properties, crystallization, and biodegradation, Polymer 48 (14) (2007) 4213–4225, https://doi.org/10.1016/j.polymer.2007.05.040.

[51] Scott D. Kimmins, Paul Wyman, Neil R. Cameron, Amine-functionalization of glycidyl methacrylate-containing emulsion-templated porous polymers and immobilization of proteinase K for biocatalysis, Polymer 55 (1) (2014) 416–425, https://doi.org/10.1016/j.polymer.2013.09.019.

[52] P. Niedziałkowski, R. Bogdanowicz, P. Zięba, J. Wysocka, J. Ryl, M. Sobaszek, T. Ossowski, Melamine-modified boron-doped diamond towards enhanced detection of adenine, guanine and caffeine, Electroanalysis 28 (1) (2016) 211–221, https://doi.org/10.1002/elan.v28.110.1002/elan.201500528.

[53] Y. Oda, A. Yonetsu, T. Urakami, K. Tonomura, Degradation of polylactide by commercial proteases, J. Polym. Environ. 8 (2000) 29–32, https://doi.org/10.1023/A:1010120128048.

[54] X. Qi, Y. Ren, X. Wang, New advances in the biodegradation of Poly(lactic) acid, Int. Biodeterior. Biodegrad. 117 (2017) 215–223, https://doi.org/10.1016/j.ibiod.2017.01.010.

[55] Fusako Kawai, Kosuke Nakadai, Emiko Nishioka, Hajime Nakajima, Hitomi Ohara, Kazuo Masaki, Haruyuki Iefuji, Different enantioselectivity of two types of poly (lactic acid) depolymerases toward poly(l-lactic acid) and poly(d-lactic acid), Polym. Degrad. Stab. 96 (7) (2011) 1342–1348, https://doi.org/10.1016/j.polymdegradstab.2011.03.022.

[56] S.B. Larson, J.S. Day, C. Nguyen, R. Cudney, A. McPherson, High-resolution structure of proteinase K cocrystallized with digalacturonic acid, Acta Crystallogr. F Struct. Biol. Commun. 65 (2009) 192–198, https://doi.org/10.1107/S1744309109002218.

[57] Christian Betzel, S. Gourinath, Pravindra Kumar, Punit Kaur, Markus Perbandt, Susanne Eschenburg, Tej P. Singh, Structure of a serine protease proteinase K from *Tritirachium album limber* at 0.98 Å resolution, Biochemistry 40 (10) (2001) 3080–3088, https://doi.org/10.1021/bi002538n.

[58] Wei Zhao, Ruijin Yang, Experimental study on conformational changes of lysozyme in solution induced by pulsed electric field and thermal stresses, J. Phys. Chem. B 114 (1) (2010) 503–510, https://doi.org/10.1021/jp9081189.

[59] Yueming Tan, Wenfang Deng, Chao Chen, Qingji Xie, Lihong Lei, Yunyong Li, Zhengfa Fang, Ming Ma, Jinhua Chen, Shouzhuo Yao, Immobilization of enzymes at high load/activity by aqueous electrodeposition of enzyme-tethered chitosan for highly sensitive amperometric biosensing, Biosens. Bioelectron. 25 (12) (2010) 2644–2650, https://doi.org/10.1016/j.bios.2010.04.040.

[60] Jesús E. Contreras-Naranjo, Victor H. Perez-Gonzalez, Marco A. Mata-Gómez, Oscar Aguilar, 3D-printed hybrid-carbon-based electrodes for electroanalytical sensing applications, Electrochem. Commun. 130 (2021) 107098, https://doi.org/10.1016/j.elecom.2021.107098.

[61] G. Martins, J.L. Gogola, L.H. Budni, B.C. Janegitz, L.H. Marcolino-Junior, M. F. Bergamini, 3D-printed electrode as a new platform for electrochemical immunosensors for virus detection, Anal. Chim. Acta 1147 (2021) 30–37, https://doi.org/10.1016/j.aca.2020.12.014.

[62] Filip Novotný, Veronika Urbanová, Jan Plutnar, Martin Pumera, Preserving fine structure details and dramatically enhancing electron transfer rates in graphene 3D-printed electrodes via thermal annealing: toward nitroaromatic explosives sensing, ACS Appl. Mater. Interfaces 11 (38) (2019) 35371–35375, https://doi.org/10.1021/acsami.9b0668310.1021/acsami.9b06683.s001.

Supplementary Information File

for

The role of the electrolysis and enzymatic hydrolysis in the enhancement of the electrochemical properties of 3D-printed carbon black/poly(lactic acid) structures

Adrian Koterwa[1,#], Iwona Kaczmarzyk[2,#], Szymon Mania[3], Mateusz Cieślik[3,4], Robert Tylingo[3], Tadeusz Ossowski[1], Robert Bogdanowicz[2], Paweł Niedziałkowski[1], Jacek Ryl[4,*]

[1] Department of Analytical Chemistry, University of Gdansk, Wita Stwosza 63, 80-308 Gdansk, Poland
[2] Department of Metrology and Optoelectronics and Advanced Materials Center, Gdansk University of Technology, Narutowicza 11/12, 80-233 Gdansk, Poland
[3] Faculty of Chemistry, Gdansk University of Technology, Narutowicza 11/12, 80-233 Gdansk, Poland
[4] Institute of Nanotechnology and Materials Engineering and Advanced Materials Center, Gdansk University of Technology, Narutowicza 11/12, 80-233 Gdansk, Poland
*** Correspondence: Jacek Ryl – jacek.ryl@pg.edu.pl
# these authors contributed equally to the manuscript

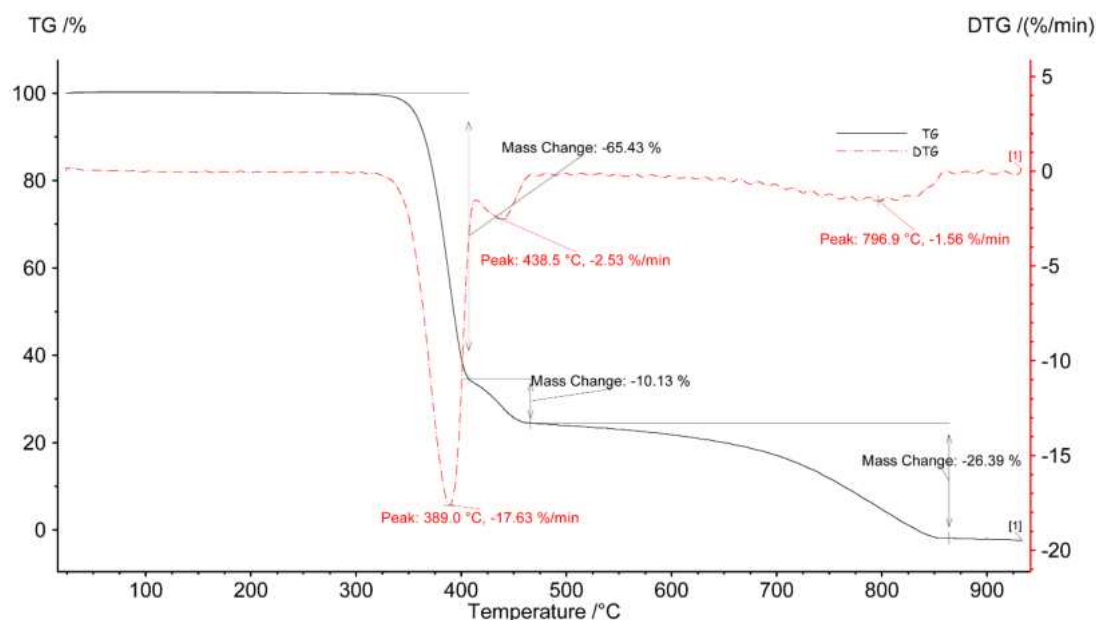## S1. Thermogravimetric analysis of the ProtoPasta CB-PLA filament

Figure S1 – Thermogravimetric analysis (TGA) of the studied CB-PLA filament

S2. The polarization curves registered during surface activation of CB-PLA electrodes during chemical-electrochemical etching synergy evaluation
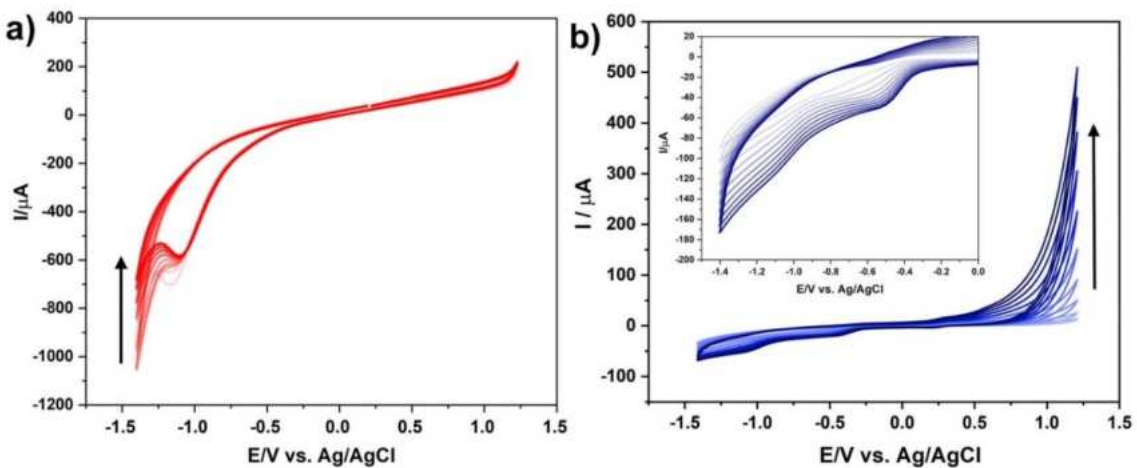

Figure S2 – a) Cyclic polarization curves registered during CB-PLA electro-activation process, 10 cycles in range -1.4 to +1.2 V vs Ag|AgCl, carried out in a) acidic (1M HCl) and b) alkaline (1M NaOH) media.

S3. The PLA hydrolysis under exposure to 1M HCl or 1M NaOH

Figure S3 shows the effect of pH during PLA activation on the electrochemical surface properties of 3D-printed electrodes, investigated with cyclic voltammetry (CV) and electrochemical impedance spectroscopy (EIS). The electrodes were exposed to the studied electrolyte for the duration of 24 h.
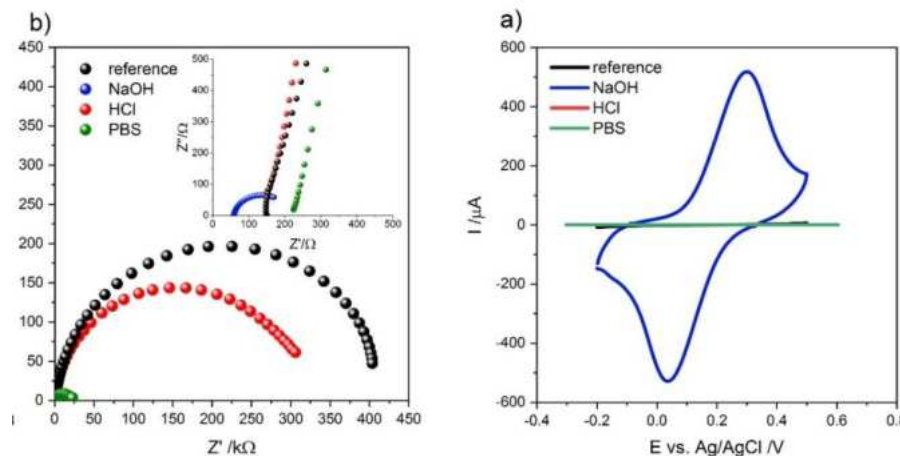

Figure S3 – a) EIS spectra and b) CV curves obtained for CB-PLA electrode subjected to polymer chemolysis in acidic (1M HCl) and alkaline (1M NaOH) media. Electrolyte: 0.5 M $Na_2SO_4 + 5$ mM $[Fe(CN)_6]^{4-/3-}$.

As can be observed the surface after exposition in hydrochloric acid shows a negligible decrease of the capacitive loop diameter compared with the untreated reference sample, suggesting a low PLA etching rate in an acidic environment (**Fig. S3a**). On the other hand, a rapid impedance decrease was observed due to CB-PLA electrode exposure to 1 M NaOH, where the polymer is efficiently etched, uncovering the carbon black filler and increasing EASA. The R_{CT} value of hydrochloric acid-treated CB-PLA electrode was estimated as 326 kΩ, which is three orders of magnitude higher than 158 Ω for sodium hydroxide-

treated electrode. The impedimetric results are confirmed by the rapid development of the faradaic currents for the ferrocyanide/ferricyanide redox process during CV scans (**Fig. S3b**). The anodic-to-cathodic peak separation after treatment in alkaline environment was estimated 263 mV, indicating an irreversible charge transfer mechanism.

S4. Standard heterogeneous rate constant k^0 for various electro-activation protocols in 1M NaOH and 1M NaCl
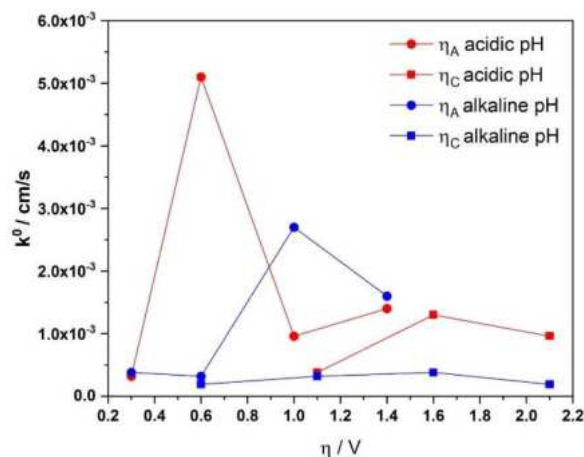

Figure S4 – $k^0 = f(\eta)$ for CB-PLA electrode after electrochemical treatment after CV scans with various cathodic (η_C) or anodic (η_A) overpotential limits, based on Table 1. Activation in 1M HCl (red line) or 1M NaOH (blue line). CV studies in electrolyte 0.5 M Na_2SO_4 + 5 mM $[Fe(CN)_6]^{4-/3-}$.

S5. Evaluation of electrochemically-active surface area, electro-activated in 1M NaOH

The below given studies refer to the electrode electro-activated by potentiodynamic polarization treatment in the optimized polarization range (-1.4 ÷ +1.2 V vs Ag|AgCl) in 1M NaOH electrolyte.
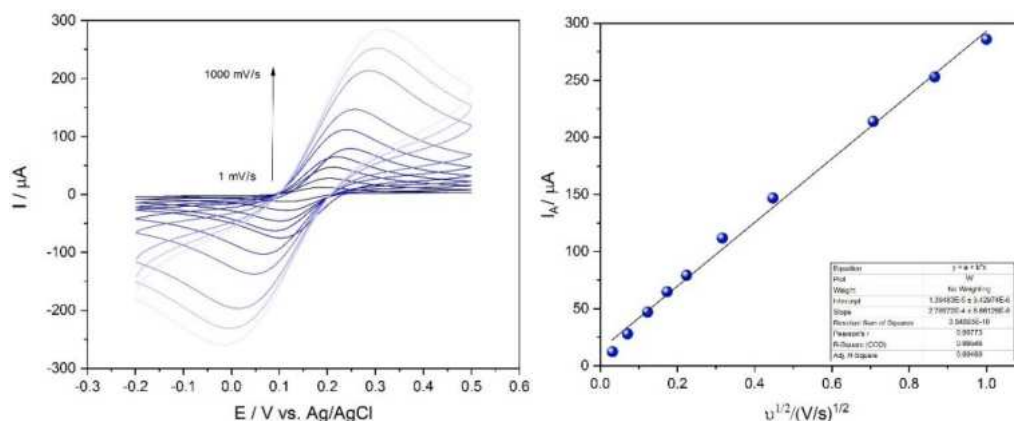

Figure S5 – a) CV scans obtained for the CB-PLA electrode in 0.5 M Na_2SO_4 + 5 mM $[Fe(CN)_6]^{4-/3-}$ at various studied polarization sweep rates, in range 1 to 1000 mV/s, b) the oxidation peak current, i_A, vs the sweep rate square-root $\upsilon^{1/2}$.

In case of the electrode characterized by the electrochemically irreversible electron transfer, the electrochemically active surface area, A, may be determined using equation below:

$$i_{p,A} = 2.99 * 10^5 n\alpha^{3/2} A\vartheta^{1/2} D_{red}^{1/2} c$$

where n is the number of electrons transferred, D_{red} is the diffusion coefficient of $[Fe(CN)_6]^{4-}$ ($6.67 \cdot 10^{-6}$ cm^2/s), c is concentration in mol/cm^3, and α is transfer coefficient (estimated as 0.5) [S1].

The resultant, estimated EASA value is 0.204 cm^2, very close to electrolyte-exposed geometric surface area of 0.196 cm^2.

Reference:

[S1] J. Ryl, A. Zielinski, L. Burczyk, R. Bogdanowicz, T. Ossowski, K. Darowicki, Chemical-Assisted Mechanical Lapping of Thin Boron-Doped Diamond Films: A Fast Route Toward High Electrochemical Performance for Sensing Devices, Electrochim. Acta, 242 (2017) 268-279. DOI: 10.1016/j.electacta.2017.05.027

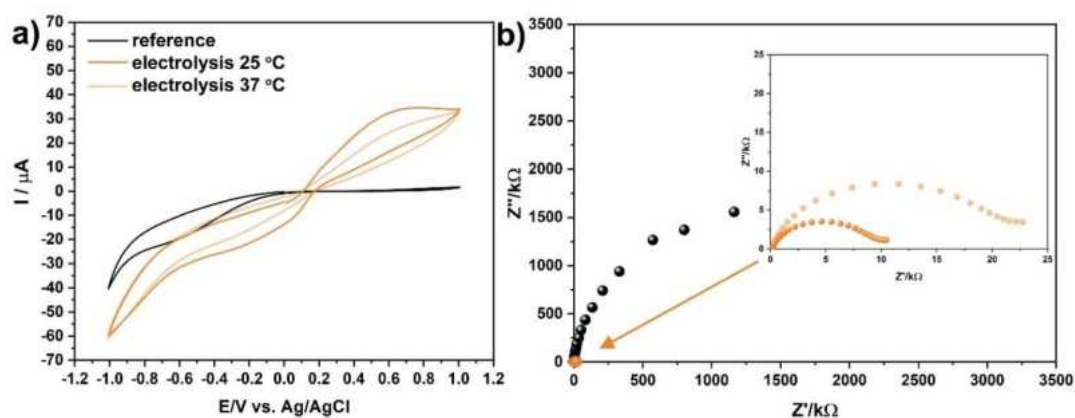### S6. The surface activation studies by electrolysis in PBS media

Figure S6 – a) CV curves and b) EIS spectra reflecting charge transfer through the CB-PLA electrode after electro-activation by electrolysis in -1.4 to +1.2 V vs Ag|AgCl polarization range, at room temperature and 37 °C (i.e. the temperature of the enzymolysis process).

S7. The polarization curves registered during surface activation of CB-PLA electrodes during enzymatic-electrochemical etching synergy evaluation
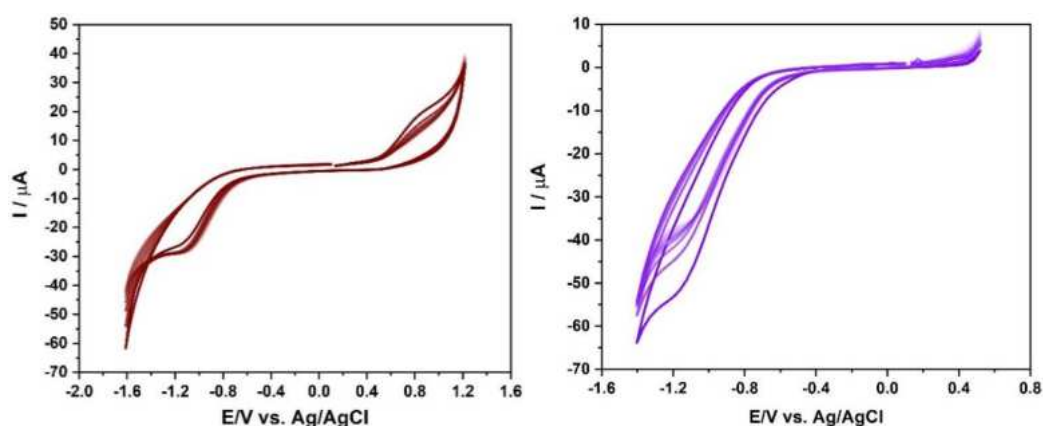

Figure S7 – Cyclic polarization curves registered during CB-PLA electro-activation process in presence of proteinase K, 10 cycles: a) polarization range -1.6 to +1.2 V vs Ag|AgCl, b) polarization range -1.4 to +0.5 V vs Ag|AgCl.

Oświadczenia

dr hab. Paweł Niedziałkowski, prof. UG   Gdańsk, 06.11.2024
Uniwersytet Gdański
Wydział Chemii
Katedra Chemii Analitycznej
Pracownia Elektroanalizy i Biosensorów
ul. Wita Stwosza 63
80-308 Gdańsk

Oświadczenie

Jako współautor publikacji wchodzącej w skład rozprawy doktorskiej mgr Adriana Koterwy oświadczam, że mój wkład w publikację:

Niedziałkowski, P., **Koterwa, A.**, Olejnik, A., Zieliński, A., Górnicka, K., Brodowski, M., Bogdanowicz, R., Ryl, J., „Deciphering the Molecular Mechanism of Substrate-Induced Assembly of Gold Nanocube Arrays toward an Accelerated Electrocatalytic Effect Employing Heterogeneous Diffusion Field Confinement, Langmuir, 2022, 38, 9597-9610, DOI:10.1021/acs.langmuir.2c01001

polegał na współopracowaniu koncepcji badań i metodologii pomiarów, interpretacji wyników elektrochemicznych, przeprowadzeniu syntezy AuNCs, przygotowaniu części manuskryptu wraz z odpowiedzią na recenzję, współfinansowaniu badań.

dr hab. Paweł Niedziałkowski
profesor Uniwersytetu Gdańskiego

Uniwersytet Gdański
Wydział Chemii
Katedra Chemii Analitycznej

dr hab. inż. Jacek Ryl, prof. PG   Gdańsk, 06.11.2024
Politechnika Gdańska
Instytut Nanotechnologii i Inżynierii Materiałowej
Zakład Elektrochemii i Fizykochemii Powierzchni
ul. Narutowicza 11/12
80-308 Gdańsk

Oświadczenie

Jako współautor publikacji wchodzącej w skład rozprawy doktorskiej mgr Adriana Koterwy oświadczam, że mój wkład w publikację:

polegał na współopracowaniu koncepcji badań i metodologii pomiarów, interpretacji wyników elektrochemicznych, wykonaniu i interpretacji pomiarów XPS oraz SEM, zaproponowaniu mechanizmu interakcji AuNC z powierzchnią elektrod, przygotowaniu części manuskryptu wraz z odpowiedzią na recenzję, finansowaniu badań.

dr hab. inż. Robert Bogdanowicz, prof. PG   Gdańsk, 06.11.2024
Politechnika Gdańska
Wydział Elektroniki, Telekomunikacji i Informatyki
Katedra Metrologii i Optoelektroniki
ul. Narutowicza 11/12
80-308 Gdańsk

Oświadczenie

Jako współautor publikacji wchodzącej w skład rozprawy doktorskiej mgr Adriana Koterwy oświadczam, że mój wkład w publikację:

Niedziałkowski, P., **Koterwa, A.**, Olejnik, A., Zieliński, A., Górnicka, K., Brodowski, M., Bogdanowicz, R., Ryl, J., „Deciphering the Molecular Mechanism of Substrate-Induced Assembly of Gold Nanocube Arrays toward an Accelerated Electrocatalytic Effect Employing Heterogeneous Diffusion Field Confinement, Langmuir, 2022, 38, 9597-9610, DOI:10.1021/acs.langmuir.2c01001

polegał na przygotowaniu części manuskryptu wraz z odpowiedzią na recenzję.

dr hab. inż. Robert Bogdanowicz, prof. PG

mgr inż. Adrian Olejnik
Politechnika Gdańska
Wydział Elektroniki, Telekomunikacji i Informatyki
Katedra Metrologii i Optoelektroniki
ul. Narutowicza 11/12
80-308 Gdańsk

Gdańsk, 06.11.2024

Oświadczenie

Jako współautor publikacji wchodzącej w skład rozprawy doktorskiej mgr Adriana Koterwy oświadczam, że mój wkład w publikację:

Niedziałkowski, P., **Koterwa, A.**, Olejnik, A., Zieliński, A., Górnicka, K., Brodowski, M., Bogdanowicz, R., Ryl, J., „Deciphering the Molecular Mechanism of Substrate-Induced Assembly of Gold Nanocube Arrays toward an Accelerated Electrocatalytic Effect Employing Heterogeneous Diffusion Field Confinement, Langmuir, 2022, 38, 9597-9610, DOI:10.1021/acs.langmuir.2c01001

polegał na przeprowadzeniu i interpretacji wyników DFT i przygotowaniu części manuskryptu.

dr hab. Paweł Niedziałkowski, prof. UG
Uniwersytet Gdański
Wydział Chemii
Katedra Chemii Analitycznej
Pracownia Elektroanalizy i Biosensorów
ul. Wita Stwosza 63
80-308 Gdańsk

Gdańsk, 06.11.2024

Oświadczenie

Jako współautor publikacji wchodzącej w skład rozprawy doktorskiej mgr Adriana Koterwy oświadczam, że mój wkład w publikację:

Koterwa A., Pierpaoli M., Nejman-Faleńczyk B., Bloch S., Zieliński A., Adamus-Białek W., Jeleniewska Z., Trzaskowski B., Bogdanowicz R., Węgrzyn G., Niedziałkowski P., Ryl J., „Discriminating macromolecular interactions based on an impedimetric fingerprint supported by multivariate data analysis for rapid and label-free Escherichia coli recognition in human urine", Biosensors & Bioelectronics,2023, 238, 115561, DOI:10.1016/j.bios.2023.115561.

polegał na współopracowaniu koncepcji badań i metodologii pomiarów, interpretacji wyników elektrochemicznych, współopracowaniu mechanizmu zmian interakcji receptor-analit, przygotowaniu części manuskryptu wraz z odpowiedzią na recenzję, współfinansowaniu badań.

dr hab. Paweł Niedziałkowski
profesor Uniwersytetu Gdańskiego

Uniwersytet Gdański
Wydział Chemii
Katedra Chemii Analitycznej

dr Mattia Pierpaoli, prof. PG
Politechnika Gdańska
Wydział Elektroniki, Telekomunikacji i Informatyki
Katedra Metrologii i Optoelektroniki
ul. Narutowicza 11/12
80-308 Gdańsk

Gdańsk, 06.11.2024

Oświadczenie

Jako współautor publikacji wchodzącej w skład rozprawy doktorskiej mgr Adriana Koterwy oświadczam, że mój wkład w publikację:

Koterwa A., Pierpaoli M., Nejman-Faleńczyk B., Bloch S., Zieliński A., Adamus-Białek W., Jeleniewska Z., Trzaskowski B., Bogdanowicz R., Węgrzyn G., Niedziałkowski P., Ryl J., „Discriminating macromolecular interactions based on an impedimetric fingerprint supported by multivariate data analysis for rapid and label-free Escherichia coli recognition in human urine", Biosensors & Bioelectronics,2023, 238, 115561, DOI:10.1016/j.bios.2023.115561.

polegał na współopracowaniu metodologii pomiarów, walidacji metody, opracowaniu i interpretacji wyników DEIS, przeprowadzaniu wieloparametrycznej analiza dyskryminacyjnej impedancji (MIDA), przygotowaniu części manuskryptu.

dr hab. inż. Robert Bogdanowicz, prof. PG
Politechnika Gdańska
Wydział Elektroniki, Telekomunikacji i Informatyki
Katedra Metrologii i Optoelektroniki
ul. Narutowicza 11/12
80-308 Gdańsk

Gdańsk, 06.11.2024

Oświadczenie

Jako współautor publikacji wchodzącej w skład rozprawy doktorskiej mgr Adriana Koterwy oświadczam, że mój wkład w publikację:

Koterwa A., Pierpaoli M., Nejman-Faleńczyk B., Bloch S., Zieliński A., Adamus-Białek W., Jeleniewska Z., Trzaskowski B., Bogdanowicz R., Węgrzyn G., Niedziałkowski P., Ryl J., „Discriminating macromolecular interactions based on an impedimetric fingerprint supported by multivariate data analysis for rapid and label-free Escherichia coli recognition in human urine", Biosensors & Bioelectronics,2023, 238, 115561, DOI:10.1016/j.bios.2023.115561.

polegał na współopracowaniu koncepcji badań i metodologii pomiarów, przygotowaniu części manuskryptu wraz z odpowiedzią na recenzję.

dr hab. inż. Robert Bogdanowicz, prof. PG

dr hab. inż. Jacek Ryl, prof. PG
Politechnika Gdańska
Instytut Nanotechnologii i Inżynierii Materiałowej
Zakład Elektrochemii i Fizykochemii Powierzchni
ul. Narutowicza 11/12
80-308 Gdańsk

Gdańsk, 06.11.2024

Oświadczenie

Jako współautor publikacji wchodzącej w skład rozprawy doktorskiej mgr Adriana Koterwy oświadczam, że mój wkład w publikację:

Koterwa A., Pierpaoli M., Nejman-Faleńczyk B., Bloch S., Zieliński A., Adamus-Białek W., Jeleniewska Z., Trzaskowski B., Bogdanowicz R., Węgrzyn G., Niedziałkowski P., Ryl J., „Discriminating macromolecular interactions based on an impedimetric fingerprint supported by multivariate data analysis for rapid and label-free Escherichia coli recognition in human urine", Biosensors & Bioelectronics, 2023, 238, 115561, DOI:10.1016/j.bios.2023.115561

polegał na współopracowaniu koncepcji badań i metodologii pomiarów, interpretacji wyników elektrochemicznych, wykonaniu i interpretacji pomiarów XPS i SEM, analizie pomiarów AFM, współopracowaniu mechanizmu zmian interakcji receptor-analit, przygotowaniu części manuskryptu wraz z odpowiedzią na recenzję, współfinansowaniu badań.

dr. Sylwia Bloch   Gdańsk, 06.11.2024
Uniwersytet Gdański
Wydział Biologii
Katedra Biologii Molekularnej
ul. Wita Stwosza 59
80-308 Gdańsk

Oświadczenie

Jako współautor publikacji wchodzącej w skład rozprawy doktorskiej mgr Adriana Koterwy oświadczam, że mój wkład w publikację:

Koterwa A., Pierpaoli M., Nejman-Faleńczyk B., Bloch S., Zieliński A., Adamus-Białek W., Jeleniewska Z., Trzaskowski B., Bogdanowicz R., Węgrzyn G., Niedziałkowski P., Ryl J., „Discriminating macromolecular interactions based on an impedimetric fingerprint supported by multivariate data analysis for rapid and label-free Escherichia coli recognition in human urine", Biosensors & Bioelectronics, 2023, 238, 115561, DOI:10.1016/j.bios.2023.115561.

polegał na przygotowaniu materiału biologicznego do badań, walidacji metody, przygotowaniu części manuskryptu.

UNIWERSYTET GDAŃSKI
Katedra Biologii Molekularnej

dr Sylwia Bloch

dr hab. Bożena Nejman-Faleńczyk, prof. UG   Gdańsk, 06.11.2024
Uniwersytet Gdański
Wydział Biologii
Katedra Biologii Molekularnej
ul. Wita Stwosza 59
80-308 Gdańsk

Oświadczenie

Jako współautor publikacji wchodzącej w skład rozprawy doktorskiej mgr Adriana Koterwy oświadczam, że mój wkład w publikację:

Koterwa A., Pierpaoli M., Nejman-Faleńczyk B., Bloch S., Zieliński A., Adamus-Białek W., Jeleniewska Z., Trzaskowski B., Bogdanowicz R., Węgrzyn G., Niedziałkowski P., Ryl J., „Discriminating macromolecular interactions based on an impedimetric fingerprint supported by multivariate data analysis for rapid and label-free Escherichia coli recognition in human urine", Biosensors & Bioelectronics,2023, 238, 115561, DOI:10.1016/j.bios.2023.115561.

polegał na współopracowaniu koncepcji badań, przygotowaniu części manuskryptu wraz z odpowiedzią na recenzję.

dr hab. Paweł Niedziałkowski, prof. UG
Uniwersytet Gdański
Wydział Chemii
Katedra Chemii Analitycznej
Pracownia Elektroanalizy i Biosensorów
ul. Wita Stwosza 63
80-308 Gdańsk

Gdańsk, 06.11.2024

Oświadczenie

Jako współautor publikacji wchodzącej w skład rozprawy doktorskiej mgr Adriana Koterwy oświadczam, że mój wkład w publikację:

Koterwa A., Bojko M., Ryl J., Łukaszuk K., Kozłowska K. Sieklicki W., Rodziewicz-Motowidło S., Niedziałkowski P., „An electrochemical biosensor for the determination of hormone Human Chorionic Gonadotropin (hCG) in human serum", Electroanalysis, 2023, vol. 35, nr 11, 1-10, DOI:10.1002/elan.202300095

polegał na współopracowaniu koncepcji badań i metodologii pomiarów, interpretacji wyników, przygotowaniu części manuskryptu wraz z odpowiedzią na recenzję, współfinansowaniu badań.

dr hab. Paweł Niedziałkowski
profesor Uniwersytetu Gdańskiego

Uniwersytet Gdański
Wydział Chemii
Katedra Chemii Analitycznej

dr hab. inż. Jacek Ryl, prof. PG
Politechnika Gdańska
Instytut Nanotechnologii i Inżynierii Materiałowej
Zakład Elektrochemii i Fizykochemii Powierzchni
ul. Narutowicza 11/12
80-308 Gdańsk

Gdańsk, 06.11.2024

Oświadczenie

Jako współautor publikacji wchodzącej w skład rozprawy doktorskiej mgr Adriana Koterwy oświadczam, że mój wkład w publikację:

Koterwa A., Bojko M., Ryl J., Łukaszuk K., Kozłowska K. Sieklicki W., Rodziewicz-Motowidło S., Niedziałkowski P., „An electrochemical biosensor for the determination of hormone Human Chorionic Gonadotropin (hCG) in human serum", Electroanalysis, 2023, vol. 35, nr 11, 1-10, DOI:10.1002/elan.202300095

polegał na konsultacji otrzymanych wyników impedancyjnych, współfinansowaniu badań.

Prof. dr hab. Sylwia Rodziewicz-Motowidło
Kierownik Katedry Chemii Biomedycznej
Wydział Chemii
Uniwersytet Gdański

07.11.2024 r. Gdańsk

OŚWIADCZENIE

Jako współautor publikacji wchodzącej w skład rozprawy doktorskiej mgr Adriana Koterwy oświadczam, że mój wkład w publikację:

Koterwa A., Bojko M., Ryl J., Łukaszuk K., Kozłowska K. Sieklicki W., Rodziewicz-Motowidło S., Niedziałkowski P., „An electrochemical biosensor for the determination of hormone Human Chorionic Gonadotropin (hCG) in human serum", Electroanalysis, 2023, vol. 35, nr 11, 1-10, DOI:10.1002/elan.202300095

polegał na konsultacjach otrzymanych wyników.

KIEROWNIK
Katedry Chemii Biomedycznej

prof. dr hab. Sylwia Rodziewicz-Motowidło

Katedra Chemii
Biomedycznej
Wydział Chemii
Uniwersytet Gdański

tel. +48 523 50 37
e-mail: s.rodziewicz-motowidlo@ug.edu.pl

ul. Wita Stwosza 63
80-308 Gdańsk

www.ug.edu.pl

mgr Kornelia Kozłowska
Uniwersytet Gdański
Wydział Chemii
Katedra Chemii Analitycznej
Pracownia Elektroanalizy i Biosensorów
ul. Wita Stwosza 63
80-308 Gdańsk

Gdańsk, 06.11.2024

Oświadczenie

Jako współautor publikacji wchodzącej w skład rozprawy doktorskiej mgr Adriana Koterwy oświadczam, że mój wkład w publikację:

Koterwa A., Bojko M., Ryl J., Łukaszuk K., Kozłowska K. Sieklicki W., Rodziewicz-Motowidło S., Niedziałkowski P., „An electrochemical biosensor for the determination of hormone Human Chorionic Gonadotropin (hCG) in human serum", Electroanalysis, 2023, vol. 35, nr 11, 1-10, DOI:10.1002/elan.202300095

polegał na pomocy w opracowaniu danych pomiarowych

Kornelia Kozłowska

dr hab. Paweł Niedziałkowski, prof. UG
Uniwersytet Gdański
Wydział Chemii
Katedra Chemii Analitycznej
Pracownia Elektroanalizy i Biosensorów
ul. Wita Stwosza 63
80-308 Gdańsk

Gdańsk, 06.11.2024

Oświadczenie

Jako współautor publikacji wchodzącej w skład rozprawy doktorskiej mgr Adriana Koterwy oświadczam, że mój wkład w publikację:

Koterwa A., Kaczmarzyk I., Mania Sz., Cieślik M., Tylingo R., Ossowski T., Bogdanowicz R., Niedziałkowski P., Ryl J., „The role of electrolysis and enzymatic hydrolysis treatment in the enhancement of the electrochemical properties of 3D-printed carbon black/poly(lactic acid) structures", Applied Surface Science, 2022, vol. 574, 1-13, 151587, DOI:10.1016/j.apsusc.2021.151587

polegał na współopracowaniu koncepcji i metodologii badań, udziale w opisie mechanizmów aktywacji elektrod, przygotowaniu części manuskryptu wraz z odpowiedzią na recenzję, współfinansowaniu badań

dr hab. Paweł Niedziałkowski
profesor Uniwersytetu Gdańskiego

Uniwersytet Gdański
Wydział Chemii
Katedra Chemii Analitycznej

dr inż. Mateusz Cieślik
Politechnika Gdańska
Instytut Nanotechnologii i Inżynierii Materiałowej
Zakład Elektrochemii i Fizykochemii Powierzchni
ul. Narutowicza 11/12
80-308 Gdańsk

Gdańsk, 06.11.2024

Oświadczenie

Jako współautor publikacji wchodzącej w skład rozprawy doktorskiej mgr Adriana Koterwy oświadczam, że mój wkład w publikację:

Koterwa A., Kaczmarzyk I., Mania Sz., Cieślik M., Tylingo R., Ossowski T., Bogdanowicz R., Niedziałkowski P., Ryl J., „The role of electrolysis and enzymatic hydrolysis treatment in the enhancement of the electrochemical properties of 3D-printed carbon black/poly(lactic acid) structures", Applied Surface Science, 2022, vol. 574, 1-13, 151587, DOI:10.1016/j.apsusc.2021.151587

polegał opracowaniu metody druku elektrody w technologii 3D, pomiarach i interpretacji badań elektrochemicznych, przygotowaniu części manuskryptu.

Mateusz Cieślik

dr hab. inż. Jacek Ryl, prof. PG   Gdańsk, 06.11.2024
Politechnika Gdańska
Instytut Nanotechnologii i Inżynierii Materiałowej
Zakład Elektrochemii i Fizykochemii Powierzchni
ul. Narutowicza 11/12
80-308 Gdańsk

Oświadczenie

Jako współautor publikacji wchodzącej w skład rozprawy doktorskiej mgr Adriana Koterwy oświadczam, że mój wkład w publikację:

Koterwa A., Kaczmarzyk I., Mania Sz., Cieślik M., Tylingo R., Ossowski T., Bogdanowicz R., Niedziałkowski P., Ryl J., „The role of electrolysis and enzymatic hydrolysis treatment in the enhancement of the electrochemical properties of 3D-printed carbon black/poly(lactic acid) structures", Applied Surface Science, 2022, vol. 574, 1-13, 151587, DOI:10.1016/j.apsusc.2021.151587

polegał na współopracowaniu koncepcji i metodologii pomiarów, interpretacji wyników elektrochemicznych, wykonaniu i interpretacji pomiarów XPS, udziale w opisie mechanizmów aktywacji elektrod, koordynowaniu prowadzonych prac, dokonaniu przeglądu literaturowego, przygotowaniu części manuskryptu wraz z odpowiedzią na recenzję, współfinansowaniu badań.

prof. dr hab. inż. Tadeusz Ossowski
Uniwersytet Gdański
Wydział Chemii
Katedra Chemii Analitycznej
ul. Wita Stwosza 63
80-308 Gdańsk

Gdańsk, 30.09.2024

Oświadczenie

Jako współautor publikacji wchodzącej w skład rozprawy doktorskiej mgr Adriana Koterwy oświadczam, że mój wkład w publikację:

Koterwa A., Kaczmarzyk I., Mania Sz., Cieślik M., Tylingo R., Ossowski T., Bogdanowicz R., Niedziałkowski P., Ryl J., „The role of electrolysis and enzymatic hydrolysis treatment in the enhancement of the electrochemical properties of 3D-printed carbon black/poly(lactic acid) structures", *Applied Surface Science, 2022, vol. 574, s.1-13, Numer artykułu:151587,* DOI:10.1016/j.apsusc.2021.151587

polegał na konsultacji przy analizie otrzymanych wyników.

prof. dr hab. inż. Tadeusz Ossowski

mgr inż. Iwona Kaczmarzyk
Politechnika Gdańska
Wydział Elektroniki, Telekomunikacji i Informatyki
Katedra Metrologii i Optoelektroniki
ul. Narutowicza 11/12
80-308 Gdańsk

Gdańsk, 06.11.2024

Oświadczenie

Jako współautor publikacji wchodzącej w skład rozprawy doktorskiej mgr Adriana Koterwy oświadczam, że mój wkład w publikację:

Koterwa A., Kaczmarzyk I., Mania Sz., Cieślik M., Tylingo R., Ossowski T., Bogdanowicz R., Niedziałkowski P., Ryl J., „The role of electrolysis and enzymatic hydrolysis treatment in the enhancement of the electrochemical properties of 3D-printed carbon black/poly(lactic acid) structures", Applied Surface Science, 2022, vol. 574, 1-13, 151587, DOI:10.1016/j.apsusc.2021.151587

polegał na przeprowadzeniu badań i interpretacji wyników elektrochemicznych, przygotowaniu części manuskryptu.

dr hab. inż. Robert Bogdanowicz, prof. PG   Gdańsk, 06.11.2024
Politechnika Gdańska
Wydział Elektroniki, Telekomunikacji i Informatyki
Katedra Metrologii i Optoelektroniki
ul. Narutowicza 11/12
80-308 Gdańsk

Oświadczenie

Jako współautor publikacji wchodzącej w skład rozprawy doktorskiej mgr Adriana Koterwy oświadczam, że mój wkład w publikację:

Koterwa A., Kaczmarzyk I., Mania Sz., Cieślik M., Tylingo R., Ossowski T., Bogdanowicz R., Niedziałkowski P., Ryl J., „The role of electrolysis and enzymatic hydrolysis treatment in the enhancement of the electrochemical properties of 3D-printed carbon black/poly(lactic acid) structures", Applied Surface Science, 2022, vol. 574, 1-13, 151587, DOI:10.1016/j.apsusc.2021.151587

polegał na przygotowaniu części manuskryptu wraz z odpowiedzią na recenzję, współfinansowaniu badań.

dr hab. inż. Robert Bogdanowicz, prof. PG